Development of novel techniques for the assessment of inter-laminar resistance in transformer and reactor cores

Hamed Hamzehbahmani

A thesis submitted to the Cardiff University in candidature for the degree of Doctor of Philosophy

Wolfson Centre for Magnetics
Cardiff School of Engineering
Cardiff University
Wales, United Kingdom

August 2014

DECLARATION

This work has not previously been accepted in substance for any degree and is not concurrently submitted in candidature for any degree.

Signed: **Hamed Hamzehbahmani** (candidate) Date: **15-08-2014**

STATEMENT 1

This thesis is being submitted in partial fulfilment of the requirements for the degree of PhD.

Signed: **Hamed Hamzehbahmani** (candidate) Date: **15-08-2014**

STATEMENT 2

This thesis is the result of my own independent work/investigation, except where otherwise stated. Other sources are acknowledged by explicit references.

Signed: **Hamed Hamzehbahmani** (candidate) Date: **15-08-2014**

STATEMENT 3

I hereby give consent for my thesis, if accepted, to be available for photocopying and for inter-library loan, and for the title and summary to be made available to outside organisations.

Signed: **Hamed Hamzehbahmani** (candidate) Date: **15-08-2014**

ACKNOWLEDGEMENTS

This work was carried out at the Wolfson Centre for Magnetics, Cardiff School of Engineering, Cardiff University and financially supported by Cogent Power Ltd. I am really grateful to Cardiff University, Cogent Power Ltd. and ABB for providing the financial support, opportunity and resources required in my study and completing this project.

Initially, I would like to express my deepest gratitude to my academic supervisors, Dr Philip Anderson and Dr Jeremy Hall for their excellent guidance, encouragement, caring, patience, and providing me with an excellent atmosphere during this project. I appreciate their vast knowledge and skill in many areas, and their advice during my study, in writing papers and this thesis.

Besides my supervisors, I would like to express my special thanks to Professor Tony Moses, former director of Wolfson centre, for his encouragement and invaluable guidance and continuous support throughout the project. I would also like to thank the other members of Wolfson centre, Dr Fatih Anayi, Dr Turgut Meydan, Dr Hugh Stanbury and Dr Yevgen Melikhov for their advice and comments at all levels of my research.

I would also like to thank Professor Keith Jenkins, Mr Simon Preece and Mr David Fox from Cogent Power Ltd., Mr Magnus Lindenmo from Cogent Power Surahammar and Dr Kurt Gramm from ABB for contributing industrial expertise and experience into my research.

I would also like to acknowledge Miss Julie Cleaver, Mrs Aderyn Reid, Ms Jeanette C Whyte, Mrs Christine Lee and Ms Chiara Singh in research office and Mr Paul Farrugia, Mr Denley Slade in electronic workshop and Mr Steve Mead, Mr Malcolm Seaborne, Mr Andrew Rankmore, Mr Mal Lyall and Mr Ron Leach and Mr Ian Andrew King in mechanical and civil workshops for taking time out from their busy schedule to help and support my project during my study in Cardiff University.

My greatest thanks are reserved to my family, especially my mother and father, for their unconditional love, support and encouragement in whole of my life.

ABSTRACT

The main aim of this project is to investigate the influence of the inter-laminar short circuit faults on the performance of magnetic cores and develop a non-destructive method to detect these kinds of defects.

The eddy current path in magnetic laminations which is magnetised by time varying magnetic field was modelled by an equivalent resistor network to calculate and predict the eddy current power losses in magnetic laminations. The model was validated over a wide range of magnetisation conditions. Based on the developed model, the influence of a wide range of magnetising frequency and peak flux density on the magnetic properties of electrical steels was studied.

An experimental-analytical technique was developed to separate magnetic loss components over a wide range of magnetisation. Two electrical steel laminations, Conventional Grain Oriented (CGO) and Non-Oriented (NO), were used in the experimental work of the relevant studies.

2-D FE based modelling was performed to simulate inter-laminar faults on stacks of laminations and visualise the distribution of eddy currents in the faulted laminations. The influence of inter-laminar faults on the eddy current power loss was experimentally investigated by introducing artificial short circuits of different configurations on stacks of Epstein size laminations of GO steel.

A non-destructive test method was developed to detect inter-laminar fault between the laminations of the magnetic cores by means of Flux Injection Probe (FIP). A prototype model of a FIP was developed and its application to quality assessment of transformer core laminations was investigated.

The research presented here can be utilised by electrical steel manufacturers and electrical machine designers to survey the effect of inter-laminar faults on the magnetic properties of magnetic cores and their quality assessment, to reduce the risk of core damage or machine failure caused by the inter-laminar faults.

LIST OF ABBREVIATIONS AND NOMENCLATURES

Abbreviations

UNFCCC	United Nations Framework Convention On Climate Change
GHG	Greenhouse Gas
SMM	Soft Magnetic Materials
HV	High Voltage
EHV	Extra High Voltage
LV	Low Voltage
FE	Finite Element
EL CID	Electromagnetic Core Imperfection Detector
FIP	Flux Injection Probe
DC	Direct Current
AC	Alternating Current
STDV	Standard Deviation
B	Magnetic Flux Density
H	Magnetic Field Strength
PWM	Pulse Width Modulation
GO	Grain Oriented Electrical Steel
CGO	Conventional Grain Oriented Electrical Steel
NO	Non-Oriented Electrical Steel
RD	Rolling Direction
TD	Transverse Direction
HiB	High Permeability Grain Oriented Electrical Steel
Si	Silicon
Fe	Iron
SST	Single Strip Tester
DAQ	Data Acquisition Card
2-D	Two Dimensional
3-D	Three Dimensional
FF	Form Factor
CC	Correction Coefficient
EDM	Electric Discharge Machining

Nomenclatures

P_{CU}	Copper losses
P_L	Load losses
P_C	Core losses
$P_{N\text{-}L}$	No-load losses
P_m	Magnetic losses
P_{me}	Mechanical losses
P_{edd}	Eddy current loss
P_h	Hysteresis loss
P_{ex}	Excess loss
J	Eddy current density
R_{eq}	Equivalent resistance of the laminations
R_{ct}	Resistance of the burr or contact resistance
U_{oc}	Open circuit voltage
I_{sc}	Short circuit current
I_e	Excitation current
φ_e	Excitation magnetic flux
V_s	Measured probe voltage
V_{se}	Probe voltage
φ_{se}	Excitation flux component
I_f	Fault current
V_f	Fault voltage
φ_f	Fault flux
v_s	Measurement winding voltage
i_e	Excitation current
N_e	Number of turns of excitation winding
N_s	Number of turns of measurement windings
T	Time period
φ_{str}	Magnetic flux leakage
u_M	Amplitude of measured voltage without inter-laminar fault
α_M	Phase of measured voltage without inter-laminar fault
u_{MF}	Amplitude of measured voltage with inter-laminar fault
α_{MF}	Phase of measured voltage with inter-laminar fault
μ_0	Permeability of vacuum
C_2	Inter-laminar capacitance of two adjacent laminations

R_2	Inter-laminar resistance between adjacent laminations
i_{edd}	Eddy currents
f	Frequency
μ	Absolute magnetic permeability
σ	Electrical conductivity
δ	Skin depth
ρ	Electrical resistivity
I_{pk}	Peak magnetising current
μ_r	Relative permeability
μ_r'	Real part of complex permeability
μ_r''	Imaginary part of complex permeability
μ_z	Absolute static permeability
B_{pk}	Peak flux density
$2a$	Thickness of lamination
B_s	Flux density at lamination surface
B_x	Local flux density
R_y	Ohmic resistance of the material along the width of the lamination
R_x	Ohmic resistance of the material along the thickness of the lamination
e_{rms}	RMS induced voltage in a lamination
w	Width of lamination
h	Length of lamination
v	Volume of lamination
R_{sh}	Shunt resistor
$V_{R\text{-}sh}$	Voltage drop across the shunt resistor
l_m	Mean path length
m	Mass of the specimen
ρ_m	Density of the sample
k_h	Hysteresis loss coefficient
k_e	Eddy current loss coefficient
k_{ex}	Excess loss coefficient
B_{av}	Average value of flux density inside the lamination
$\mathcal{R}_m$	Magnetic reluctance

TABLE OF CONTENTS

CHAPTER 1 INTRODUCTION AND OBJECTIVES OF THE PROJECT

CHAPTER 2 MAGNETISM, MAGNETIC MATERIALS AND RELATED ISSUES

CHAPTER 3 PREVIOUS RELATED WORK

CHAPTER 5 IRON LOSS SEPARATION AND EXPERIMENTAL RESULTS OF EDDY CURRENT POWER LOSS OF SINGLE STRIPS

CHAPTER 6 MODELLING AND ANALYSIS OF EDDY CURRENT POWER LOSS OF MAGNETIC CORES AFFECTED BY INTER-LAMINAR FAULTS AND EXPERIMENTAL RESULTS

CHAPTER 7 EXPERIMENTAL STUDY ON INTER-LAMINAR SHORT CIRCUIT FAULTS AT RANDOM POSITIONS IN LAMINATED MAGNETIC CORES

CHAPTER 8 INTER-LAMINAR INSULATION FAULT DETECTION IN MAGNETIC CORES USING FLUX INJECTION PROBE

CHAPTER 9 GENERAL CONCLUSION AND SUGGESTIONS

APPENDIX I LIST OF PUBLICATIONS

APPENDIX II REMEMBRANCE

LIST OF TABLE CAPTIONS

CHAPTER 2

CHAPTER 3

CHAPTER 4

CHAPTER 5

CHAPTER 6

CHAPTER 7

CHAPTER 8

LIST OF FIGURE CAPTIONS

CHAPTER 2

CHAPTER 3

CHAPTER 4

CHAPTER 5

CHAPTER 6

CHAPTER 7

CHAPTER 8

CHAPTER 1

Introduction and Objectives of the Project

1.1. Introduction

Reducing climate change and achieving stabilisation of greenhouse gas atmospheric concentrations is the objective of the United Nations Framework Convention on Climate Change (UNFCCC). This requires significant reduction in global energy related to Carbon Dioxide (CO_2) emissions. G-8 leaders requested a 50 % reduction in greenhouse gas (GHG) emissions by 2050 to prevent the most serious effects of climate change on the world. Achieving this goal requires reviewing and changing the methods of energy production, transmission and consumption across all regions of the world [1.1]. In this respect, higher efficiency or lower losses has been considered as a major challenge in all energy resources and related facilities.

Electrical energy, as a major resource of energy, has a significant impact on the CO_2 emission. Total power loss of the electric networks of EU countries is approximately 7-8 % of the total electric power production. For this, high voltage (HV) and extra high voltage (EHV) transmission line losses are approximately 34 %, medium and low voltage (LV) distribution line losses are 36 % and distribution transformer losses are 30 % of total energy loss [1.2].

Compared to other electrical machines, motors and generators, transformers are very efficient. Typical efficiencies of transformers are better than 97 % and for the largest units operating and under efficient loads are up to 99.9 %. In EU countries there are nearly 5 million distribution transformers in operation and therefore they contribute approximately 30 million tons of CO_2 emissions. Total power losses of the distribution transformers are about 2-3 % of the total electric power production. The total power losses in the distribution transformers can be estimated as 30 % copper losses P_{CU} or load losses P_L that depend on the transformer load; and 70 % core losses P_C or no-load losses P_{N-L} also called magnetic losses P_m which depend on the voltage applied to the transformer [1.2].

1.2. Magnetic losses in magnetic cores

Electrical machines, i.e. motors, generators and transformers, are integral and vital parts of industry and power systems. In the design and analysis of electric machines, power loss plays an important role which is usually divided into three major categories; copper losses P_{cu}, mechanical losses P_{me} and magnetic losses P_c. The copper loss takes place in the electrical windings of the machine. The mechanical loss arises from the rotation of the rotating part of rotating machines (or from the movement of the sliding part of linear machines). The two main sources of the magnetic loss in transformers, and other magnetic devices, are the eddy current loss P_{edd} and the hysteresis loss P_h [1.3]-[1.5]. This work is specifically focused on the eddy current power loss in laminated magnetic cores, which have been shown to be extremely significant.

Magnetic cores are one of the main parts of the electrical machines and other magnetic devices. The main role of the magnetic core is to concentrate the magnetic field to make the maximum possible magnetic coupling between the primary and secondary windings of a transformer, or stator and rotor of a rotating machine [1.6]. Since magnetic cores are exposed to time-varying magnetic fields, eddy currents are induced in the cores and consequently, energy is converted into heat in the resistance of the eddy current path [1.7]. This process results in power loss which is known as eddy current power loss.

A practical way to minimise eddy current power loss, and heating of the magnetic cores, is to make them highly resistive against eddy currents by minimising length of the eddy current path. This can be achieved by dividing them into thin laminations. Magnetic cores of commercial electrical machines, and other magnetic devices, are constructed from stacks of electrical steel laminations, typically 0.23-0.50 mm thick. Laminations are separated electrically by insulating layers to prevent electrical contact between them and pressed together using clamping devices [1.8]–[1.9]. This limits the circulation of eddy currents to the thickness of a single lamination, rather than the whole core, and hence reducing the eddy current power loss and the overall heating effect in the magnetic cores [1.6].

1.3. Inter-laminar short circuit faults

The design and operation of electrical machines, requires accurate quantification of core losses over a wide range of frequency and magnetic flux density by taking into account critical circumstances. One of the major critical circumstances in electrical machines is inter-laminar short circuit faults between the laminations of the cores and its consequences on the power loss and other magnetic properties.

Inter-laminar short circuit faults lead to circulating eddy currents between the laminations, which are larger than in normal operation. Inter-laminar faults could lead to excessive local power loss and local heating in the damaged area and may eventually cause burning or melting the iron core and thus it raises the potential of a complete machine failure [1.10]–[1.14]. Inter-laminar faults, which lead to inter-laminar fault current between the laminations, are one of the main concerns at the design and manufacturing of electrical machines and other magnetic devices. Interests in the study of the quality of magnetic cores, the impact of inter-laminar faults on power loss, and other properties of the machines, and detection of these kinds of faults have grown. This is because of the demands of overall quality and efficiency improvement of the systems.

1.4. Objectives of the project and structure of the thesis

Causes of inter-laminar short circuit faults in magnetic cores are well known. It is also distinguished that the main consequence of the inter-laminar faults in a magnetic core is increasing the eddy current power loss and hence total core losses of the machine [1.10]–[1.14]. Therefore it is widely accepted that the magnetic cores should be safeguarded against this kind of fault. However the effect of inter-laminar faults on the equivalent configuration and magnetic properties of the magnetic cores and related issues are still questionable and a greater understanding is required to find the answers. Previous research is mainly focused on experimental investigations considering inter-laminar faults between adjacent laminations of the core at set points [1.15]–[1.18]. Analytical models have been also reported to predict the effect of inter-laminar faults on eddy current power loss, and some other magnetic properties of the core [1.17]–[1.18]. However some determinant factors, e.g. skin effect, has been ignored to simplify modelling and investigation of the inter-laminar faults. Additionally, no conclusive agreement has been reported between the prediction and experimental results.

Considering the above issues, this project was oriented to achieve the following objectives:

1. Develop enhanced modelling techniques for eddy current power loss in steel laminations
2. Create models for laminated stacks subjected to inter-laminar faults
3. Experimentally investigate the effect of inter-laminar faults on power loss of laminated stacks

4. Develop novel non-destructive method for the detection of edge defects in core stacks

In order to achieve these aims, an analytical model was initially developed to estimate eddy current power loss in magnetic cores over a wide range of flux density and magnetising frequency in which skin effect, complex relative permeability and non-linearity of the material were highlighted. The model was then modified to predict extra power loss of stacks of laminations caused by the inter-laminar faults.

In the experimental part of the project inter-laminar faults were introduced artificially along sides of stacks of Epstein size laminations of 3 % grain oriented silicon steel and total power loss was measured at peak flux densities up to 1.7 T and magnetising frequencies up to 1 kHz. The results were compared and supported by the analytical results. Experimental works were also performed to study the effect of inter-laminar short circuit faults at random positions on the total power loss of stacks of laminations. A non-destructive magnetic method was also developed by means of a Flux Injection Probe (FIP) to detect inter-laminar faults between laminations.

References

[1.1] D Maheswaran, K K Jembu Kailas, "*Energy Efficiency in Electrical Systems*", Proceeding of IEEE International Conference on Power Electronics, Drives and Energy Systems, Dec, *Bengaluru,* India 2012

[1.2] S. Yurekten, A. Kara, K. Mardikyan, "*Energy Efficient Green Transformer Manufacturing With Amorphous Cores*", Proceeding of International Conference on Renewable Energy Research and Applications, Madrid, Spain 2013

[1.3] Y. Zhang, M.C. Cheng, and P. Pillay, "*A Novel Hysteresis Core Loss Model for Magnetic Laminations,*" IEEE Trans. Energy Convers., vol. 26, no. 4, pp. 993–999, Dec. 2011.

[1.4] G. Bertotti, "*General Properties of Power Losses in Soft Ferromagnetic Materials*," IEEE Trans. Magn. Vol. 24, January1988 pp. 621-630

[1.5] Y. Chen and P. Pillay, "*An Improved Formula for Lamination Core Loss Calculations in Machines Operating With High Frequency and High Flux Density Excitation*," IEEE 37th IAS Annual Meeting, vol. 2, 13-18 Oct 2002, pp. 759–766

[1.6] B S Guru, H R Hiziroglu, "*Electric Machinery and Transformers*", Third edition, Oxford university press, 2001

[1.7] Z Popovic, B D Popovic "*Introductory Electromagnetics*" Prentice Hall, 1999

[1.8] G. A. McCo, T. Litman, and J. D. Douglass, "*Energy-Efficient Electric Motor Selection Handbook",* Portland, OR: Bonneville Power Administration, Jan. 1993, Rev. 3.

[1.9] M. Ibrahim and P. Pillay, "*Advanced Testing and Modelling of Magnetic Materials Including a New Method of Core Loss Separation for Electrical Machines*" IEEE Transaction on Industry Applications, Vol. 48, NO. 5, Sep/Oct 2012, pp. 1507 – 1515

[1.10] S B Lee, G B Kliman, M R Shah, W T Mall, N K Nair and R M Lusted "*An Advanced Technique for Detecting Inter-Laminar Stator Core Faults in Large Electric Machines*" IEEE Trans On Ind. App, Vol. 41, NO. 5, Sep/Oct 2005, pp. 1185–1193

[1.11] S B Lee, G B Kliman, M R Shah, N K Nair and R M Lusted "*An Iron Core Probe Based Inter-Laminar Core Fault Detection Technique for Generator Stator Cores*" IEEE Trans. Energy Convers., Vol. 20, No. 2, Jun. 2005, pp. 344–351

[1.12] S B Lee, G Kliman, M Shah, D Kim, T Mall, K Nair and M Lusted, "*Experimental Study of Inter-Laminar Core Fault Detection Techniques Based on Low Flux Core Excitation*" IEEE Trans On Energy Convers, Vol. 21, No. 1, March 2006, pp 85-94

[1.13] C A Schulz, S Duchesne, D Roger and J N Vincent "*Short Circuit Current Measurements Between Transformer Sheets*", IEEE Trans Magn, VOL. 46, NO. 2, Feb 2010, pp 536-539

[1.14] C A Schulz, D Roger, S Duchesne and J N Vincent, "*Experimental Characterization of Interlamination Shorts in Transformer Cores*", IEEE Trans Magn, VOL. 46, NO. 2, Feb 2010, 614-617

[1.15] M B Aimoniotis and A J Moses, "*Evaluation of Induced Eddy Currents in Transformer Sheets Due to Edge-Burrs, Employing Computer Aided Design Programs*," in Athens Power Tech '93 Proc., 1993, VOL. 2, pp. 847–849

[1.16] A J Moses and M Aimoniotis, "*Effects of Artificial Edge Burrs on the Properties of A Model Transformer Core*," Physica Scripta, VOL. 39, 1989, pp. 391–393

[1.17] R Mazurek, P Marketos, A J Moses and J N Vincent "*Effect of Artificial Burrs on the Total Power Loss of a Three-Phase Transformer Core*", IEEE Trans. Magn., VOL. 46, NO. 2, 2010, pp.638 -641

[1.18] E Lamprecht, R Gräf, "*Fundamental Investigations of Eddy Current Losses in Laminated Stator Cores Created Through the Impact of Manufacturing Processes*" 1st International conference on Electric Drives Production (EDPC), Sept. 2011, pp. 29-35.

CHAPTER 2

Magnetism, Magnetic Materials and Related Issues

2.1. Introduction

Electrical steels, as the most important magnetic material, are marketed mainly in terms of magnetic power loss performance under a particular peak flux density and power frequency of 50 Hz or 60 Hz. Magnetic permeability of electrical steel is also considered as an important property. In this chapter, the basic background related to the work carried out in the thesis are described. Fundamental terms in magnetic, magnetic materials, magnetisation process and magnetic power loss mechanisms in electrical steel are discussed. Theory of transformer and related issues are also studied.

2.2. Fundamental Terms in Magnetism

Magnetic fields are generated by moving electric charges such as current-carrying wire or the orbital motions and spins of electrons in a permanent magnet [2.1]. The response of a material to an external magnetic field ***H*** is known as magnetic induction or magnetic flux density ***B***. Magnetic field is measured in Amps/meter (*A/m*) and magnetic flux density in Tesla (*T*). The relationship between ***B*** and ***H*** is a characteristic feature of the material itself. In vacuum or free space there is a linear correlation between ***B*** and ***H*** and defined by [2.2]:

$$\boldsymbol{B} = \mu_0 \boldsymbol{H} \tag{2-1}$$

where μ_0 is permeability of vacuum or free space and equal to $\mu_0 = 4 \times \pi \times 10^{-7}$ (*H/m*). Local amplitude and direction of ***B*** and ***H*** might be different inside the material, which is explained by Magnetisation ***M*** and is related to ***B*** and ***H*** by [2.3]:

$$\boldsymbol{B} = \mu_0 (\boldsymbol{H} + \boldsymbol{M}) \tag{2-2}$$

The magnetic flux density ***B*** is not always a good measure to characterise magnetic properties of a magnetic material since it may include contributions from external magnetic sources. The inherent properties of a given material are therefore always characterised by the Magnetisation ***M*** (A/m) or magnetic polarisation ***J*** (Tesla). Therefore equation (2-2) can be written as [2.4]:

$$\boldsymbol{B} = \mu_0 \boldsymbol{H} + \boldsymbol{J} \tag{2-3}$$

where $\boldsymbol{J} = \mu_0 \boldsymbol{M}$ is defined as the magnetic polarisation. For magnetic materials, the magnetisation ***M*** is related to the magnetic field ***H*** by:

$$\boldsymbol{M} = \chi \boldsymbol{H} \tag{2-4}$$

where χ is susceptibility of the material. Substituting (2-4) in (2-2) gives:

$$\boldsymbol{B} = \mu_0 (1 + \chi) \boldsymbol{H} = \mu_0 \mu_r \boldsymbol{H} \tag{2-5}$$

where $\mu_r = 1 + \chi$ is relative permeability of the material. Permeability quantities the ability of a material to respond to the applied magnetic fields.

2.3. Classification of the Magnetic Materials

Magnetic materials are classified by means of the susceptibility χ or relative permeability μ_r. Paramagnetic materials such as air and aluminium have a relative permeability slightly higher than unity. Diamagnetic material such as copper has μ_r marginally less than unity. Both of these materials respond linearly to an applied magnetic field. Relative permeability of some diamagnetic and paramagnetic materials are shown in Tables 2-1 and 2-2, respectively [2.5].

Table 2-1 Relative permeability μ_r of some diamagnetic materials [2.5]

Material	Relative Permeability
Bismuth	0.999 981
Beryllium	0.999 987
Copper	0.999 991
Methane	0.999 969
Silver	0.999 980
Water	0.999 991

Table 2-2 Relative permeability μ_r of some paramagnetic materials [2.5]

Material	Relative Permeability
Air	1.000 304
Aluminium	1.000 023
Oxygen	1.001 330
Manganese	1.000 124
Palladium	1.000 800
Platinum	1.000 014

Relative permeability of ferromagnetic materials are much greater than unity and vary with the applied magnetic field ***H***. Electrical steels are one of the most common types of ferromagnetic materials and are widely used in electrical machines and magnetic devices. These materials will be discussed in the next section.

2.4. Electrical Steels

Electrical steels are the most important soft magnetic materials (SMM) which are used as the magnetic core of transformers, rotating machines and other magnetic devices. Magnetic permeability and electric resistivity of the core material are two determinant factors in the qualification of the material, performance of the core and the electrical machines themselves. Hadfield et al. in 1903 discovered that adding a small amount of silicon or aluminium to high purity iron increases the electrical resistivity of the material which causes a reduction of magnetic loss by a factor of four [2.6]. Adding silicon also results in high magnetic permeability and prevents aging of the steel. The silicon content used by Hadfield was around 2 % in weight [2.7]; modern electrical steels have a silicon content of about 3.2 wt % which results in a high resistivity of about 50×10^{-8} Ω.m [2.3]. Although higher silicon content creates even higher resistivity, it makes the material extremely brittle and difficult to produce, roll and handle during the machining process. The brittleness restricts the maximum silicon content to 3.4 % in commercial material [2.6]. However Abe et al. in 1989 showed that the best magnetic properties are achieved by 6.65 % wt silicon content [2.7].

Electrical steels are manufactured as thin sheet laminations of thicknesses from 0.1 mm to 1.0 mm, and coated on either side to prevent electrical connection between the adjacent layers in the stacks. Electrical steels are qualified based on the specific power loss in W/Kg under AC magnetisation at a particular operating frequency and a particular peak flux density [2.9]. Texture (orientation of the grain material) is one of the most important parameters to determine the magnetic properties of the steels. “The texture is a population of crystallographic orientations whose individual components are linked to their location within the microstructure” [2.9]. Goss in 1934 proposed a texture layout for silicon steels to describe the direction of the magnetisation. The basic model of Goss layout is shown in Fig 2-1 [2.10].

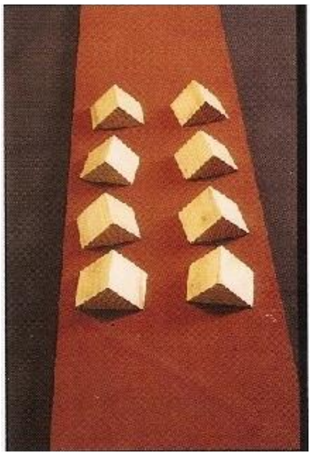

Fig 2-1 Model of Goss layout of GO steels [2.10]

Based on the Goss layout modem commercial magnetic materials are classified into non-oriented (NO) and grain-oriented (GO) electrical steels. This classification is actually based on the orientation of the texture or magnetic anisotropy of the materials [2.6].

2.4.1. Non Oriented (NO) electrical steels

Non-oriented electrical steels are silicon steels in which magnetic properties are practically the same in any direction of magnetisation in the plane of the material. The ideal texture for a non-oriented silicon steel is a random cube texture [001], where each grain has the [100] plane in the sheet plane, and the properties are nearly isotropic [2.9].

In magnetic cores of rotating machines, the field is in the plane of the sheet, but the angle between the field and rolling direction is variable. NO electrical steel laminations are mainly used in motor and generator stator cores, where good isotropic magnetic properties are required, and E-I laminations of small transformer cores [2.8] – [2.11]. Statistical data show that NO electrical steels account for more than 90 % of the total electrical steel production in the world. Non-oriented electrical steel sheets are usually manufactured in thicknesses of 0.35 mm, 0.50 mm, 0.65 mm and 1.00 mm and are classified according to the value of the maximum specific total loss in W/kg [2.9].

2.4.2. Grain Oriented (GO) electrical steels

Grain oriented electrical steel was first discovered by Norman Goss in 1930 and was commercialised by Armco in 1940. It is a 3 wt % silicon iron alloy with an considerably large grain size. The grains of the material are oriented in a specific direction to achieve exceptionally good magnetic properties in one direction. Goss texture of GO material is in the [001] direction in the length of the lamination. The <001> type texture directions are the easy directions of magnetisation and therefore creates high magnetic permeability and low magnetic losses [2.11]–[2.12]. In transformer cores, the magnetisation direction is always parallel to the length of the limbs and yokes of the core, and therefore GO steels are the ideal material to manufacture of these cores [2.12].

The improvement in the magnetic properties of GO steels has continued almost without stop since it was commercialised. Grain alignment of GO steels was improved by Nippon steel in 1970 to produce an improved class of GO steel of 3.25 % silicon content with higher permeability. This material was branded as HiB, also known as highly grain oriented HGO. Therefore from mid of 1970s two types of GO steel have been produced: Conventional Grain Oriented (CGO) and improved grades (HGO) [2.11]. The average angle of the grade alignment with the rolling direction (RD) is around 7^o in CGO and 3^o in HiB steel, and therefore HiB steel is more isotropic material with higher permeability and lower power loss in RD [2.13]–[2.15]. GO electrical steel laminations are produced normally in thicknesses from 0.23 mm to 0.35 mm.

As an example, the average power losses of GO steel produced by Cogent Orb works, reflecting the recent development of GO steel in terms of power loss reduction is shown in Fig 2-2 [2.11].

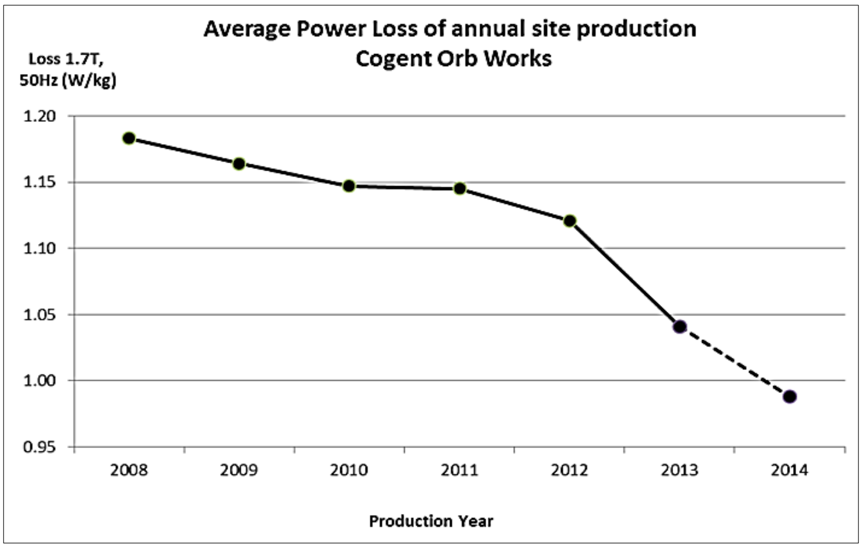

Fig 2.2 Average power loss of annual site production by Cogent Orb Works [2.10]

Based on the Goss layout of Fig 2-1, isotropic texture of NO steel and anisotropic texture of GO steel are shown schematically in Figs 2-3-a and 2-3-b, respectively.

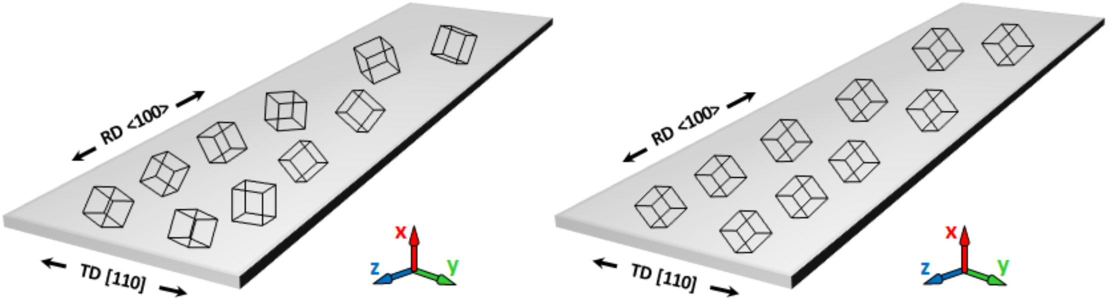

(a) (b)

Fig 2-3 (a) Isotropic texture of NO steel grains (b) anisotropic texture of GO steel grains (reproduced based on [2.16])

2.5. Magnetisation Process in Ferromagnetic Materials

A magnetic circuit comprises of a ferromagnetic core and a winding carrying current *i* to generate magnetic field ***H*** in the core is shown in Fig 2-4-a. A typical magnetisation curve, also known as the *B*-*H* loop or hysteresis loop of this magnetic circuit is shown in Fig 2-4-b.

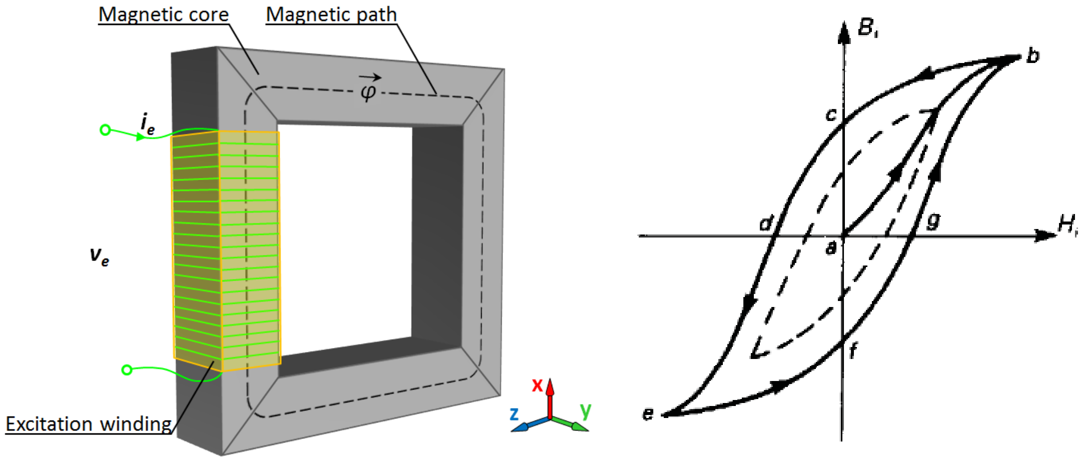

(a) (b)

Fig 2-4 (a) 3-D view of a basic magnetic circuit (b) typical *B-H* loop of a ferromagnetic material showing initial magnetisation path (*ab*), saturation point (at *b*) remanence (at *c*), the coercive force (at *d*), and an inner loop (dotted curve) [2.17]

A hysteresis loop shows the relationship between the magnetic flux density ***B*** and the applied magnetic field ***H***. Hysteresis loops can be obtained by changing the magnetic field ***H*** and measuring the magnetic flux ***B*** in the magnetic circuit. The magnetisation process of ferromagnetic materials depends not only on the applied magnetic field, but also on the magnetisation history of the material. If an external magnetic field ***H*** is applied to a demagnetised ferromagnetic material, the magnetisation process can be then represented by point *a* at the origin of the *B-H* loop. By increasing the magnetising current of the coil gradually, the *B-H* curve follows the path *a-b* which is known as "initial magnetisation curve" of the material. After point *b* an additional increase in the magnetic field leads to very little increase in the magnetic flux density. This region is known as "magnetic saturation" [2.16]. Magnetic saturation is an important inherent property of the ferromagnetic materials which determines the maximum level of the magnetic flux that can be achieved by the material [2.19].

By reducing the current *i* in the magnetising coil, flux density does not go back over curve *a-b*; it follows a different curve. At point *c*, when the magnetising current is zero, it can be seen that some magnetic flux remains in the material. The value of the flux density at point *c* is "remanent flux density". In order to reduce the magnetic flux to zero, the magnetising current should be reversed. The value of magnetic field to return the flux density to zero, point *d*, is known as the "coercive field" or "coercivity of the material". As the magnetising current is increased beyond the coercive field, the material again goes to magnetic saturation, but in the opposite direction. Reducing the current to zero and increasing in the positive direction returns the flux density ***B*** to zero. It should be noted that the curve does not return to the origin of the *B-H* loop as some field is required to remove the remanent flux density. By increasing the current in the positive direction, the hysteresis loop of *bcdefgb* will form [2.16], as shown in Fig 2-4-b.

Magnetic properties of the magnetic materials are defined based on the hysteresis loop and its key points. From this point, magnetic materials are classified into two categories [2.17]:

Soft Magnetic Materials have a narrow hysteresis loop, low remanent flux density and small coercive field; and therefore they can be magnetised and demagnetised easily. The magnetic behaviour of the soft magnetic materials can be approximated by their initial magnetisation curve, path *a-b* of Fig 2-4-b.

Hard Magnetic Materials have wide hysteresis loop, high remanence flux density and high coercive field. These materials are used in permanent magnets.

Typical hysteresis loops for soft and hard magnetic materials are shown in Fig 2-5.

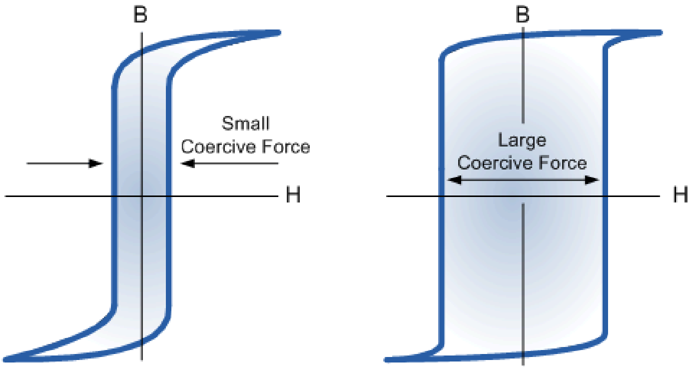

(a) (b)

Fig 2-5 Comparison between hysteresis loops of (a) soft and (b) hard magnetic materials [2.18]

2.6. Magnetic Power Losses in Magnetic Materials

AC magnetisation process of the magnetic material results in power dissipation in the material which is known as “magnetic power losses”. Magnetic loss, also known as core loss or iron loss, is the most important quantity for the characterisation of the quality of the electrical steel laminations. Magnetic power losses of the electrical steels are usually available in watts per kilogram (W/kg) at a given magnetising frequency and peak flux density and therefore it is important to understand how these losses arise in the magnetic materials. Eddy current power loss and hysteresis power loss are two of the main sources of the magnetic losses. In operation, both losses are present and should be taken into account in the design and analysis of the electrical steels and magnetic cores [2.3]. A more detailed model of magnetic losses is given in chapter 4.

2.6.1. Eddy current power loss

When a time-varying magnetic field is applied to a conducting material, an *emf* is induced in the material, in accordance with Faraday's law of induction. Considering the electrical conductivity of the material, the induced *emf* across a closed path inside the material sets up a current along that path to circulate and penetrate conducting parts. The direction of the eddy current is perpendicular to the direction of the magnetic field, while the distribution pattern depends on the shape of the conductor.

Eddy currents are induced in any conducting material exposed to time-varying magnetic fields, and therefore they occur in all types of electrical equipment which are operating by time-varying magnetic fields. The induced eddy current in magnetic cores of electrical machines, which is the main discussion of this thesis, is converted to heat in the resistance of the eddy current path, which is known as *eddy current power loss* [2.3] and [2.21].

2.6.2. Hysteresis power loss

The area of the hysteresis loop of the magnetic materials has an important physical concept. It indicates the amount of energy converted into heat during one cycle of the magnetisation process [2.21]. Ferromagnetic materials have a number of domains in their structures. Domains are very small regions in the magnetic material and are like small permanent magnets placed in random positions. An example of domain structure of a typical unmagnetised GO electrical steel is shown in Fig 2-6.

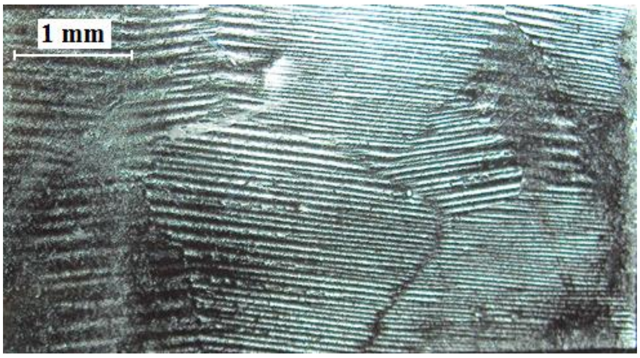

Fig 2-6 Domain structure of a typical grain oriented steel

In a non-magnetised material the domains are arranged in such a pseudo-random manner, that the resultant magnetic field of the material is zero. This situation corresponds to the point "*a*" of the hysteresis loop of Fig 2-4-b. When the material is exposed to an external magnetic field, the randomly directed domains of the material align in parallel to the axis of the applied field, point "*b*" of the curve. After removing the external field, some of the domains remain in their aligned position, which create the remanent flux density in the material. An opposite magnetic field is required to return all of the domains to the randomly distributed position, which is known as the demagnetising field. The demagnetising process, which corresponds to path *c-d* of the ***B-H*** curve and is happening in each cycle of the magnetisation, requires consumption of electrical power which is known as Hysteresis power loss [2.3] and [2.20].

The word "hysteresis" is extracted from ὑστέρησις, an ancient Greek word meaning "deficiency" or "lagging behind". Description of the magnetic properties of the magnetic materials by the Hysteresis term was initially coined by Sir James Alfred Ewing in 1890 [2.22].

Experimental methods are available to measure magnetic power loss of the magnetic material. The standard methods of measuring magnetic losses of the electrical steels are Epstein frame [2.23] and single strip tester [2.24]. Frequency-dependent measurements are also available to separate the components of the magnetic losses [2.25]-[2.26].

2.7. Transformers

Transformers are electric devices that transform AC electric power at one voltage level to AC electric power at a different voltage level, but at the same frequency, using the action of a magnetic field. Transformers basically consist of two, or more, windings wound around a ferromagnetic core. The windings are linked together through a common magnetic field in the core. One of the windings is connected to an AC power source and the other one connected to the load; the former is known as primary winding and the latter as secondary winding [2.27]. The power transferred between the winding is unchanged, except for a typically small power loss that occurs in the transformation process [2.17].

Operation of the transformers is based on the principle of the magnetic induction discovered by Michael Faraday in 1831[1]. He discovered that when time varying magnetic field links a circuit, a voltage is induced which is proportional to the number of turns linked by the magnetic flux. Therefore if two windings with different number of turns are linked by a common time varying magnetic field, different voltages will induce in the windings [2.17]. The basic configuration of a transformer in which the magnetic core carries a time varying magnetic flux as a

---

[1] Electromagnetic induction was discovered independently by Michael Faraday and Joseph Henry in 1831; however, Faraday was the first person who published the results.

common magnetic field between the primary and secondary windings is shown in Fig 2-7-a. Faraday's original transformer, made from two coils of copper wire insulated with cotton and wrapped around a solid soft iron core of outer diameter of 6 inches is shown in Fig 2-7-b.

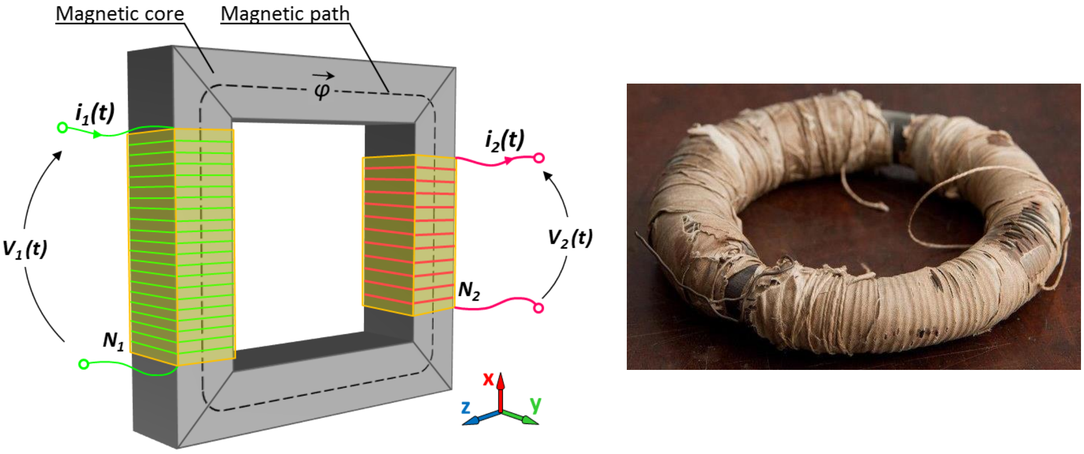

(a) (b)

Fig 2-7 (a) Basic configuration of a transformer
(b) Faraday's original transformer with solid soft iron, made in 1831 [2.27]

Transformers are nowadays vital and integral parts of modern life and are available from very small scale and capacity to very large sizes and are applicable in different purposes. Regardless of the size and application, principle of all of transformers is the same. One of the major applications of the transformers is in power systems to transform voltage level between different parts of the grids. These transformers are categorised in two parts. Step-up transformers are located in power stations to increase the output voltage of the power generators to the suitable transmission line voltage level. Step-down transformers convert the high voltage of the transmission line to a suitable distribution voltage level and deliver the electric power to the loads and consumers. A typical step-up power transformer of 21.5/500 KV and a typical step-down distribution transformer of 20/0.4 KV are shown in Figs 2-8-a and 2-8-b, respectively.

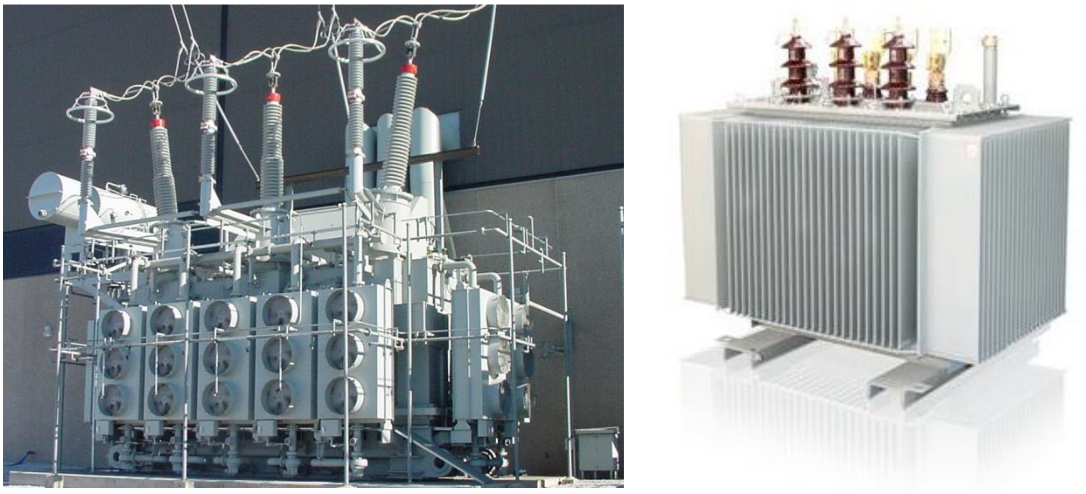
(a) (b)

Fig 2-8 (a) Three phase 21.5/500 KV generator step-up transformer [2.28]
(b) three phase 20/0.4 KV step-down distribution transformer [2.29]

2.7.1. Theory of transformers

The theory of transformers can be initially studied by means of an ideal transformer which is defined as a lossless device with infinite magnetic permeability in the magnetic core. Schematic and model of an ideal transformer are shown in Figs 2-9-a and 2-9-b, respectively.

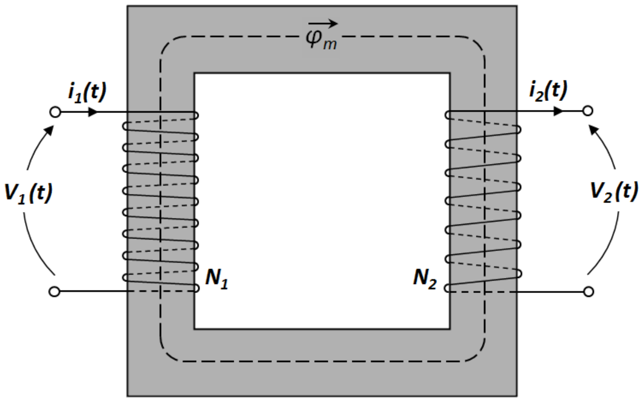

(a)

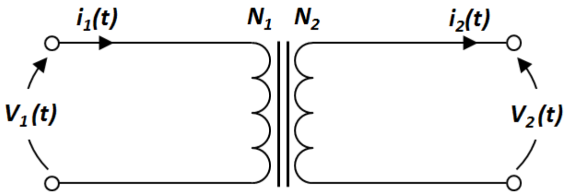

(b)

Fig 2-9 (a) Schematic and (b) model of an ideal transformer

The primary and secondary voltages of an ideal transformer are directly proportional to the number of the winding turns as follow [2.30]:

$$\frac{v_1}{v_2} = \frac{N_1}{N_2} = a \tag{2-6}$$

where *a* is defined as the turns ratio of the transformer. The relationship between the primary and secondary currents of an ideal transformer is given by:

$$N_1 i_1 = N_2 i_2 \tag{2-7}$$

Therefore the relationship between the voltages, currents and number of the primary and secondary windings of an ideal transformer is given by:

$$\frac{v_1}{v_2} = \frac{i_2}{i_1} = \frac{N_1}{N_2} = a \tag{2-8}$$

According to Faraday's law of induction the magnetic flux φ in the core induces an *emf* in the primary and secondary windings as:

$$e_1 = N_1 \frac{d\varphi}{dt} \tag{2-9}$$

$$e_2 = N_2 \frac{d\varphi}{dt} \tag{2-10}$$

In the ideal transformers the induced voltages e_1 and e_2 are equal to the primary and secondary voltages, therefore:

$$\frac{v_1}{v_2} = \frac{e_1}{e_2} = \frac{N_1}{N_2} = a \tag{2-11}$$

Under sinusoidal excitation voltage of the primary, the magnetic flux in the core varies sinusoidally and can be expressed as:

$$\varphi(t) = \varphi_{pk} \sin \omega t \tag{2-12}$$

where φ_{pk} is the peak magnetic flux and ω is the angular frequency. From (2-10) and (2-12) the induced voltage on the secondary winding can be obtained as:

$$e_2(t) = N_2 \frac{d\varphi}{dt} = \omega N_2 \varphi_{pk} \cos \omega t \tag{2-13}$$

The *rms* value of the no-load secondary voltage is given by:

$$e_{rms} = \frac{\omega N_2 \varphi_{pk}}{\sqrt{2}} = \frac{2\pi}{\sqrt{2}} f N_2 \varphi_{pk} = 4.44 f N_2 \varphi_{pk} \qquad [V] \tag{2-14}$$

And the average over a time period *T*:

$$e_{av} = \frac{2}{T} \int_0^{T/2} e_2(t) dt = \frac{2}{T} \int_0^{T/2} \omega N_2 \varphi_{pk} \cos \omega t \, dt = 4 f N_2 \varphi_{pk} \quad [V] \tag{2-15}$$

Considering the cross section area (*A*) of the core, peak flux density is given by:

$$B_{pk} = \frac{\varphi_{pk}}{A} \tag{2-16}$$

Substituting φ_{pk} from (2-16) into (2-14) and (2-15) leads to:

$$e_{rms} = 4.44 f N_2 B_{pk} A \qquad [V] \tag{2-17}$$

$$e_{av} = 4 f N_2 B_{pk} A \qquad [V] \tag{2-18}$$

Equations (2-17) and (2-18) are used to obtain a desired peak flux density in the transformer cores under sinusoidal excitations.

2.7.2. Equivalent circuit of real transformers

The ideal model of the transformer shown in Fig 2-9 was obtained by ignoring power losses of the transformer and assuming infinite magnetic permeability and electric resistivity for the core.

Although transformers are efficient devices, in the accurate modelling power losses should be considered. Power losses in real transformers are mainly classified in two components. Copper loss P_{cu} dissipated in the resistances of the windings and magnetic loss P_m dissipated in the magnetic core. Copper losses of the transformers can be modelled by the equivalent resistance of each winding connected in series with the windings. Magnetic losses are proportional to the voltage applied to the transformer and therefore can be modelled by a resistance connected across the primary winding of the transformer.

Furthermore since the magnetic permeability of the core material is finite, a part of the generated magnetic flux, known as flux leakage, escape the core and passes through only one of the windings. This concept is shown in Fig 2-10 in which φ_{11} and φ_{22} are the primary and secondary flux leakages, respectively. Flux leakage produces a self-inductance in each winding and should be considered in the accurate modelling of the real transformers [2.3] and [2.30].

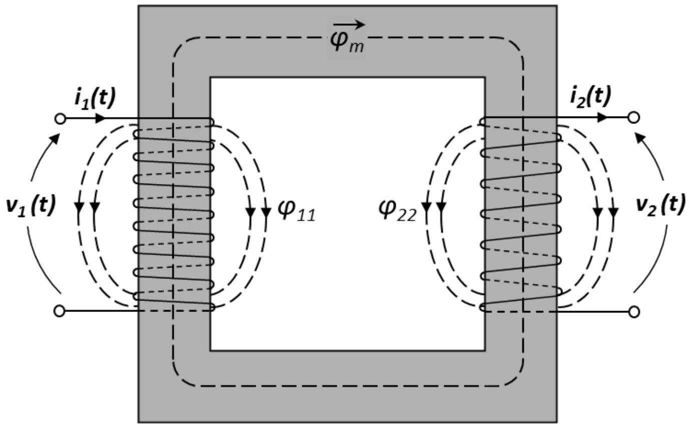

Fig 2-10 Transformer model with flux leakage,
φ_{11} primary flux leakage and φ_{22} secondary flux leakage

Core excitation or magnetising current is another issue that should be modelled in a real transformer. This current, in the linear part of the *B-H* curve, is proportional but lagging by 90° to the applied voltage and therefore can be modelled by adding a reactance connected in parallel to the primary winding.

The final result of an equivalent circuit model of a real transformer including resistances and self-inductances of the windings, core loss and magnetising reactance is shown in Fig 2-11. Experimental methods are available to measure the components of the equivalent circuit of the transformers [2.3] and [2.30].

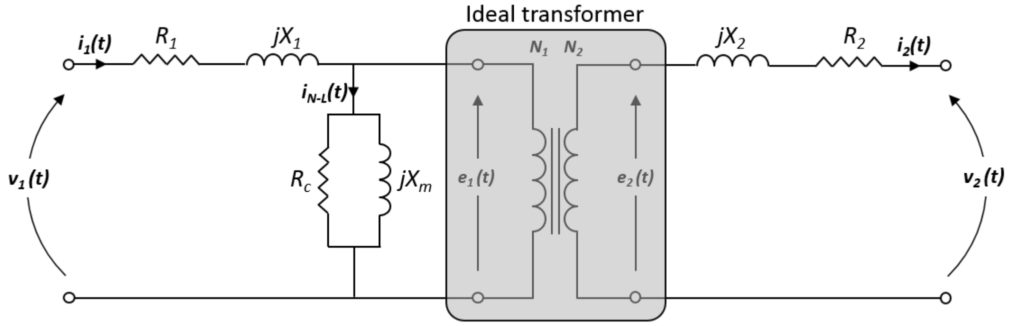

Fig 2-11 Equivalent circuit of a real transformer

The equivalent circuit of Fig 2-11 is an accurate model of the transformers and is widely used in the design and study of transformers, but some other effects e.g. effect of high frequency excitation and effect of core saturation are still required for special purposes.

2.8. Summary

In this chapter fundamental concepts of magnetism, magnetic materials and related issues were studied. These concepts are required in the works and investigations carried out in this thesis. These concepts were studied as required in the thesis; however each particular issue has physical and technical importance in the relevant studies and has been investigated in detail in the recent researches.

References

[2.1] D C Jiles, "*Introduction to Magnetism and Magnetic Materials*", Second edition, Chapman & Hall/CRC, London, 1998

[2.2] M Getzlaff, "*Fundamentals of Magnetism*" Springer-Verlag Berlin Heidelberg 2008

[2.3] R M D Vecchio, B Piulin, P T Feghali, D M Shah, and R Ahuja, "*Transformer Design Principles: with Applications to Core-Form Power Transformers*", 2nd edition Boca Raton, FL: CRC Press, 2010

[2.4] K H J Buschow, F R de Boer, "*Physics of Magnetism and Magnetic Materials*", Kluwer Academic/Plenum Publishers, 2004

[2.5] B S Guru, H R Hiziro, "*Electric Machinery and Transformers*" Third edition, Oxford University Press, Inc. 2001

[2.6] A J Moses, "*Electrical Steels: Past, Present and Future Developments*," IEE Proceedings-Science Measurement and Technology, vol. 137, pp. 233-245, 1990

[2.7] M Abe, Y Takada, T Murakami, Y Tanaka, "Magnetic properties of commercially produced Fe-6.5 wt % Si sheet ", Journal of Materials Engineering, Vol 11, Issue 1, pp 109-116, 1989

[2.8] F Fiorillo, "Characterization and Measurement of Magnetic Materials", Elsevier academic press, 2004

[2.9] D S Petrovi, "Non-Oriented Electrical Steel Sheets", Journal of materials and technology 44 (2010) 6, pp. 317–325

[2.10] P Beckley, "Electrical Steels: A Handbook for Producers and Users," First edition, European Electrical Steels, Newport, South Wales, 2000

[2.11] K Jenkins, "Current Status and Future Developments of GO Electrical Steel", proceeding of 6th international conference on Magnetism and Metallurgy, June 2014, pp 75-79

[2.12] B D CULLITY and C D GRAHAM, "Introduction to Magnetic Materials" Second edition, IEEE press, 2009

[2.13] T Suzuki, H Nakayama, T Yamamoto and S Taguchi, "Transformer Characteristics of Orient core-Hi-B," IEEE Transactions on Magnetics, Vol. 8, pp. 321-323, 1972

[2.14] T Yamamoto, S Taguchi, A Sakakura and T Nozawa, "Magnetic Properties of Grain-Oriented Silicon Steel with High Permeability Orient core Hi-B," IEEE Transactions on Magnetics, Vol. 8, pp. 677-681, 1972

[2.15] S. Taguchi, S. Yamamoto and A. Sakakura, "New Grain-Oriented Silicon Steel with High Permeability Orient core Hi-B," IEEE Transactions on Magnetics, Vol. 10, pp. 123-127, 1974

[2.16] Available at: http://www.dierk-raabe.com/electrical-steels-fe-3-si/, August 2014

[2.17] R G Carter, "Electromagnetism for Electronic Engineering" Ventus Publishing ApS, 2009

[2.18] A Hubert and R Schäfer, “Magnetic Domains, The Analysis of Magnetic Microstructures”, third edition, Springer-Verlag Berlin Heidelberg 1998

[2.19] Available at: http://www.electronics-tutorials.ws/electromagnetism, August 2014

[2.20] B S Guru and H R Hizirou, “Electric Machinery and Transformers” third edition, Oxford University press, 2001

[2.21] W Chandrasena, P G McLaren, U D Annakkage, R P Jayasinghe, D Muthumuni and E Dirks, “Simulation of Hysteresis and Eddy Current Effects in a Power Transformer”, Electric Power Systems Research 76 (2006), pp. 634–641

[2.22] I D Mayergoyz, “Mathematical Models of Hysteresis and their Applications”: Second Edition (Electromagnetism), Academic Press. 2003

[2.23] Standard Test Method for Alternating-Current Magnetic Properties of Materials at Power Frequencies Using Wattmeter–Ammeter–Voltmeter Method and 25-cm Epstein Test Frame, ASTM A343/A343M-03, 2003.

[2.24] BS EN 10280:2001 + A1:2007, Magnetic Materials - Methods of Measurement of the Magnetic Properties of Electrical Sheet and Strip by Means of a Single Sheet Tester, British Standard, 2007

[2.25] G.Bertotti, “General Properties of Power Losses in Soft Ferromagnetic Materials,” IEEE Trans Magn Vol. 24, January1988 pp. 621-630

[2.26] D. M. Ionel, M. Popescu, S. J. Dellinger, et al., “On The Variation With Flux And Frequency Of Core Loss Coefficients In Electrical Machine”, IEEE Trans. Magn Vol. 42, No. 3, pp. 658-666, May/June 2006

[2.27] Ri Channel, available at: http://www.richannel.org/levitating-barbecue, August 2014

[2.28] MITSUBISHI ELECTRIC, Available at: http://www.meppi.com/Products/Transformers/, August 2014

[2.29] ABB, Available at: http://new.abb.com/products/transformers/distribution/medium, August 2014

[2.30] S J Chapman, “Electric Machinery Fundamentals”, McGraw-Hill, Inc. 2004

CHAPTER 3

Previous Related Work

3.1. Introduction

In this chapter previous related work on the effect of inter-laminar short circuit faults on transformer cores is discussed. Methods of inter-laminar fault detection and testing the effectiveness of insulation coating of electrical steel laminations are also reviewed.

3.2. Effect of Inter-laminar Short Circuit faults on the Magnetic Properties of Transformer Cores

In 1989 Moses and Aimoniotis investigated effect of edge burrs on total and local power loss of a single phase transformer core by applying artificial short circuits in a controlled manner [3.1]. The transformer core was assembled from grain oriented 3 % silicon iron and magnetised at flux densities of 1.3 T, 1.5 T and 1.7 T and a frequency of 50 Hz. Artificial shorts were introduced by drilling 0.3 mm holes close to the edge of the core and inserting a steel pin or insulating rod to short out the required number of laminations in the core. Fig 3-1-a shows schematic view of the core showing position of the artificial burrs and Fig 3-1-b shows the method of producing the artificial burrs.

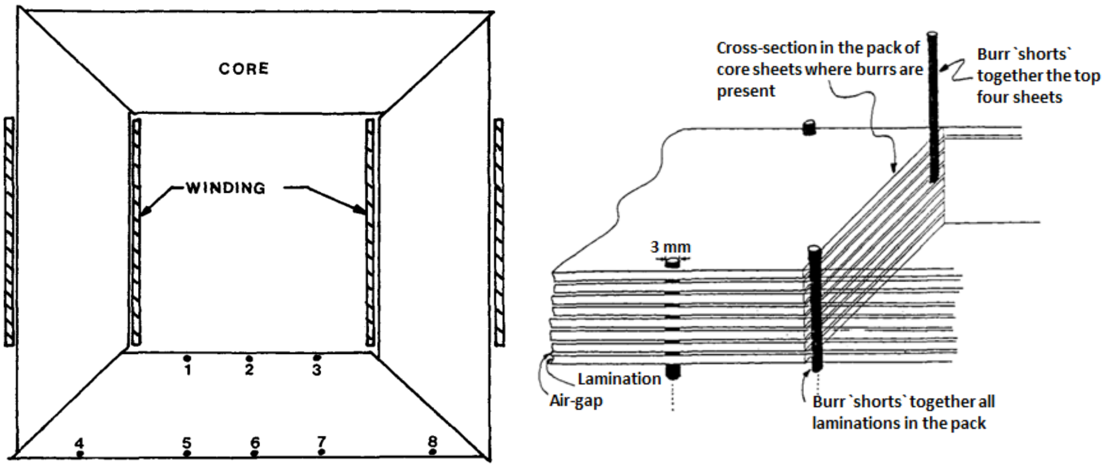

(a) (b)

Fig 3-1 (a) Schematic plan view of single phase core showing positions of artificial burrs
(b) Method of producing artificial burrs [3.1]

The total power loss of the core was measured by sensing the primary current and the secondary induced *emf*. Fig 3-2 shows the total power loss of the core for three combinations of artificial shorts compared with the nominal loss of the core.

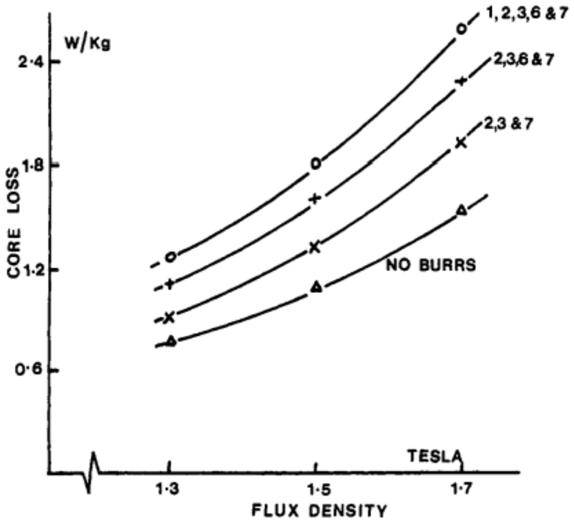

Fig 3-2 (a) Total core loss variation with flux density for different burr configurations [3.1]

An array of thermistors was used to measure the localised power loss when artificial shorts were applied on the core. The localised power loss of the core was measured at 32 points on specific laminations using the initial rate of rise of temperature technique. Fig 3-3-a shows the position of the thermistors on the core to measure localised power loss and Fig 3-3-b shows the localised power loss measured across the core by applying artificial burrs 3 and 7.

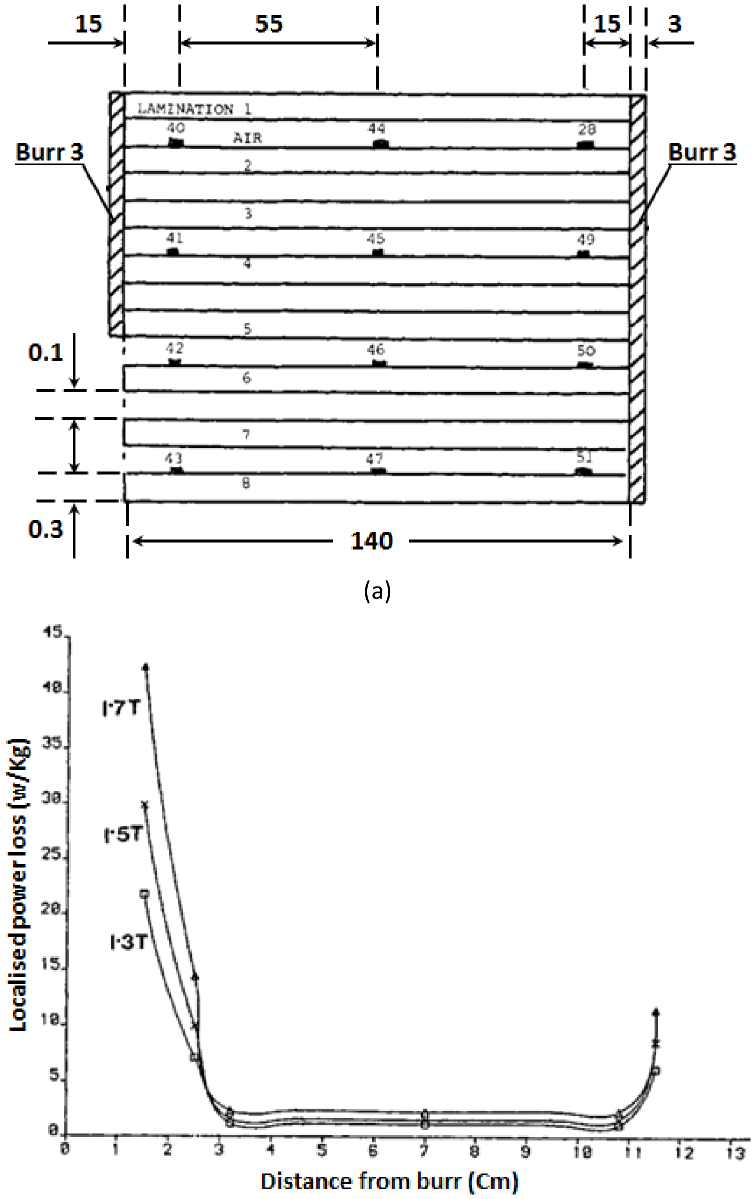

(a)

(b)

Fig 3-3 (a) Position of thermistors in stack for measurement of local loss under partial burr conditions, dimensions in mm (b) Variation of localised loss on a line between burrs 3 and 7 [3.1]

The results of total and localised power loss shown that the power losses increase rapidly as more laminations were shorted together and as more closed paths between the shorted points were introduced. Furthermore the localised power loss close to the artificial burrs was very high.

Aimoniotis and Moses in 1993 simulated the paths and computed the values of eddy currents in a transformer core model using FE based analysis. Different types of inter-laminar short circuits were simulated and their effect on the induced eddy currents was investigated [3.2]. The end part of the core including eight shorted laminations, on either sides, due to burrs are shown in Fig 3-4-a. The contour of the equivalent surfaces, show the electric paths of the eddy currents in the core. Fig 3-4-b shows the variation of the *rms* value of the eddy current along a line situated just below the surface of the third lamination in the core and parallel to the surface.

Based on the FE results it was found that in presence of edge burrs in a laminated transformer core, high eddy currents are induced in the burred area. The values of the eddy currents depend on the number of burred laminations. No change in the total core loss occurs if burrs appear on one edge of the core limb or yoke only, e.g. when burrs and laminations do not form close paths perpendicular to the direction of the magnetisation vector ***B***.

Schulz et al. in 2010 predicted the additional eddy current power loss caused by an individual short circuit between two laminations. In the proposed model, excitation conditions, the placement of the contact points and contact resistances were considered. A schematic and equivalent circuit of two laminations with an inter-laminar short on one side only and two sides are shown in Figs 3-5-a and 3-5-b, respectively [3.3]. In the equivalent circuits of Fig 3-5, R_{eq} is the equivalent resistance of the laminations and R_{ct} is resistance of the burr or contact resistance. In order to determine U_{oc} and R_{eq} experimentally, artificial low-resistance inter-laminar shorts were applied on different pairs of grain oriented transformer sheets and exposed to a magnetic field.

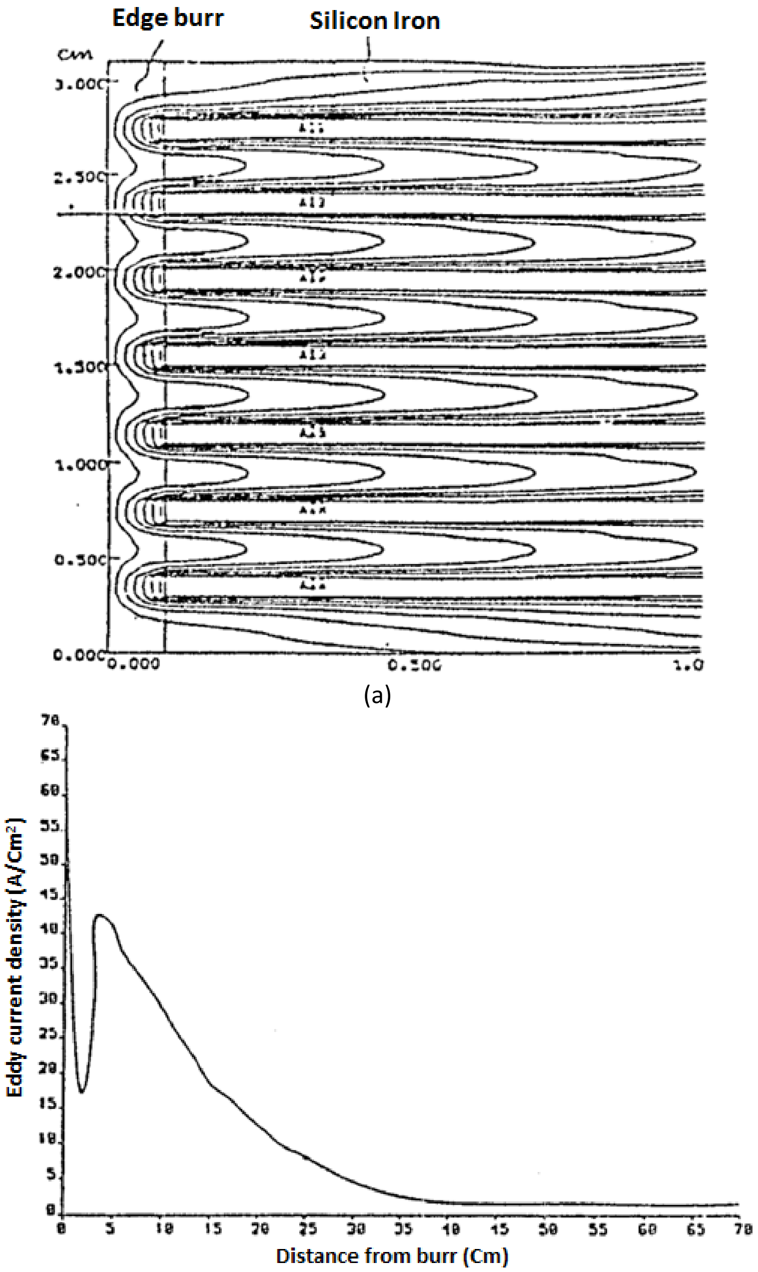

(a)

(b)

Fig 3-4 (a) Eddy current density at the end part of the core model consisting 8 shorted laminations on either sides (b) Variation of eddy current density along a lamination (third from the top) of the core model consisting of eight laminations [3.2]

Measurements were performed first in an open-circuit condition and then in short-circuit condition. In order to allow for a separation of R_{eq} and R_{ct}, the voltage drop on the contact resistances U_{ct} was also measured.

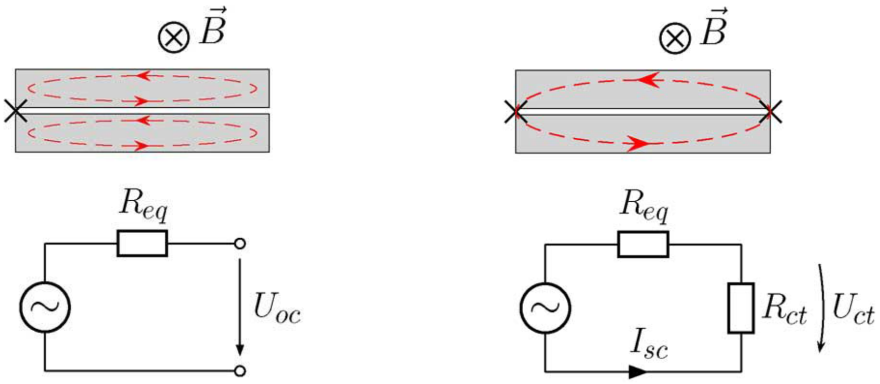

(a) (b)

Fig 3-5 Schematic view of cross section with faults and eddy currents indicated
(a) measurements at open-circuit condition and (b) short-circuit condition [3.3]

Experimental results of the relevant quantities R_{eq}, U_{oc} and I_{sc} as a function of the flux density for different core widths *C* are shown in Fig 3-6.

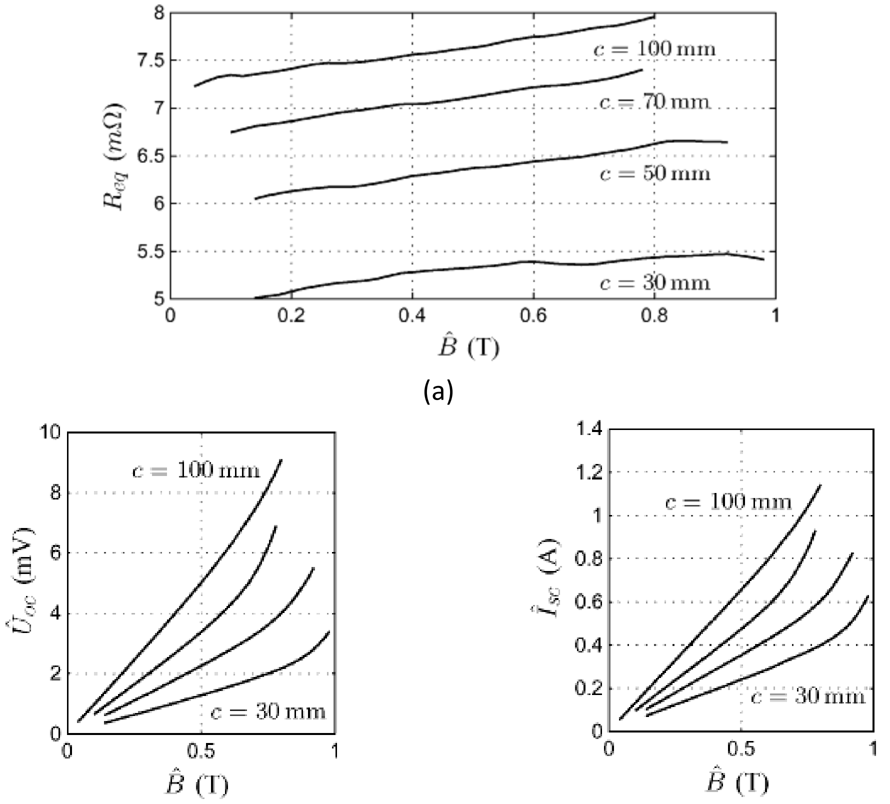

(a)

(b) (c)

Fig 3-6 Behaviour of an inter-laminar short as a function of flux density
and for different core widths (c) [3.3]

At the first glance, both U_{oc} and I_{sc} seem proportional to the flux density. There is a small, but constant, increase in the equivalent resistance R_{eq} with the flux density. The linear increase in R_{eq} shows that the equivalent resistance of an inter-laminar short depends on the complex interaction between the eddy currents circulating in the individual laminations and the short circuit current circulating between the shorted laminations. As a result, the eddy current distribution caused by an inter-laminar short circuit forms a complex problem, involving the anisotropic magnetic properties of the material, electric properties, and many geometric parameters.

One year later in 2011, Lamprecht and Graf investigated the impact of the inter-laminar faults caused by edge burr on the eddy current power loss of a ring core sample [3.4]. Artificial shorts were introduced on sides of the core using galvanic nickel with a thickness of roughly 0.1 mm. Fig 3-7-a shows dimension of the core and Fig 3-7-b shows a cross section of the core sample coated with galvanic nickel.

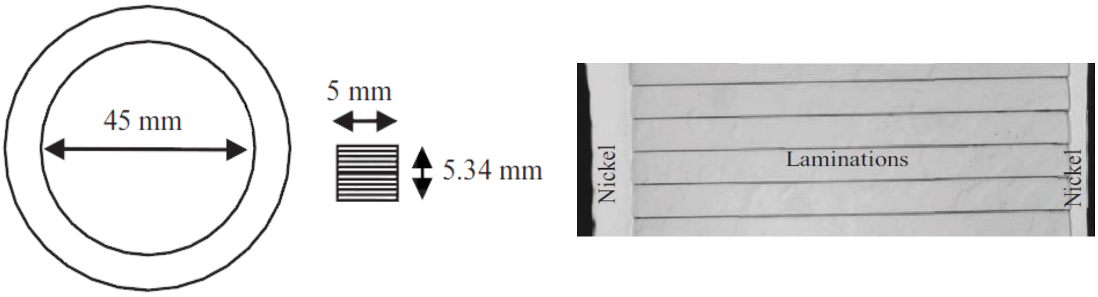

(a) (b)

Fig 3-7 Cross section of galvanically coated ring core sample [3.4]

FE analysis was performed using the ANSYS Maxwell 3D simulation tool to analyse the eddy current paths in the core and to predict the loss values caused by the applied short circuit. An example of circulation of the eddy currents in a stack of four laminations is shown in Fig 3-8. Based on FE modelling, a simple equivalent circuit model was introduced for a stack of laminations with inter-laminar faults, as shown in Fig 3-9. The model was then simulated with an analogue circuit simulation software.

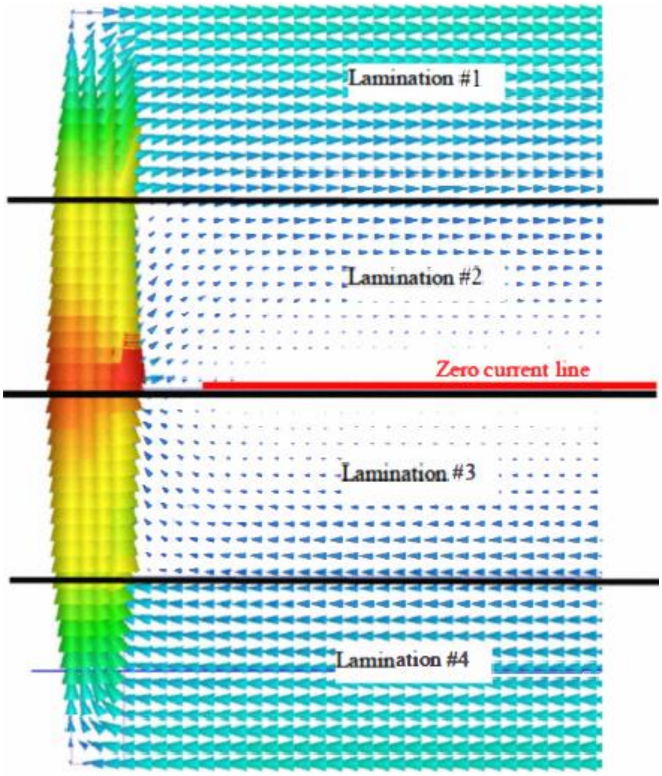

Fig 3-8 Eddy current density/direction in four shorted laminations [3.4]

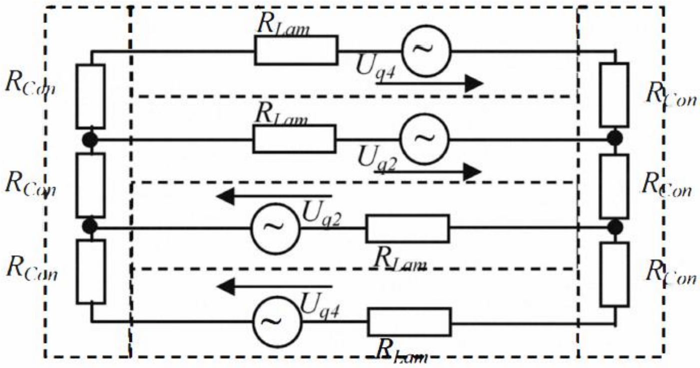

Fig 3-9 Equivalent electric circuit model of a stack of four shorted laminations [3.4]

Fig 3-10 shows the results of the eddy current loss calculation based on the electric circuit model in comparison with the FEM results. The calculation and simulation were performed at a magnetic flux density of 1.0 T and at a frequency of 400 Hz. Fig 3-10 shows that the calculated total eddy current losses of the electric circuit model are roughly 10 % higher than the finite element values.

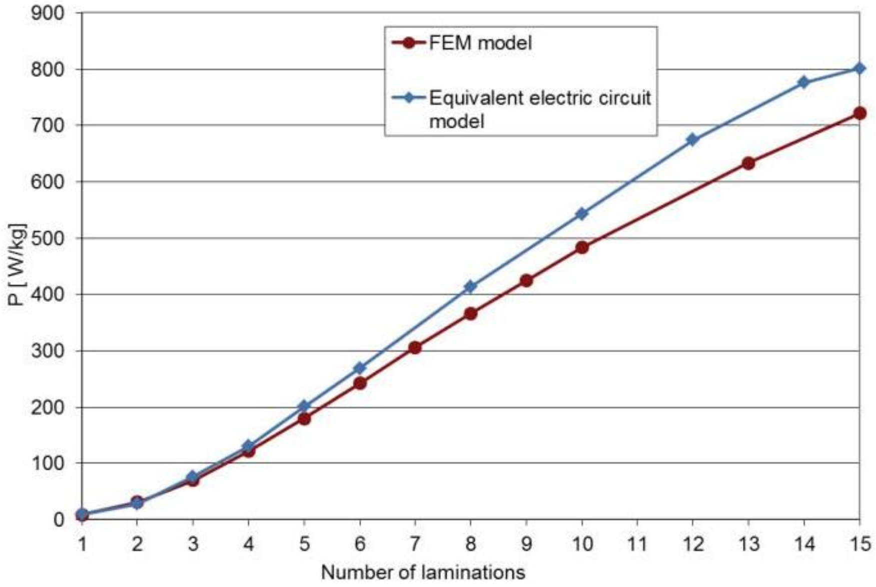

Fig 3-10 Variation of finite element and modelling of eddy current losses vs number of laminations [3.4]

Comparison between the FEM, calculation and experimental results of the eddy current loss of a stack of 15 shorted laminations at a frequency of 400 Hz and a magnetic flux density of 1.0 T are shown in Table 3-1.

Table 3-1 Comparison of specific eddy current loss of a stack of 15 shorted laminations at flux density of 1.0 T and frequency of 50 Hz [3.4]

Method	**Specific eddy current losses *B*=1.0 T, *f*=400 Hz [W/kg]**
Finite Element Analysis (Maxwell 3D)	722
Equivalent electric circuit model	801
Measurement	1038

The measured eddy current loss value is significantly higher than the simulated and calculated values. The difference was explained by the galvanic coating process. Thickness of the coating applied at the edge of the core varies between 0.1 mm and 0.4 mm while in the FEM and calculation models a constant thickness of 0.1 mm was considered. Further the anomalous eddy current loss due to the impact of the domain structure of the material might lead to higher power loss.

Bielawski et al. in 2012 reported the influence of the inter-laminar faults on the quality of a transformer core. A 3-D numerical simulation was performed to visualize the current flowing at the shorted points in a pack of two laminations. Two small blocs connecting two laminations on each side correspond to the contacts introduced by edge burrs [3.5]. A cross sectional view of the model and 3-D view of the numerical model is shown in Figs 3-11-a and 3-11-b, respectively.

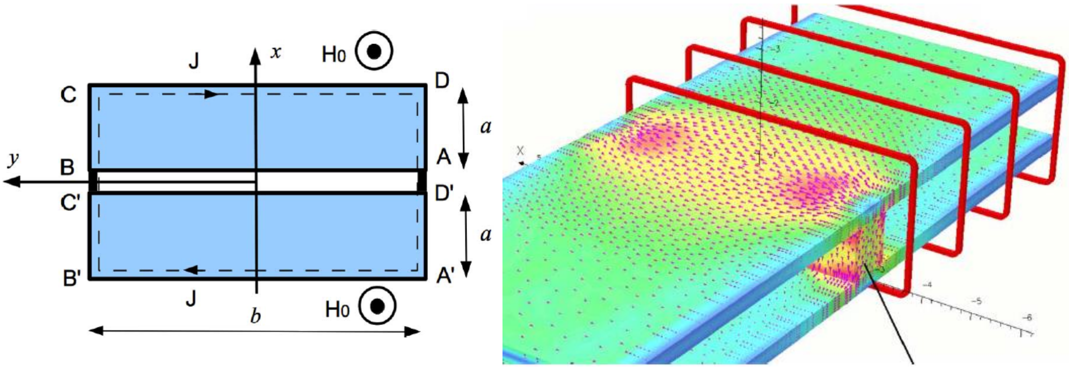

(a) (b)

Fig 3-11 (a) Detrimental effect caused by two burrs
(b) 3-D numerical simulation of an elementary short-circuit [3.5]

The FEM results showed that when the edge burrs form low contact resistance between two adjacent laminations, the induced eddy current flows between the laminations and form a large loop inside the core. In the analytical modelling the set of two shorted laminations were considered as a double thickness lamination.

Mazurek et al. in 2012 studied the effect of inter-laminar fault on a 350 kVA, three-phase, five packet transformer core. Artificial burrs were applied at three stages to short out 33, 50 and 66 laminations at set positions. The total power loss of the core was measured using a three phase power analyser and local power loss near the burr was measured by means of initial rate of rise of temperature method (IRRTM). The results are shown in Figs 3-12-a and 3-12-b, respectively [3.5].

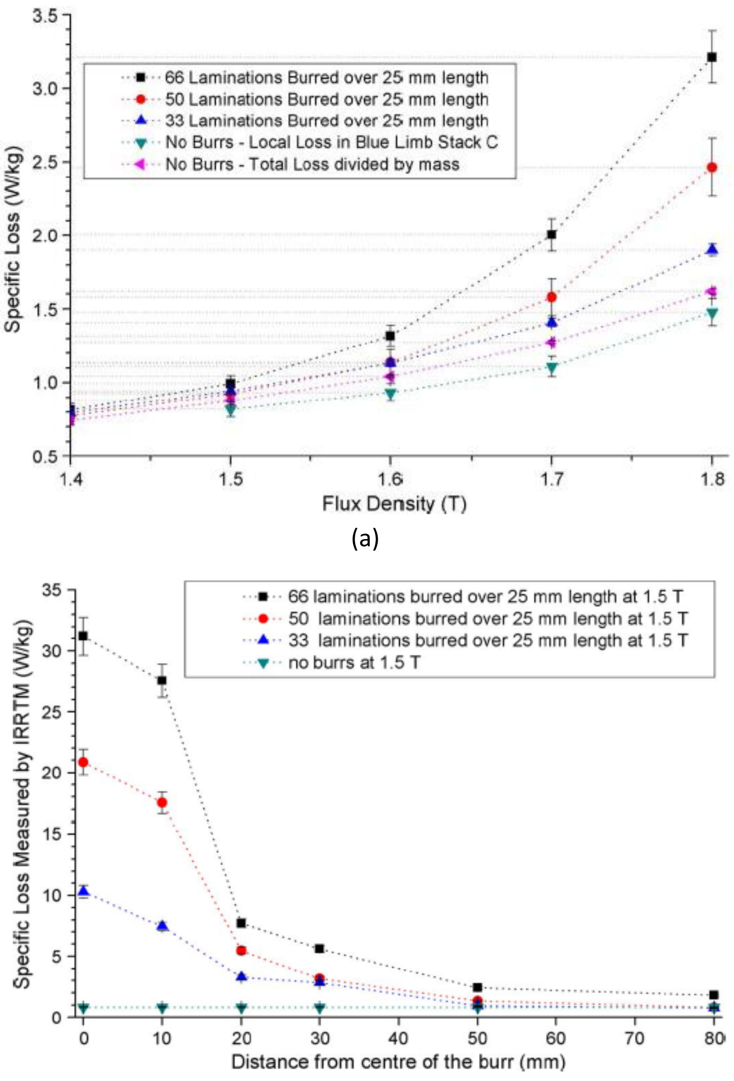

(a)

(b)

Fig 3-12 (a) Variation of specific loss with overall flux density of the core for burrs of different heights compared with the non-burred core (b) Variation of local loss measured using the IRRTM with distance from the centre of the burred region [3.5]

Experimental results showed that in the case of largest burr region shorting 66 laminations, the specific total power loss increases by 13 % at 1.5 T and by 100 % at 1.8 T. Furthermore, local power loss showed that in the presence of the edge burrs the highest rise of temperature and hence the highest local loss occurred at their centre and local loss increases as far as 70 mm from the edge of the burred region, for this particular core and applied burr.

3.3. Methods of inter-laminar short circuit fault detection

Core quality assessment of the electrical machines is a major concern for both the original equipment manufacturer and the customer. In the past, detection of hot spots in magnetic cores was done qualitatively by turning off the power and immediately crawling into the bore and feeling the surface [3.6]. Various methods have been recently developed to detect inter-laminar short circuit faults in the magnetic cores, which have been used in research and industrial works [3.6]–[3.16]. In almost all of these techniques the magnetic cores under test are magnetised either locally [3.6]–[3.7] or totally [3.13]-[3.14] and a signal is measured resulting from the injected flux. The measured signal can be interpreted to provide information about the quality of the test sample and detecting possible inter-laminar faults. The difference between different methods is related to the measured signal and the sensor which is implemented to measure the fault signal. In this part the existing methods of inter-laminar fault detection are reviewed.

3.3.1. Full ring test

The traditional method to inspection the health of stator cores is the full ring test, also known as thermal loop test or traditional method, as cited in [3.8]. In this method an external winding is wound around the yoke of the core in a toroidal manner to magnetise it at 80 % to 100 % of rated flux. Fig 3-13 shows a typical exciting circuit of ring test. The excitation magnetic flux generated by the external winding excites the possible inter-laminar faults in the core and induces inter-laminar fault current in the damaged area. After the core warms up a thermographic camera, also known as thermal imaging camera, is used to detect hot spots on the inner surface of the core caused by the inter-laminar faults. Fig 3-14 shows a hydro generator core under ring test in which the operator is using a thermal camera to detect the inter-laminar faults [3.9].

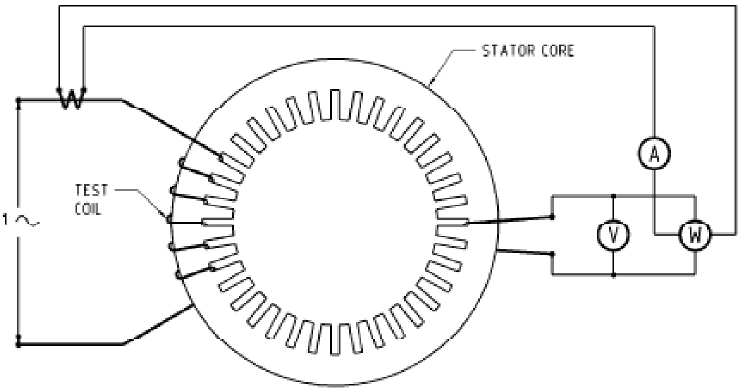

Fig 3-13 Magnetising system of full ring tester [3.9]

Fig 3-14 Hydro generator core ring flux test using infrared camera for core temperature monitoring [3.9]

Lee et al. in [3.10] introduced artificial short circuits on a three phase stator core by welding 4 slots on the core surface. The change in the temperature was measured, using a thermal camera, over 30 minutes in 1 minute intervals; the final result is shown in Fig 3-15. The stator core temperature in the healthy part and maximum hot spot temperature were 34.0 ^{o}C and 61.2 ^{o}C, respectively.

The main drawback of the ring test is the requirement for a MVA-level, low-power-factor power source to excite the magnetic core at the rated flux. Furthermore, this method is only able to detect hot spots on the surface of the core; all other inter-laminar faults, especially more critical ones in the slot wall, on the slot bottom and at the heart of the core, are not detectable by this test. Also an inter-laminar fault between a few laminations which lead to low local heat cannot be detected by this method. Also the method needs special equipment, e.g. a thermal camera, to detect the inter-laminar faults which can make it more expensive.

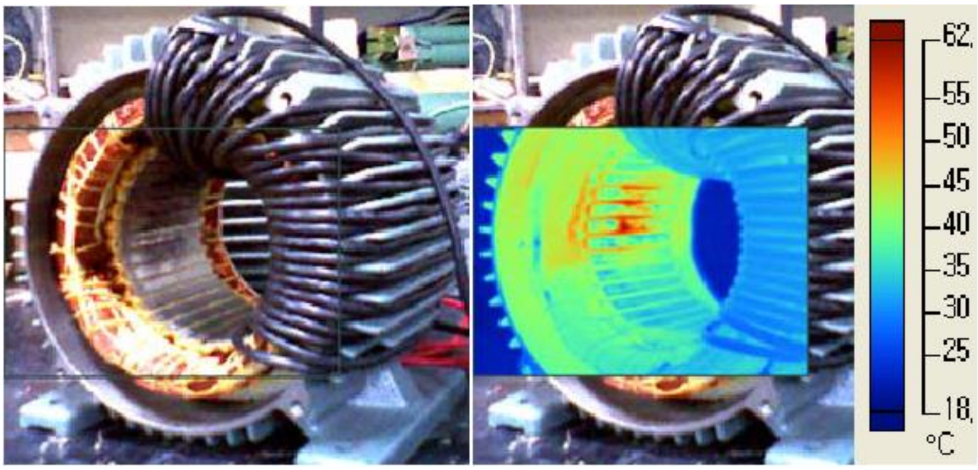

Fig 3-15 Thermal image of temperature distribution under core loss test after 30 min with artificial fault welded in 4 slots [3.10]

3.3.2. ELectromagnetic Core Imperfection Detector (EL CID)

In 1978 **EL**ectromagnetic **C**ore **I**mperfection **D**etector (EL CID) as a low-flux test was developed to detect inter-laminar faults, especially in large generator cores [3.11]. The excitation configuration of the EL CID test is the same as full ring test but at about 3-4 % of the rated flux level, which leads to a significant reduction in the power requirement and safety risks, as cited in [3.8]. In this test method a flux sensing probe, including an air core coil of many turns wound around a “horse shoe” shape coil known as a Chattock Coil or Maxwell Worm, is used to scan in the axial direction along the inner surface of the core to detect abnormality in the flux patterns caused by the inter-laminar fault current [3.8]. Fig 3-16 shows a schematic of an EL CID probe positioned between adjacent teeth of a stator core.

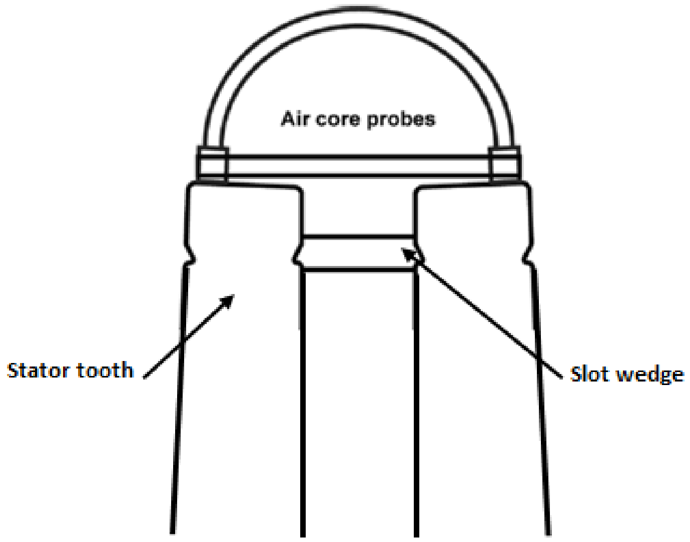

Fig 3-16 Probe locations for the air core probe for inter-laminar core fault detection [3.8]

The output voltage of the probe is processed to provide the actual current signal. The processed signal is a Sine signal which is in phase with the main core flux and with the excitation current in a healthy core. Possible inter-laminar faults change the phase of the signal. Experimental work was performed by Romary et al. [3.14] on a three phase stator core by applying short circuits between 5 up to 30 laminations. Schematics of the faulty laminations and typical components of the detected current by the EL CID detector for different numbers of shorted laminations are shown in Figs 3-17-a and 3-17-b, respectively. In these figures *x* represents the position of the probe relatively to the centre of the faulty core.

Compared to the full ring test, the EL CID method offers many advantages, e.g. reduced power requirement, set-up and test time, higher accuracy to detect deep-seated faults, and easily understood results. However the measured signal by the air cored Chattock probe is very small and as a result the signal-to-noise ratio is relatively low. Therefore, with a few inter-laminar shorts, interpretation of the output data is difficult. In 2001 Posedel [3.17] proposed a double Chattock coil probe with a calibration procedure and quantitative analysis to improve interpretation of the EL CID data; however, the fundamental shortcomings of EL CID are still remaining.

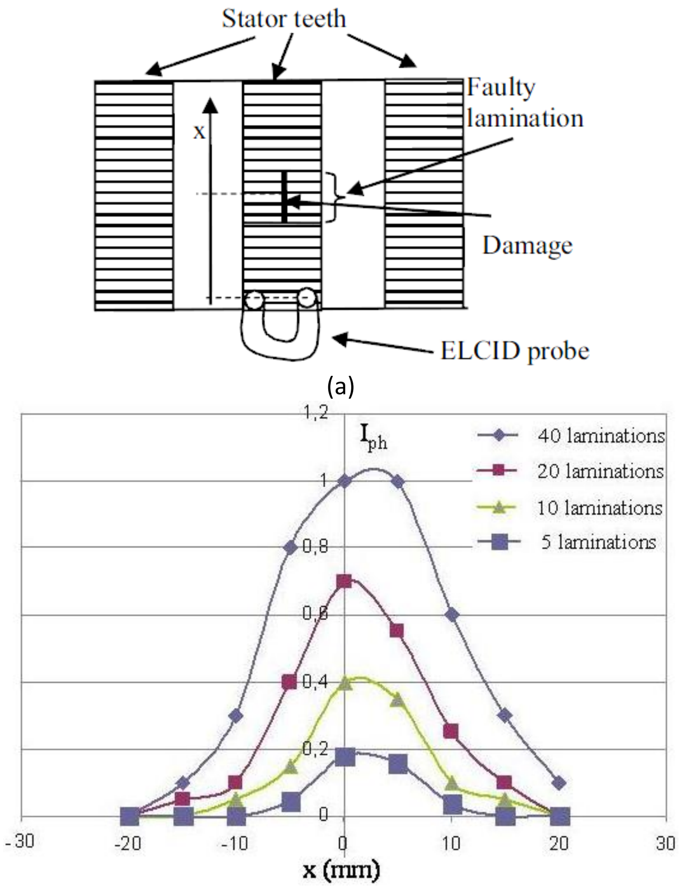

(a)

(b)

Fig 3-17 (a) Schematic of the defect on the core
(b) Output current of an EL CID probe in presence of short circuit is a stator core [3.14]

Photographs of a hydro-generator under test with the EL CID test and a robotic EL CID test probe are shown in Figs 3-18-a and 3-18-b, respectively.

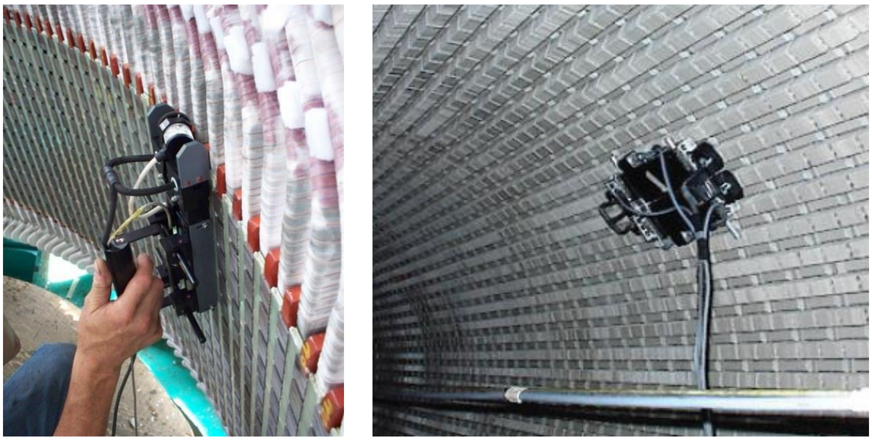

(a) (b)

Fig 3-18 (a) Hydro generator under test by an EL CID probe [3.15]
(b) Robotic EL CID test in progress on a turbo generator [3.16]

3.3.3. Iron Core Probe EL CID Method

As mentioned in section 3.3.2, the main drawback of the EL CID method is the low signal to noise ratio of the measured signal. This problem is more serious for low inter-laminar fault currents. Lee et al. in 2005 proposed a developed EL CID method using a thin sheet iron core probe [3.20]. The main idea of the developed method is to replace the air cored probe of the EL CID method with an iron cored probe to improve the signal to noise ratio of the measurement and increase the sensitivity of the inter-laminar fault detection. The excitation level of this method is set at 75 mT, which is similar to the air core probe EL CID method (3-4 % of rated flux). Fig 3-19 shows a schematic of an iron core EL CID placed between adjacent teeth of a stator core [3.20].

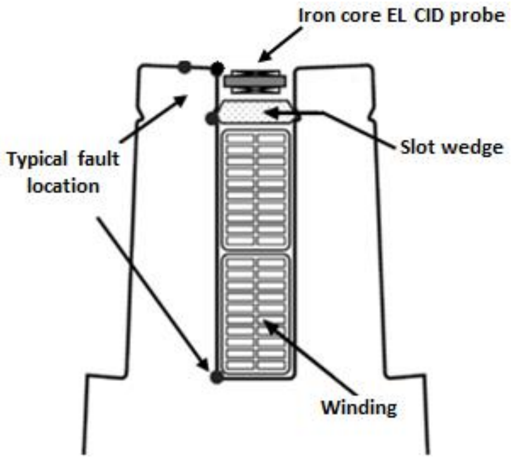

Fig 3-19 Iron core probe for inter-laminar core fault detection [3.20]

The configuration of the excitation system in the iron core probe EL CID tester is shown in Fig 3-20. The measured quantities in this method are the output voltage of the iron core probe v_s and the excitation current of the excitation winding i_e. The *rms* values and relative phase of these quantities are used to analyse and detection of the inter-laminar faults. Distribution of the magnetic flux and a phasor diagram of the system in the case of a healthy stator core are shown schematically in Fig 3-21-a and 3-21-b, respectively.

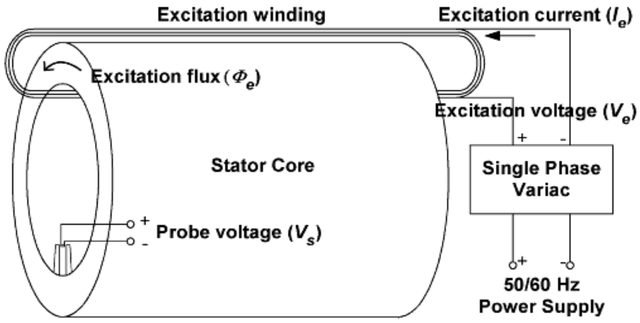

Fig 3-20 Excitation system configuration in iron core probe EL CID method [3.20]

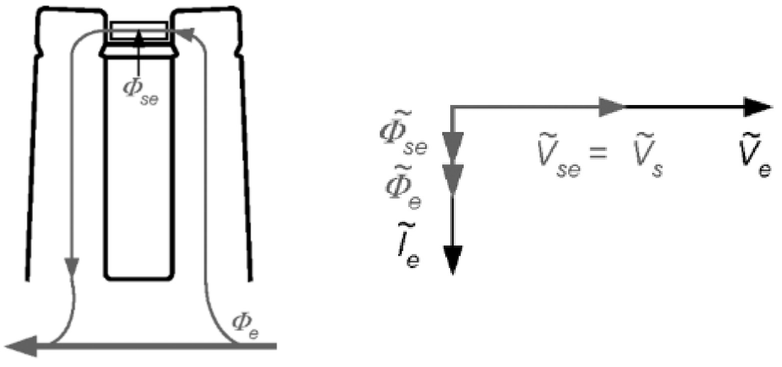

(a) (b)

Fig 3-21 (a) Flux distribution and (b) phasor diagram of a healthy core [3.20]

In the phasor diagram of Fig 3-21-b, I_e , V_e , and φ_e represent the excitation current, voltage, and magnetic flux, respectively. V_s ,V_{se} are the measured probe voltage and the probe voltage due the excitation, and φ_{se} is the excitation flux component measured in the probe. In a healthy core, since the excitation flux φ_e is the only flux component in the core V_s and V_{se} are equal, as shown in Fig 3-21-b.

When an inter-laminar fault appears in the core, a voltage V_f is induced in the fault current loop and generates a fault current I_f. The fault current induces an additional fault flux φ_f, which changes the distribution of the total flux in the core and the probe itself. Distribution of the total flux in a faulty core depends on the location of fault. Two examples of flux distribution and the related phasor diagram in a stator core with inter-laminar fault on the slot and on the tooth are shown in Figs 3-22 and 3-23, respectively.

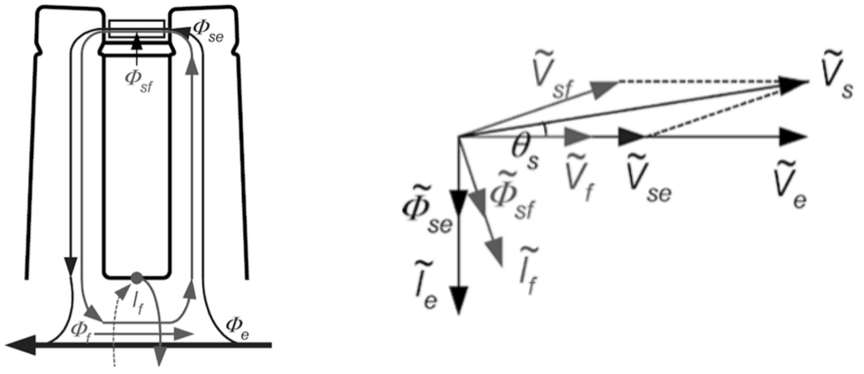

(a) (b)

Fig 3-22 (a) Flux distribution and (b) Phasor diagram for slot fault [3.20]

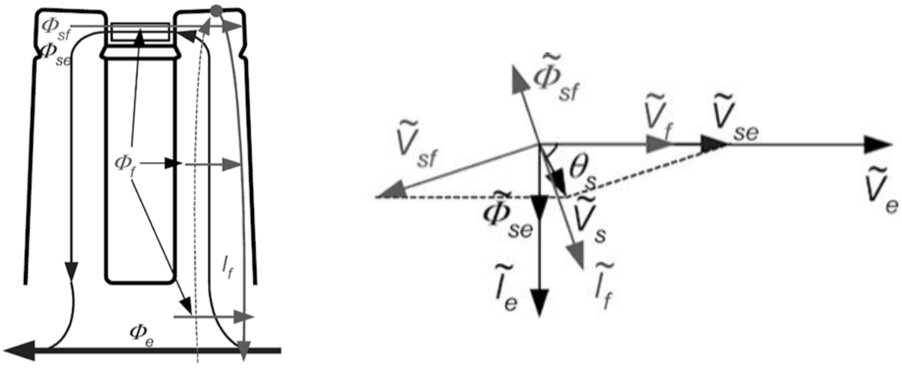

(a) (b)

Fig 3-23 (a) Flux distribution and (b) Phasor diagram for tooth fault [3.20]

For both inter-laminar faults shown in Figs 3-22-a and 3-23-a, V_f is in phase with the excitation voltage V_e, however the phase angle between V_f and I_f depends on the impedance of the fault current loop. The inductive component of the fault impedance ($\omega_e L_f$) depends on physical dimension of the probe and slot which is a fixed value; while the resistive component R_f depends on the fault location, the fault contact resistance, and the contact resistance between the shorted points.

The proposed inter-laminar core fault detector was tested on a 120-MW machine stator core. Inter-laminar faults of varying intensity were applied intentionally on the core at different locations, as shown schematically in Fig 3-24-a. As an example the final processed result of slot 47, fault current (I_f) and phase angle between V_s and V_{se} (θ_s) is shown in Fig 3-24-b. The numbers shown on the graph represent the number of shorted laminations.

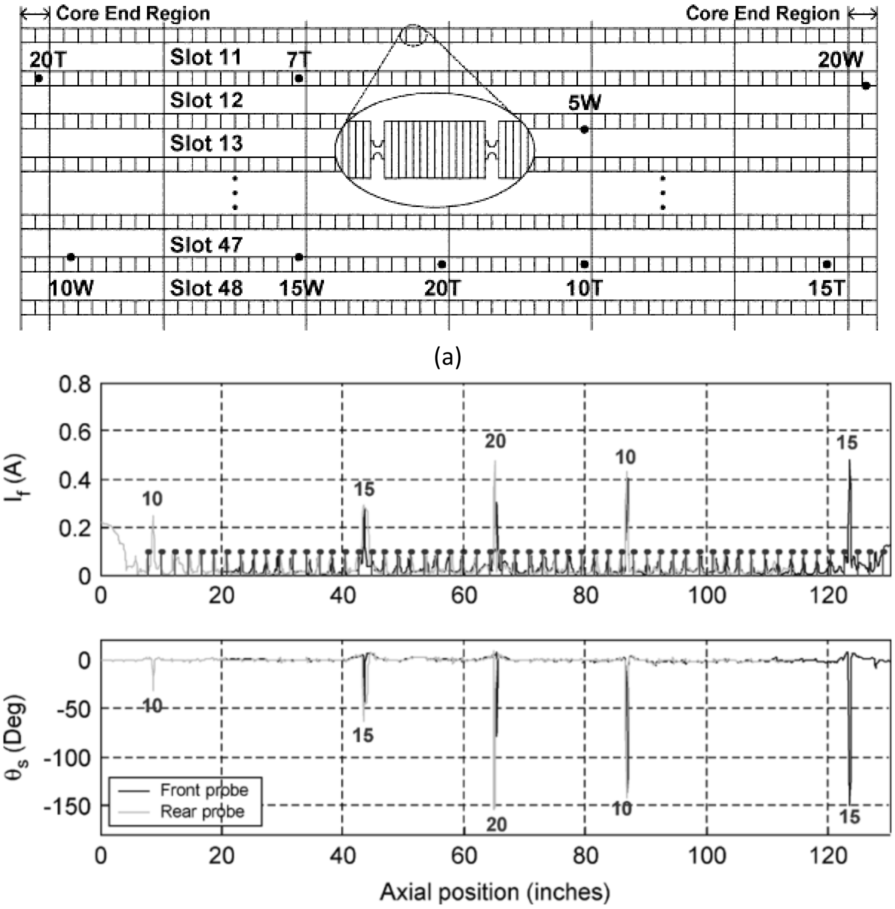

(a)

(b)

Fig 3-24 (a) Map of welded faults in test machine (b) Scan result of slot 47 [3.20]

The results shown in Fig 3-24-b prove the accuracy of the method and also its capability to distinguish between the numbers of the shorted laminations.

The main advantage of the iron core probe is related to the increased level and stability of the measured magnetic flux. Implementing the iron core probe instead of the existing air core probes increases the signal sensitivity, which lead to an increment in the signal-to-noise ratio and consequently allows signal variations due to a few inter-laminar faults to be detected by the system. This technique is now increasingly used by manufacturers to detect inter-laminar short circuit faults in stator cores.

3.3.4. Inter-laminar fault detection using Flux Injection Probe (FIP)

As mentioned earlier in chapter one, in the presence of an inter-laminar fault, a fault current loop is formed between the shorted points which result in increase in the local power loss and local heat. From this point of view, scanning the inner surface of the stator core, or in general scanning the surface of the laminated cores, to measure localised power loss could detect possible short circuits between laminations. Kliman et al in 2004 proposed an electro-magnetic method in which the magnetic core is magnetised locally by means of a Flux Injection Probe (FIP). The measured power loss of the magnetised zone, also known as test zone, being indicative of the condition and quality of the test zone [3.6]-[3.7]. In the absence of inter-laminar faults in the test zone, the measured power loss corresponds to the nominal loss of the material. However, in the presence of an inter-laminar fault in the test zone, an increase of the power loss can be observed [3.6].

Fig 3-25 shows the basic concept of this method applied to a typical synchronous generator core lamination.

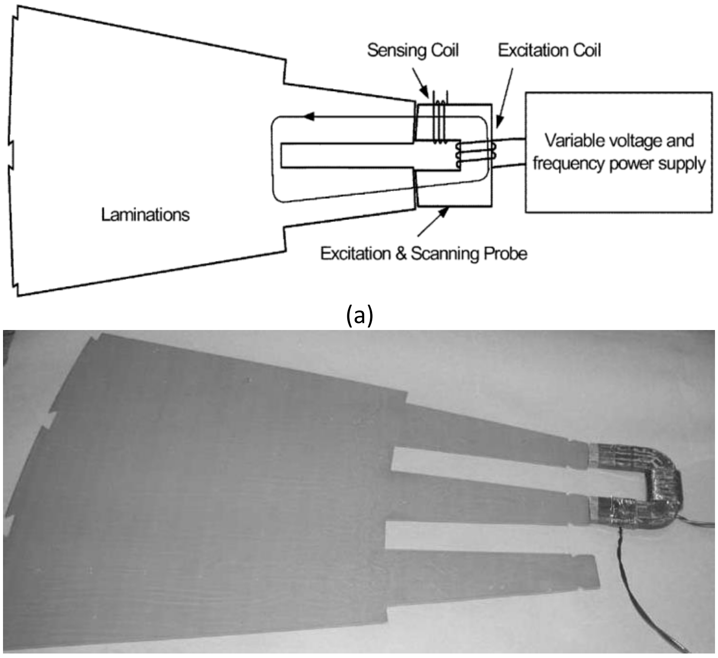

(a)

(b)

Fig 3-25 (a) Flux injection probe concept applied to a lamination segment
(b) Application of the injection probe on a typical lamination segment [3.6]

A small laminated “U-shape” core is placed between a pair of adjacent teeth as shown in the figure. Excitation and measurement windings are wound around the magnetic probe. The excitation winding is connected to a variable voltage and frequency power supply to inject magnetic flux into the core under test. An induced voltage resulting from the injected flux into the test zone is measured using the measurement winding. The excitation winding current and the output voltage of the measurement winding are used to measure the power loss of the magnetised zone as:

$$p = \frac{1}{T}\int_{t}^{t+T} \frac{N_e}{N_s} v_s(t) i_e(t) dt \tag{3-1}$$

where, v_s and i_e represent the measurement winding voltage and excitation current, N_e and N_s are the number of turns of the excitation and measurement windings, and T is the time period. The core loss measurement obtained from a flux injection probe is used to detect and qualify the inter-laminar faults. As the probe is scanned axially along the core, a plot of the magnetic core loss will indicate the location and intensity of the inter-laminar fault.

Fig 3-26-a shows a stack of stator laminations in which a flux injection probe is located between two adjacent teeth to detect inter-laminar faults. In this system artificial shorts between up to 20 sheets were applied on the laminations. Fig 3-26-b shows the magnetic core loss as a function of the number of shorted laminations. Fig 3-26-b shows that the total power loss measured by the probe increases by increasing the number of the shorts, due to the increment in the inter-laminar fault current in the test zone. However there is a high level of noise in the measured power loss. This problem was eliminated by using a differential flux injection probe. The idea is to use two identical probes side by side to measure the difference between the magnetic core losses close to the sections of the stator core. A basic configuration of a differential probe is shown in Fig 3-27-a. Result of the measurement with the same set-up as Fig 3-26-a is shown in Fig 3-27-b.

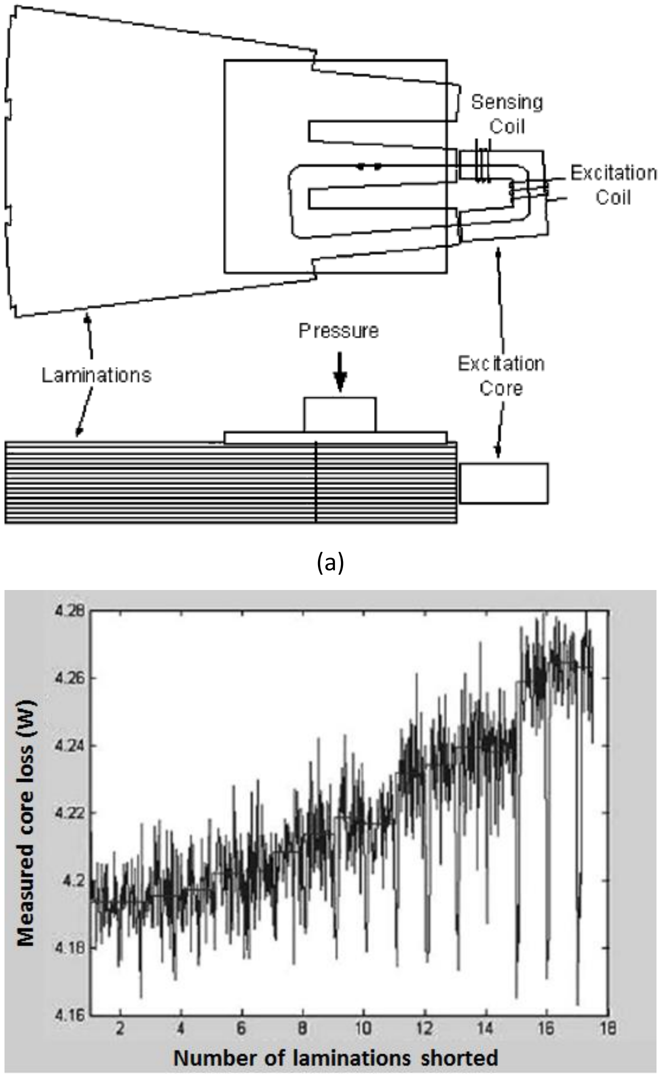

(a)

(b)

Fig 3-26 (a) Application of flux injection probe to test lamination
(b) Measured core loss as a function of the number of faulted laminations [3.6]

In this method since the stator core is magnetised locally a low power source is required to excite the probe and the core under test; it can be considered as the main advantage of this method. This method is also very quick and compared to other methods, i.e. the iron core EL CID method, interpretation the output signals is very easy. In addition to detecting inter-laminar faults, this method is able to qualify the state of compression of the core. However inter-laminar faults involving a small number of laminations might be difficult to be detected using this system.

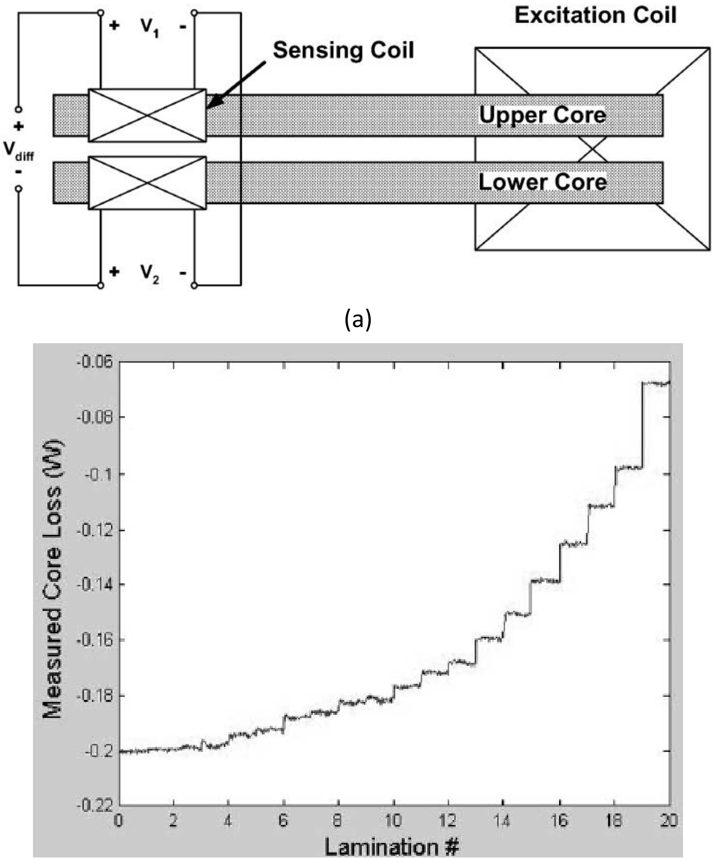

(a)

(b)

Fig 3-27 (a) Differential injection probe concept (b) Measured apparent differential core loss as a function of the number of faulted laminations [3.6]

3.3.5. Inter-laminar fault detection by measuring the tooth leak field

In the case of an inter-laminar short circuit fault the induced voltage in the lamination is short circuited between the shorted laminations, which can affect the flux leakage around the damaged area. Therefore in a stator core by measuring core tooth flux leakage, or in the transformer core through the measurement of the limb or yoke flux leakage, possible inter-laminar faults could be detected. The magnetising system of this method is similar to that used in the EL CID test method and the magnetic core is magnetised at about 5 % of the rated flux. A pick-up coil is implemented to scan the surface of the magnetic core to measure the magnetic flux leakage φ_{str}, as shown in Fig 3-28 [3.17].

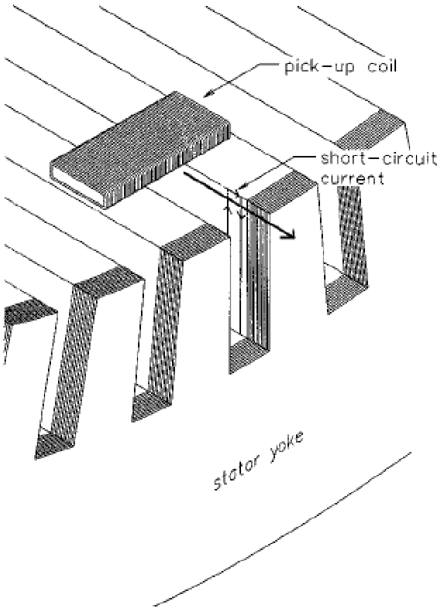

Fig 3-28 Pick-up coil to measure tooth flux leakage [3.17]

In the case of a healthy core, the induced voltage in the pick-up coil is [3.17]:

$$u_M = \int_0^l \frac{\varphi_{str}}{dt} . \frac{w}{l} dl \tag{3-2}$$

where φ_{str} is magnetic flux leakage, w is number of turns and l is length of the pick-up coil. Since the flux leakage varies with the magnetising current I_M, the induced voltage can be written as:

$$u_M = f\ (I_M) \tag{3-3}$$

In the absence of the inter-laminar fault, the induced voltage in the pick-up coil is a linear function of the magnetising current; or the function f in (3-3) is a linear function of the current I_M. In the presence of inter-laminar fault, the fault current I_f will induce a voltage in the pick-up coil. Unlike in the EL CID method, inter-laminar faults cannot be detected from the output voltage of the pick-up coil. Inter-laminar faults are characterised by an increased in both amplitude and phase angle of the measured voltage, as shown in Fig 3-29.

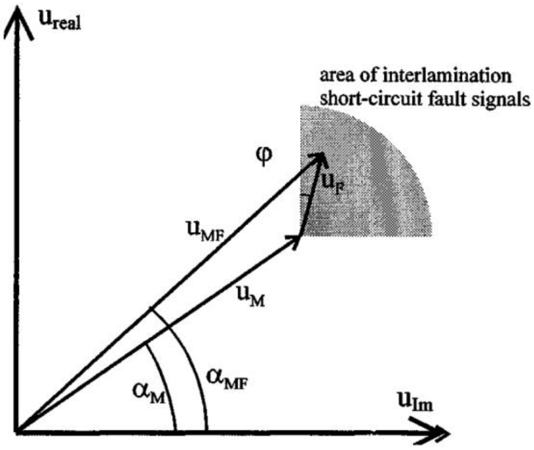

Fig 3-29 Phasor diagram of the fault detection [3.17]

In Fig 3-29, u_M and α_M are the amplitude and phase of the measured voltage without inter-laminar fault, and u_{MF} and α_{MF} are the amplitude and phase of the measured voltage with inter-laminar fault, and φ is the phase angle of the fault current. Therefore the phase and amplitude deviations $\Delta\alpha$ and Δu_M caused by the inter-laminar fault can be defined as:

$$\Delta u = u_M - u_{MF} \qquad \Delta\alpha = \alpha_M - \alpha_{MF}$$

Typical experimental result of the amplitude and phase angle changes on a magnetic core with different inter-lamination faults is shown in Fig 3-30. The results of this test can help to detect any inter-laminar faults in the magnetic core [3.17].

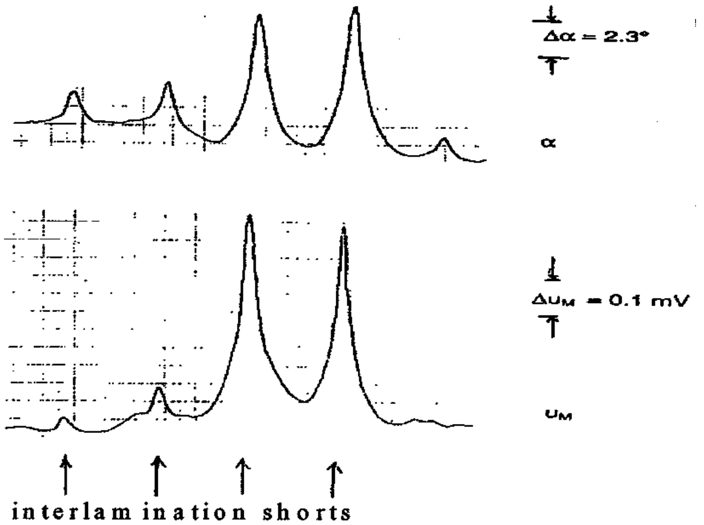

Fig 3-30 Amplitude and phase angle changes at interlamination short-circuits [3.17]

Disadvantages of the classical inter-laminar fault detection methods are avoided by the measurement of the tooth flux leakage. The measurement of the tooth flux leakage provides correct information about inter-laminar faults in the core, as shown in Fig 3-30. However compare to the other methods, e.g. FIP method, interpreting the result difficult.

3.3.6. Inter-laminar eddy current fault measurement using Rogowski coil

Schulz et al. in 2010 developed an experimental method to measure the inter-laminar fault current in a stack of laminations using a Rogowski coil around the damaged (burred) laminations [3.18]. A Rogowski coil consists of a winding wound around a non-magnetic core and placed close to a conductor to measure alternating currents. The winding forms a mutual inductance coupled with the conductor. Output voltage of the coil is related to the vibration of the current in the conductor. For a circular coil with rectangular cross section, the relation is [3.18]:

$$u_2 = \frac{\mu_0 N h}{2\pi} ln\left[\frac{c}{b}\right]\frac{di_1}{dt} \tag{3-4}$$

where μ_0 is the vacuum permeability, N is number of turns, h is height of the coil, c and b are outer and inner radius of the coil and i_1 is the current in the conductor. Integration of the output signal yields a voltage which is proportional to the current. Fig 3-31-a shows a Rogowski coil and Fig 3-31-b shows its application to measure inter-laminar fault current between two laminations [3.18].

(a) (b)

Fig 3-31 (a) Top view of a Rogowski coil (b) Application of a Rogowski coil to measure inter-laminar fault current between two laminations [3.18]

In this investigation, artificial short circuits were applied between two transformer laminations by creating two contact points on opposite sides of the sheet. In order to insert the Rogowski coil between the laminations, a small gap was made between the laminations, as shown in Fig 3-31-b. The additional air gap between the laminations does not affect the short circuit current; because the permeability of the lamination material is much higher than that of air (μ_r>>1). A low-noise amplification and integration circuit was used to amplify the output voltage of the Rogowski coil.

Short circuit current and power loss, as a function of core width, measured by the Rogowski coil are shown in Figs 3-32-a and 3-32-b, respectively. The results show that for extremely narrow cores, the short circuit current is a non-linear function of the core width; however, for wider cores the function can, with good accuracy, be approximated by a linear function. Inter-laminar fault current of a real scale transformer can be estimated by extrapolating the result of Fig 3-32. For example, for a very large transformer core of 60 cm width at a peak flux density of 1.7 T and frequency of 50 Hz, the peak short circuit current was estimated to be 9.8 A.

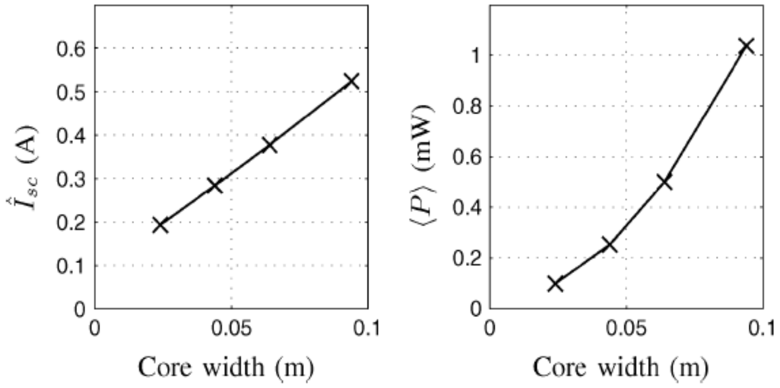

Fig 3-32 Inter-laminar short circuit current and power loss as a function of core width [3.18]

Although measuring inter-laminar fault current by Rogowski coil provides reliable measurements in a stack of laminations, it requires a gap between the laminations to place the coil. This might be a challenge in real scale transformers which is the main drawback of this method.

3.3.7. Capacitive short circuit detection method

It is well known that a capacitance, in the simplest way, consists of two conducting plates which are insulated by a di-electric plate. From this point of view in a stack of electrical steel lamination adjacent sheets form a capacitance, as shown in Fig 3-33. Schulz et al. in 2008 developed a non-magnetic method to detect inter-laminar faults in magnetic cores by measuring the capacitive effect between the transformer core laminations [3.19].

Since the insulation coating used in transformer lamination, and in general in electrical steels, is very thin the resulting capacitance between adjacent laminations is high enough to be easily measured. As an example, capacitive effect for Epstein-sized lamination (30 mm × 300 mm) with approximately 3 µm insulation on each side is in the range of 5 *nF* [3.19].

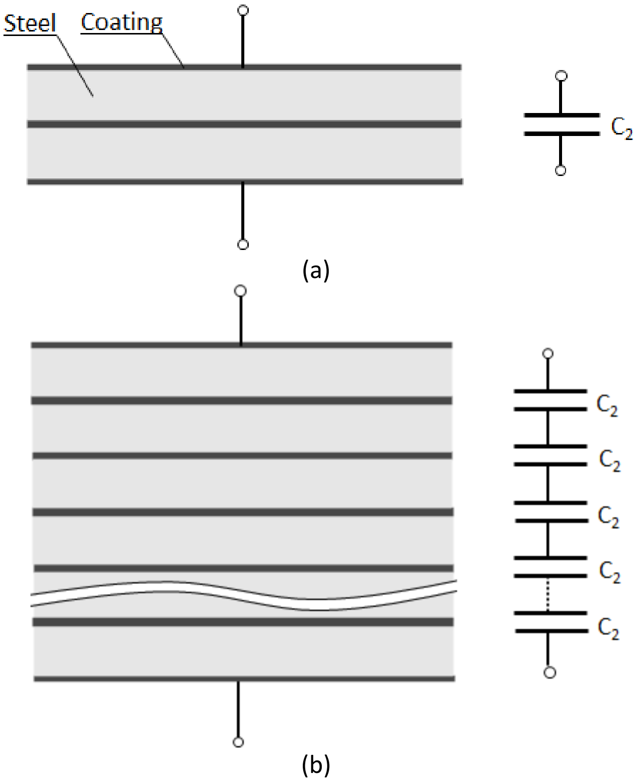

Fig 3-33 Capacitance effect (a) between two adjacent lamination
(b) between two ends of a stack of lamination

According to Fig 3-33, a stack of laminations forms a series of plate capacitors and the total capacitance is measured as [3.19]:

$$C_N = \frac{C_2}{N-1} \tag{3-5}$$

where N is the number of laminations in the stack and C_2 is the equivalent capacitance of adjacent laminations. It is assumed that C_2 is the same between any pair of sheets. If inter-laminar fault appears between two laminations, N is reduced by one and the equivalent capacitance increases. Therefore, if the capacitance between adjacent laminations C_2 and the number of laminations in the stack N are known initially, the number of inter-laminar faults can be detected.

This method cannot recognise whether the inter-laminar fault appears at one, two or more points; it will detect harmless faults as well as harmful ones. This method is also unable to find the location of the inter-laminar fault in the core. Furthermore, since laminations of the stator cores are welded together or held together through either key bar or the housing of stator yoke [3.8] this method is not applicable to detect the inter-laminar fault between stator laminations. However this is a non-destructive, simple and easy-to-implement method to detect inter-laminar faults in transformer core laminations. And also this method does not require exciting the magnetic core under test.

3.4. Methods for testing the effectiveness of the insulation coating

As mentioned earlier in chapter 1, magnetic cores are constructed from thin sheet laminations to reduce eddy current power loss. This method is effective if the laminations are electrically insulated from each other. Therefore convenient methods of the evaluating the insulation coating of the electrical steels are required to get good knowledge about surface resistance of the individual laminations and inter-laminar resistance in a stack of laminations.

3.4.1. Two probe configuration

When we speak about resistance measurement, the first idea might be to use an Ohm-meter. Fig 3-34 shows a basic configuration of measuring surface resistance of a magnetic lamination by pressing the probes of an Ohm-meter onto the surface of a single lamination [3.21].

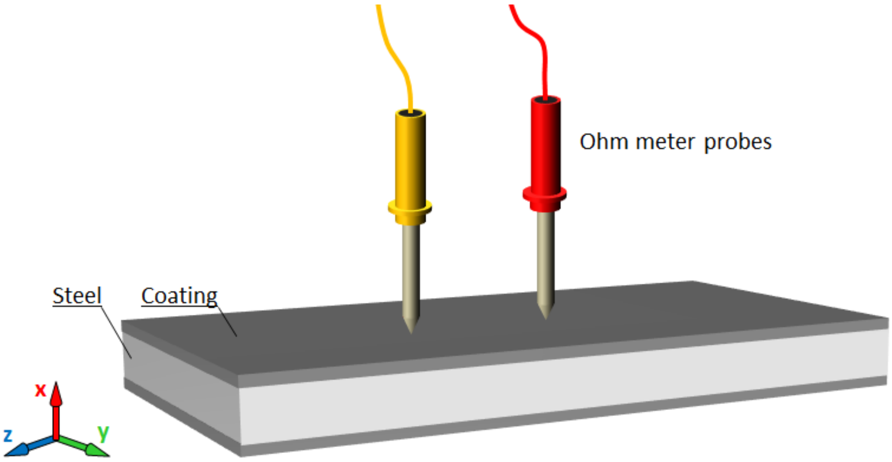

Fig 3-34 Basic configuration of measuring surface resistance of a magnetic lamination (reproduced based on [3.21])

Certainly this is not a scientific and reliable method. Measuring the surface insulation resistance of electrical steels is more special in some important parameter like pressure should be considered, which is un-quantified and un-controlled in the configuration of Fig 3-32 [3.21]. However this method can be used generally as a quick way of checking whether the insulation coating is healthy or damaged.

Other two probes techniques have been reported in which the resistance between two particular points is measured by applying a specific voltage between two points of the lamination and measuring the current drawn from the power supply [3.22]. The first possible configuration is shown in Fig 3-35.

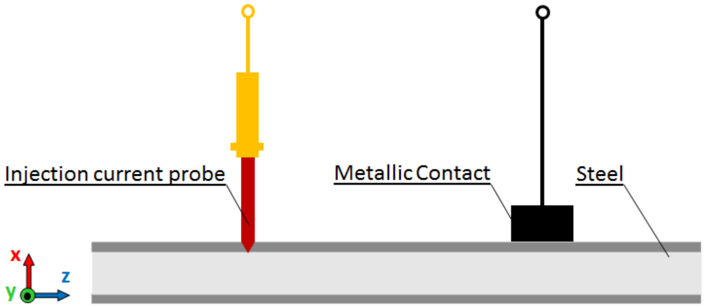

Fig 3-35 Measurement of the insulation resistance of one insulation film between the measuring electrode and the metal core (reproduced based on [3.22])

In this method the insulation resistance of one side of the lamination between the measuring electrode and the steel core of the lamination can be measured. The widest application of this method is the Franklin test method [3.23]–[3.25] and is accepted by many standards; ASTM, IEC, JIS, and BS, as cited in [3.22].

Another method measuring of insulation resistance is shown in Fig 3-36 in which the insulation resistance of one or two insulation coatings (depending on whether the lamination is coated on one or both sides) between the measuring electrodes is measured. This method is accepted by national standards, such as GOST, BS and DIN, as cited in [3.22]; however, different standards offers different pressures, voltages and electrode sizes.

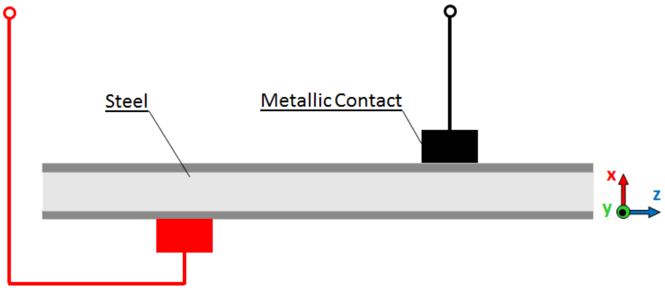

Fig 3-36 Measurement of the insulation resistance of one or two insulation coatings between two measuring electrodes (reproduced based on [3.22])

Measurement of the insulation resistance of the insulation coatings between two laminations is another method in the surface resistance investigation. Two possible configurations of this method are shown in Fig 3-37. This method is offered by national standard TGL, as cited in [3.22].

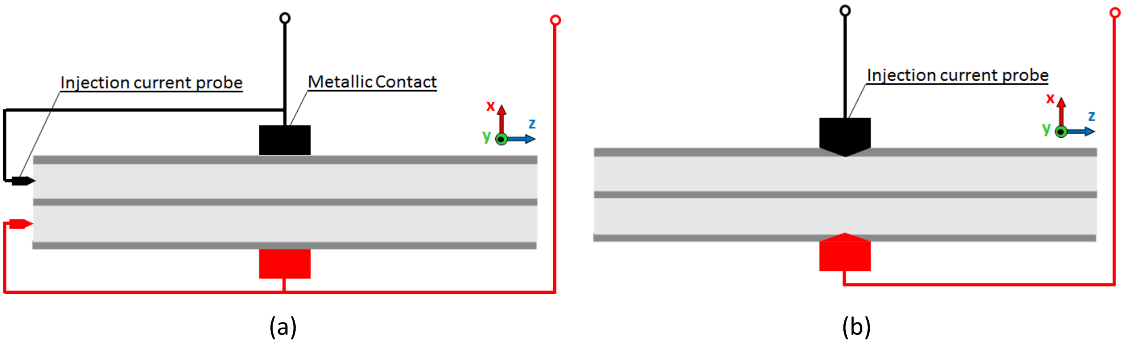

Fig 3-37 Measurement of the insulation resistance of the insulation coatings between two laminations; injection current (a) from side and (b) from top of the laminations (reproduced based on [3.22])

Another method in this category is measuring the resistance between the top and bottom layers in a stack of laminations, under a specific pressure. Fig 3-38 shows a possible configuration for this test [3.21]. This method is similar to the capacitive short circuit detection method while here the total resistance between the electrodes is measured. This method is applicable only to transformer cores but not for stator cores, because in the stator cores laminations are welded or shorted together through either key bar or the housing of stator yoke at the outer side.

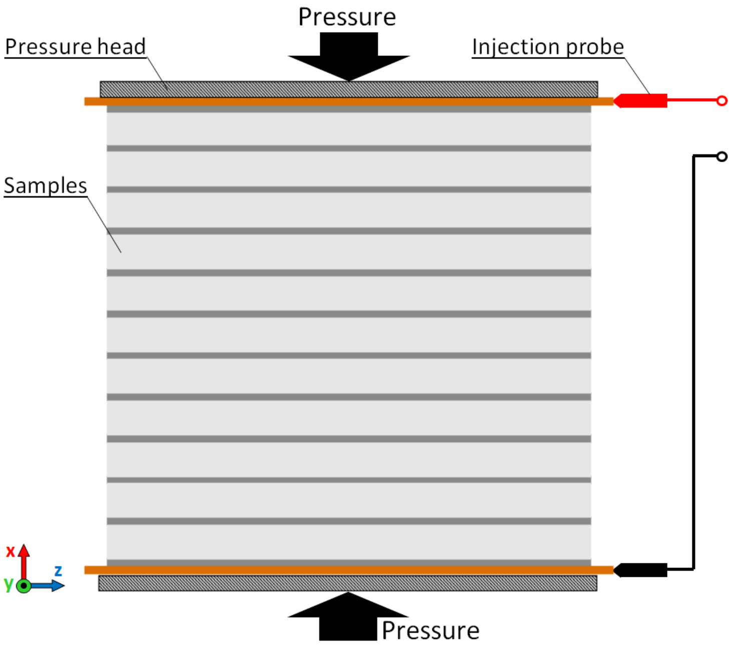

Fig 3-38 Measuring insulation resistance in a stack of lamination (reproduced based on [3.21])

3.4.2. Two surface test system or Four probes configuration

The four probes measuring technique, also known as four terminal measuring technique or two surface test system, is a common method to measure resistance between two adjacent laminations, when a high level of accuracy is required [3.26]. According to the reference standard [3.26] two 250 × 250 mm electrical steel laminations with insulating coating on both sides are required. A schematic of the four probe configuration is shown in Fig 3-39.

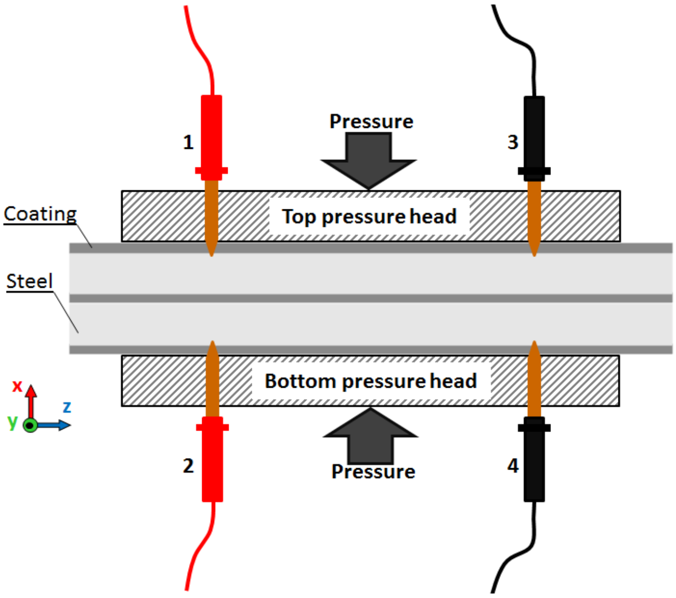

Fig 3-39 Four probes configurations, 1 and 2 contacts carrying currents, 3 and 4 contacts measuring voltages (reproduced based on [3.26])

In this test method the average resistance between adjacent insulating surfaces under specified pressure is measured. A constant direct current is injected to the laminations through metallic contact (drill bits) and a voltage is measured using a digital voltmeter. Since the inter-laminar resistance is extremely high, a small current flows through the contacts and hence a very small voltage is produced at the voltage probes. Therefore high accuracy facilities are required to measure the real value of the inter-laminar resistance [3.26]. A block diagram of the measuring system is shown in Fig 3-40.

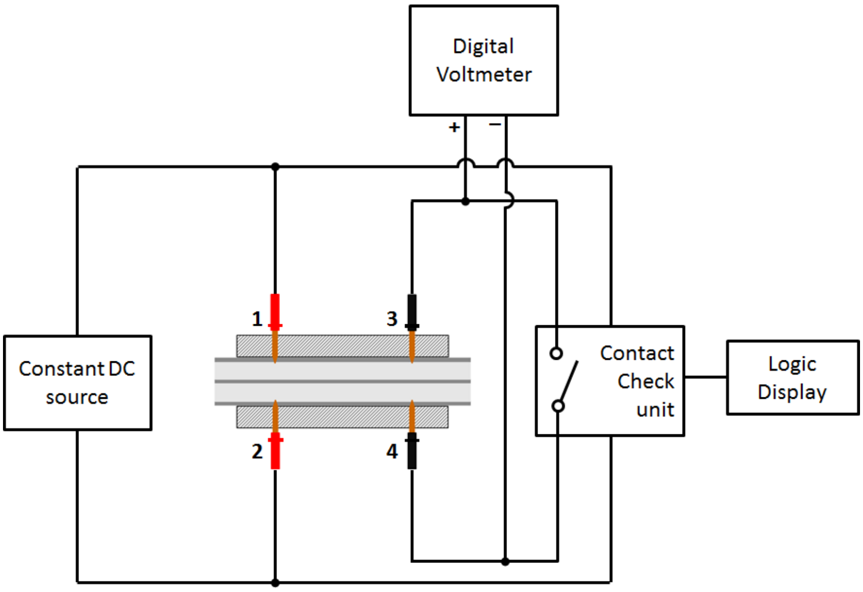

Fig 3-40 Block diagram of two surface test system (reproduced based on [3.26])

The constant current source of the tester provides a constant DC current through the insulation. The resulting voltage is measured by a suitable voltmeter and eventually the insulation resistance is determined by Ohm's law. Since the thickness of the coating may vary across the lamination surface, several measurements are suggested at different points. The number of measurements on each sample depends on the nature of the surface insulation and the required accuracy [3.26].

In commercial four probe measurement systems two constant current ranges are considered to optimise the accuracy of the measurement; 1 µA for inter-laminar resistance greater than 1200 kΩ and 10 µA for inter-laminar resistance less than 1200 kΩ. An indicator light is also provided that warns the operator if the current range is not suitable for a given sample [3.26].

3.4.3. Surface insulation resistance measurement by Franklin tester

The Franklin tester is a standard test method to measure the coating surface resistance of magnetic laminations [3.23]–[3.26]. The principal of the measurement is similar to the method described in Fig 3-35 in which the surface resistance is measured, under a certain pressure, by injecting a controlled DC current into the steel and measuring a voltage drop on the surface of the lamination.

In this method ten metallic electrodes with fixed cross section area of 64.5 mm^2 each are applied to the surface of the specimen. A standard pressure of 129 N per electrode, equal to 2 N/mm^2 is applied on each electrode. Two electrical contacts are made on the surface of the steel using a spiral drill which perforates the insulating coating. A DC constant voltage of 500 mV is applied between the drills and electrodes. 5 Ω resistances are connected in series with each electrode to limit the current to 1 A in the case of a short circuit between the drills and electrodes [3.24]. A basic configuration and a photograph of a commercial type of the Franklin tester is shown in Fig 3-41-a and 3-41-b, respectively.

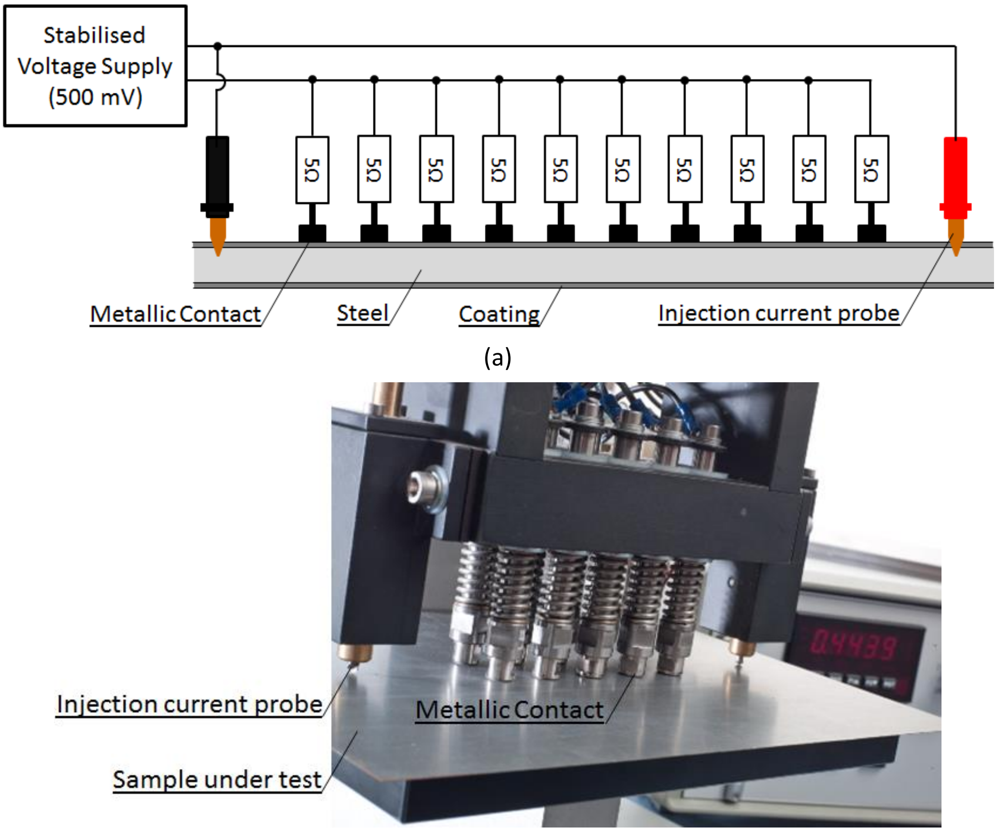

(a)

(b)

Fig 3-41 (a) Measurement principle of the Franklin device (reproduced based on [3.24])
(b) Magnetic lamination under Franklin test [3.26]

According to the IEC 404-11 standard, two measuring modes are defined with the Franklin Tester to convert the measured values into an equivalent surface resistance:

- Method **A**: Measurement of the insulation coating through 10 electrodes
- Method **B**: Measurement of the insulation coating as through a single resistance per electrode

In mode **A**, *M* measurements are performed at different points and the current flowing through the ten electrodes is recorded. The coefficient of the surface insulation resistance *C* is then calculated as follows [3.24]:

$$C = A\left[\frac{V}{\frac{1}{M}\sum_{j=1}^{M} I_{tj}} - \frac{R}{10}\right] (\Omega.mm^2) \qquad (3\text{-}6)$$

where *V* is the applied voltage (500 mV), *R* is the resistance connected to each electrode (5 Ω), *M* is number of the measurement, *A* is area of the ten electrodes (645 mm^2) and I_{tj} is total current of each measurement.

The electrical circuit of the tester is modified in mode **B** by reducing the test voltage to 250 mV and removing the resistances of 5 Ω. In order to measure the currents flowing through each electrode, low value resistances are inserted at a point outside the connection of the stabilising circuit. One hundred measurements are performed; the equivalent surface resistances are then calculated (R_i=0.25/I_i) and sorted in order of the magnitude [3.24].

The major problem with surface insulation resistance measurement by the Franklin tester is poor repeatability [3.23]–[3.25]. The repeatability of the measurements has been investigated in [3.24] by ten successive measurements at the same place and the same material; the results are poor and standard deviations (STDV) of the measurement is quite high (even more than 100 %). This is the main drawback of the Franklin tester. An example of surface resistance measurement using the Franklin tester for five samples from the same coil is shown in Table 3-2 which shows a high level of standard deviation.

Table 3-2 Franklin tester result for 5 samples from the same coil [3.23]

Sample	Average total current (mA)	Relative standard deviation (%)	C (Ω cm^2)
1- Side 1	98	107	30
Side 2	198	59	13
2- Side 1	94	73	31
Side 2	186	49	14
3- Side 1	85	66	34
Side 2	184	59	14
4- Side 1	108	69	26
Side 2	153	63	18
5- Side 1	86	68	34
Side 2	257	62	9

Another issue which should be considered in the Franklin tester is the applied pressure from the electrodes to the surface of the specimen. The applied pressure, on one hand, should be high enough to make a suitable electrical contact between the electrodes and sample; and on the other hand, should be as close as possible to the real condition of the electrical machines. Laminations of real electrical machines are not pressed uniformly and the pressure around the clamping devices is higher than the other parts. The pressure defined on the standard Franklin tester (2 N/mm^2) is higher than the average value in electrical machines. However, it can be justified that the insulation coatings are supposed to tolerate the worst conditions [3.24].

Apart from the drawbacks of the Franklin tester, this method can provide a reasonable assessment of insulation coatings quality and has been widely used in industry. Fig 3-42 shows three commercial models of the Franklin tester device.

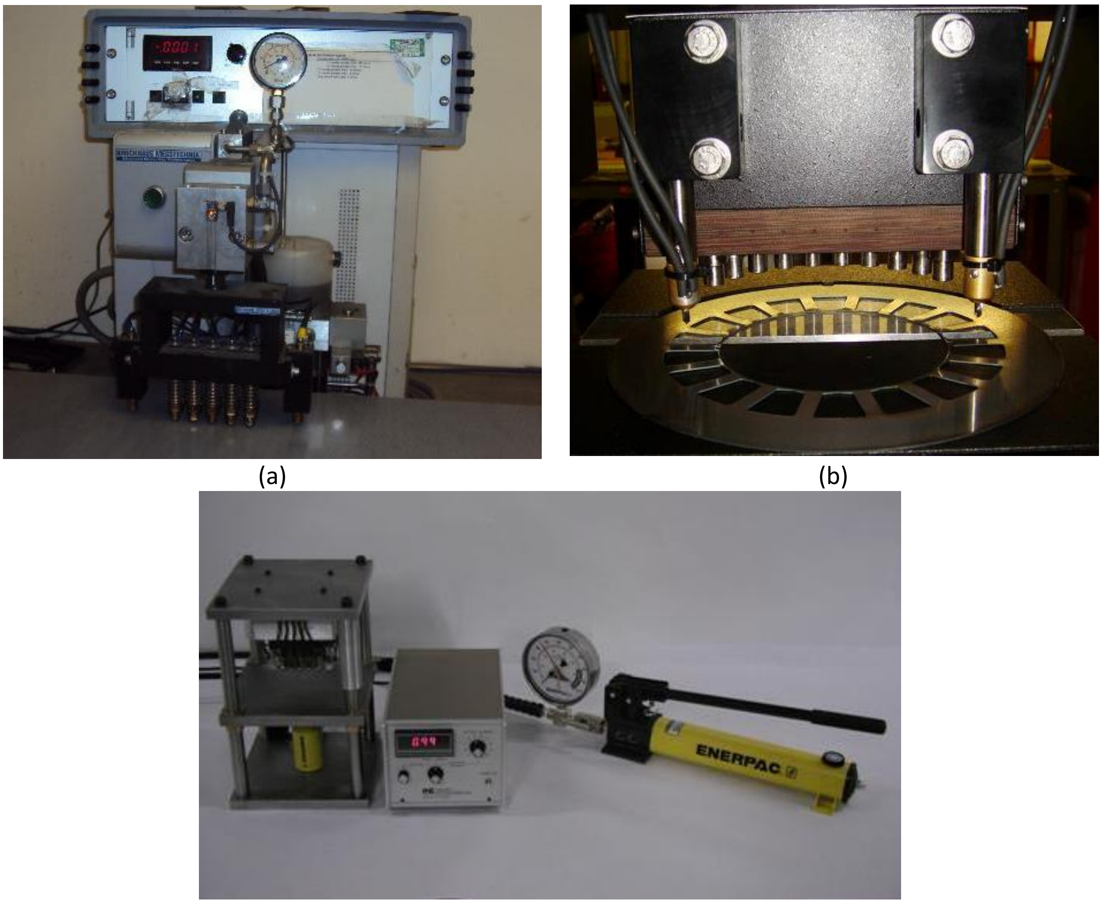

(a) (b)

(c)

Fig 3-42 Commercial models of Franklin tester to measure surface resistance of (a) large scale laminations (b) stator core laminations and (c) a portable type of Franklin tester

3.5. Summary

As shown in part 3.2, in most of the previous work it was assumed that the inter-laminar faults occur between the adjacent laminations of the core at set points which result in a short circuit volume with well-known location and physical dimensions; while in practice they appear at random positions which create different patterns of inter-laminar faults. Furthermore, important factors such as skin effect, non-uniform flux density distribution, complex relative permeability and non-linear relation of ***B (H)***, are neglected in the literature. Therefore no close agreement between the analytical modelling of the extra power loss caused by the inter-laminar faults and that of the experimental work has been achieved.

In part 3.3 existing methods of inter-laminar fault detection are reviewed. From the magnetising point of view, the fault detection methods can be categorised as *High induction* or *Low induction*. In the first category the core should be magnetised at rated flux density while in the second category the core is magnetised at about 3-4 % of the rated induction.

The main drawbacks of the high induction methods can be listed as follow:

- Requirement for a powerful and low-power-factor power source
- Unsatisfactory assessment criteria
- Inadequate detection of the inter-laminar short circuits
- High costs

On the other hand, the advantages of the low induction methods over the high induction method can be listed as follow:

- Requirement for a low-power power source
- The control during a repair is easy and can be performed immediately
- The measurement indicates all inter-laminar short circuits, even those which are not hot
- Low cost

As a general vision and to compare and summarise the mentioned methods, their advantages and disadvantages are presented in Table 3.3.

Table 3-3 Summary of inter-laminar fault detection methods

No	Method	Base	Advantages	Disadvantages
1	Full ring test	Detecting hot spots of the core by a thermal camera	☑ Easy to set-up and control	☒ Requirement for a power-full and low-PF power source ☒ Time consumer ☒ Unable to detect the faults on wall and surface of the tooth ☒ Unable to detect the faults with low temperature ☒ Requirement for special facilities ☒ High cost
2	EL CID	Measuring magnetic potential between two points by using an air core coil	☑ Low induction ☑ Reduced set-up High sensitivity to deep-seated faults ☑ Easy to interpret the results	☒ Low signal-to-noise ratio ☒ Difficulty of data interpretation ☒ Difficulty of scanning and interpretation in the stepped core-end region
3	Iron Core Probe EL CID	Measuring magnetic potential between two points by using an iron core probe	☑ Low induction ☑ Increased level and stability of the measured flux ☑ Fast in surface scanning ☑ Low noise	☒ Difficulty of data interpretation ☒ Difficulty of scanning and interpretation in the stepped core-end region
4	FIP	Locally magnetise the laminations and measuring power loss	☑ Low induction ☑ Very quick ☑ Easy to interpret ☑ Enable to detect state of core compression	☒ Unable to detect the inter-laminar faults with a few numbers of laminations
5	Leakage field probe	Detecting the faults by measuring leakage field	☑ Low induction ☑ Fast in surface scanning	☒ Difficulty of data interpretation
6	Rogowski coil	Measuring fault current between laminations by Rogowski coil	☑ Easy to setup and control ☑ Easy to interpret the output signal	☒ Requires a gap between the laminations ☒ Weak signal at the output of the sensing coil
7	Capacitive effect	Fault detection by measuring equivalent capacitance between laminations	☑ Non-destructive and simple ☑ Easy to implementation ☑ No need to magnetise the laminations	☒ Unable to detect the location of the fault ☒ Unable to identify the number of the short circuits between two adjacent laminations ☒ Not applicable to stator cores

Except for the last two methods, all of the existing techniques were basically developed for stator cores of generators; however considering the magnetic circuit and related criteria of the transformer core they could be modified and re-designed for transformer cores, or other magnetic cores.

In part 3.4 techniques for testing the effectiveness of insulation coating of the electrical steels are reviewed. The last two methods, four probes configuration and Franklin tester are more applicable in industry. These two methods are summarised in Table 3.4.

Table 3-4 Summary of the testing the effectiveness of insulation coating

No	Method	Base	Advantages	Disadvantages
1	Four probes configuration	Measuring inter-laminar resistance by injecting current and measuring voltage	☑ An standardised method ☑ Easy to implement ☑ Easy to setup and control ☑ Easy to interpret the output signal	☒ Destructive test ☒ Non applicable to more than two laminations ☒ Depend strongly on the applied pressure
2	Franklin device	Measuring surface resistance by injecting current and measuring voltage	☑ An standardised method ☑ Easy to interpret the output signal	☒ Destructive test ☒ Poor repeatability and high level standard deviations ☒ Depend strongly on the applied pressure ☒ Relatively expensive

As a general note on this chapter, although previous research and studies on the effect of inter-laminar short circuit faults on the performance of the magnetic cores shows good achievements, but considering the real nature and circumstance of the inter-laminar faults and also concerns of the manufacturers of the electrical machines, there is still a wide gap in this field. Furthermore non-destructive and reliable methods are required to detect inter-laminar short circuit faults, especially in transformer cores.

References

[3.1] A J Moses and M B Aimoniotis, "*Effects of Artificial Edge Burrs on the Properties of a Model Transformer Core*," Physica Scripta, VOL. 39, 1989, pp. 391–393

[3.2] M B Aimoniotis and A J Moses, "*Evaluation of Induced Eddy Currents in Transformer Sheets Due to Edge-Burrs, Employing Computer Aided Design Programs*," in Athens Power Tech '93 Proc., 1993, VOL. 2, pp. 847–849

[3.3] C A Schulz, D Roger, S Duchesne, and J N Vincent, "*Experimental Characterization of Interlamination Shorts in Transformer Cores*," IEEE Trans Magn., vol. 46, no. 2, Feb. 2010, pp. 614–617,

[3.4] E Lamprecht and R Graf, "*Fundamental Investigations of Eddy Current Losses in Laminated Stator Cores Created Through the Impact of Manufacturing Processes*" Proceeding of 1st International Electric Drives Production Conference (EDPC), 2011, pp. 29-35

[3.5] J P Bielawski, S Duchesne, D Roger, C Demian and Th Belgrand, "*Contribution to the Study of Losses Generated by Inter-Laminar Short-Circuits*", IEEE Trans On Magn, Vol. 48, No. 4, April 2012, pp 1397-1400

[3.6] G B Kliman, S B Lee, M R Shah, R M Lusted, and N K Nair, "*A New Method for Synchronous Generator Core Quality Evaluation*," IEEE Trans. Energy Convers., Vol. 19, NO. 3, , Sep. 2004, pp. 576–582

[3.7] J M Bourgeois and F Lalonde, "*Apparatus and Method for Evaluation a Condition of a Magnetic Circuit of an Electric Machine*," U.S. Patent 5 990 688, Nov. 23, 1999

[3.8] S B Lee, G B Kliman, M R Shah, W T Mall, N K Nair and R M Lusted "*An Advanced Technique for Detecting Inter-Laminar Stator Core Faults in Large Electric Machines*" IEEE Trans On Ind. App, Vol. 41, NO. 5, Sep/Oct 2005, pp. 1185–1193

[3.9] M. M. Znidarich "*Hydro Generator Stator Cores Part 2-Core Losses, Degradation Mechanisms, Testing and Specification*", Proc. AUPEC, pp.1 -9 2008

[3.10] K Lee, J Hong, K Lee, S B Lee and E J Wiedenbrug, "*A Stator Core Quality Assessment Technique for Inverter-fed Induction Machines*", IEEE Industry Applications Society Annual Meeting, Oct 2008, pp 1-8

[3.11] J. Sutton, "*El-CID—an Easier Way to Test Stator Cores*," Elect. Rev., Jul. 1980

[3.12] D R Bertenshaw, J F Lau and D J Conley, "*Evaluation of EL CID Indications Not Associated With Stator Core Inter-Laminar Insulation Faults*" IEEE Electrical Insulation Conference, June 2011, pp 254- 260

[3.13] D B Paley "*Current Low Power Core Testing Using El CID*" IEEE Colloquium "Understanding your condition monitoring (Ref. No. 1999/117)" April 1999, pp 7/1-7/4

[3.14] R Romary, C Demian, P Schlupp, J Y Roger, and T Szkudlapski, "*Real Scale Experimental Devices for Stator Core Fault Analysis*," in Proc. 8th IEEE SDEMPED, Sep. 2011, pp. 71–76.

[3.15] Maine Industrial Repair Services Inc, Available at: http://www.maineindustrial.com, July 2014

[3.16] IRIS POWER, Available at: http://www.irispower.com, July 2014

[3.17] Z Posedel, "*Inspection of Stator Cores in Large Machines with a Low Yoke Induction Method—Measurement and Analysis of Interlamination Short-Circuits*", IEEE Trans on energy conversion, Vol. 16, NO. 1, March 2001, pp. 81-86

[3.18] C A Schulz, S Duchesne, D Roger and J N Vincent "*Short Circuit Current Measurements between Transformer Sheets*", IEEE Trans Magn, VOL. 46, NO. 2, Feb 2010, pp 536-539

[3.19] C A Schulz, S p Duchesne, D Roger and J N Vincent, "*Capacitive Short Circuit Detection In Transformer Core Laminations*", JMMM, 320 (2008) e911–e914

[3.20] S B Lee, G B Kliman, M R Shah, N K Nair and R M Lusted "*An Iron Core Probe Based Inter-Laminar Core Fault Detection Technique for Generator Stator Cores*" IEEE Trans. Energy Convers., Vol. 20, No. 2, Jun. 2005, pp. 344–351

[3.21] P. Beckley "*New Initiatives in the Assessment of Surface Insulation Resistance of Coatings on Electrical Steels*" Journal of Materials Engineering, , Volume 12, Issue 1, March 1990, pp 47-50

[3.22] Z Godec, “*Comparison of Tests for Insulating Coatings on Steel Sheet*” IEEE Trans on Electrical Insulation Vol. EI-15 No.2, April 1980, pp. 95-103

[3.23] BS EN 10282: 2001 “*Method of Test for the Determination of Surface Insulation Resistance of Electrical Sheet and Strip*”

[3.24] M C Marion-Pera, “*Characterization of SiFe Sheet Insulation*”, IEEE Trans On Magn, Vol 31 . No 4. JULY 1995

[3.25] MC Marion-Pera, “*Analysis and Comparison of Magnetic Sheet Insulation Tests*” Journal of Magnetism and Magnetic Materials 133 (1994) 396-398

[3.26] ASTM A 937/A937M-1, “*Standard Method for Determining Inter-Laminar Resistance of Insulating Coatings Between Two Adjacent Test Surfaces*” August 2001

[3.27] SIMENS, Available at: http://www.energy.siemens.com, July 2014

CHAPTER 4

Eddy Current Loss Modelling of a Single Lamination Based on the Equivalent Circuit of the Lamination over a Wide Range of Frequency and Flux Density

4.1. Introduction

Magnetic cores are one of the main parts of electrical machines and other magnetic devices. The main role of the magnetic cores is concentrating the magnetic field to make the maximum possible magnetic coupling between the primary and secondary windings of the transformers or stator and rotor of the rotating machines [4.1]. When a time varying magnetic field links the windings, it induces an *emf* in the coils in accordance with Faraday's law of induction. As the coils are wound over the magnetic iron core, an *emf* is also induced in the magnetic material by the same time varying flux. Since the magnetic materials are also good conductor of electricity, the induced *emf* along a closed path inside the magnetic material sets up a current along that path which is known as an *eddy current* [4.1]. The main effect of the induced eddy current in the magnetic cores is heating of the core because of the rather high resistance of the iron to the current path. This heat represents a power loss in the core which is known as *eddy current power loss*. Excessive heating can damage or destroy the magnetic cores [4.2].

In this chapter, analytical modelling based on an equivalent circuit of the magnetic laminations is proposed to calculate and predict the eddy current power loss of magnetic laminations. In the relevant studies skin effect, non-uniform distribution of flux density, the hysteretic relationship of ***B*** and ***H*** or non-linearity of the material are determinant factors, especially at high magnetising frequencies and high relative permeabilities. The effect of these factors on the eddy current power loss and other magnetic properties of the lamination are discussed properly and considered in the modelling. An analytical-experimental technique was also developed to separate core loss components obtained from the experimental measurements of power losses, over a wide frequency range to separate the eddy current power loss and compare to the analytical results.

4.2. Nature of eddy currents and eddy current power loss

Eddy currents i_{edd} are induced in any conducting material exposed to time-varying magnetic fields, and therefore they occur in all types of electrical equipment which operate in time-varying magnetic fields. Fig 4-1 shows a schematic of the induced eddy current in a conductive plate caused by a time varying magnetic field.

Eddy currents were first observed by François Arago (1786-1853), the 25th president of France, who was also a mathematician, physicist and astronomer. In 1824 he discovered the phenomenon of rotatory magnetism; which showed that almost all bodies in nature are susceptible of electromagnetic actions and could be magnetised. This discovery was completed later by an English scientist, Michael Faraday (1791-1867) [4.3].

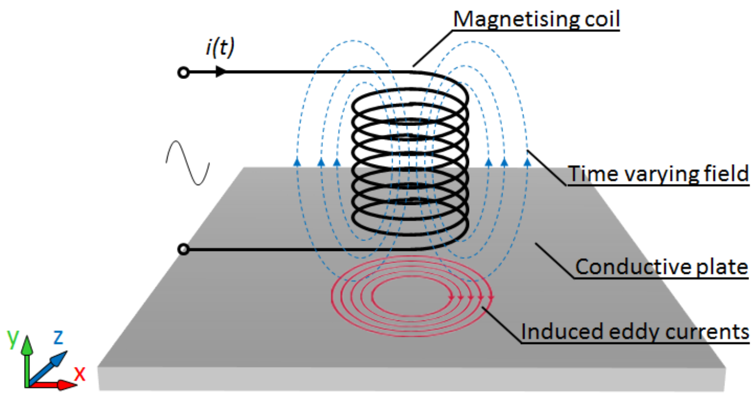

Fig 4-1 Induced eddy current in conductive plate exposed to time-varying magnetic field

Heinrich Lenz (1804-1865), a Russian physicist, in 1833 stated that the magnetic field caused by current flow in a test object opposes the original magnetic field that caused the current flow in the object. This phenomenon was named as Lenz's law in electrodynamics in his honour. Based on Lenz's law, the induced eddy current in the test objects generates a secondary flux which cancel a part of the primary flux equal to the amplitude and phase of the field generated by the eddy current [4.3]. However Léon Foucault (1819-1868) a French physicist was the first person who really discovered eddy currents. In his experiment he placed a rotating copper wheel in the gap between the poles of an electromagnet. With no current passing through the coils, the wheel rotated easily. However the required force for the rotation of the wheel becomes greater after energising the coil and at the same time the wheel started heating up [4.3]. In the 19th century, eddy currents were sometimes called Foucault currents, in Foucault's honour [4.4].

Similar to all electric currents, eddy currents generate heat in the materials and electromagnetic force in the surrounding space. The generated heat could be implemented in induction furnaces and the electromagnetic forces could be used to create movement or levitation forces or to make braking effect. Eddy currents however are sometimes an undesirable effect, for instance magnetic power loss in magnetic cores of electrical machines [4.2]. Whether eddy currents are beneficial or detrimental, an accurate method of prediction is necessary at the design and operating stages of the equipment.

4.2.1. Skin effect in conductive materials

When a time-varying magnetic field is applied to a conducting material, an *emf* is induced in the material, in accordance with Faraday's law of induction. Considering the electrical conductivity of the material, the induced *emf* along each particular closed path inside the material forms a current along that path to circulate and penetrate conducting parts. The direction of the eddy current is perpendicular to the direction of the applied magnetic field, while the distribution pattern depends on the shape of the conductor. Fig 4-2 shows the induced eddy current in the cross section of a cubic and a cylindrical shape conducting materials.

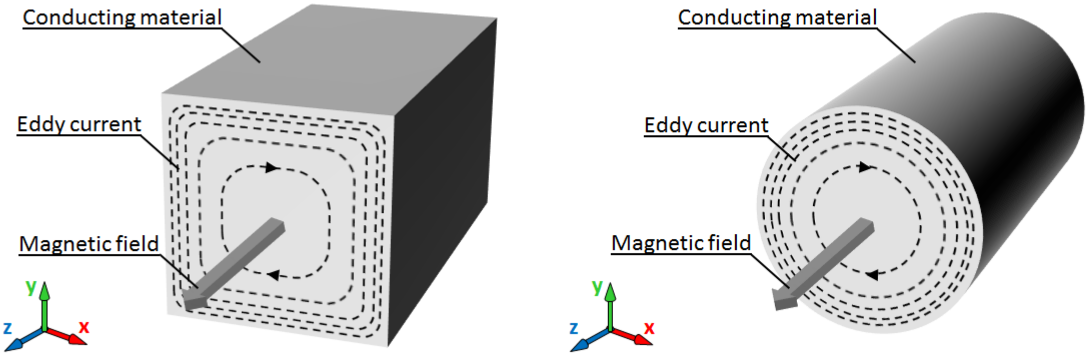

(a) (b)

Fig 4-2 Induced eddy current in conducting materials exposed to time-varying magnetic field

Regardless of the driving magnetic field and shape of the material, eddy current density, and other time-varying currents, have a tendency to pass through the conductor surface. By increasing the frequency, the current becomes restricted to a narrow layer close to the conductor surface [4.5]. This decrement in current density is known as the *skin effect* and *depth of penetration* or *skin depth* is a measure of the depth at which the amplitude of the current density falls to e^{-1} (about 0.367) of its value at the surface of the conductor. The skin depth δ of any conducting material is defined by [4.5]:

$$\delta = \sqrt{\frac{2}{\omega\mu\sigma}} = \frac{1}{\sqrt{\pi f \mu\sigma}} \tag{4.1}$$

where f [Hz], μ [H/m] and σ [S/m] are frequency, absolute magnetic permeability and electrical conductivity of the material, respectively. Therefore the eddy current, and other time-varying currents" flows principally at the skin of the conductor, between the outer surface and the level of the skin depth, as shown in Fig 4-3.

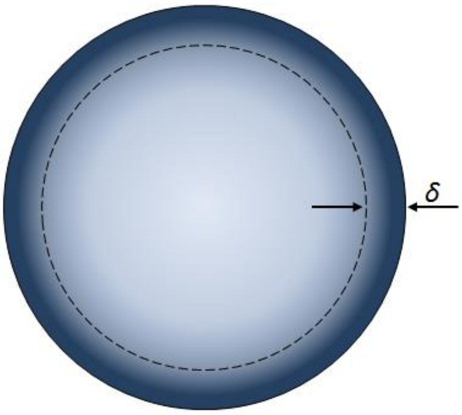

Fig 4-3 Distribution of eddy current in cross section area of a cylindrical conductor; δ is skin depth

From equation (4.1), for a particular material with given permeability μ and conductivity σ the penetration of the eddy current, which is quantified by skin depth δ, is highly frequency dependent. For small diameter circular conductors at low operating frequency, skin effect might be negligible. However at higher frequencies, where the skin depth is smaller, the effective cross-section and hence the effective resistance of the conductor is reduced and it affects the characteristics of the conductor. Therefore skin depth δ is a determinant parameter in the eddy current modelling and estimating, especially at high frequencies and high permeabilities; this will be discussed in detail in section 4-7.

4.2.2. Laminated magnetic cores of electrical machines

The induced eddy currents in the magnetic cores of electrical machines are converted to heat in the resistance of the eddy current path. This process results in power loss which is known as *eddy current power loss*. A practical way to avoid difficulties of the eddy current power loss and heating the magnetic cores is to make them highly resistive against the eddy currents direction by minimising length of the eddy current path. This can be achieved by dividing them into thin laminations [4.1]. Magnetic cores of the commercial electrical machines and other magnetic devices are constructed from stacks of electrical steel laminations, typically 0.23-0.50 mm thick. Laminations are separated electrically by insulating layers to prevent electrical contact between them and pressed together using clamping devices [4.6]-[4-8]. This limits the circulation of eddy currents to the thickness of single lamination, rather than the whole core, and hence reducing the eddy current power loss and overall heating effect in magnetic cores [4.1]. Fig 4-4 shows the paths for the induced eddy currents in magnetic cores with solid and laminated structures under time-varying magnetic flux density.

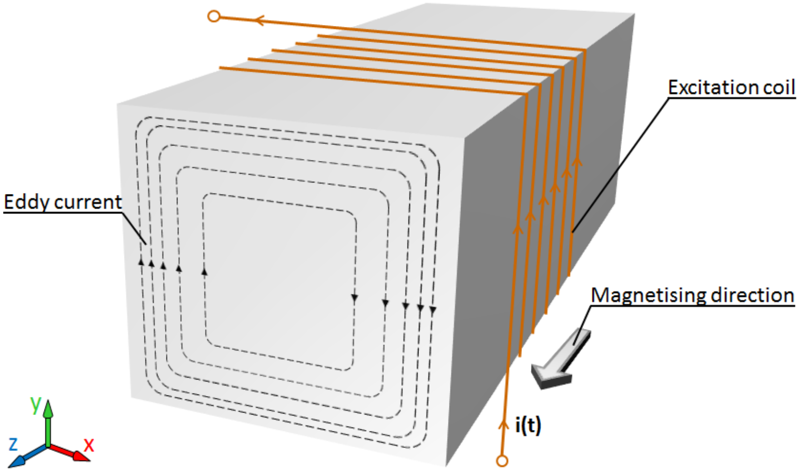

(a)

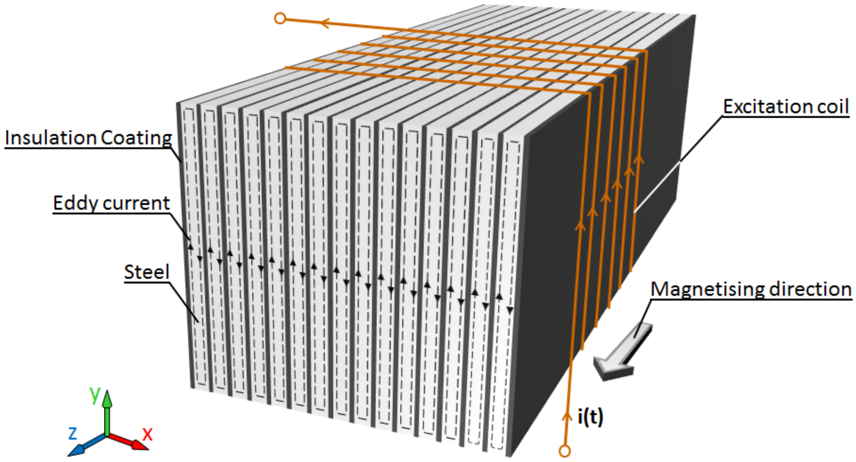

(b)

Fig 4-4 Eddy current in (a) solid core and (b) laminated magnetic core, reproduced based on [4.1]

Apart from the eddy current reduction, laminating the magnetic cores can reduce skin effect at low frequency magnetisation. However since high frequency magnetisation results in significant reduction in skin depth, it should be taken into account in accurate modelling of the eddy current modelling and eddy current power loss. Examples of laminated stator-rotor cores of rotary machines and transformer core are shown in Figs 4-5-a and 4-5-b, respectively.

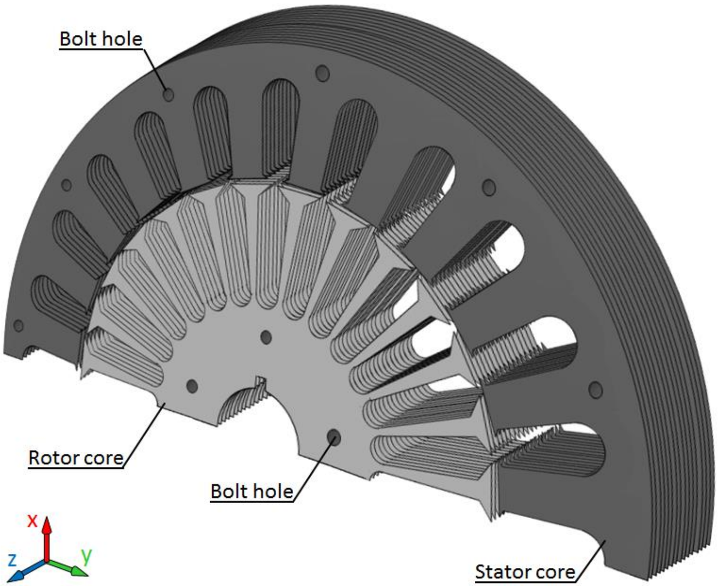

(a)

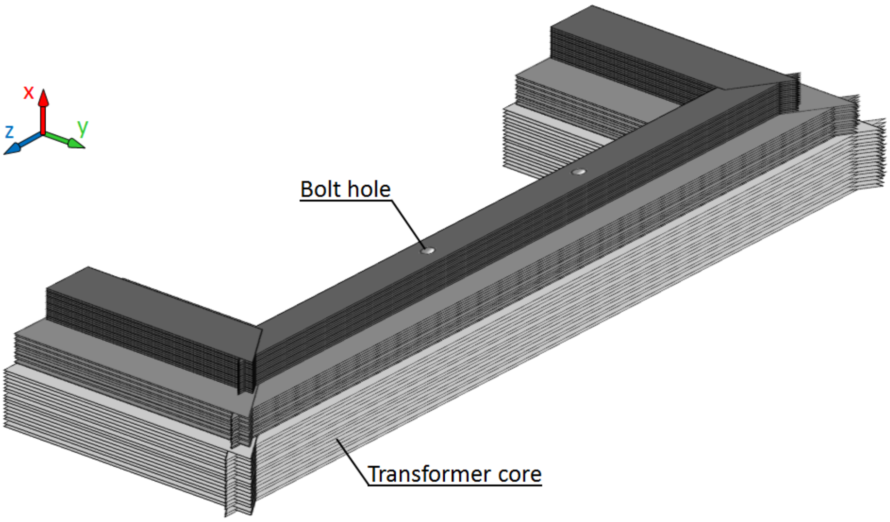

(b)

Fig 4-5 Laminated magnetic cores (a) stator-rotor core of a rotary machine

(b) section of a multi-packet transformer core

4.3. Flux density distribution inside a magnetic lamination taking skin effect into account

As described in part 4.2 eddy currents are induced in the magnetic cores as a result of time-varying magnetic field applied to the laminations. Therefore magnetic flux density and induced eddy currents are interrelated and their distribution inside the laminations is a determinant factor in the study of eddy current power loss. Based on Lenz’s law eddy currents also have a demagnetising effect tending to reduce the amplitude of flux density from the surface of the lamination to the centre. Fig 4-6 shows a unit area of a single strip magnetic lamination of thickness *t=2a* exposed to a sinusoidal magnetic field of $H_s \, Cos \, \omega t$, applied in rolling direction (*z* direction) [4.9].

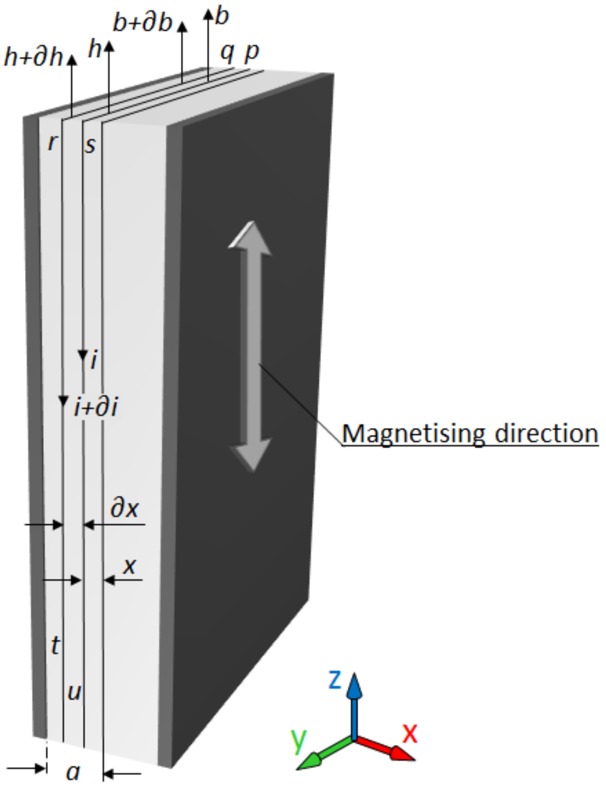

Fig 4-6 Cross section area of a magnetic lamination of thickness *t=2a*

(reproduced based on [4.9])

In Fig 4-6, *i*, *h* and *b* represent the instantaneous values of eddy current density ***i***, magnetic field strength ***H*** and magnetic flux density ***B*** at distance *x* from the centre of the lamination, respectively. These quantities are functions of both distance *x* and time t. The magnetic flux density distribution along the lamination thickness is solved initially at a particular relative permeability μ and electrical resistivity ρ; therefore $b=\mu h$ and the flux density at the surface of the lamination is $b = \mu\ \boldsymbol{H}_s \cos\omega t = \boldsymbol{B}_s \cos\omega t$ and the flux in the element of width ∂x is $b\partial x$ [4.9]. For the directions of the arrows shown in Fig 4-6, the induced electromotive force round the circuit *pqrs* in the figure is [4.9]:

$$\rho(i+\partial i)-\rho i=\frac{\partial(b.\partial x)}{\partial t}=\partial x\frac{\partial b}{\partial t}$$

$$\rho\frac{\partial i}{\partial x}=\frac{\partial b}{\partial t} \tag{4-2}$$

The current in the element area *srtu* is $i.\partial x$ and the magneto-motive force round this circuit is:

$$i\,\partial x=(h+\partial h)-h$$

$$i=\frac{\partial h}{\partial x}=\frac{1}{\mu}\frac{\partial b}{\partial x} \tag{4-3}$$

From equations (4-2) and (4-3):

$$\frac{\partial^2 b}{\partial x^2}=\frac{\mu}{\rho}\frac{\partial b}{\partial t} \tag{4-4}$$

Equation (4-4) is a differential equation which defines flux density $\boldsymbol{B}$ as a function of distance *x* and time *t* and has the value $\boldsymbol{B}_s \cos\omega t$ when *x* is *+a* or *–a*. A possible solution of (4-4) is:

$$\boldsymbol{B}(x,t) = h\ cos\ \omega t + k\ sin\ \omega t \tag{4-5}$$

where *h* and *k* are functions of *x*. Substituting this value for *b* in the differential equation of (4-4) results in:

$$\frac{\partial^2}{dx^2}(h\ cos\omega t + k\ sin\ \omega t) = \frac{\rho}{\mu}\frac{\partial}{\partial t}(h\ cos\omega t + k\ sin\ \omega t)$$

$$\omega(-h\ sin\ \omega t + k\ cos\ \omega t) = \frac{\rho}{\mu}\left(\frac{\partial^2 h}{\partial x^2}\ cos\omega t + \frac{\partial^2 k}{\partial x^2}\ sin\ \omega t\right) \tag{4-6}$$

This is true for all values of time *t*. Hence from (4-6):

$$h = -\frac{\rho}{\mu\omega}\frac{\partial^2 k}{dx^2} \tag{4-7}$$

$$k = \frac{\rho}{\mu\omega}\frac{\partial^2 h}{dx^2} \tag{4-8}$$

Substituting (4-8) in (4-7):

$$h = -\frac{\rho}{\mu\omega}\frac{\partial^2}{dx^2}\left(\frac{\rho}{\mu\omega}\frac{\partial^2 h}{dx^2}\right)$$

$$h = -\frac{1}{4}\left(\frac{\rho}{\pi f\mu}\right)^2\frac{\partial^4 h}{dx^4} = -\frac{1}{4p^4}\frac{\partial^4 h}{dx^4} \tag{4-9}$$

where

$$p = \sqrt{\frac{\pi\mu f}{\rho}} = \frac{1}{\delta} \tag{4-10}$$

where f is frequency of magnetising current and δ is skin depth which was defined by equation (4-1). The complete solution of (4-9) is therefore:

$$h = C_1 e^{px} cos\, px + C_2 e^{px} sin\, px + C_3 e^{-px} cos\, px + C_4 e^{-px} sin\, px \tag{4-11}$$

where C_1, C_2, C_3 and C_4 are constants; and from (4-8):

$$k = \frac{1}{2p^2}\frac{\partial^2 h}{dx^2} \tag{4-12}$$

Substituting (4-11) into (4-12) gives:

$$k = -C_1 e^{px} sin\, px + C_2 e^{px} cos\, px + C_3 e^{-px} sin\, px - C_4 e^{-px} cos\, px \tag{4-13}$$

Substituting (4-11) and (4-13) into (4-5) will result:

$$\begin{aligned} B(x,t) = C_1 e^{px} cos\,(\omega t + px) + C_2 e^{px} sin(\omega t + px) + C_3 e^{-px} cos\,(\omega t \\ - px) - C_4 e^{-px} sin(\omega t - px) \end{aligned} \tag{4-14}$$

Since, by symmetry, ***B*** does not change sign with *x* for any value of *t*, by putting *ωt* equal to zero and *π/2* successively, that neither *h* nor *k* must change sign with *x*, and hence $C_1=C_3$ and $C_2=-C_4$ satisfy both these conditions. Therefore from (4-14):

$$\begin{aligned} B(x,t) = C_1[e^{px} cos\,(\omega t + px) + e^{-px} cos\,(\omega t - px)] \\ + C_2[e^{px} sin\,(\omega t + px) + e^{-px} sin\,(\omega t - px)] \end{aligned} \tag{4-15}$$

At the surface of the lamination $B(x,t)=B_s \cos \omega t$, and thus from (4-5):

$h=B_s$ and $k=0$ when $x=+a$ or $x=-a$

Therefore from (4-11) and (4-13):

$$B_s = C_1[e^{pa} + e^{-pa}]cos\, pa + C_2[e^{px} - e^{-px}]sin\, pa \tag{4-16}$$

$$0 = C_1[e^{pa} - e^{-pa}]sin\, pa - C_2[e^{px} - e^{-px}]cos\, pa \tag{4-17}$$

Substituting $cosh\, pa = \frac{1}{2}(e^{pa} + e^{-pa})$ and $sinh\, pa = \frac{1}{2}(e^{pa} - e^{-pa})$ in (4-16) and (4-17) and solving the equations will give:

$$C_1 = \frac{B_s cosh\, pa\, cos\, pa}{cosh\, 2pa + cos\, 2pa} \tag{4-18}$$

$$C_2 = \frac{B_s sinh\, pa\, sin\, pa}{cosh\, 2pa + cos\, 2pa} \tag{4-19}$$

And from (4-11) and (4-13):

$$h = 2C_1 cosh\, px\, cos\, px + 2C_2\, sinh\, px\, sin\, px \tag{4-20}$$

$$k = -2C_1 sinh\, px\, sin\, px + 2C_2\, cosh\, px\, cos\, px \tag{4-21}$$

Therefore:

$$\frac{h}{B_s} = \frac{cosh\, p(a-x) cos\, p(a+x) + cosh\, p(a+x) cos\, p(a-x)}{cosh\, 2pa + cos\, 2pa} \tag{4-22}$$

$$\frac{k}{B_s} = \frac{sinh\, p(a-x) sin\, p(a+x) + sinh\, p(a+x) sin\, p(a-x)}{cosh\, 2pa + cos\, 2pa} \tag{4-23}$$

Substituting *h* and *k* from (4-22) and (4-23) into (4-5) will result:

$$B(x,t) = B_s \sqrt{\frac{(cosh\, 2px + cos\, 2px\,)}{(cosh\, 2pa + cos\, 2pa)}}\; Cos(\omega t - \beta) \tag{4-24}$$

And as a function of skin depth δ:

$$B(x,t) = B_s \sqrt{\frac{\left(cosh\,\frac{2x}{\delta} + cos\,\frac{2x}{\delta}\right)}{\left(cosh\,\frac{2a}{\delta} + cos\,\frac{2a}{\delta}\right)}}\; Cos(\omega t - \beta) \tag{4-25}$$

Where *β* phase angle of the flux density:

$$\tan\beta = \frac{k}{h} = \frac{sinh\,p(a-x)sin\,p(a+x) + sinh\,p(a+x)sin\,p(a-x)}{cosh\,p(a-x)cos\,p(a+x) + cosh\,p(a+x)cos\,p(a-x)} \tag{4-26}$$

Equation (4-25) defines flux density along the thickness of the lamination as a function of distance *x*, skin depth *δ* and time *t.* Therefore from equations (4-25) and (4-26) it can be concluded that at high frequencies the magnetic field inside the lamination is not homogeneous because of the skin effect; there is also a phase lag depending on penetration depth inside the lamination. Substituting *x=±a* into (4-24) or (4-25), flux density at the surface or boundary of the lamination will be:

$$B(x,t) = B_s\,cos\,\omega t \tag{4-27}$$

which is a skin depth independence function of time.

4.4. Effect of flux density on the relative permeability

Equation (4-25) was obtained from the solution of Maxwell’s equation (4-4) with an assumption of a linear dependence of ***B*** and ***H***. This assumption can be only applied when the surface induction of the lamination does not reach the knee of the ***B***-***H*** curve. Therefore the distribution of the magnetic flux density along the lamination thickness varies along the ***B-H*** curve and hence depends on the peak flux density. The Non-linear relationship of ***B-H*** affects the relative permeability of the magnetic materials. As a result, distribution of the magnetic flux density across the lamination thickness varies with relative permeability of the material. Therefore in order to consider the effect of peak flux density on distribution of flux density along the lamination thickness and complete the solution of (4-25), the variation of the relative permeability of the material as a function of peak flux density should be considered. This function is expressed as a fourth-order polynomial [4.10]:

$$\mu\left(B_{pk}\right) = A_4 B_{pk}^4 + A_3 B_{pk}^3 + A_2 B_{pk}^2 + A_1 B_{pk} + A_0 \tag{4-28}$$

where B_{pk} is peak flux density and A_4 to A_0 are curve fitting coefficients obtained from the measured magnetic permeability at low frequency [4.10]. The relation between the peak value of magnetic field strength and peak value of magnetic flux density is:

$$B_{pk} = \mu_0 \mu_r H_{pk} \tag{4-29}$$

The peak magnetising field was calculated from the measured peak magnetising current I_{pk}, number of winding turns of the magnetising coil N, and the mean magnetic path length of the magnetic circuit l_m.

$$H_{pk} = \frac{N I_{pk}}{l_m} \tag{4-30}$$

Therefore the effective relative permeability μ_r as a function of magnetic flux density can be obtained using the following equation:

$$\mu_r = \frac{B_{pk} l_m}{\mu_0 N I_{pk}} \tag{4-31}$$

As a practical example, based on equations (4-30) and (4-31), the relative permeability of a single lamination of grain oriented 3 % silicon steel material of thickness 0.3 mm at peak flux densities 0.1 T to 1.8 T and 50 Hz frequency was measured, using a single strip tester (SST); the results are shown in Table 4-1 and Fig 4-7. The polynomial function of this curve was obtained using the polynomial solver of MATLAB, which is shown in the figure.

Table 4-1 Variation of the effective relative permeability of CGO with peak flux density at magnetising frequency of 50 Hz

B_{pk} (T)	Measured permeability
0.1	9.31E+03
0.2	1.50E+04
0.3	1.99E+04
0.4	2.24E+04
0.5	2.48E+04
0.6	2.78E+04
0.7	3.12E+04
0.8	3.35E+04
0.9	3.64E+04
1.0	3.82E+04
1.1	4.07E+04
1.2	4.19E+04
1.3	4.24E+04
1.4	3.89E+04
1.5	3.13E+04
1.6	1.93E+04
1.7	7.75E+03
1.8	2.23E+03

Fig 4-7 shows that the relative permeability of the material varies significantly with flux density; therefore the non-linear relationship ***B-H*** of the material is necessary to complete the solution of (4-25). Fig 4-7 also shows that at low flux densities and near saturation, the permeability of the material is relatively low and according to (4-1), at each particular frequency, the impact of skin effect is less significant than the high permeability regions of the curve.

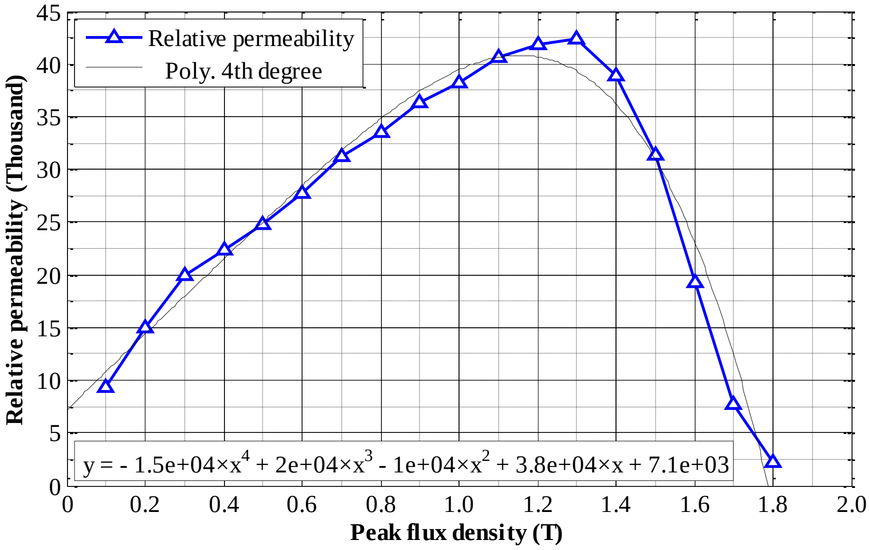

Fig 4-7 Variation of the effective relative permeability of CGO with peak flux density at magnetising frequency of 50 Hz

In the analytical modelling of this chapter, for this particular material, peak flux density of 1.3 T with relative permeability of μ_r=4.24E+04 was considered as a high permeability point and peak flux density of 1.7 T with relative permeability of μ_r=7.75E+03 was considered as a low permeability point.

4.5. Determination of complex relative permeability at high frequencies

In spite of the fact that transformer cores, and in general magnetic cores, mostly work at power frequencies, 50 Hz or 60 Hz, there are circumstances where they are subjected to high frequency magnetic fields, e.g. transient over voltages containing high-frequency components, during frequency response measurements and PWM excitations [4.11] and [4.12]. In order to analyse these phenomena in magnetic cores, it is convenient to consider the relative magnetic permeability of the material as the complex quantity $\mu_r = \mu_r' - j\mu_r''$ in which μ_r' and μ_r'' are real functions of the magnetising frequency f [4.12]. Therefore in order to improve the accuracy of the analytical modelling of magnetic cores at high frequencies, changes in the complex permeability over frequency should be observed. In this part the effect of high frequency on the relative permeability of the magnetic laminations is discussed.

A cross sectional view of the sample of Fig 4-6 with thickness of 2a in *x-y* plane is shown in Fig 4-8. The size of the lamination, given as *Δy* by *Δz*, is chosen to be small enough to consider the magnetic field inside it as uniform for low frequencies. In Fig 4-8, the *z*-direction and *y*-direction represent rolling and transverse directions respectively; rolling direction is perpendicular to the *x-y* plane.

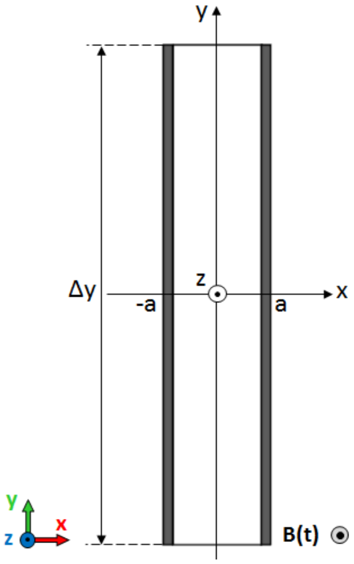

Fig 4-8 Single strip lamination of thickness t=2a in x-y plane

If eddy current loops inside the lamination are assumed to be large enough along the *y*-direction, the field consideration becomes one dimensional and could be reduced to a single equation for the *z*-component of the magnetic field which depends only on *x*, therefore equation (4-4) can be written in terms of the magnetic field in *z*-direction (rolling direction) ***H**ₓ* [4.12] and [4.13]:

$$\frac{\partial^2 \widehat{H}_z(x,t)}{\partial x^2} = \mu_0 \mu_z \sigma \, \frac{\partial \widehat{H}_z(x,t)}{\partial t} \tag{4-32}$$

where μ_z is permeability of the material in *z*-direction and *σ=(1/ρ)* is conductivity of the material. The symbol "^" shows complex values. For the time-harmonic case, the solution of this equation is given by:

$$\widehat{H}_z(x,t) = K_1 e^{j\omega t - \gamma x} + K_2 e^{j\omega t + \gamma x} \tag{4-33}$$

where constants K_1 and K_2 depend on the boundary conditions and γ is the propagation constant given by:

$$\gamma = \sqrt{j\omega\mu_0\mu_z\sigma}$$

The propagation constant is related to the skin depth $\delta = 1/\sqrt{\pi\mu_0\mu_z f\sigma}$ by:

$$\gamma = \frac{(1+j)}{2\delta}$$

The solution corresponds to two damped waves moving in opposite directions. Their magnitudes depend on the following boundary conditions imposed on each side of the lamination sample:

$$H_z(\pm b, t) = H_0 e^{j\omega t}$$

With these symmetrical boundary conditions, the magnetic field at any point inside the lamination sample can be obtained from (4-33) as:

$$\widehat{H}_z(x,t) = \frac{H_0}{1+e^{-2\gamma a}}\left(e^{j\omega t-\gamma(x+a)} + e^{j\omega t+\gamma(x-a)}\right) \tag{4-34}$$

The averaged magnetic flux density in *z*-direction ($\widehat{\mathrm{B}}_\mathrm{z}$) can be evaluated in terms of total magnetic flux *φ(t)* through the cross section (*2aΔy*) as:

$$\hat{B}_z(x,t) = \frac{\varphi(t)}{2a\Delta y} = \frac{\int_{-a}^{a}\mu_0\mu_z H_z(x,t)\Delta y dx}{2a\Delta y} \tag{4-35}$$

Substituting (4-34) in (4-35) and solving the integration leads to:

$$\hat{B}_z(x,t) = \frac{\mu_0\mu_z H_0 e^{j\omega t}}{a\gamma}\left(\frac{e^{2a\gamma}-1}{e^{2a\gamma}+1}\right)$$

$$\hat{B}_z(x,t) = \frac{\mu_0\mu_z H_0 e^{j\omega t}}{a\gamma}\tanh(a\gamma) \tag{4-36}$$

The effective relative complex permeability of a lamination in z-direction is the ratio of the average flux density to the surface magnetic field intensity. This relationship is given by:

$$\hat{\mu}_z^{eff} = \mu_z' - j\mu_z'' = \frac{\hat{B}_z(x,t)}{\mu_0 \hat{H}_z^{exp}} = \frac{\mu_0 \mu_z H_0 e^{j\omega t}}{a\gamma \mu_0 H_0 e^{j\omega t}} \tanh(a\gamma)$$

$$\hat{\mu}_z^{eff} = \mu_z \frac{\tanh(a\gamma)}{a\gamma} \tag{4-37}$$

where μ_z' and μ_z'' are real and imaginary parts of complex relative permeability in the *z*-direction and are real functions of the magnetising frequency *f*. μ_z is the absolute static permeability of the material in the rolling direction which is equal to the value of μ_r at low frequencies [4.14].

4.5.1. Influence of peak flux density on complex relative permeability

Equation (4-37) shows that complex relative permeability is highly skin depth dependent. On the other hand, equation (4-1) shows that for a given material with specific conductivity, σ, skin effect depends on magnetising frequency *f* and relative permeability of the material μ_r. Furthermore the influence of the peak flux density on the relative permeability of the material was shown in part 4.4. Therefore in the study of complex relative permeability of the materials, the influence of both peak flux density B_{pk} and magnetising frequency *f* should be taken into account. Based on equation (4-37) the real and imaginary parts, and also, the amplitude and phase angle of the effective complex permeability of the material with the specifications given in part 4.4 as a function of the magnetising frequency at two particular surface flux densities 1.3 T and 1.7 T are shown in Figs 4-9 and 4-10, respectively. The calculations were performed using the following parameters: conductivity of σ=2.17E+06 S/m which was measured based on [4.15] and particular relative permeability μ_r=4.24E+04 at peak flux density of 1.3 T and μ_r=7.75E+03 at peak flux density of 1.7 T, which was derived from the experimental result of Fig 4-7.

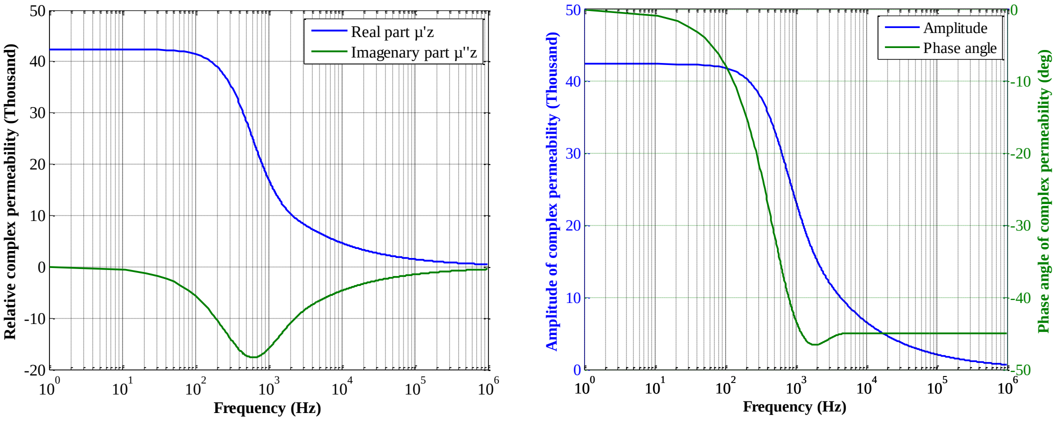

(a) (b)

Fig 4-9 Frequency dependence of (a) the real and the imaginary parts and (b) the amplitude and phase angle of relative complex permeability of a single magnetic lamination at B_{pk}=1.3 T

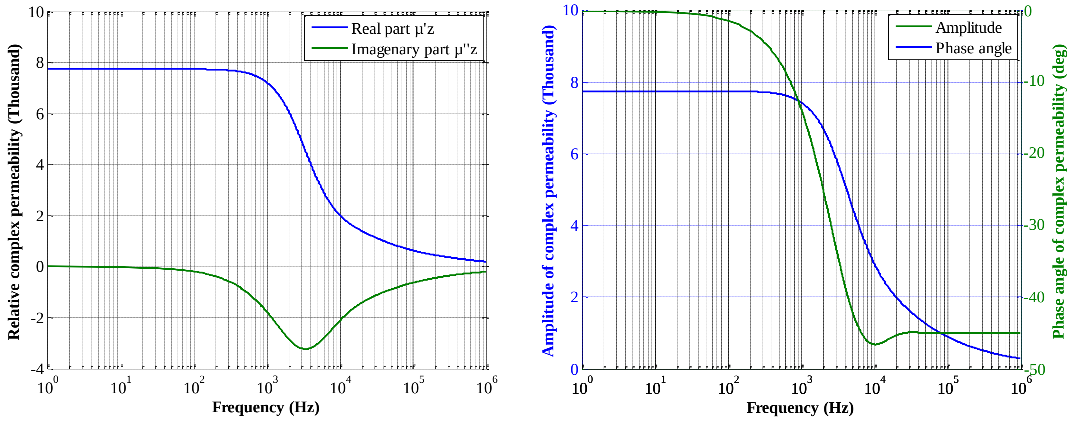

(a) (b)

Fig 4-10 Frequency dependence of (a) the real and the imaginary parts and (b) the amplitude and phase angle of relative complex permeability of a single magnetic lamination at B_{pk}=1.7 T

Figs 4-9 and 4-10 show that the effective permeability observed at high frequencies is not large in comparison with the permeabilities observed under normal operating conditions at low frequencies, e.g. power frequencies 50 Hz or 60 Hz. There is also a phase angle in permeability of the material which depends on skin depth and hence frequency and peak flux density.

Complex permeability takes into account the influence of skin effect on the magnetic properties of the material. At low frequencies, e.g. power frequencies 50 Hz or 60 Hz, this effect is negligible due to the skin depth being significantly greater than the lamination thickness $\delta >> a$. However at high frequencies skin depth becomes significant and leads to significant drop in the magnetic permeability of the material. Considering the relation between magnetic flux density ***B*** and magnetic field strength ***H***, the phase angle of the relative complex permeability represents the phase shift between ***B*** and ***H***.

Therefore from Figs 4-9 and 4-10 it could be concluded that at low frequencies where $\delta >> a$, the complex relative permeability of the material remains constant and is equal to the relative static permeability (μ_r) and also the phase shift between ***B*** and ***H*** is almost zero. On the other hand, at high frequencies where $\delta << a$ the amplitude of the complex relative permeability drops and the phase angle becomes significant. However since the skin effect itself depends on both magnetising frequency and magnetic permeability, variation of peak flux density affects the profile of the complex relative permeability versus magnetising frequency, as permeability of the material varies with peak flux density. Therefore according to Figs 4-9 and 4-10, two behaviours are observed at high permeability, e.g. 1.3 T and low permeability at low flux densities and near saturation, e.g. 1.7 T.

4.6. Analytical results and discussion on distribution of magnetic flux density along the lamination thickness

A flowchart was designed to clarify the procedure for determining the flux density distribution across the lamination thickness, as shown in Fig 4-11. According to this flowchart, the magnetising frequency f and amplitude of the peak flux density B_{pk} are initially set at the required values. Relative permeability at the specific peak flux density is then read from the measured values of Fig 4-7, which is necessary to take the non-linearity of the material into account. Complex relative permeability of the material is then calculated using equation (4-37). Local flux density B_x at the specific values of magnetising frequency and amplitude of surface flux density will be then calculated using equation (4-25).

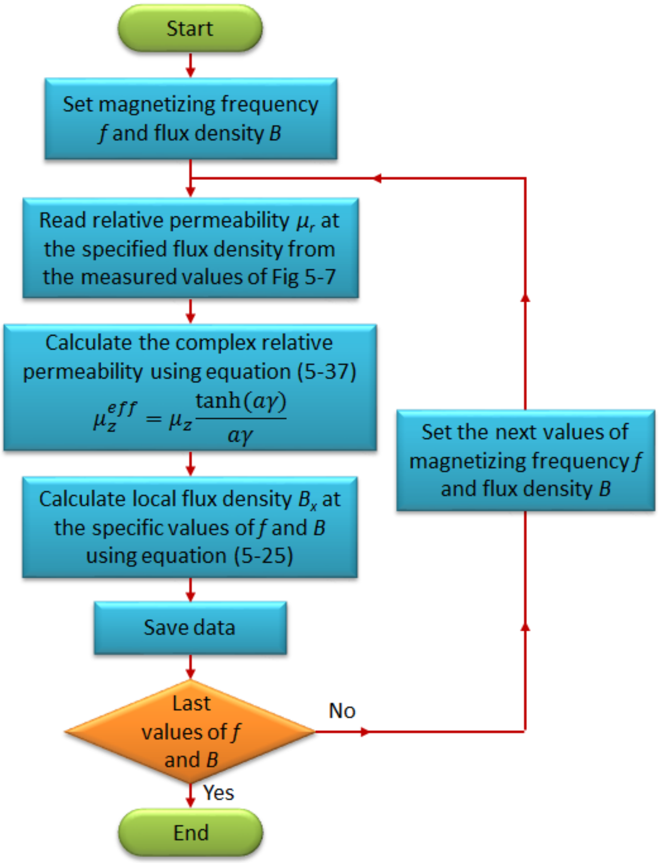

Fig 4-11 Flowchart of the determination of flux density distribution inside the magnetic laminations

In the first step the distribution of magnetic flux density at different points inside the lamination versus magnetising frequency f and two particular surface flux densities 1.3 T and 1.7 T was investigated. This investigation was carried out at distances x_1=0.14 mm, x_2=0.12 mm, x_3=0.10 mm, x_4=0.05 mm from the centre line of the lamination, according to the schematic of Fig 4-12. In order to show the impact of the complex permeability on the magnetic properties of the material these characteristics were obtained for constant and frequency dependent (complex) permeabilities. The characteristics of each position inside the lamination were compared together at peak flux densities of 1.3 T, as a high permeability point, and 1.7 T, as a low permeability point. The results of the flux density distribution, normalised by the value at the surface (B_x/B_s), are shown in Fig 4-13.

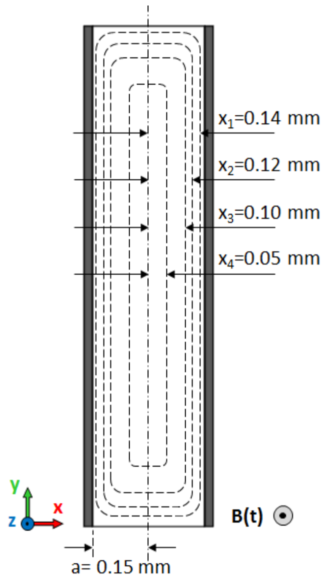

Fig 4-12 Single strip lamination of thickness 2a=0.3 mm in *x-y* plane magnetised in *z*-direction

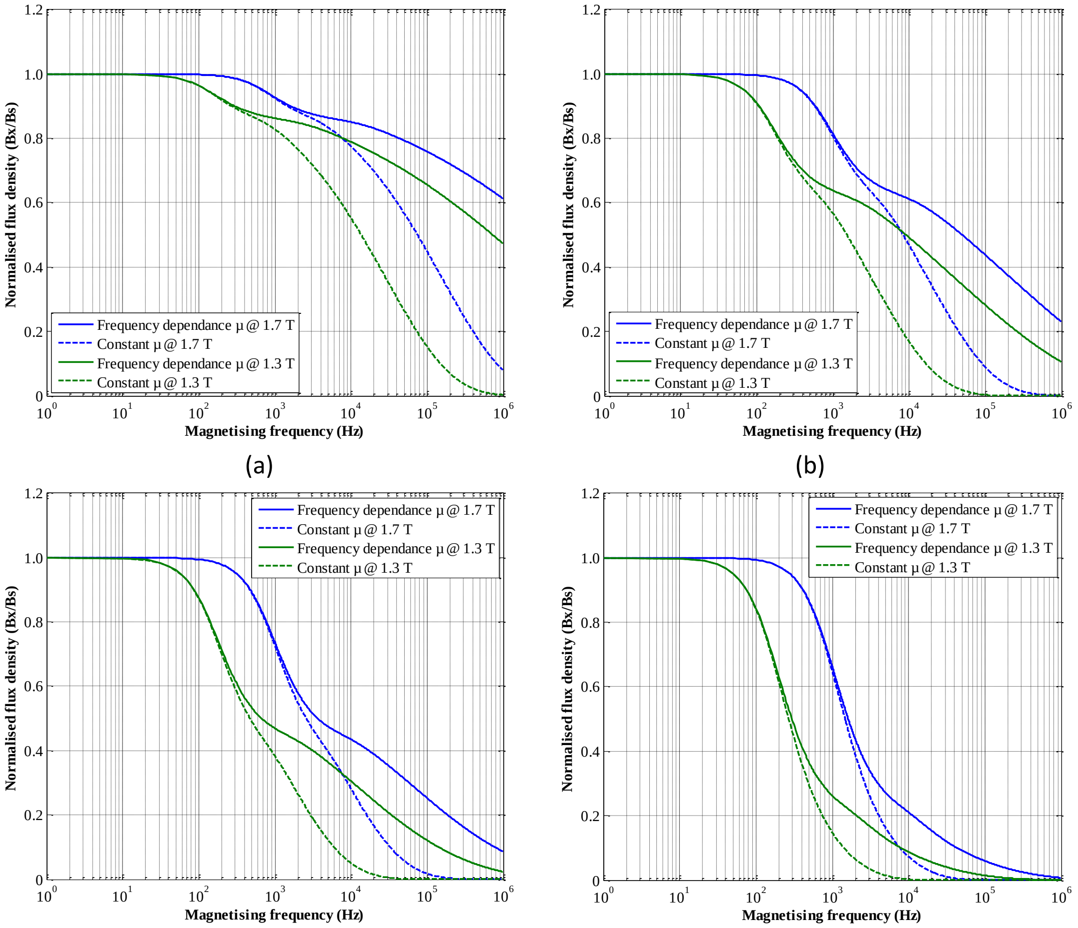

(a)

(b)

(c)

(d)

Fig 4-13 Comparison between distribution of normalised flux density versus magnetising frequency with frequency dependence and constant permeability at surface flux densities of B_{pk}=1.3 T and B_{pk}=1.7 T and different position from lamination surface (a) x_1=0.14 mm (b) x_2=0.12 mm (c) x_3=0.10 mm and (d) x_4=0.05 mm

As a general comparison, the distributions of flux density inside the lamination at the specified points were compared at each flux density. The results at peak surface flux densities of B_{pk}=1.3 T and B_{pk}=1.7 T are shown in Figs 4-14-a and 4-14-b, respectively. These characteristics were obtained for the material with the same properties as section 4.5.1.

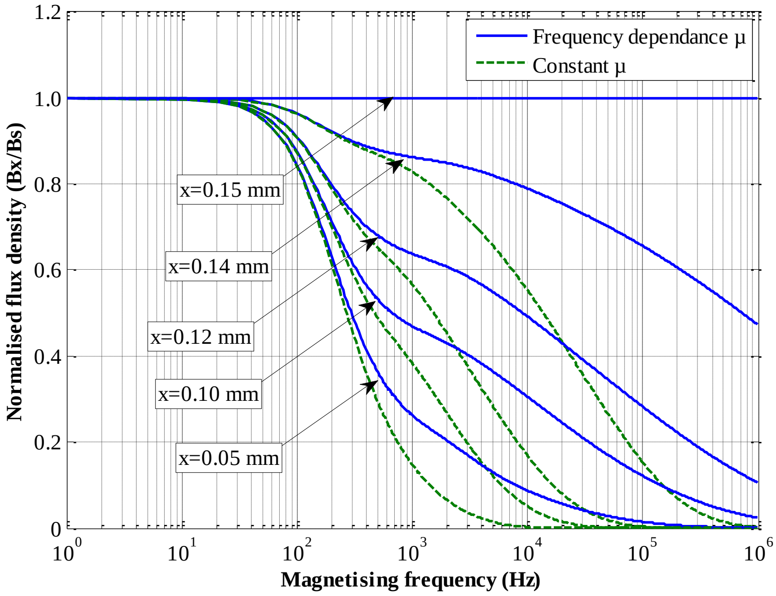

(a)

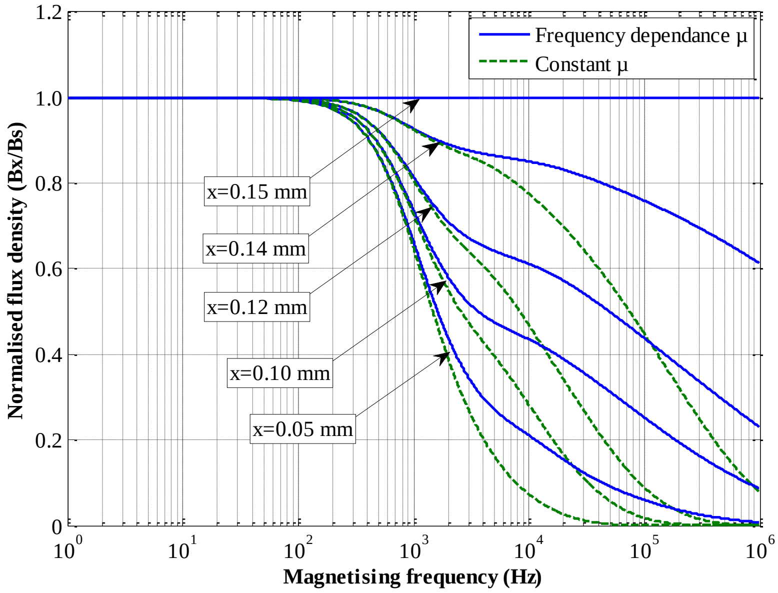

(b)

Fig 4-14 Normalized magnetic flux density versus magnetising frequency with constant and frequency dependence permeability at different position from lamination surface and peak surface flux densities (a) B_{pk}=1.3 T (b) B_{pk}=1.7 T

Three important points could be concluded from the results of Figs 4-13 and 4-14:

1. At low frequencies, where the impact of skin effect is negligible, magnetic flux density at any point inside the lamination is constant. On the other hand, at higher frequencies skin effect becomes significant and magnetic flux density decreases by increasing frequency from the surface to the centre of the lamination.
2. From equation (4-1), at each particular frequency the impact of skin effect is more significant at high values of magnetic permeabilities; while at low values, at low flux densities and near saturation, the impact of skin effect is less. Therefore at each particular frequency, flux density at any point inside the lamination is higher at higher values of magnetic permeabilities.
3. According to equation (4-37) and Figs 4-9 and 4-10, complex permeability is a function of skin effect; therefore at low frequencies, where skin effect is negligible, the difference between the results of magnetic flux density by constant permeability and complex permeability at each point inside the lamination is negligible. On the other hand by increasing frequency the impact of skin effect becomes significant and leads to significant different between these two values.

As a final note on Figs 4-13 to and 4-14, hysteresis relationship between ***B*** and ***H*** and complex relative permeability are two determinant factors in the study of magnetic properties of magnetic laminations which should be considered in relevant studies to increase accuracy of the results.

In the next step of this investigation based on the flowchart of Fig 4-11 the distribution of normalised magnetic flux density (B_x/B_s) along the lamination thickness x for different values of the magnetising frequency f were calculated. The results at two particular surface flux densities 1.3 T and 1.7 T; are shown in Figs 4-15-a and 4-15-b, respectively.

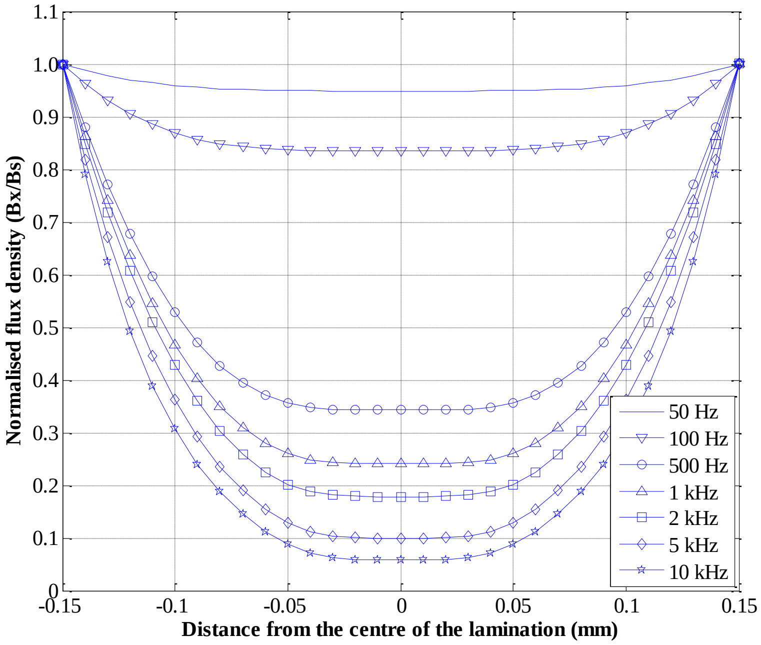

(a)

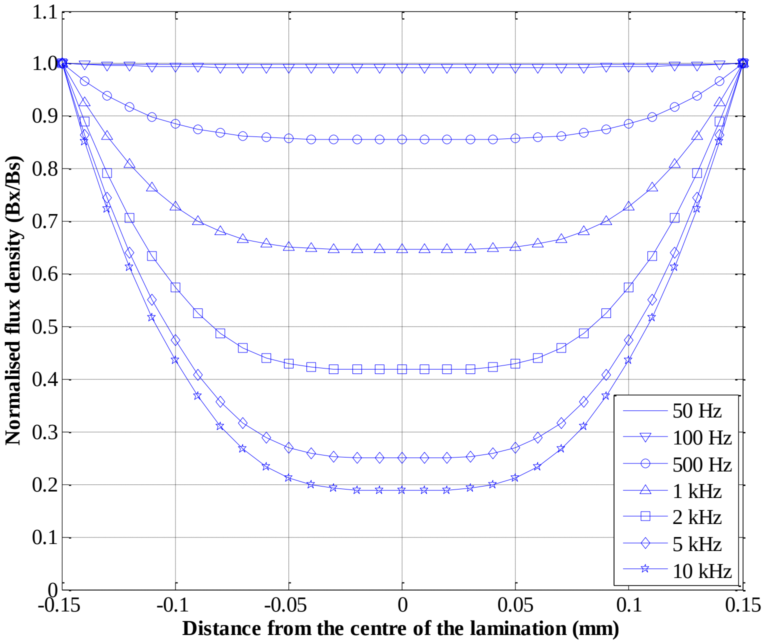

(b)

Fig 4-15 Normalized magnetic flux density penetration into magnetic lamination of thickness $2a$=0.3 mm at different frequencies (a) B_s=1.3 T (b) B_s=1.7 T

Fig 4-15 shows new information regarding the flux density distribution in the magnetic laminations. From equation (4-25), half of the laminations thickness "*a*" and skin depth "*δ*" are two determinant factors in the qualification of the flux density distribution across the lamination thickness. At low frequencies, $\delta >> a$, flux density distributes uniformly across the lamination thickness. However, at high frequencies where $\delta << a$, the flux density at the central region of the lamination is nearly zero, and corresponding high flux density is noted near the surfaces of the lamination; and hence magnetic flux density distribution tends to be non-uniform across the lamination.

Variation of magnetic permeability is also a determinant factor which affects the distribution of flux density across the lamination. Comparing the corresponding curves of flux density distribution of Figs 4-15-a and 4-15-b shows that flux density distribution at low permeabilities is more uniform compared with higher permeabilities; the reason is strongly related to skin effect which is more significant at higher permeabilities. In order to clarify this issue, a 3-D plot of normalised magnetic flux density penetration into the lamination, at a magnetising frequency of 500 Hz, 1 KHz, 2 KHz, 5 KHz and 10 KHz and peak flux density from 0.1 T to 1.8 T are shown in Fig 4-16.

In summary, at each particular frequency, at low flux densities and near saturation which correspond to low magnetic permeability, flux density distributes almost uniformly. However at flux densities corresponding to high permeabilities the flux density distribution is non-uniform. Therefore as stated earlier in this part, Fig 4-16 shows that magnetising frequency and peak flux density are two determinant factors in the investigation of flux density distribution and other magnetic properties of the electrical steels.

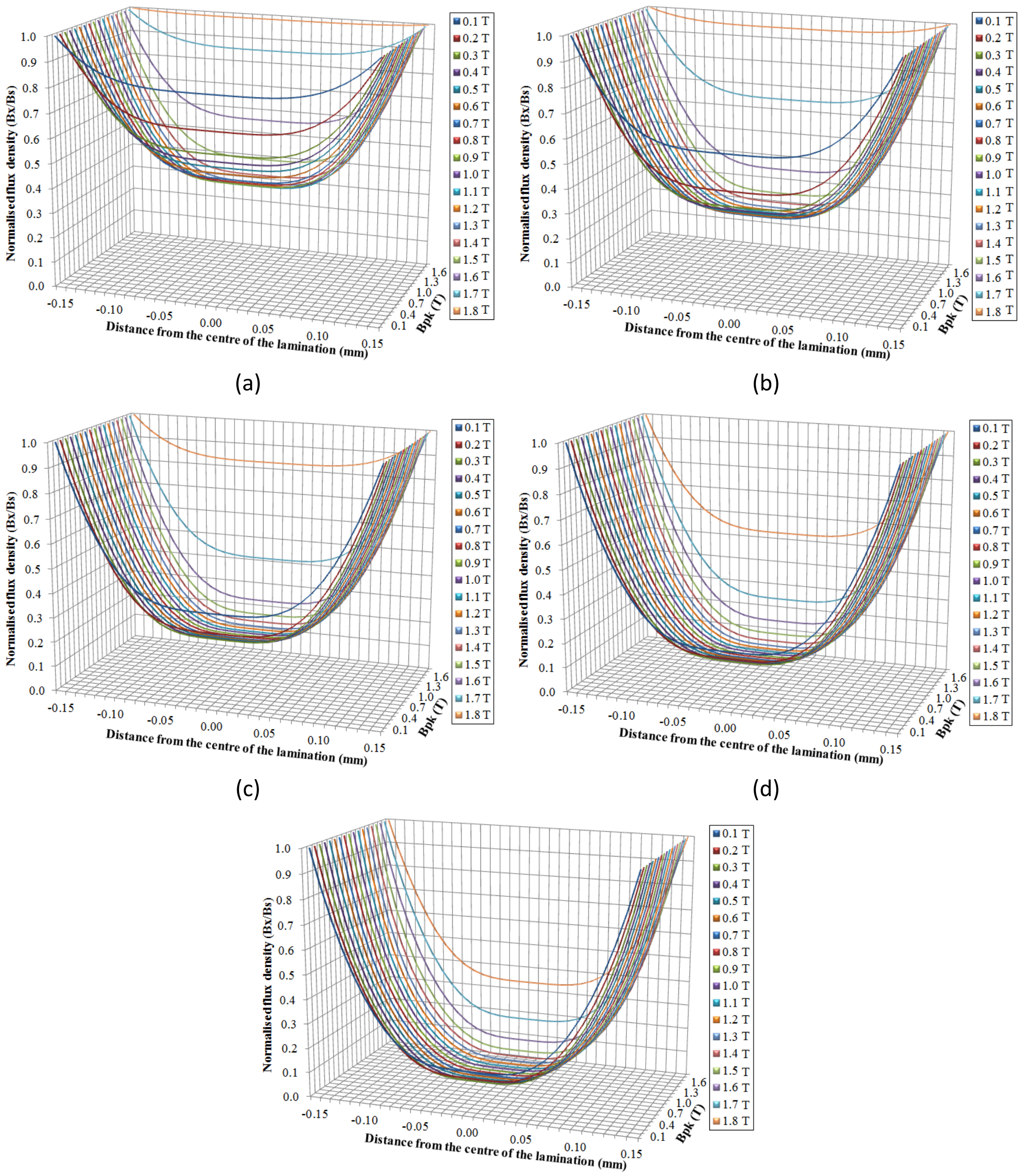

(a)

(b)

(c)

(d)

(e)

Fig 4-16 3-D plot of normalized magnetic flux density penetration into magnetic lamination with thickness of 2a=0.3 mm at peak flux density from 0.1 T to 1.8 T and magnetising frequency of (a) 500 Hz (b) 1 KHz (c) 2 KHz (d) 5 KHz and (e) 10 KHz

4.7. Eddy current power loss analysis based on the equivalent circuit of the magnetised lamination

The electrical resistance of a given object depends primarily on two factors; the properties of the material, and the physical dimensions of the object. For a given material, with specific electrical resistance ρ, length l and cross section area of A, the resistance is defined by:

$$r = \rho \frac{l}{A} \tag{4-38}$$

As mentioned in section 4-2, eddy current losses are attributed to the fact that a time-varying magnetic field induces a time-varying voltage (*emf*) in the conductive material which result in eddy current and hence eddy current power loss. From this point of view and considering equation (4-38), the eddy current path in the magnetic laminations which are magnetised by flux density ***B***, can be modelled by means of equivalent resistors arranged along the thickness and width of the laminations [4.16]. In this method the idea is to simulate the eddy current paths of the magnetic laminations by an equivalent electrical circuit in which the components depend on the steel properties and physical dimensions of the laminations.

Since flux density distribution and hence eddy current distribution are frequency dependent, eddy current power loss analysis based on the equivalent electric circuit of the lamination will be investigated in two parts. Section 4-7-1 describes power loss modelling at low frequencies where the skin depth δ is greater than the thickness of the lamination a, i.e. $\delta >> a$, and section 4-7-2 describes modelling at high frequencies where skin depth δ is less than the thickness of the lamination a, i.e. $\delta << a$. Apart from the magnetising frequency, the effect of the relative permeability of the material is considered in the loss modelling, the results are discussed in part 4-7-3.

4.7.1. Eddy current power loss modelling at low frequencies

Fig 4-17-a shows a 3-D view of a magnetic sheet of thickness *2a*, width *w* and height *h* under time varying flux density ***B*** and Fig 4-17-b shows the resistive equivalent circuit of the eddy current path in the lamination.

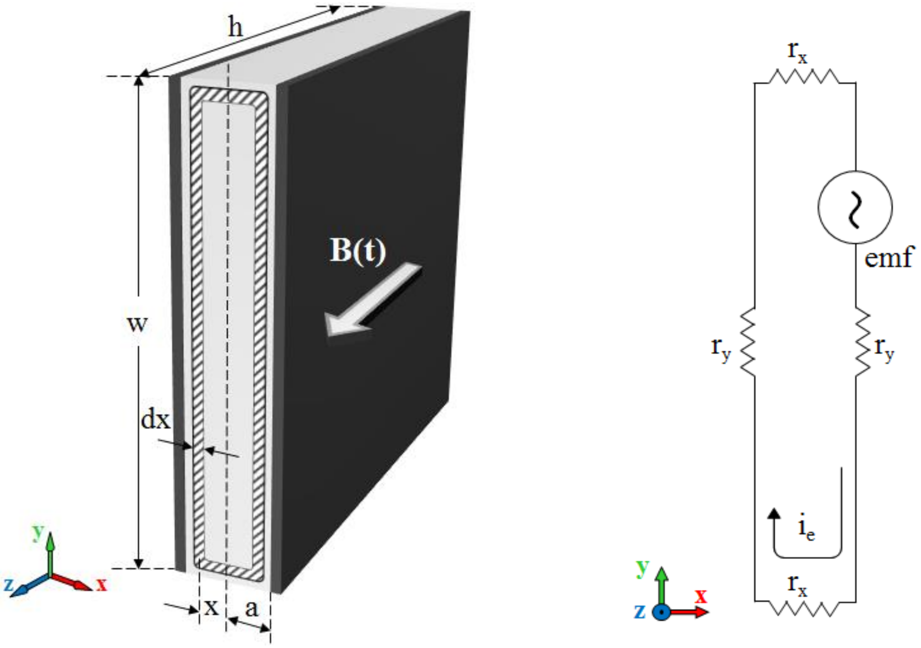

(a) (b)

Fig 4-17 (a) Single strip magnetic lamination (b) equivalent electric circuit of eddy current path

In this figure, R_y and R_x are the *Ohmic* resistance of the material along the width and thickness of the lamination, respectively and *emf* represent the induced voltage in the magnetised lamination. Considering the partial area which is specified in Fig 4-17-a, the resistance of the eddy current path in the *y*-direction is:

$$R_y = \rho\frac{l}{S} = \rho\frac{w}{hdx} \tag{4-39}$$

Since the width to thickness of the electrical steel laminations (*w/2a*) is very high, e.g for Epstein size lamination of 30 mm wide and 0.3 mm thick is 100/1, the resistance along the thickness of the lamination r_x can be neglected and therefore the total resistance of the eddy current path is:

$$R_t = 2R_y = \rho\frac{2w}{hdx} \tag{4-40}$$

The total induced *emf* along the path indicated in Fig 4-17-a can be obtained by Faraday's law:

$$e_{ind} = -\frac{d\varphi}{dt} = -\frac{d(BA)}{dt} \tag{4-41}$$

In parts 4-3 and 4-6 it was shown that at low frequencies flux density is constant from the edge to the centre line of the lamination and was explained by the equation (4-27). Therefore substituting flux density from (4-27) in (4-41) results in:

$$e_{ind} = -A\frac{d}{dt}(B_s cos\,(\omega t - \gamma))$$

$$e_{ind} = 2\pi f A B_s sin\,(\omega t - \gamma) \tag{4-42}$$

On the other hand, the area of the path indicated in the Fig 4-17-a is *A=2xw*, therefore the *rms* induced voltage in the lamination is:

$$e_{rms} = \sqrt{2}\pi f 2xwB_s \qquad [Volt] \tag{4-43}$$

Based on equation (4-43) the induced voltage in a 300 mm long, 30 mm high and 0.3 mm thick single strip lamination at flux densities 1.3 T, 1.5 T and 1.7 T and frequency 50 Hz is shown in Fig 4-18. At low frequencies, since flux density across the thickness of the lamination is almost constant, the induced *emf* in the lamination is a linear function of *x*, as shown by the equation (4-43) and Fig 4-18.

From Ohm's law the eddy current in the specified path of Fig 4-17-a can be obtained as:

$$di_e = \frac{e_{rms}}{R_t} = \frac{\sqrt{2}\pi f 2xwB_m}{(\rho\frac{2w}{hdx})} = \frac{\sqrt{2}\pi f x B_m h}{\rho} d_x \tag{4-44}$$

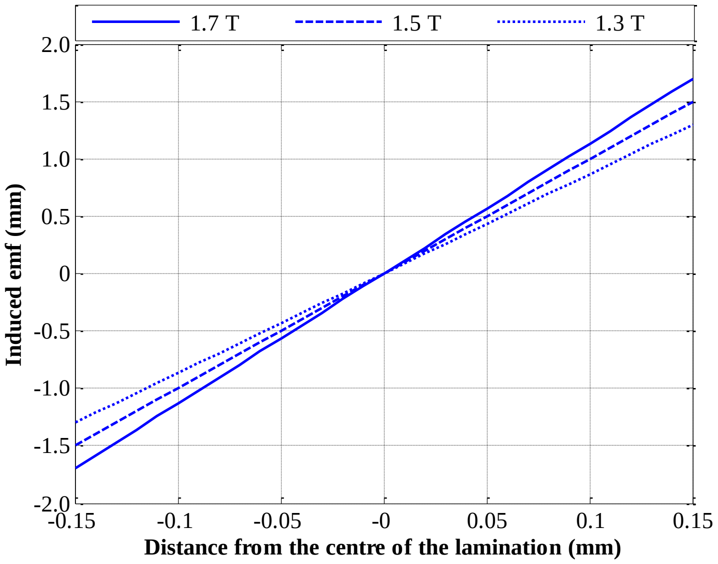

Fig 4-18 Induced voltage in a single lamination at 50 Hz frequency

Therefore eddy current power loss of the specified path of Fig 4-17-a is:

$$dp_e = R_t(di_e)^2 = \frac{4\pi^2 f^2 B_s^2 wh}{\rho} x^2 dx \tag{4-45}$$

The total eddy current power dissipated in the whole of the lamination can be obtained by integrating (4-45) from *0* to *a*:

$$p_e = \int_0^a dp_e = \int_0^a \frac{4\pi^2 f^2 B_s^2 wh}{\rho} x^2 dx$$

$$p_e = \frac{4\pi^2 f^2 B_m^2 wha^3}{3\rho} \qquad [W] \tag{4-46}$$

Equation (4-46) describes the total eddy current loss of thin sheet laminations based on the resistive equivalent circuit of the eddy current path. This equation is valid under certain assumptions, where the magnetising frequency does not result in significant skin effect and flux density penetrates uniformly along the lamination thickness [4.17]. The total volume of the lamination is *v=2awh*, therefore eddy current power loss per cubic meter of thin sheet laminations at low frequencies is:

$$p_e = \frac{4\pi^2 B_m^2 f^2 wha^3}{3\rho(2awh)} = \frac{2\pi^2 B_m^2 f^2 a^2}{3\rho} \qquad [W/m^3] \tag{4-47}$$

Equation (4-47) is known as the conventional equation of eddy current power loss of thin sheet laminations at low frequencies.

4.7.2. Eddy current power loss modelling at high frequencies

Non-uniform distribution of flux density across the lamination thickness at high frequency can affect the eddy current loss modelling at high frequencies. Eddy current power loss modelling of the magnetic laminations at high frequencies, based on the resistive equivalent circuit, is presented. Considering Fig 4-17-a, equation (4-41) can be written as:

$$e_{ind} = -\frac{d(B_x A)}{dt} = -(2xw)\frac{dB_x}{dt} \tag{4-48}$$

Substituting ***B*** from (4-25) for high frequencies into (4-48) will result:

$$e_{ind}(x,t) = -(2xw)\frac{d}{dt}\left(B_s \sqrt{\frac{\left(\cosh\frac{2x}{\delta} + \cos\frac{2x}{\delta}\right)}{\left(\cosh\frac{2a}{\delta} + \cos\frac{2a}{\delta}\right)}}\,\cos(\omega t - \gamma)\right)$$

$$e_{ind}(x,t) = (2xwB_s\omega)\sqrt{\frac{\left(\cosh\frac{2x}{\delta} + \cos\frac{2x}{\delta}\right)}{\left(\cosh\frac{2a}{\delta} + \cos\frac{2a}{\delta}\right)}}\,\sin(\omega t - \gamma) \tag{4-49}$$

where B_s is the peak flux density at the surface of the lamination. Equation (4-49) shows the induced voltage in the magnetic lamination as a function of x, f, δ. The *rms* induced voltage in the lamination is obtained:

$$e_{rms} = \sqrt{2}xwB_s\omega\sqrt{\frac{\left(cosh\,\frac{2x}{\delta}+cos\,\frac{2x}{\delta}\right)}{\left(cosh\,\frac{2a}{\delta}+cos\,\frac{2a}{\delta}\right)}} \tag{4-50}$$

Equation (4-50) can be written as:

$$e_{rms} = \sqrt{2}\pi f 2xwB_s\sqrt{\frac{\left(cosh\,\frac{2x}{\delta}+cos\,\frac{2x}{\delta}\right)}{\left(cosh\,\frac{2a}{\delta}+cos\,\frac{2a}{\delta}\right)}} \tag{4-51}$$

At low frequencies, *i.e.* when $\delta >> a$, the quantity under the square root of the equation (4-51) approaches unity and it will be the same as (4-43) which was obtained at low frequencies. The induced voltages in a 300 mm long, 30 mm height and 0.3 mm thick single strip lamination at frequencies 500 Hz, 1 kHz, 2 kHz and 5 kHz and a flux density of 1.7 T, derived from (4.51), are shown in Fig 4-19.

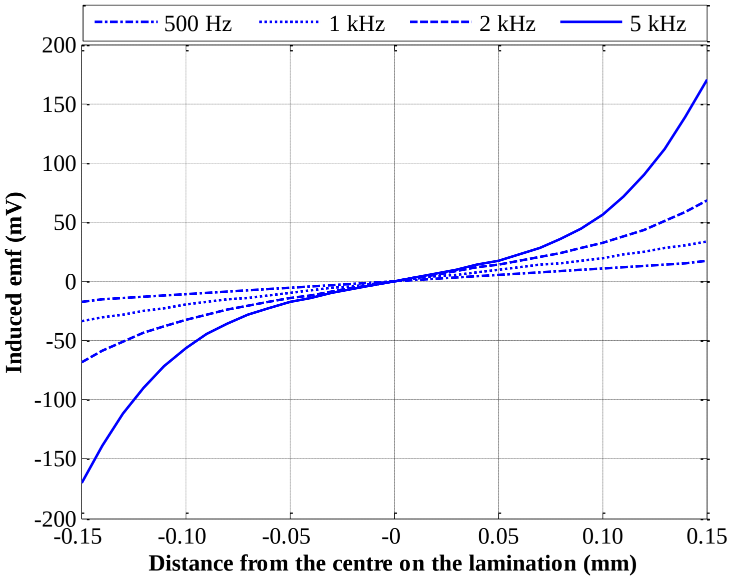

Fig 4-19 Induced voltage in a single lamination at high frequencies, typically at peak flux density of B_{pk}=1.7 T

Unlike the induced *emf* in lamination at low frequencies, Fig 4-19 shows a nonlinear relation between the induced *emf* in the lamination and distance from the centre of the lamination. This fact is basically related to non-uniform distribution of flux density along the lamination thickness at high frequencies, caused by skin effect. Following the same method as section 4-7-1, eddy current in the specified path of Fig 4-17-a at high frequencies is obtained as:

$$di_e = \frac{e_{rms}}{R_t} = \frac{\sqrt{2}\pi f x B_s h}{\rho}\sqrt{\frac{\left(cosh\ \frac{2x}{\delta} + cos\ \frac{2x}{\delta}\right)}{\left(cosh\ \frac{2a}{\delta} + cos\ \frac{2a}{\delta}\right)}}\ dx \tag{4-52}$$

Therefore the eddy current power loss in the specified path of Fig 4-17-a at high frequencies is obtained as:

$$dp_e = \frac{e_{rms}^2}{R_t} = \frac{4\pi^2 f^2 B_s^2 wh}{\rho}\left(\frac{cosh\ \frac{2x}{\delta} + cos\ \frac{2x}{\delta}}{cosh\ \frac{2a}{\delta} + cos\ \frac{2a}{\delta}}\right)x^2 dx \tag{4-53}$$

and the total eddy current power loss in the lamination is:

$$p_e = \int_0^a \frac{4\pi^2 f^2 B_s^2 wh}{\rho}\left(\frac{cosh\ \frac{2x}{\delta} + cos\ \frac{2x}{\delta}}{cosh\ \frac{2a}{\delta} + cos\ \frac{2a}{\delta}}\right)x^2 dx$$

$$p_e = \frac{4\pi^2 f^2 B_s^2 wh}{\rho(cosh\ \frac{2a}{\delta} + cos\ \frac{2a}{\delta})}\int_0^a (cosh\ \frac{2x}{\delta} + cos\ \frac{2x}{\delta})x^2 dx$$

$$p_e = \frac{\pi^2 f^2 B_s^2 wh\delta^3}{2\rho(Cosh\ \frac{2a}{\delta} + Cos\ \frac{2a}{\delta})}\left[\frac{4a}{\delta}\left(cos\ \frac{2a}{\delta} - cosh\ \frac{2a}{\delta}\right) + sinh\frac{2a}{\delta}\left((\frac{2a}{\delta})^2 + 2\right) + sin\frac{2a}{\delta}\left((\frac{2a}{\delta})^2 - 2\right)\right] \tag{4-54}$$

Equation (4-54) describes the total eddy current power loss of thin sheet laminations of length *h*, width *w* and thickness *2a* in Watts at high frequencies based on the equivalent circuit of the lamination. Considering the total volume of the lamination *v=2awh*, eddy current power loss of thin sheet laminations at high frequencies per cubic meter is:

$$p_e = \frac{\pi^2 f^2 B_s^2 \delta^3}{4a\rho(Cosh\ \frac{2a}{\delta} + Cos\ \frac{2a}{\delta})}\Big[\frac{4a}{\delta}\Big(cos\ \frac{2a}{\delta} - cosh\ \frac{2a}{\delta}\Big) + sinh\frac{2a}{\delta}\Big((\frac{2a}{\delta})^2 + 2\Big) + sin\frac{2a}{\delta}\Big((\frac{2a}{\delta})^2 - 2\Big)\Big] \qquad (4\text{-}55)$$

Equation (4-55) shows eddy current power loss of single laminations at high frequency magnetisations as a function of peak surface flux density B_s, magnetising frequency *f*, skin depth *δ*, thickness of the lamination *2a* and resistivity of the material *ρ*. This is a general equation to estimate total eddy current power loss of magnetic laminations of length *h*, width *w* and thickness *2a* (in w/m^3) based on the resistive equivalent circuit of the eddy current path. In this equation the effect of non-uniform flux density distribution across the thickness of the lamination caused by skin effect is considered.

4.7.3. Analytical results of eddy current power loss of a single strip lamination

The analytical model of eddy current power loss of sections 4.7.1 and 4.7.2, was developed based on the distribution of flux density across the lamination thickness. Therefore the designed flowchart of the determination of flux density distribution, shown in Fig 4-11, was developed to determination of the eddy current power loss of single laminations, as shown in Fig 4-20. In order to investigate the analytical modelling and compare the results, based on the designed flowchart of Fig 4-20 characteristics of the eddy current power loss versus magnetising frequency obtained by the conventional equation of (4-47) and the developed equation of (4-55) at peak flux densities 1.3 T and 1.7 T are shown in Fig 4-21.

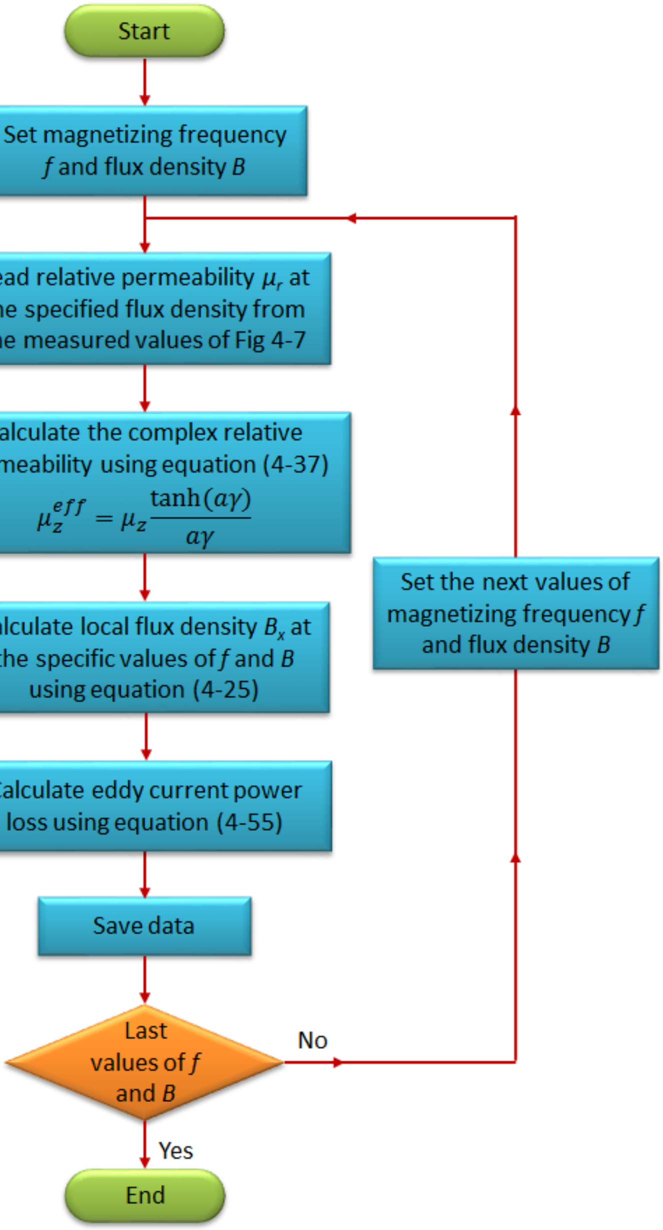

Fig 4-20 Flowchart of the determination of eddy current power loss

This characteristic was also calculated by equation (4-55) with constant and frequency dependent values of relative permeabilities; the results are shown in Fig 4-22. These calculations were performed for an Epstein size lamination of CGO *Fe* 3 % *Si* of 0.3 mm thick, 30 mm width and 305 mm length with the same magnetic and electric properties as stated in section 4-6.

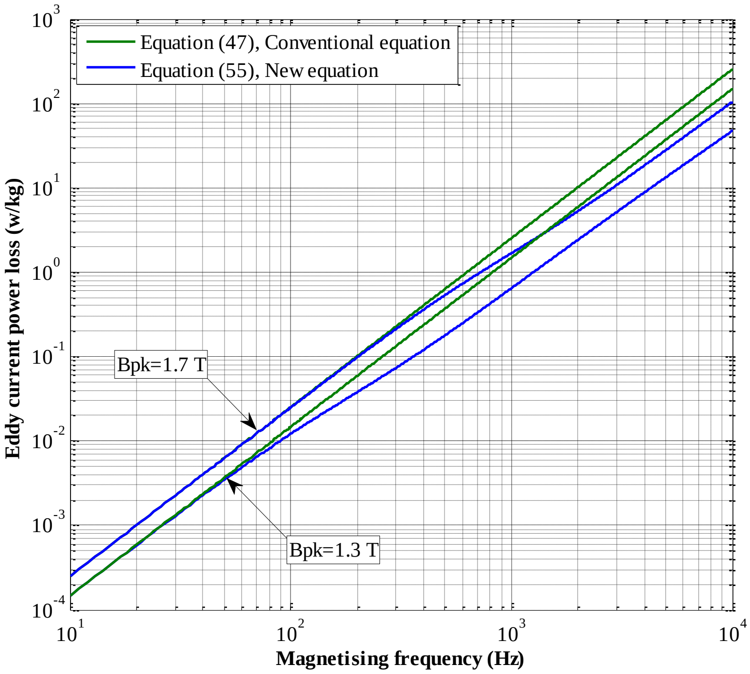

Fig 4-21 Comparison of eddy current power loss vs. magnetising frequency with constant and frequency dependence relative permeability at peak flux densities B_{pk}=1.3 T and B_{pk}=1.7 T

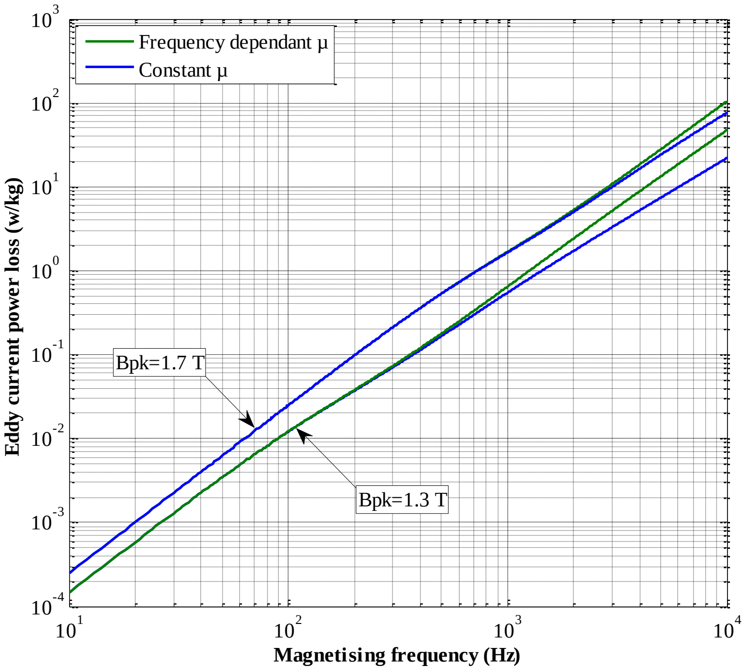

Fig 4-22 Comparison of eddy current power loss vs. magnetising frequency from conventional equation and new equation at peak flux densities B_{pk}=1.3 T and B_{pk}=1.7 T

Using equation (4-47) the whole thickness of the lamination is involved in the resistance of the eddy current path and hence eddy current power loss, because this equation was obtained based on uniform flux density distribution through the lamination thickness in which skin effect is ignored. However significant skin effect at high frequencies forces eddy current to flow in a smaller area and according to (4-40) increases the resistance of eddy current path. As a consequence, induced eddy currents in the lamination and hence eddy current power loss will be reduced. Fig 4-21 shows that the difference between the eddy current power losses obtained by equations (4-47) and (4-55) increases by increasing the magnetising frequency which is related to the impact of skin effect on eddy current and eddy current power loss. At low frequencies the difference between these two values could be negligible, e.g. at 50 Hz the difference is less than 0.2 %; while this value at 10 kHz is about 60 %. Therefore, Fig 4-21 shows that at high frequencies the calculated eddy current loss without accounting for skin effect will be an overestimate.

In section 4-5 the importance of skin effect on the relative permeability of the material at high frequency was shown by means of complex relative permeability. Ignoring this effect leads to higher relative permeability for the material at high frequencies which results in lower eddy current power loss. Fig 4-22 shows that the difference between the eddy current power losses obtained by constant and frequency dependent relative permeability increases by increasing magnetising frequency; so that for the material with the mentioned specifications, the maximum difference at 10 KHz is 26.67 %.

Another conclusion from Figs 4-21 and 4-22 is related to the effect of flux density amplitude on the characteristics. As stated in part 4.6, at each particular frequency, skin effect is more significant at high values of magnetic permeability. Therefore Figs 4-21 and 4-22 show less discrepancy at flux density of 1.7 T with lower relative permeability and high discrepancy at flux density of 1.3 T with higher relative permeability.

4.8. Conclusion

In this chapter based on the physical dimensions of the magnetic laminations and also magnetic and electrical properties of the material, an equivalent circuit was proposed for the lamination to calculate and predict the eddy current power loss. In this modelling important factors, *i.e.* skin effect, non-uniform flux density distribution, complex relative permeability and non-linear relation of ***B*** and ***H*** were considered. Therefore the proposed model provides accurate loss calculation in a wide range of flux density and magnetising frequency.

The most important achievements of this chapter are listed here:

1. In the study of the magnetic properties of magnetic materials the skin effect plays an important role at high magnetising frequencies and high relative permeabilities. Therefore in order to carry out accurate modelling and obtain real results, skin effect and its impacts on the other parameters and magnetic properties should be considered in the calculations and experimental processes.
2. Based on the analytical modelling it was found that the effective permeability observed at high frequencies is not large in comparison with the permeabilities observed under normal operating conditions at low frequencies. There is also a phase angle in permeability of the material at high frequencies.
3. For a given material with specific conductivity σ, skin effect depends not only on the magnetising frequency f but also on the relative permeability of the material μ_r. Furthermore since electrical steel laminations are non-linear materials, relative permeability of the materials depends strongly on the amplitude of peak flux density. Therefore, at each specific frequency, magnetic materials have different responses to different peak flux densities.
4. At low frequencies where skin effect is negligible, flux density along the thickness of the lamination is distributed almost uniformly. Increasing the

magnetising frequency leads to the distribution of the flux density to be non-uniform and decreases from the surface to the centre of the lamination. The distribution pattern of flux density extremely depends on the magnetising frequency and relative permeability of the material.

5. Eddy current loss modelling over a wide range of frequencies and flux density requires accounting for the skin effect and its impacts on the magnetic properties of the material.

References:

[4.1] Bhag S. Guru, Huseyin R. Hiziroglu, *"Electric Machinery and Transformers",* Third edition, Oxford university press, 2001

[4.2] J Lammeraner, and M Stafl "*Eddy currents*", ILIFFE Books Ltd., London, 1966

[4.3] Eddy current, Wikipedia, The Free Encyclopedia, Retrieved August 22, 2012, from http://en.wikipedia.org/wiki/Eddy_current

[4.4] D G Fink, D Christiansen, "*Electronics Engineers' handbook*" McGraw-Hill, 1989

[4.5] Z Popovic, B D Popovic "*Introductory Electromagnetics*" Prentice Hall, 1999

[4.6] BS EN 10282:2001 "Method Of Test for the Determination of Surface Insulation Resistance of Electrical Sheet And Strip"

[4.7] B Weiser, A Hasenzagl, T Booth, and H Pfützner, "*Mechanisms of Noise Generation of Model Transformer Cores*" JMMM, vol. 160, pp. 207-209, 1996

[4.8] B Weiser and H Pfützner, "*Relevance of Magnetostatic Forces for Transformer Core Vibrations*" J. Phys. IV France, vol. 08, pp. Pr2-591-Pr2-594, 1998

[4.9] F. Brailsford, "*Physical Principles of Magnetism*", Van Nostrand, 1966

[4.10] M. Ibrahim and P. Pillay, "*Advanced Testing and Modelling of Magnetic Materials Including a New Method of Core Loss Separation for Electrical Machines*", IEEE Transaction on Industry Applications, Vol. 48, NO. 5, Sep/Oct 2012, pp. 1507 – 1515

[4.11] A J Moses, J Leicht, P Anderson, "*Apparent Permeability of Electrical Steel Under PWM Magnetisation*", Journal of Magnetism and Magnetic Materials 304 (2006) e543–e545

[4.12] K. Abeywickrama, T. Daszczynski, Y. Serdyuk, and S. Gubanski, "*Determination of Complex Permeability of Silicon Steel for Use in High-Frequency Modelling of Power Transformers*" IEEE Trans Magn. , Vol. 44, No. 4, pp. 438–444, Apr. 2008

[4.13] D. Roger, E. Napieralska-Juszczak, and A. Henneton, "*High Frequency Extension of Non-Linear Models of Laminated Cores*" Int. J. Comput. Math Elect Electron Eng, Vol. 25, No. 1, pp. 140–156, 2006

[4.14] V. Leger, C. Ramiarinjaona, R. Barrue and R. Lebourgeois "*Composite Magnetic Materials Based on Nanocrystalline Powders for Middle- and High-Frequency Applications Up To 1 Mhz*" Journal of Magnetism and Magnetic Materials 191 (1999), pp.169-173

[4.15] P Anderson, D R Jones and J Hall, "*Measurement of Resistivity of Soft Magnetic Laminations at Elevated Temperatures*", JMMM, Vol 304, Issue 2, 2006, pp. e546-e548

[4.16] G Loisos, A J Moses, P Beckley, "*Electrical Stress on Electrical Steel Coatings*", JMMM, 254–255 (2003) 340–342

[4.17] F Fiorillo, "*Measurement and Characterisation of Magnetic Materials*", Elsevier Academic Press, 2004

CHAPTER 5

Iron Loss Separation and Experimental Results of Eddy Current Power Loss of Single Strip Lamination

5.1. Introduction

The core loss data provided by steel manufacturers or obtained from experiments are usually in the form of curves or tables of total loss in watts per kilogram (W/kg) or watts per pound (W/lb) for typical flux densities and frequencies [5.1]-[5.2]. However, in order to support the analytical results it is often useful to separate the power loss of the magnetic materials into its components.

An experimental-analytical technique was developed to separate core loss into components obtained from the experimental measurements of power losses over a wide frequency range. Total power loss of Epstein size laminations of, Conventional Grain Oriented (CGO) at peak flux densities of 1.3 T, 1.5 T, 1.7 T and 1.8 T and Non-Oriented (NO) at peak flux densities of 1.1 T, 1.3 T and 1.5 T at magnetising frequencies from 10 Hz to 1000 Hz was measured. Eddy current power loss of the samples was separated at each frequency and flux density and finally the results were compared to the analytical results shown in chapter 4.

5.2. Principal of magnetic loss measurement using Single Strip Tester (SST)

A computer-controlled system had been developed within the Wolfson Centre for Magnetics providing high accuracy and automatic measurements. It does not require any discrete instrument since a program written in LabVIEW is used to calculate magnetic properties [5.3]. Fig 5-1 shows a schematic diagram of the measuring system of the Single Strip Tester (SST).

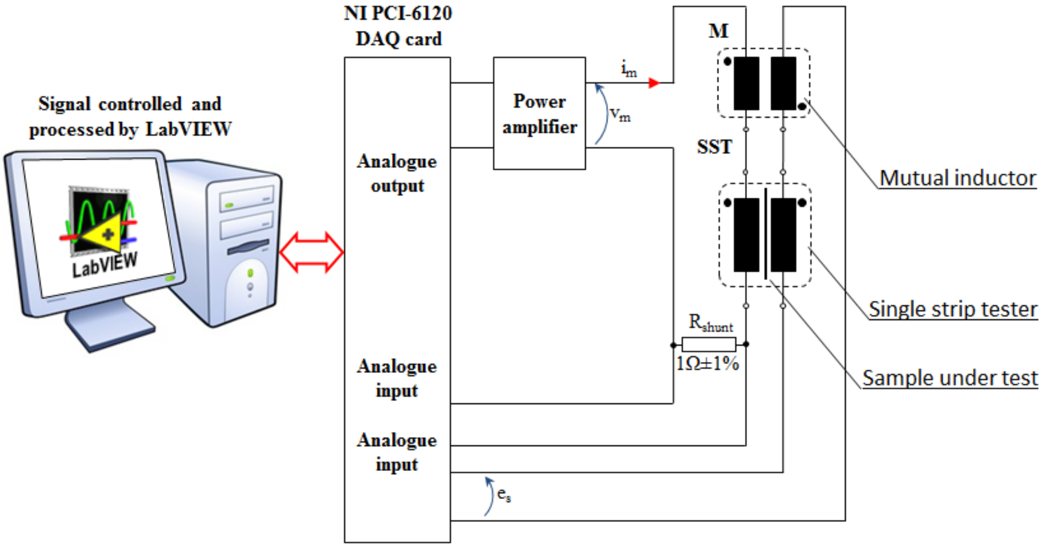

Fig 5-1 Schematic diagram of computer-controlled Single Strip Tester (SST) measuring system (reproduced based on [5.3])

This measuring system comprises a personal computer (PC), in which LabVIEW version 8.50 from National Instruments was already installed, a NI PCI-6120 data acquisition (DAQ) card, a power amplifier, a 1 Ω shunt resistor (R_{sh}), and an air-flux compensated single strip tester (SST). In the magnetising core of the SST a double vertical yoke is used, as shown in Fig 5-2. Each yoke was made from GO steel and its physical dimensions are detailed in Fig 5-2-a.

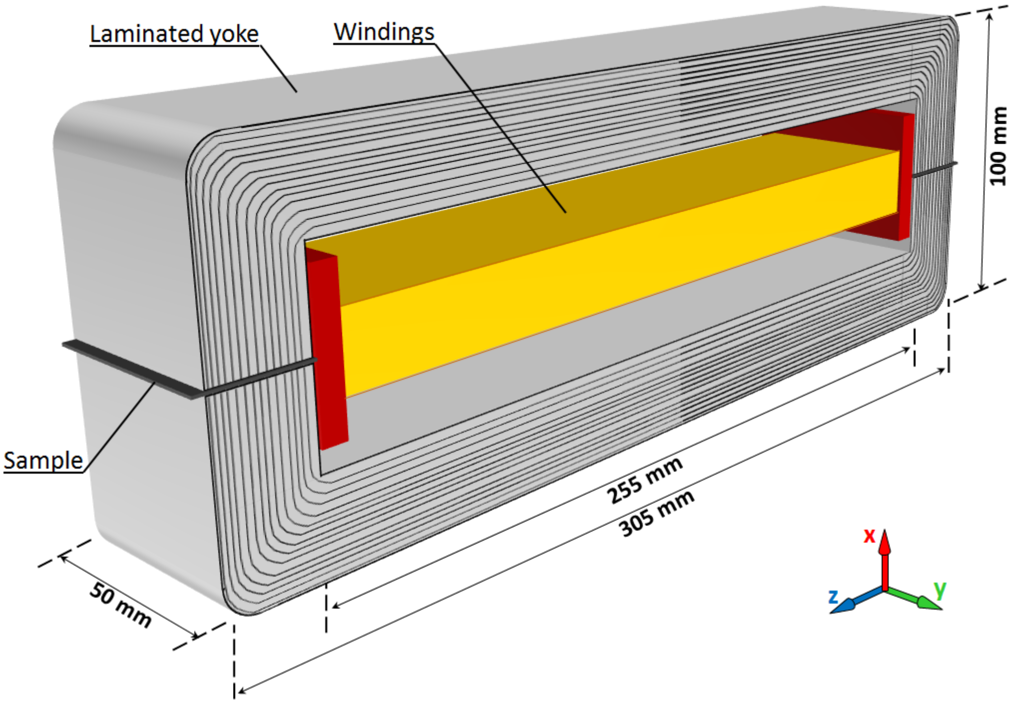

(a)

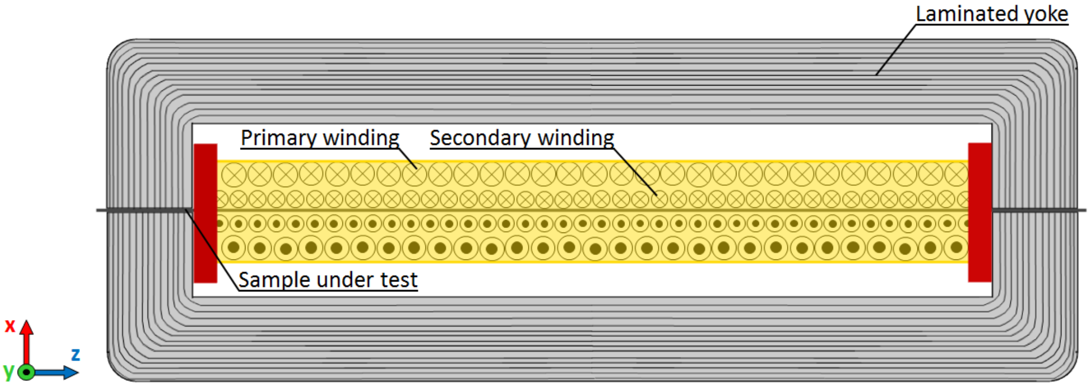

(b)

Fig 5-2 Single strip tester (a) perspective view showing physical dimensions, and (b) side view

A 250 turn secondary winding (N_2) was wound around a plastic former and an 865 turn primary winding (N_1) was wound around the secondary winding. Magnetic lamination samples of standard Epstein strip (305 mm long, 30 mm wide) to be tested are placed between the yokes, as shown in Fig 5-2.

The mutual inductor was used to compensate for the effect of air flux by connecting its primary winding in series with the SST primary winding, while connecting the secondary winding in series opposition with the SST secondary winding. The mutual inductance was adjusted by passing an alternating current through the primary winding in the absence of the test sample and modifying the number of turns until the voltage of the secondary circuit was less than 0.1 % of the SST secondary voltage. Hence, the induced voltage in the combined secondary winding is only due to the flux density in the test sample.

The magnetising voltage of the primary winding was generated by the LabVIEW program via a voltage output of the DAQ card. There were 20,000 data points per magnetisation cycle to make the signal waveform as smooth as possible. The voltage drop across the shunt resistor ($V_{R\text{-}sh}$), and the combined secondary voltage (e_s) were read for calculation of flux density ***B*** and magnetic field strength ***H***, respectively. The sampled waveforms of $V_{R\text{-}sh}$ and e_s had 1,800 points per cycle, which is sufficiently large enough to avoid quantising errors.

The instantaneous magnetic field strength (h) of the SST was calculated inside the LabVIEW program from:

$$h = \frac{N_1 V_{R-sh}}{l_m R_{sh}} \tag{5-1}$$

where l_m is the mean magnetic path, which is the distance between the inner edges of the yoke (0.255 m), as shown in Fig 5-2-a. The instantaneous flux density (b) was obtained by mean of digital integration of the combined secondary voltage e_s as:

$$b = \frac{l\,\rho_m}{N_2\,m} \int e_s\ dt \tag{5-2}$$

where l is the specimen length, m is the mass of the specimen and ρ_m is the density of the sample. The specific power loss of the sample (P_s) was calculated from:

$$P_s = \frac{1}{T\,\rho_m} \int_0^T h\,\frac{db}{dt}\,dt \tag{5-3}$$

where T is the magnetising cycle period. The AC relative permeability ($\mu_{r\text{-}AC}$) of the material was derived from:

$$\mu_{r-AC} = \frac{\boldsymbol{B}}{\mu_0\,\boldsymbol{H}} \tag{5-4}$$

where μ_0 is permeability of free space and $\boldsymbol{H}$ is the peak value of magnetic field. $\boldsymbol{B}$ and $\boldsymbol{H}$ were determined numerically by using the maximum function in LabVIEW.

The control of the flux density waveform was implemented in LabVIEW as shown in the block diagram of Fig 5-1. A feedback control system was used to control the flux density and secondary induced voltage waveforms to be sinusoidal. The form factor (*FF*) of the secondary induced voltage was maintained to be 1.111 ± 0.02 %, which is better than the value recommended in [5.4]. The test procedure of the measuring system is shown in the flowchart of Fig 5-3.

According to this flowchart firstly, a table of $\boldsymbol{B}$ values and the measurement criteria which are 0.02 % error of $\boldsymbol{B}$ and 0.02 % error of the ideal *FF* of the secondary induced voltage are read. Secondly, a first magnetising waveform is applied to the SST. If the criteria are met, the b and h waveforms will be averaged to minimise random errors and improve repeatability [5.5], otherwise the magnetising waveform is adjusted by the feedback algorithm. After averaging, the criteria are re-checked then the measurement data for this point is saved. A spread sheet file is generated if all the values of $\boldsymbol{B}$ are measured and the sample is demagnetised by reducing the magnetisation gradually to zero. A photograph of the SST measurement system is shown in Fig 5-4.

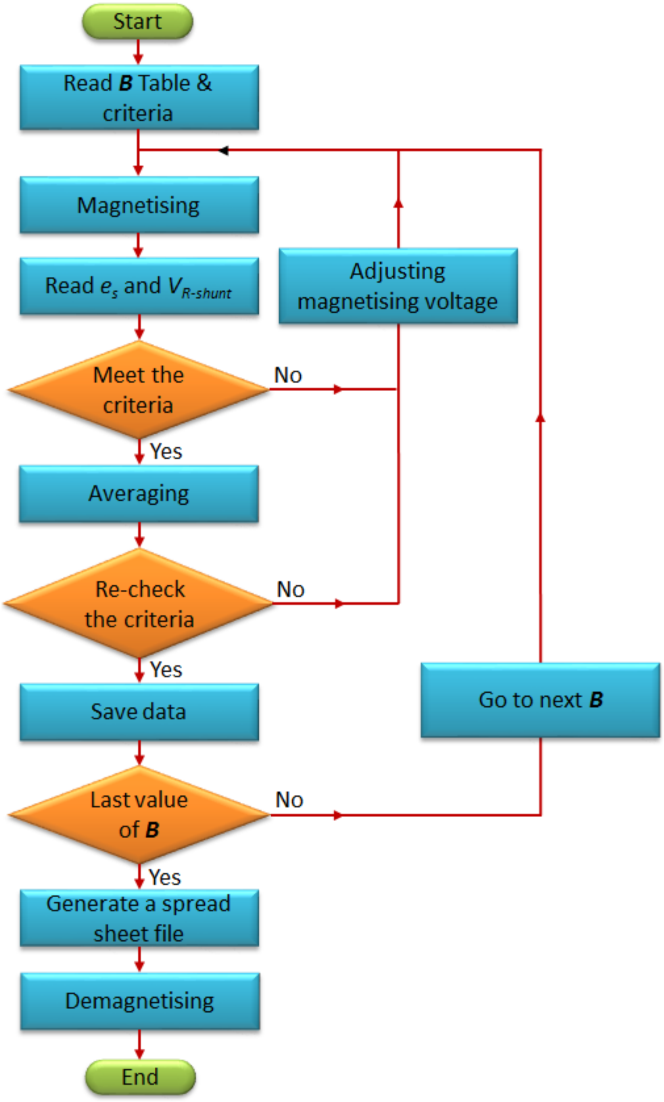

Fig 5-3 Flowchart of each measurement of the single strip tester, reproduced based on [5.3]

5.3. Separation of core loss of magnetic laminations

Since the 19th century, core losses due to time-varying magnetic fields have been separated into two main terms: hysteresis losses p_h (also referred to as static losses) and eddy current losses p_e (dynamic losses) [5.6]. Thus, total core loss was given by:

$$\begin{aligned} p_c &= p_h + p_e \\ &= k_h f B_{pk}^n + k_e (f B_{pk})^2 \end{aligned} \tag{5-5}$$

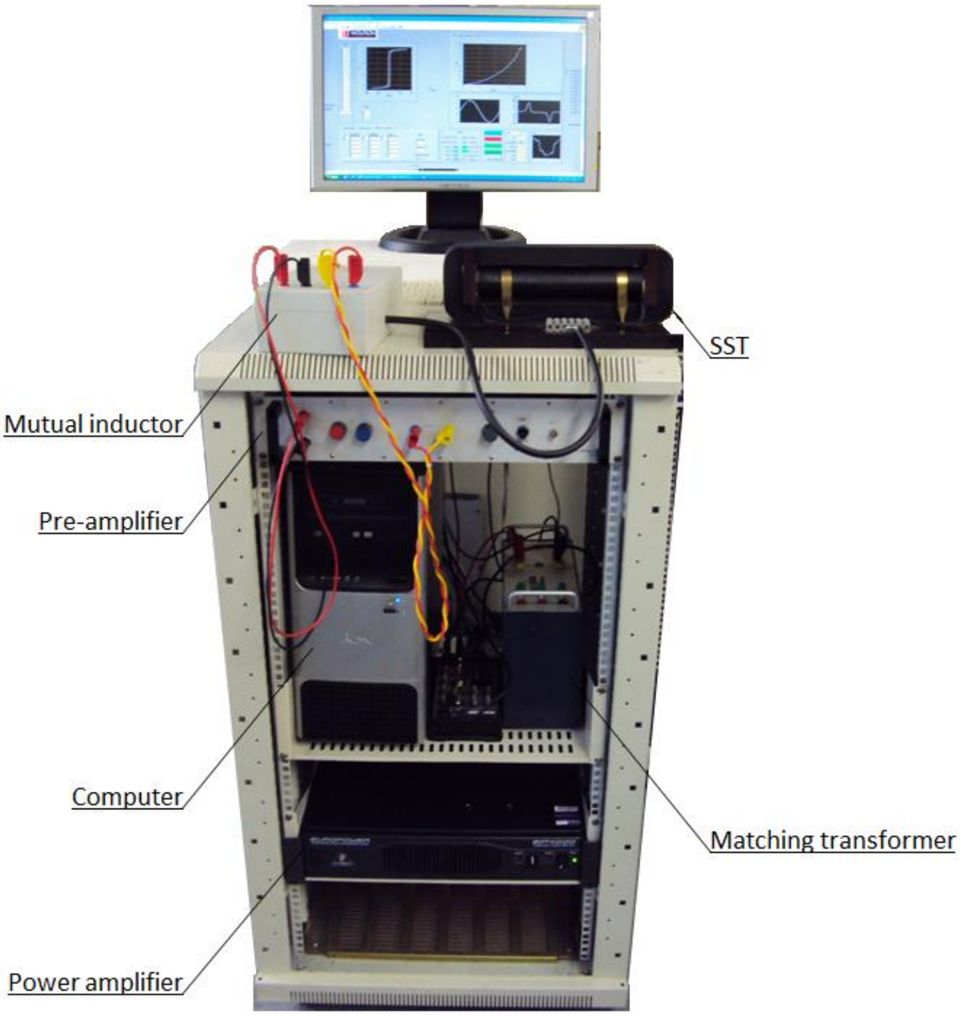

Fig 5-4 Photographs of measurement system of the single strip tester

where f is magnetising frequency, B_{pk} is peak flux density, n is constant, k_h and k_e are hysteresis and eddy current loss coefficients, respectively. A modified version of (5-5) was used as [5.4]:

$$p_c = k_h f B_{pk}^{(a+bB_{pk})} + k_e(fB_{pk})^2 \tag{5-6}$$

In which the flux density dependent term ($a+bB_{pk}$) is replaced by the constant n in (5-5). Hysteresis power loss in (5-6) represents the additional hysteresis component loss under dynamic magnetisation. a and b are frequency dependence coefficients. However, the two term formulation of iron power loss shows a large difference in comparison with the experimental results, especially at high flux density and high excitation frequency [5.7]. This difference is usually explained by the excess losses or anomalous loss p_a. An additional term of iron loss was proposed by Bertotti [5.8] to explain these excess losses based on the statistical loss theory, and the total core loss is expressed as:

$$\begin{aligned} p_c &= p_h + p_e + p_a \\ &= k_h f B_{pk}^n + k_e (f B_{pk})^2 + k_{ex} (f B_{pk})^{1.5} \end{aligned} \tag{5-7}$$

where k_{ex}, the excess loss coefficient, depends on material micro-structure, conductivity and the cross section area of the lamination [5.8]. Calculating the coefficients of (5-5) or (5-7) results in separation of the components of the core loss. However since loss components depend on the operating frequency and flux density, separation of the core loss components is credible within a defined frequency and flux density range [5.7]. In more recently developed models this range is extended by allowing the coefficients of the loss components to vary with the variations of the frequency and flux density [5.1] and [5.9].

5.3.1. Loss separation based on the two term formulation

The static hysteresis energy loss per cycle is predicted by calculating the area enclosed by the ***B*** and ***H*** loop under DC excitation. However, when time varying magnetic fields are applied to the magnetic material, the area enclosed by the ***B*** and ***H*** loop represents the total core loss per cycle. Therefore, an analytical method, known as *extrapolation method*, is usually implemented to separate the core loss components using the total core loss measurements at different frequencies. In this method, the hysteresis power loss is separated by extrapolating total core loss per cycle versus magnetising frequency curves at different flux densities to zero frequency. The power loss at zero frequency represents the static hysteresis loss per cycle. Therefore dividing (5.5) by the magnetising frequency leads to [5.9]:

$$\frac{p_c}{f} = \frac{p_h}{f} + \frac{p_e}{f}$$
$$= k_h B_{pk}^n + k_e f B_{pk}^2 \qquad (5\text{-}8)$$

This equation is a linear function of the magnetising frequency f at each peak flux density B_{pk} and can be written as:

$$\frac{p_c}{f} = D + Ef \qquad (5\text{-}9)$$

where $D = k_h B_{pk}^n$ is hysteresis power loss per cycle and $E = k_e B_{pk}^2$. Mathematical methods are available to calculate these coefficients [5.1], [5.7] and [5.9]. Fig 5.5 shows a typical separation of core loss components based on the two terms formulation and using the extrapolation method [5.7].

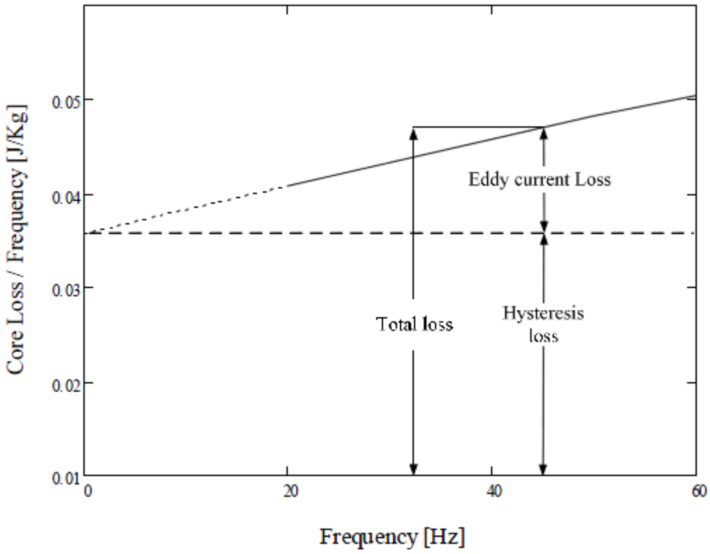

Fig 5.5 Separation of core loss by the extrapolation method [5.7]

Therefore, from the equation (5-9) and Fig 5.5 it can be noted that the extrapolation method is based on a constant hysteresis power loss per cycle and a linear relation of the eddy current power loss per cycle at all frequencies.

5.3.2. Loss separation based on the three term formulation

The extrapolation method is also applicable to separate loss components in the three terms formulation. Dividing (5-7) by the magnetising frequency leads to [5.1]:

$$\frac{p_c}{f} = \frac{p_h}{f} + \frac{p_e}{f} + \frac{p_a}{f}$$
$$= k_h B_{pk}^n + k_e f B_{pk}^2 + k_{ex}\sqrt{f} B_{pk}^{1.5} \quad (5\text{-}10)$$

And in terms of constant coefficients:

$$\frac{p_c}{f} = D + Ef + G\sqrt{f} \quad (5\text{-}11)$$

Similar to the method mentioned in part 5-2-1, equation (5-11) can be plotted versus magnetising frequency *f*. A powerful solver is available within Microsoft Excel which enables the sum of the squares of the difference between the measured loss values and that given by equation (5-11) to be minimised by changing the values of the constants *D*, *E* and *G*. However in [5.9] and [5.10] a more reasonable method is implemented to obtain the coefficients of (5-11) in which the core loss data are used to plot curves of power loss per cycle p_c/f versus square root of frequency $\sqrt{f}$, not frequency *f*, for different values of peak flux density B_{pk}. Therefore (5-11) can be represented by:

$$\frac{p_c}{f} = D + E(\sqrt{f}\,)^2 + G\sqrt{f} \quad (5\text{-}12)$$

where *D*, *G* and *E* are coefficients of power loss components and can be obtained by polynomial curve fitting. Comparing (5-12) and (5-10) leads to:

$$D = k_h B_{pk}^n$$
$$E = k_e B_{pk}^2$$
$$G = k_a B_{pk}^{1.5}$$

Therefore by using this method, for given flux densities, the loss coefficients k_h, k_e and k_a can be obtained.

As stated initially, from Fig 5.5 and equations (5-11) and (5-12) it can be concluded that in the extrapolation method the hysteresis power loss per cycle is assumed independent of the frequency and the eddy current power loss per cycle is assumed as a linear function of frequency. Therefore the total hysteresis loss is simply calculated by multiplying the hysteresis power loss per cycle by the operating frequency f and the total eddy current power loss is calculated by multiplying the eddy current power loss per cycle by square root of the operating frequency $\sqrt{f}$.

5.3.3. *Practical example of loss separation*

As a practical example on loss separation, power loss of an Epstein size lamination of CGO was measured using the measuring system described in part 5.2. Specific power loss of the sample typically at peak flux density of 1.7 T and magnetising frequency from 10 Hz to 1000 Hz together with specific loss per cycle are shown in Table 5-1.

Table 5-1 Eddy current power loss of an Epstein size lamination at 1.7 T and different magnetising frequencies

Magnetising frequency (Hz)	Measured power loss (W/kg)	Power loss per cycle (W/kg/Hz)
10	0.173	0.0194
25	0.520	0.0229
50	1.38	0.0304
100	3.73	0.0402
200	10.9	0.0587
400	34.6	0.0945
800	119	0.1626
1000	179	0.1962

Total power loss per cycle versus square root of frequency is shown in Fig 5-6. Following the method mentioned in part 5.2.2, in order to obtain the coefficients of the loss components, the polynomial function of this curve was obtained using the polynomial curve fitting function in Microsoft Excel.

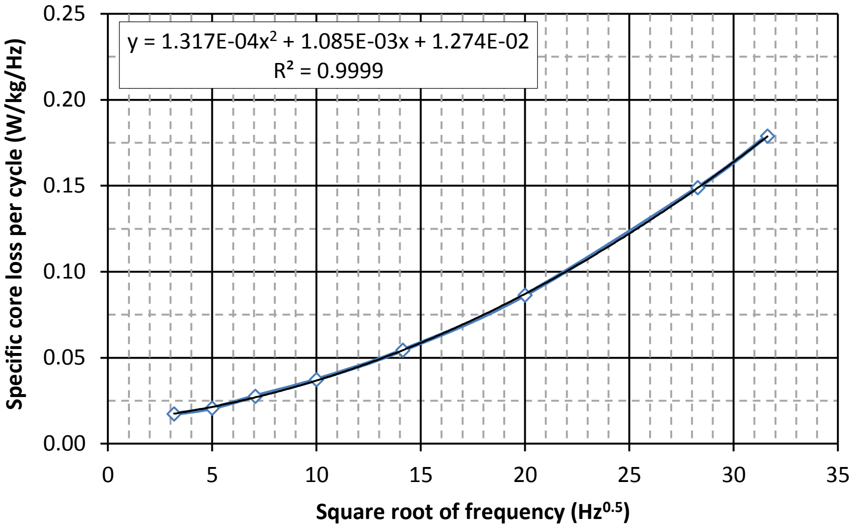

Fig 5-6 Total power loss per cycle of an Epstein size magnetic lamination of CGO versus square root of frequency $\sqrt{f}$ at peak flux density of 1.7 T

As shown in Fig 5-6, the value of the fitting residual of the equation is very close to unity, i.e. R^2=0.999, indicating a very good approximation. Comparing the polynomial function of Fig 5-6 and equation (5-12), the coefficients of the loss components of this particular sample are obtained as:

$$D = k_h B_{pk}^{n} = 1.274 \times 10^{-2}$$

$$E = k_e B_{pk}^{2} = 1.317 \times 10^{-4}$$

$$G = k_a B_{pk}^{1.5} = 1.085 \times 10^{-3}$$

Using these coefficients and based on the equations (5-10) and (5-11), loss components of the sample at different frequencies were calculated; the results are shown in Table 5-2. Eddy current and hysteresis power losses per cycle versus magnetising frequency for this particular material at peak flux density of 1.7 T are shown in Fig 5-7. As shown in this figure, from the extrapolation method, hysteresis loss per cycle is assumed independent of the frequency and the eddy current loss per cycle is a linear function of the magnetising frequency.

Table 5-2 Loss components of an Epstein size lamination of CGO at peak flux density of 1.7 T and different magnetising frequencies

f (Hz)	Measured power loss (W/kg)	P_e (W/kg)	P_h (W/kg)	P_a (W/kg)	$P_t = P_e + P_h + P_a$ (W/kg)	Difference* (%)
10	0.1731	0.0132	0.1270	0.0343	0.1745	0.81
25	0.5203	0.0825	0.3175	0.1356	0.5356	2.86
50	1.385	0.3300	0.6350	0.3836	1.349	-2.70
100	3.731	1.320	1.270	1.085	3.675	-1.52
200	10.89	5.280	2.540	3.069	10.89	-0.01
400	34.59	21.12	5.080	8.680	34.88	0.83
800	119.1	84.48	10.16	24.55	119.2	0.08
1000	178.9	132.0	12.70	34.31	179.0	0.06

* Difference between the measured loss and total loss from the extrapolation method

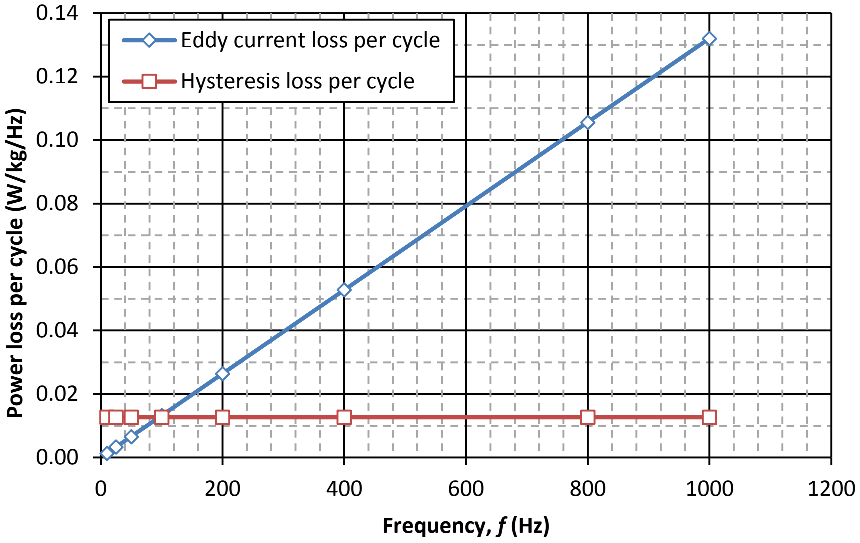

Fig 5-7 Eddy current and hysteresis power loss per cycle versus frequency at peak flux density of 1.7 T

It is now useful to compare the eddy current power loss per cycle of the sample from the equations (4-47) and (4-55) of chapter 4. The results are shown in Table 5-3 and Fig 5-8. According to Fig 5-8 a close agreement between eddy current power losses per cycle from the equations (4-47) and (4-55) was found at low frequencies. Furthermore the eddy current power loss per cycle from the equation (4-47) is a linear function of frequency; but not from the equation (4-55).

Table 5-3 Eddy current power loss of an Epstein size lamination at peak flux density of 1.7 T and different magnetising frequencies obtained from equations (4-47) and (4-55)

Magnetising frequency (Hz)	**Eddy current power loss (W/kg)**		**Eddy current power loss per cycle (W/kg/Hz)**	
	Equation (4-47)	**Equation (4-55)**	**Equation (4-47)**	**Equation (4-55)**
10	0.0132	0.0132	1.32E-03	1.32E-03
25	0.0825	0.0824	3.30E-03	3.30E-03
50	0.3300	0.3290	6.60E-03	6.58E-03
100	1.320	1.308	1.32E-02	1.31E-02
200	5.280	5.107	2.64E-02	2.55E-02
400	21.11	18.78	5.28E-02	4.70E-02
800	84.43	60.65	1.06E-01	7.58E-02
1000	131.9	86.21	1.32E-01	8.62E-02

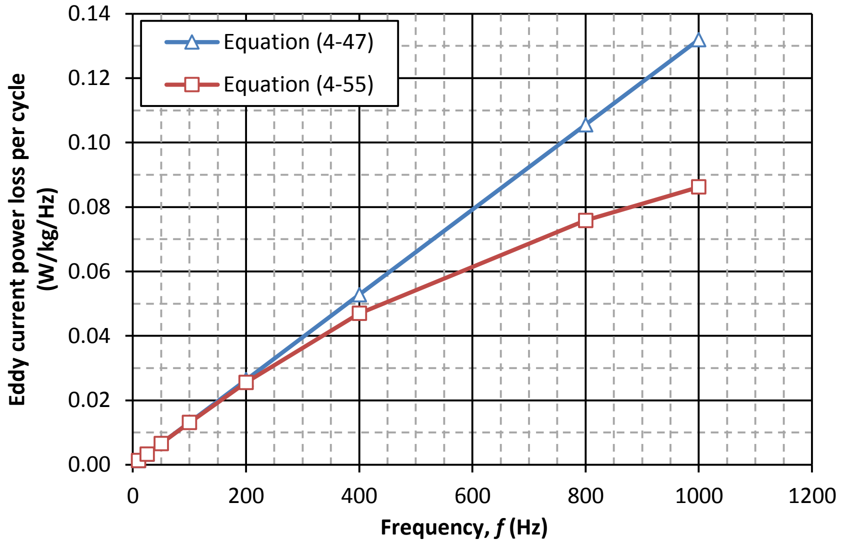

Fig 5-8 Eddy current power loss of an Epstein size lamination at peak flux density of 1.7 T and different magnetising frequencies obtained from the equations (4-47) and (4-55)

The reason is directly related to the skin effect of the eddy current at high frequencies, because in equation (4-47) skin effect was neglected. The uniform flux density distribution along the thickness of the lamination was assumed in (4-47); while in the equation (4-55), skin effect has been considered. On the other hand, from the equation (4-25) and Figs 4-15 and 4-16 it can be concluded that the local hysteresis loop and hence the hysteresis power loss per cycle varies at each point inside the lamination. This variation affects the total hysteresis power loss per cycle, making it dependent on the magnetic field distribution, which is strongly affected by the skin effect and magnetising frequency.

Another conclusion from Fig 5-8 is, at low frequencies both curves are in close agreement but by increasing the frequency the discrepancy between them increases which offers further proof of the frequency dependence of the loss components. Therefore the separation of core loss components by the extrapolation method, assuming constant hysteresis energy loss per cycle, is only valid at low frequencies, where the magnetic field distribution along the lamination is uniform, i.e. when the skin effect is negligible ($a/\delta<<1$). A comparison of the eddy current power loss per cycle versus frequency from equations (4-47) and (4-55) is shown in Fig 5-9 for the same material and peak flux density as Fig 5-8.

Fig 5-9-a shows a close agreement between the results from the equation (4-47) and that of the extrapolation method with the maximum difference less than 0.06 %. On the other hand, Fig 5-9-b shows a close agreement between the eddy current power loss per cycle from the equation (4-55) and the extrapolation method at low frequencies; however the difference between these two values increases by increasing the frequency, where at 1000 Hz the difference is approximately 35 %. Furthermore, the eddy current power loss per cycle from equation (4-47) is a linear function of frequency; but not from equation (4-55). The difference between these two equations is related to the skin effect and flux density distribution along the lamination thickness, which have been considered in equation (4-47), but not in equation (4-55).

5.4. Developed extrapolation method to separate core loss at high frequencies and experimental results

As stated in chapter 5, at low frequencies the induced eddy currents are small and skin effect could be neglected; while at high frequencies, skin effect becomes significant and the peak flux density varies across the lamination thickness. As a consequence, the local ***B-H*** loop and hence the hysteresis power loss per cycle change at any point inside the lamination.

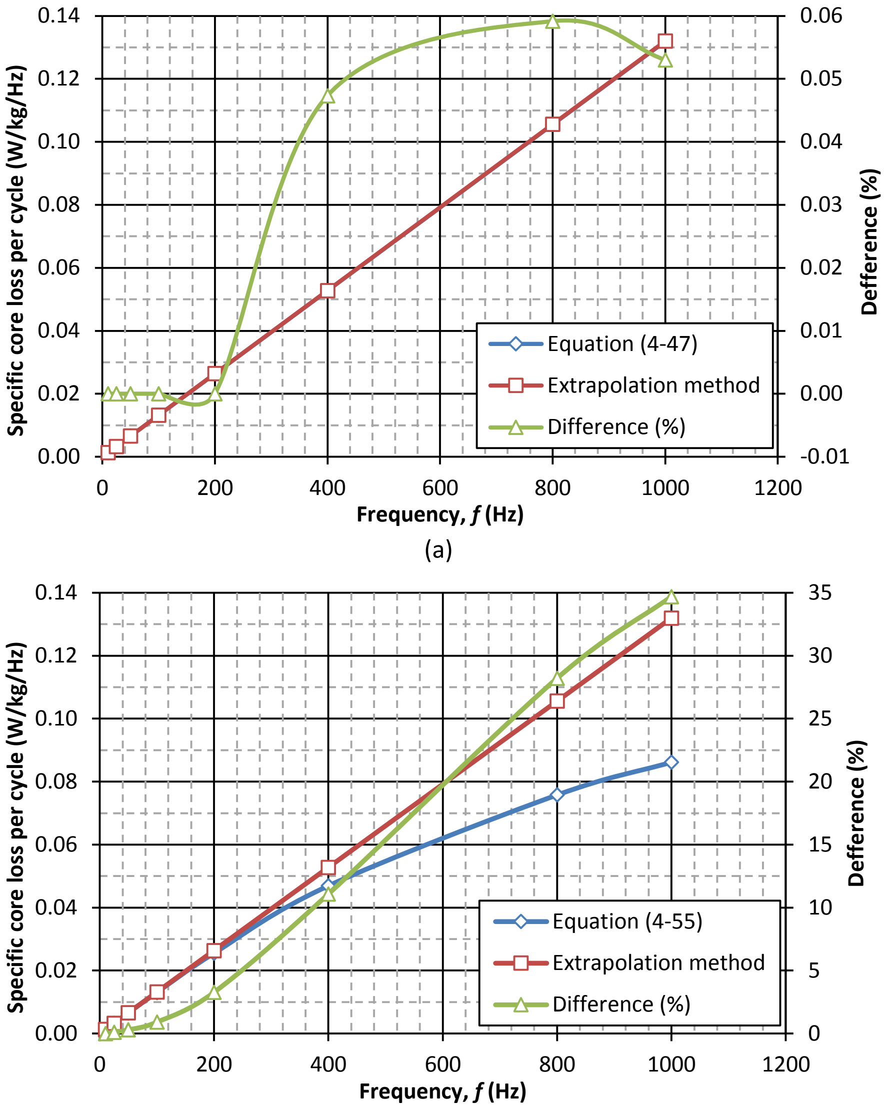

(b)

Fig 5-9 Comparison between eddy current power loss per cycle of an Epstein size lamination of CGO from the extrapolation method and (a) equation (4-47) (b) equation (4-55); at B_{pk}=1.7 T

This change affects the total hysteresis power loss per cycle, making it dependent on the distribution of the magnetic field along the lamination thickness, which is strongly affected by the magnetising frequency [5.7]. Therefore, the separation of core loss components by the extrapolation method, assuming constant hysteresis power loss per cycle, is only valid at low frequencies, where the magnetic field distribution along the lamination is uniform, *i.e.* when the skin effect is negligible. Accurate core loss separation at high frequencies requires taking the non-uniform flux density distribution along the lamination thickness into account.

Based on the extrapolation method, a new experimental-analytical method was developed to separate eddy current power loss from the experimental results accounting for the non-uniform flux density distribution and skin effect at high frequencies. In this method in order to improve the coefficients of the core loss components at high frequencies, the average value of the flux density profile along the lamination thickness, at each frequency and flux density is considered. Therefore a dimensionless correction coefficient (CC) was defined at each particular magnetising frequency and peak flux density as:

$$CC = \frac{B_{av}}{B_s} \tag{5-13}$$

where B_s is the peak flux density at the surface of the lamination and B_{av} is the average value of flux density inside the lamination which is defined by:

$$B_{av} = \frac{1}{2a}\int_{-a}^{a} B(x)\, dx \tag{5-14}$$

where *2a* is thickness of the lamination and *B(x)* is flux density as a function of distance from the centre line of the lamination *x* which was defined by equation (4-25) in chapter 4.

5.4.1. Experimental results of power loss measurement for GO steels

The total power loss of an Epstein sized magnetic lamination of 0.3 mm thick of CGO 3 % *SiFe* at peak flux densities of 1.3 T, 1.5 T, 1.7 T and 1.8 T and magnetising frequencies from 10 Hz to 1000 Hz was measured using the measuring system described in part 5-2. The results are shown in Table 5-4. In order to separate eddy current loss, the correction coefficient was calculated using equations (5-13) and (5-14) at each frequency and flux density. The results are shown in Fig 5-10. The results presented in Fig 5-10 show that the correction coefficient is close to unity at low frequencies and it decreases with increasing frequency.

Table 5-4 Total power loss of an Epstein size lamination of CGO measured by a single strip tester

Magnetising frequency (Hz)	**Total power loss (W/kg)**			
	***B_{pk}*=1.3 T**	***B_{pk}*=1.5 T**	***B_{pk}*=1.7 T**	***B_{pk}*=1.8 T**
10	0.0738	0.1072	0.1731	0.1944
25	0.2442	0.3417	0.5203	0.5720
50	0.6738	0.9457	1.385	1.522
100	1.922	2.611	3.731	4.021
200	5.669	7.720	10.89	11.74
400	17.46	24.38	34.59	37.78
800	57.72	82.81	119.1	130.1
1000	85.65	124.1	178.9	196.2

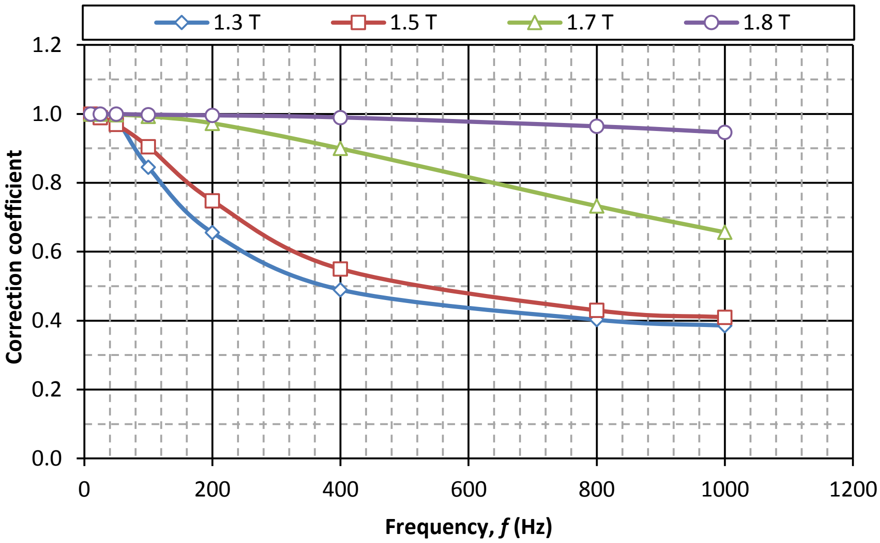

Fig 5-10 Correction coefficient of eddy current power loss of single strip Epstein size lamination of CGO

Based on the new extrapolation method eddy current power loss of the sample was separated at each flux density and frequency and the results were compared with the predicted results obtained by the flowchart of Fig 5-20. Specific core losses per cycle versus square root of frequency, eddy current power losses and a comparison of the analytical and experimental results are shown separately at each flux density in Figs 5-11 to 5-18 and Tables 5-5 to 5-8, respectively.

Comparison between the prediction results from the analytical modelling and the experimental results from the developed extrapolation method show a close agreement with the maximum difference of less than 4 %.

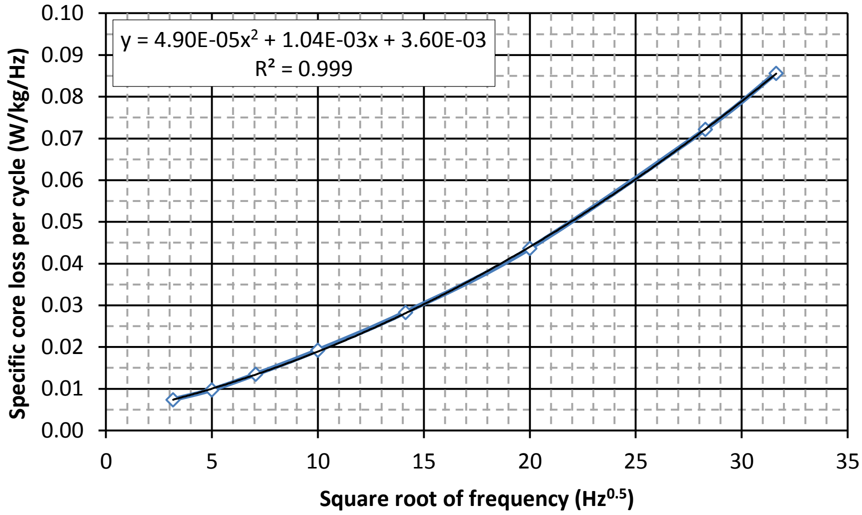

Fig 5-11 Specific core loss per cycle versus square root of frequency of single strip Epstein size lamination of CGO at peak flux density 1.3 T

Table 5-5 Power loss components of an Epstein size lamination of CGO at peak flux density 1.3 T

Frequency (Hz)	***Total measured loss (W/kg)***	***P_{e1} (W/kg)***	***CC***	***$P_{e2}=P_{e1}\times CC$ (W/kg)***	***P_{e3} (W/kg)***	***Difference (%) $(P_{e3}-P_{e2})/P_{e3}$***
10	0.0738	0.0049	1.000	0.0049	0.0051	3.92
25	0.2442	0.0306	1.000	0.0306	0.0315	2.78
50	0.6738	0.1225	0.985	0.1207	0.1209	0.20
100	1.922	0.4900	0.846	0.4145	0.4250	2.46
200	5.669	1.960	0.656	1.285	1.307	1.63
400	17.46	7.840	0.490	3.841	3.970	3.23
800	57.72	31.36	0.403	12.64	13.07	3.30
1000	85.65	49.00	0.386	18.91	19.16	1.28

P_{e1}: From extrapolation method, P_{e2}: From developed extrapolation method, P_{e3}: From modelling

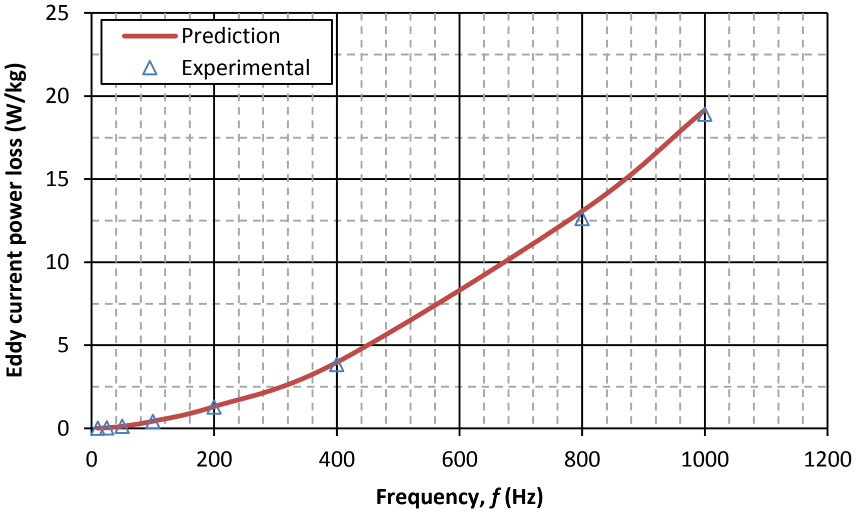

Fig 5-12 Comparison between prediction and experimental results eddy current power loss of single strip Epstein size lamination of CGO at peak flux density 1.3 T

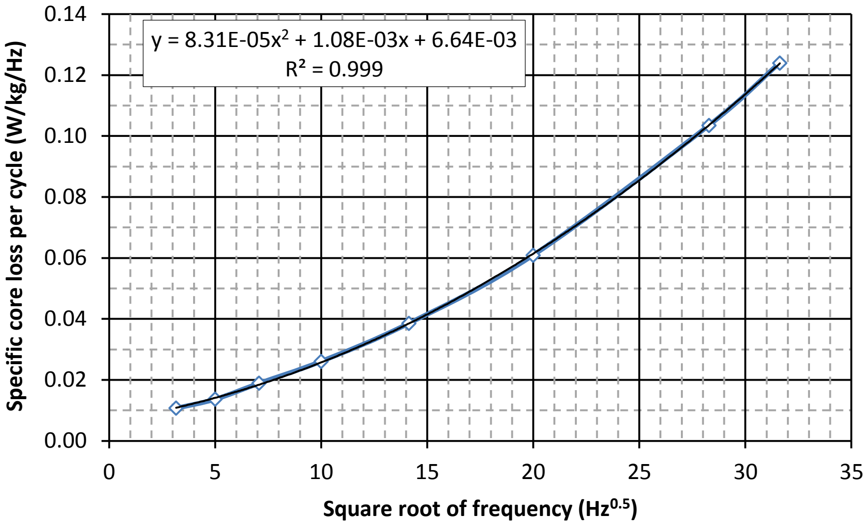

Fig 5-13 Specific core loss per cycle versus square root of frequency of single strip Epstein size lamination of CGO at peak flux density 1.5 T

Table 5-6 Power loss components of an Epstein size lamination of CGO at peak flux density 1.5 T

Frequency (Hz)	***Total measured loss (W/kg)***	***P_{e1} (W/kg)***	***CC***	***$P_{e2}=P_{e1}\times CC$ (W/kg)***	***P_{e3} (W/kg)***	***Difference (%) $(P_{e3}-P_{e2})/P_{e3}$***
10	0.1072	0.0083	1.000	0.0083	0.0083	0.12
25	0.3417	0.0519	0.990	0.0514	0.0517	-0.55
50	0.9457	0.2078	0.970	0.2015	0.2010	0.26
100	2.611	0.8310	0.905	0.7521	0.7400	1.60
200	7.720	3.324	0.748	2.486	2.380	4.28
400	24.38	13.29	0.550	7.313	7.130	2.50
800	82.81	53.18	0.430	22.87	22.91	-0.18
1000	124.0	83.10	0.410	34.07	33.72	1.03

P_{e1}: From extrapolation method, P_{e2}: From developed extrapolation method, P_{e3}: From modelling

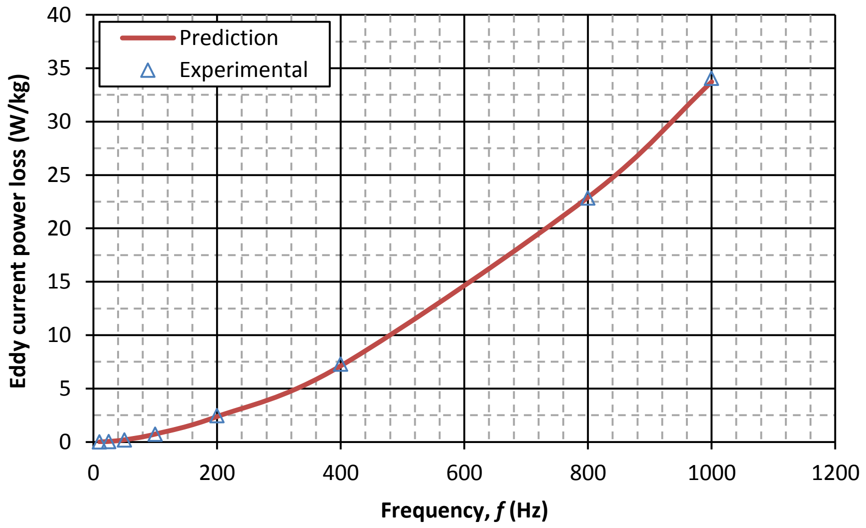

Fig 5-14 Comparison between prediction and experimental results eddy current power loss of single strip Epstein size lamination of CGO at peak flux density 1.5 T

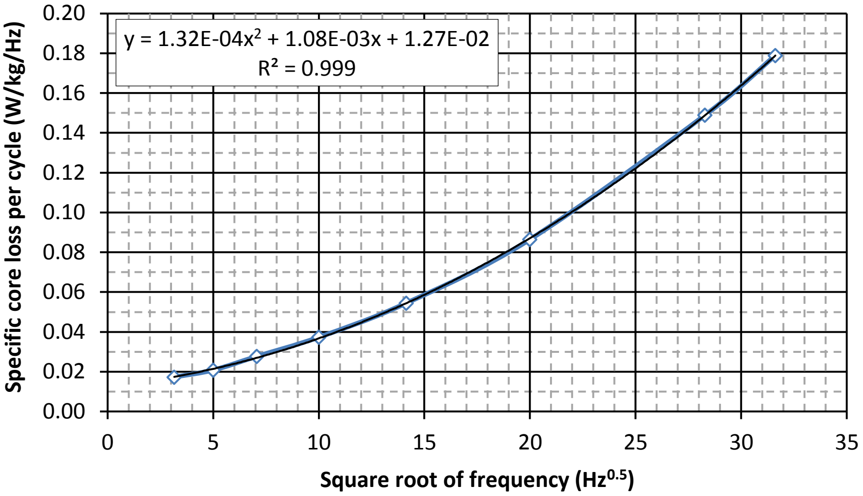

Fig 5-15 Specific core loss per cycle versus square root of frequency of single strip Epstein size lamination of CGO at peak flux density 1.7 T

Table 5-7 Power loss components of an Epstein size lamination of CGO at peak flux density 1.7 T

Frequency (Hz)	***Total measured loss (W/kg)***	***P_{e1} (W/kg)***	***CC***	***$P_{e2}=P_{e1}\times CC$ (W/kg)***	***P_{e3} (W/kg)***	***Difference (%) $(P_{e3}-P_{e2})/P_{e3}$***
10	0.1731	0.0132	1.00	0.0132	0.0132	0.00
25	0.5203	0.0825	1.00	0.0825	0.0824	0.12
50	1.385	0.3300	0.998	0.3293	0.3290	0.10
100	3.731	1.320	0.993	1.311	1.308	0.21
200	10.89	5.280	0.973	5.138	5.107	0.61
400	34.59	21.12	0.900	19.06	18.78	1.47
800	119.1	84.48	0.733	62.52	60.65	2.98
1000	178.9	132.0	0.657	89.76	86.21	3.96

P_{e1}: From extrapolation method, P_{e2}: From developed extrapolation method, P_{e3}: From modelling

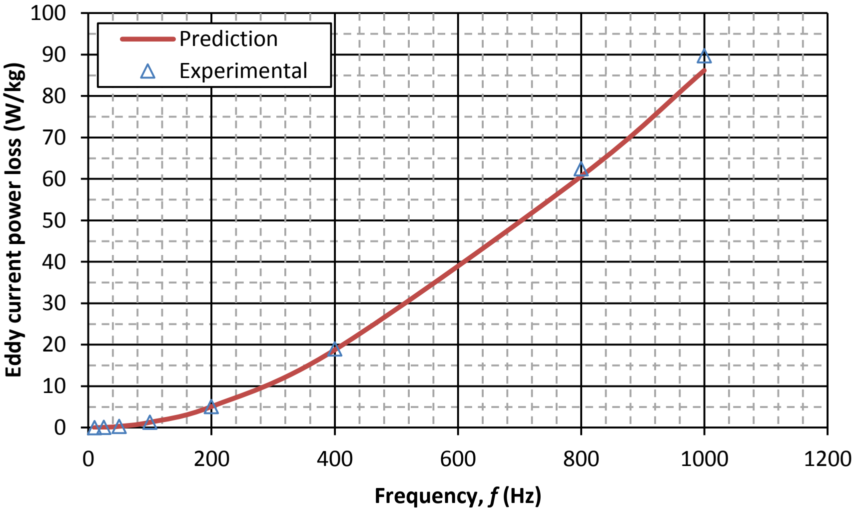

Fig 5-16 Comparison between prediction and experimental results eddy current power loss of single strip Epstein size lamination of CGO at peak flux density 1.7 T

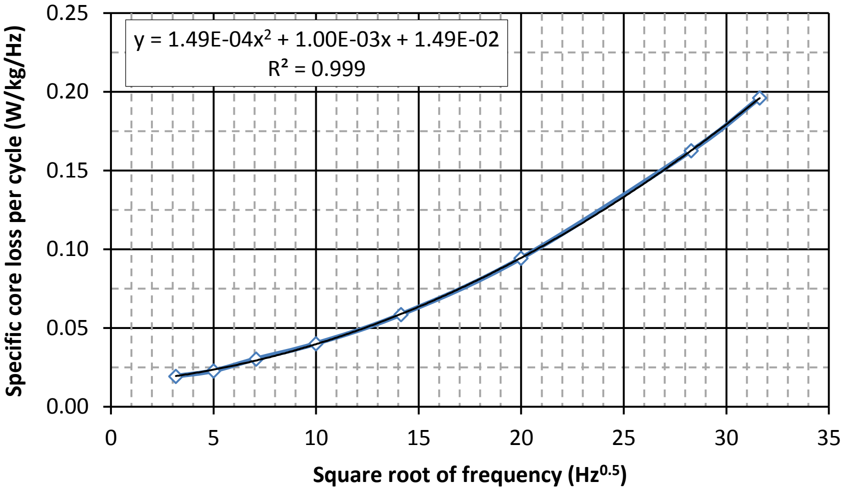

Fig 5-17 Specific core loss per cycle versus square root of frequency of single strip Epstein size lamination of CGO at peak flux density 1.8 T

Table 5-8 Power loss components of an Epstein size lamination of CGO at peak flux density 1.8 T

Frequency (Hz)	***Total measured loss (W/kg)***	***P_{e1} (W/kg)***	***CC***	***$P_{e2}=P_{e1}\times CC$ (W/kg)***	***P_{e3} (W/kg)***	***Difference (%) $(P_{e3}-P_{e2})/P_{e3}$***
10	0.1944	0.0149	1.00	0.0149	0.0150	0.40
25	0.5720	0.0934	1.00	0.0934	0.0940	0.66
50	1.522	0.3735	1.00	0.3735	0.3759	0.64
100	4.021	1.494	0.998	1.491	1.503	0.80
200	11.74	5.976	0.996	5.952	5.990	0.63
400	37.78	23.90	0.990	23.66	23.79	0.52
800	130.1	95.62	0.964	92.20	92.22	0.02
1000	196.2	149.4	0.947	141.4	140.9	-0.36

P_{e1}: From extrapolation method, P_{e2}: From developed extrapolation method, P_{e3}: From modelling

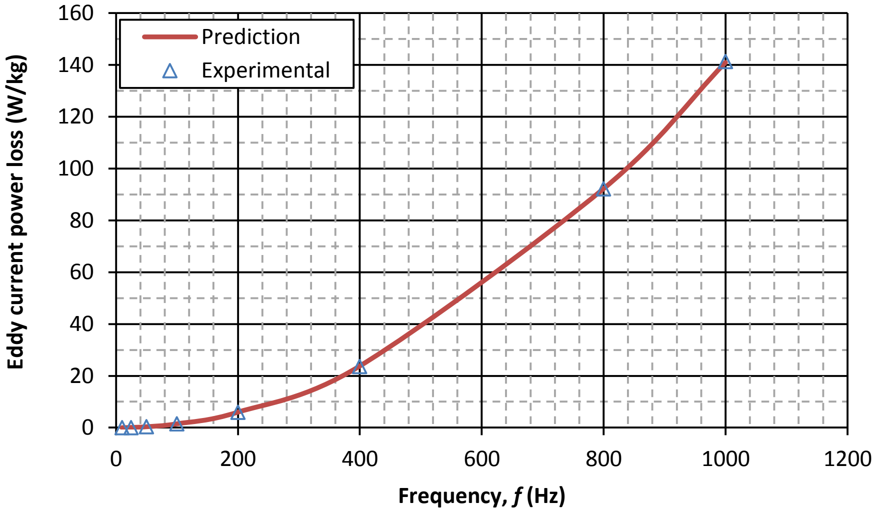

Fig 5-18 Comparison between prediction and experimental results eddy current power loss of single strip Epstein size lamination of CGO at peak flux density 1.8 T

In section 5.2.3 the eddy current power loss per cycle from equations (4-47) and (4-55) was compared with the result from the extrapolation method; the results of the comparison are shown in Fig 5-9. A comparison of the developed extrapolation method and the analytical method based on the flowchart of Fig 5-20 at a peak flux density of 1.7 T is shown in Fig 5-19.

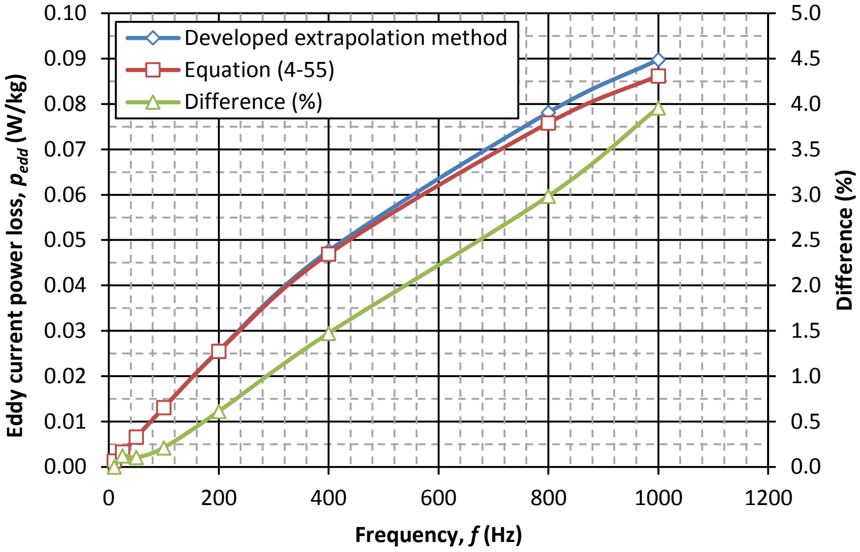

Fig 5-19 Eddy current power loss per cycle of an Epstein size lamination at peak flux density 1.7 T from equation (4-55) and the developed extrapolation method

Fig 5-19 shows a close agreement between the results of the analytical modelling and the developed extrapolation method at all frequencies with the maximum difference of less than 4 % at a magnetising frequency of 1000 Hz. Therefore the analytical and experimental methods which have been developed in this project are sufficiently accurate and reliable to calculate and separate eddy current power loss of the magnetic laminations in a wide range of frequency and flux density.

5.4.2. Experimental results of power loss measurement for NO steel

A similar investigation to that discussed in section 5.4.1 was carried out on an Epstein sized lamination of 0.5 mm thick Non-oriented steel. Total power losses measured by single strip tester at flux densities of 1.1 T, 1.3 T and 1.5 T and magnetising frequencies from 10 Hz to 1000 Hz are shown in Table 5-9.

Table 5-9 Total power loss of an Epstein size lamination of Non-oriented measured by single strip tester

Magnetising frequency (Hz)	Total power loss (W/kg)		
	B_{pk}=1.1 T	B_{pk}=1.3 T	B_{pk}=1.5 T
10	0.352	0.477	0.659
25	0.992	1.35	1.82
50	2.32	3.19	4.38
100	5.81	8.32	11.5
200	16.2	23.8	33.9
400	49.9	76.1	111
800	166	256	360
1000	249	381	545

The eddy current power loss of the sample was separated at each flux density and frequency based on the developed extrapolation method and the results were compared with the prediction results from equation (4-55) and the flowchart of Fig 5-20. Correction coefficients of eddy current power loss versus frequency at different flux densities are shown in Fig 5-20. Specific core losses per cycle versus the square root of frequency, eddy current power losses and a comparison between the analytical and experimental results, separately for each flux density, are shown in Figs 5-21 to 5-26 and Tables 5-10 to 5-12.

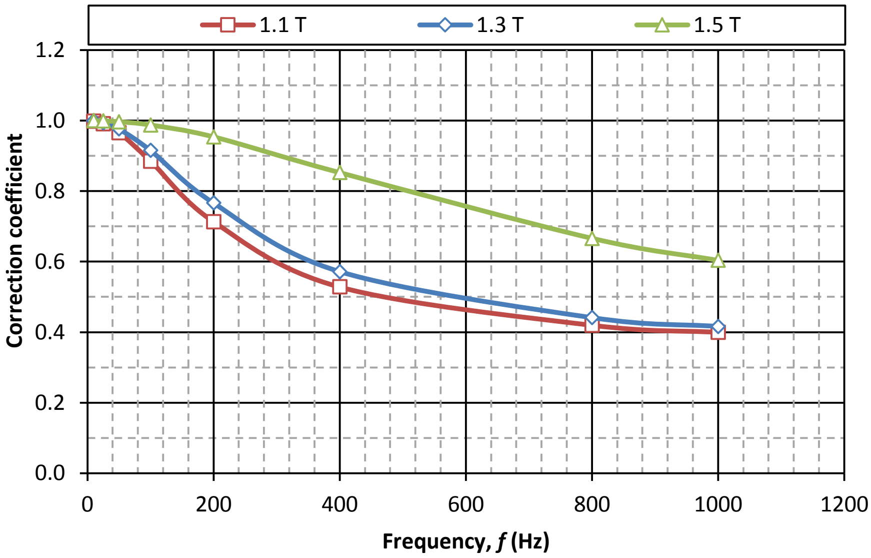

Fig 5-20 Correction coefficient of eddy current power loss of single strip Epstein size lamination of Non-oriented

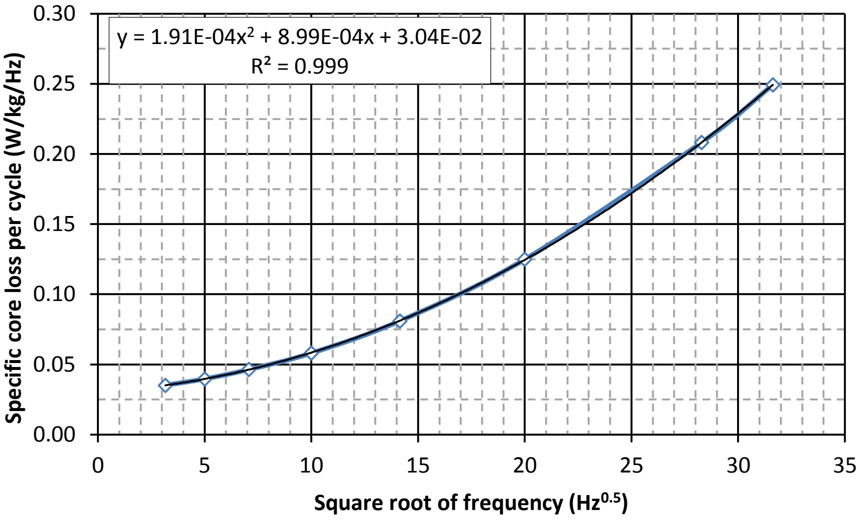

Fig 5-21 Specific core loss per cycle versus square root of frequency of single strip Epstein size lamination of NO at peak flux density 1.1 T

Table 5-10 Power loss components of an Epstein size lamination of NO at peak flux density 1.1 T

Frequency (Hz)	***Total measured loss (W/kg)***	***P_{e1} (W/kg)***	***CC***	***$P_{e2}=P_{e1}\times CC$ (W/kg)***	***P_{e3} (W/kg)***	***Difference (%) $(P_{e3}-P_{e2})/P_{e3}$***
10	0.352	0.019	0.999	0.019	0.020	2.69
25	0.992	0.119	0.991	0.118	0.121	2.47
50	2.32	0.478	0.966	0.461	0.473	2.50
100	5.81	1.91	0.885	1.69	1.73	2.45
200	16.2	7.64	0.713	5.45	5.52	1.18
400	49.9	30.6	0.528	16.1	16.3	1.10
800	166	122	0.420	51.4	52.2	1.71
1000	249	191	0.400	76.4	78.2	2.30

P_{e1}: From extrapolation method, P_{e2}: From developed extrapolation method, P_{e3}: From modelling

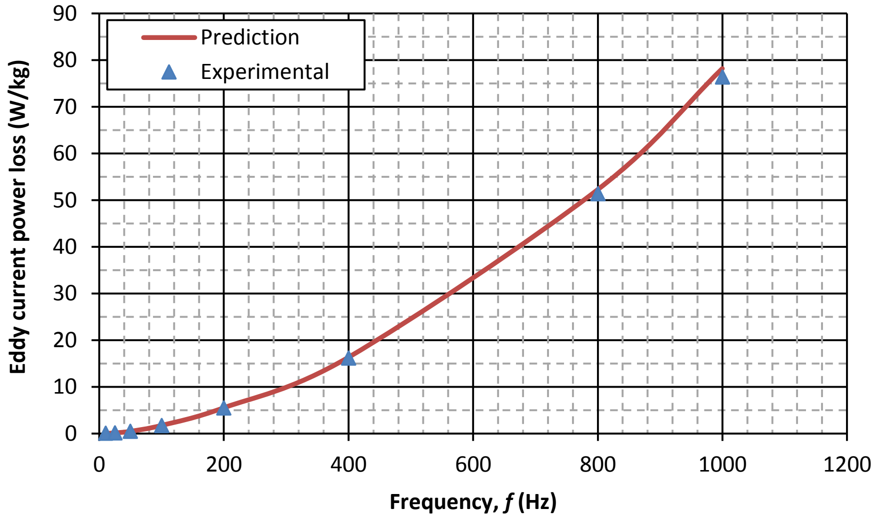

Fig 5-22 Comparison between prediction and experimental results eddy current power loss of single strip Epstein size lamination of NO at peak flux density 1.1 T

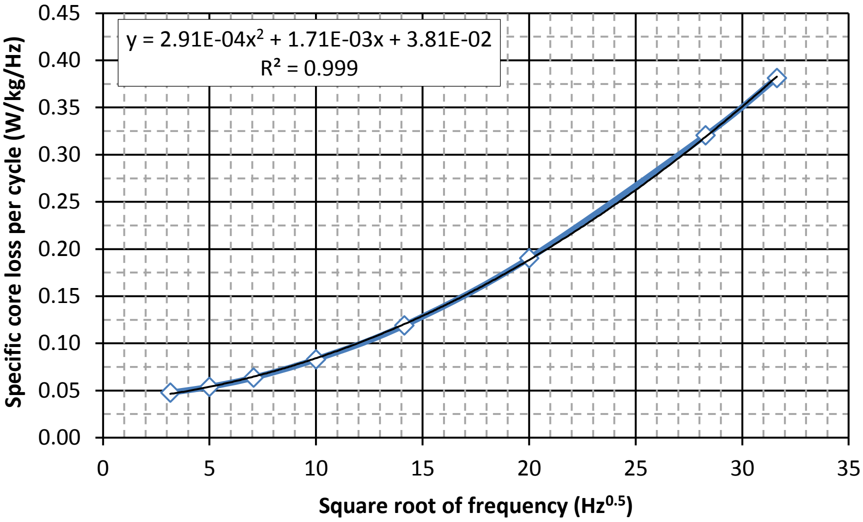

Fig 5-23 Specific core loss per cycle versus square root of frequency of single strip Epstein size lamination of NO at peak flux density 1.3 T

Table 5-11 Power loss components of an Epstein size lamination of NO at peak flux density 1.3 T

Frequency (Hz)	***Total measured loss (W/kg)***	***P_{e1} (W/kg)***	***CC***	***$P_{e2}=P_{e1}\times CC$ (W/kg)***	***P_{e3} (W/kg)***	***Difference (%) $(P_{e3}-P_{e2})/P_{e3}$***
10	0.477	0.029	0.999	0.029	0.029	1.12
25	1.35	0.182	0.994	0.181	0.181	0.25
50	3.19	0.728	0.976	0.710	0.721	1.53
100	8.32	2.91	0.915	2.66	2.72	2.03
200	23.8	11.6	0.766	8.92	8.94	0.22
400	76.1	46.6	0.572	26.7	26.7	0.20
800	256	186	0.441	82.2	84.1	2.33
1000	381	291	0.416	121	123	1.68

P_{e1}: From extrapolation method, P_{e2}: From developed extrapolation method, P_{e3}: From modelling

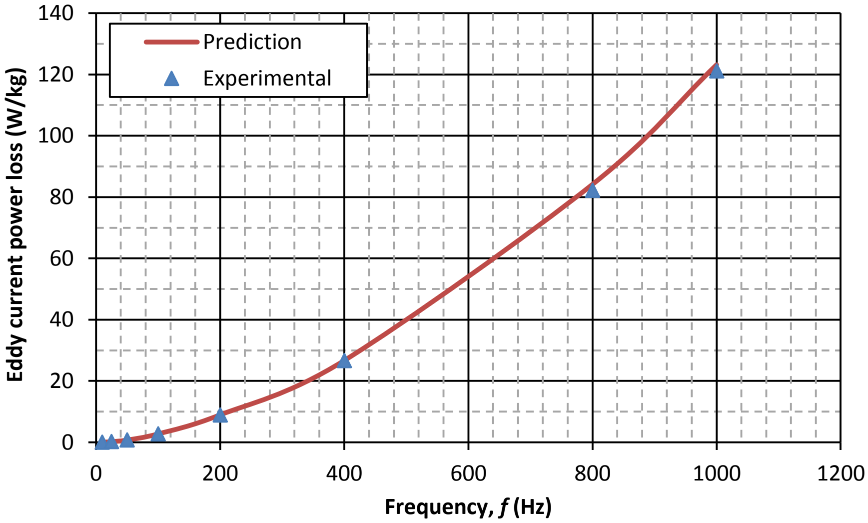

Fig 5-24 Comparison between prediction and experimental results eddy current power loss of single strip Epstein size lamination of NO at peak flux density 1.3 T

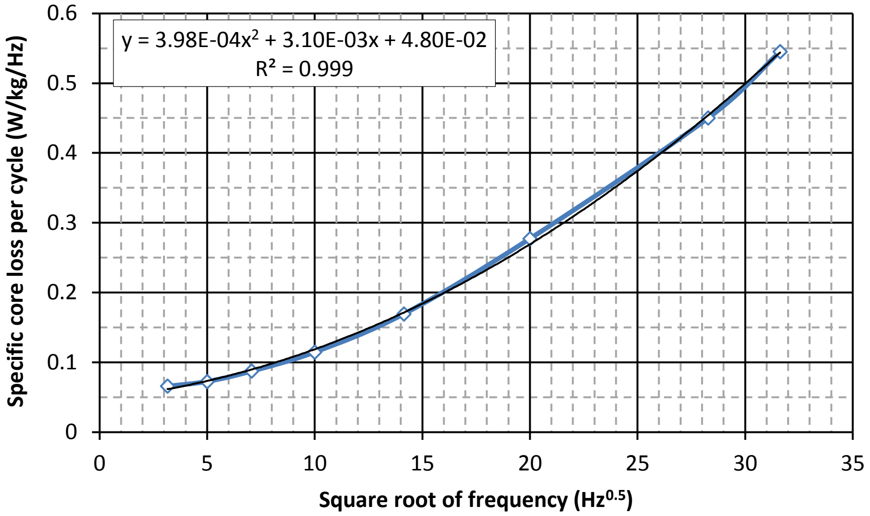

Fig 5-25 Specific core loss per cycle versus square root of frequency of single strip Epstein size lamination of NO at peak flux density 1.5 T

Table 5-12 Power loss components of an Epstein size lamination of NO at peak flux density 1.5 T

Frequency (Hz)	***Total measured loss (W/kg)***	***P_{e1} (W/kg)***	***CC***	***$P_{e2}=P_{e1}\times CC$ (W/kg)***	***P_{e3} (W/kg)***	***Difference (%) $(P_{e3}-P_{e2})/P_{e3}$***
10	0.659	0.040	1.00	0.040	0.040	0.51
25	1.82	0.249	0.999	0.249	0.250	0.54
50	4.38	0.995	0.997	0.992	0.997	0.52
100	11.5	3.98	0.988	3.93	3.95	0.39
200	33.9	15.9	0.954	15.2	15.2	-0.09
400	111	63.7	0.853	54.3	53.5	-1.50
800	360	254	0.666	169	165	-3.09
1000	545	398	0.604	240	234	-2.88

P_{e1}: From extrapolation method, P_{e2}: From developed extrapolation method, P_{e3}: From modelling

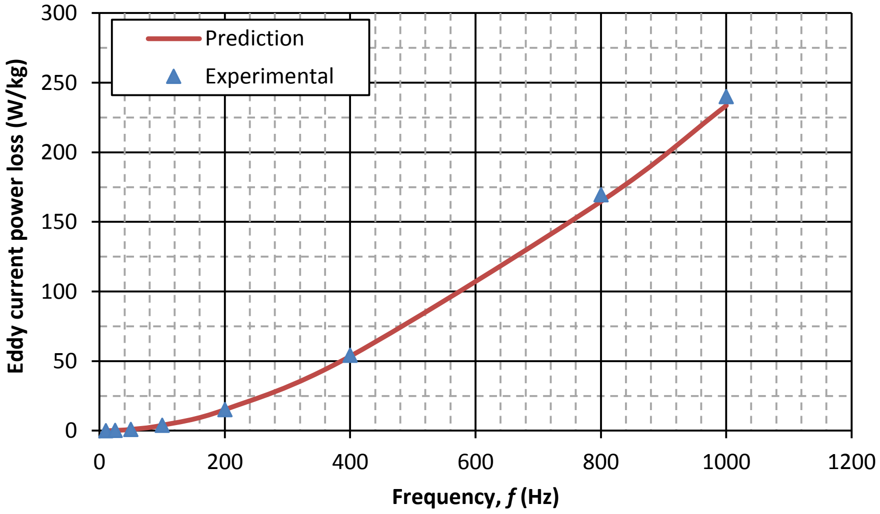

Fig 5-25 Comparison between prediction and experimental results eddy current power loss of single strip Epstein size lamination of NO at peak flux density 1.5 T

5.4.3. Discussion

As a final investigation on this work, comparison of the correction coefficients (CC) of eddy current power loss at different flux densities, led to an interesting result. The results presented in Fig 5-10 for GO steel and 5-20 for NO steel show that the correction coefficient is close to unity at low frequencies and decreases by increasing the magnetising frequency; however the rate of decrease varies with the amplitude of the flux density. As an example the final value of CC of GO steel at 1.3 T is 0.386 while this value at 1.8 T is 0.946. Considering the definition of CC from equations (5-13) and (5-14), the variations of the curves of Figs 5-10 and 5-20 can be explained by the flux density distribution inside the lamination. Using equation (5-25) and based on the flowchart of Fig 5-11, flux density distributions along the lamination thickness, typically at magnetising frequency of 1000 Hz, and peak flux densities of 1.3 T, 1.5 T, 1.7 T and 1.8 T for the GO steel and peak flux densities of 1.1 T, 1.3 T and 1.5 T for NO steel were calculated. The results are shown in Figs 5-27-a and 5-27-b, respectively.

Fig 5-27 proves that at a specific frequency, the flux density distribution along the lamination, and hence skin depth, depends on the flux density amplitude itself. For example for the GO steel at 1.3 T, as a high permeability point, flux density distributes extremely non-uniformly, while at 1.8 T, as a low permeability point, flux density distributes almost uniformly. Obviously this phenomenon is directly related to the skin effect which is affected by the non-linear relation of ***B-H***. From the equation of the skin depth $\delta = 1/\sqrt{\pi\mu_0\mu_z f\sigma}$, for a given material at a specific frequency, the only parameter that could vary with flux density is the relative permeability of the material. In part 4.4 of chapter 4 it was shown that the relative permeability of the electrical steels varies with peak flux density. Considering this variation, skin effect at a specific frequency, varies with peak flux density.

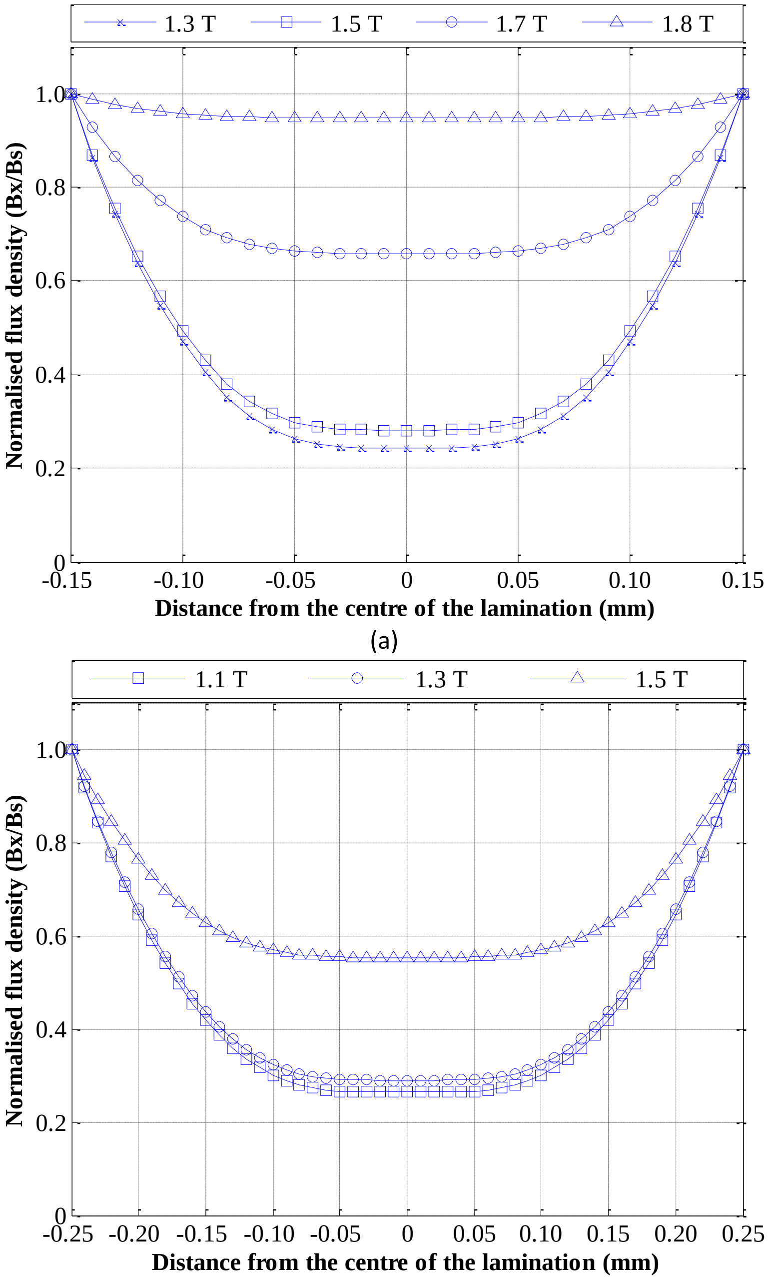

(a)

(b)

Fig 5-27 Flux density distribution along the thickness of the lamination at 1000 Hz and different flux densities (a) GO steel of 0.3 mm thickness (b) NO steel of 0.5 mm thickness

Variations of skin depth at different frequencies from 50 Hz up to 10 kHz together with relative permeability of the material versus peak flux density for the GO and NO steels are shown in Figs 5-28-a and 5-28-b, respectively. These figures show significant skin effect at high values of permeabilities; however this effect becomes negligible at low permeabilities, at low flux densities and near saturation.

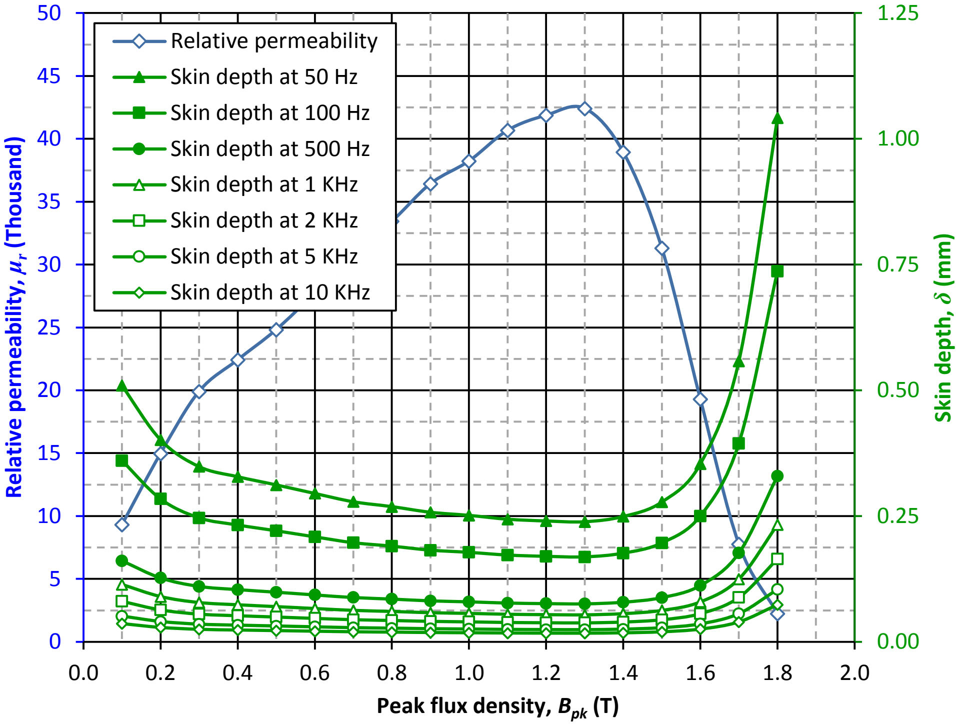

(a)

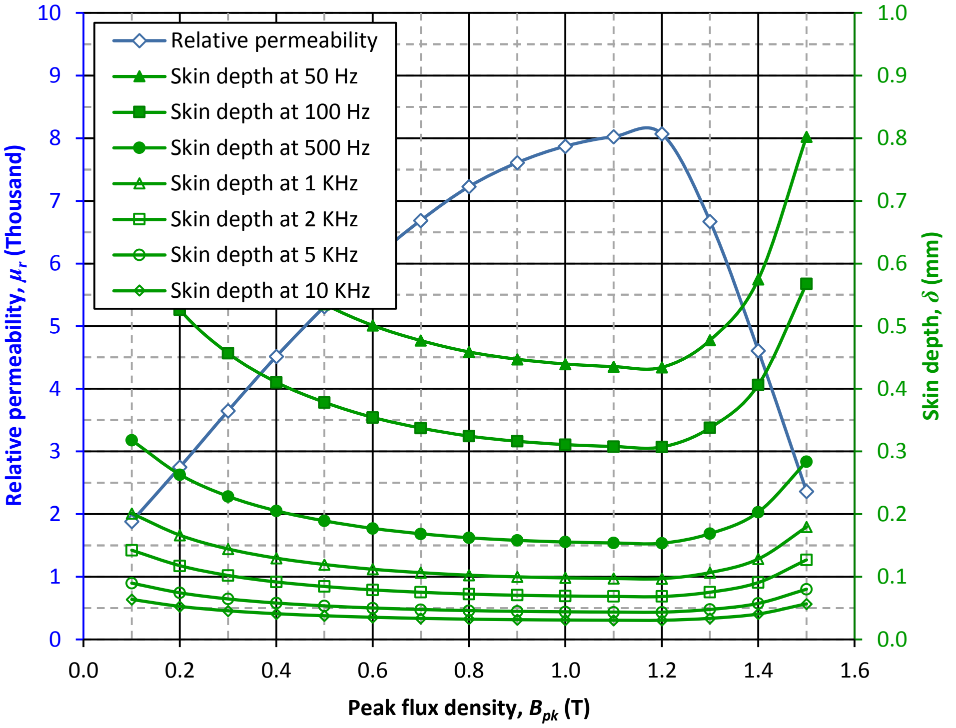

(b)

Fig 5-28 Effect of flux density on magnetic relative permeability and skin depth of the magnetic material at magnetising frequencies from 50 Hz up to 10 kHz
(a) GO steel of 0.3 mm thickness (b) NO steel of 0.5 mm thickness

The results represented in Fig 5-28 shows that relative permeability of the material makes a significant effect on the skin depth of eddy current; and that at each magnetising frequency skin depth increases at high flux densities. According to (5-13) and (5-14) the correction coefficient of eddy current loss is based on the flux density distribution of Figs 5-15 and 5-16 which is related to the impact of skin effect. As shown in Fig 5-28 at peak flux densities corresponding to high permeabilities, the impact of skin effect is more significant; while at low permeabilities at low flux densities and near saturation, the impact of skin effect is less. Furthermore as depicted in Figs 5-10 and 5-20, at each particular frequency, the correction coefficient at high permeability points is lower than its value at low permeability points. Therefore based on the results represented in Figs 5-10, 5-20, 5-27 and 5-28, at each particular frequency a similar variation rate is expected for CC curves and skin depth versus peak flux density. These characteristics were calculated at two particular frequencies 400 Hz and 1 kHz and flux densities of 1.3 T, 1.5 T and 1.7 T for the GO steel and 1.1 T, 1.3 T and 1.5 T for the NO steel. The results are shown in Figs 5-29-a and 5-29-b, respectively.

As expected, at each frequency the increasing rate of both skin depth and CC curves are similar, therefore it could be concluded that the correction coefficient of eddy current power loss is a function of skin depth, while the skin depth of the material varies with magnetising frequency, relative permeability and amplitude of peak flux density. Based on the above mentioned concepts, a significant difference between the prediction and extrapolation results (without applying CC) at low flux densities and negligible difference at high flux densities is expected. Table 5-13 shows these values for the GO steel, typically at 1.3 T and 1.8 T.

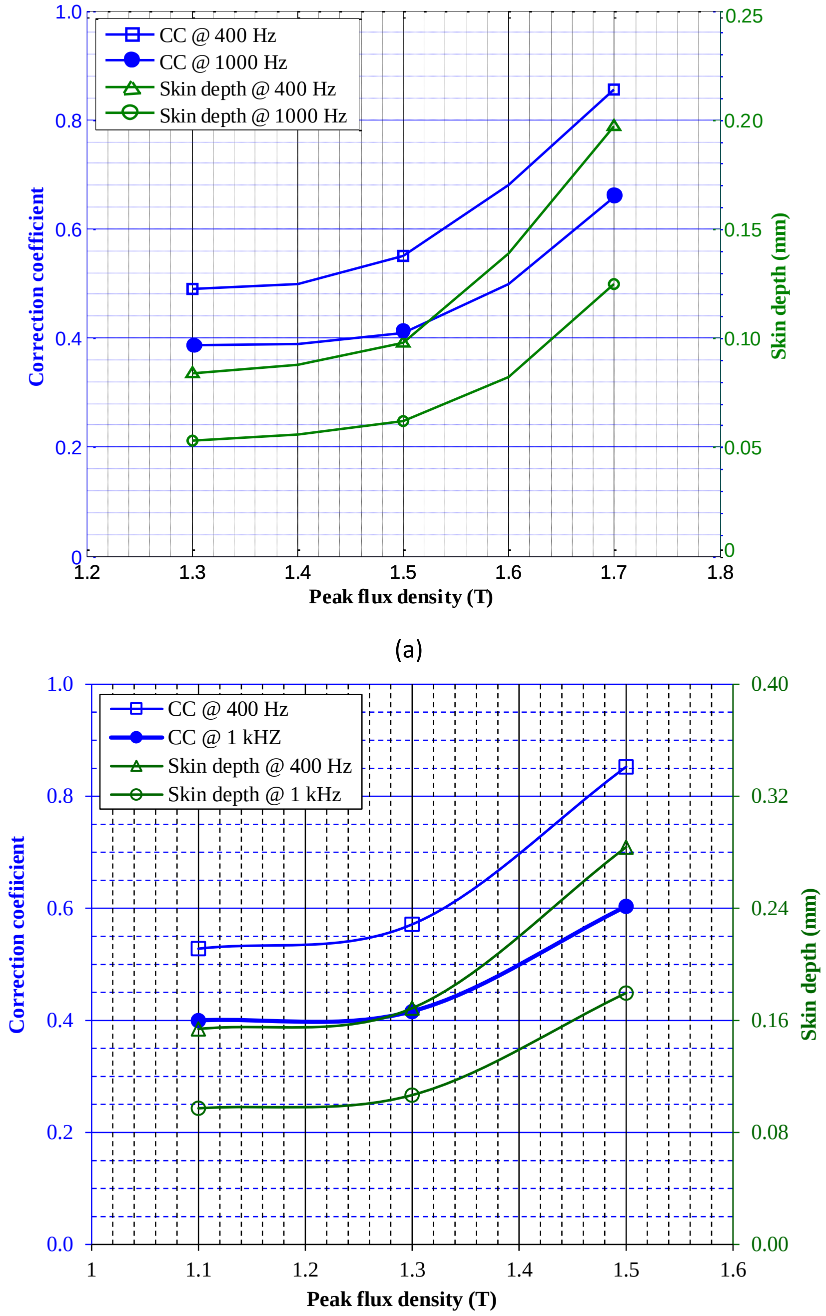

(a)

(b)

Fig 5-29 Comparison of correction coefficient of eddy current power loss and skin depth versus peak flux density at 400 Hz and 1 kHz (a) GO steel of 0.3 mm thickness (b) NO steel of 0.5 mm thickness

Table 5-13 Extrapolation and prediction results of eddy current power loss of an Epstein size lamination of CGO at peak flux densities 1.3 T and 1.8 T

Magnetising frequency (Hz)	***B_{pk}=1.3 T***			***B_{pk}=1.8 T***		
	Eddy current power loss (W/kg)		***Difference†† (%)***	***Eddy current power loss (W/kg)***		***Difference†† (%)***
	Extrapolation method†	***Prediction***		***Extrapolation method†***	***Prediction***	
10	0.0049	0.0051	-4.08	0.0149	0.0150	-0.671
25	0.0306	0.0315	-2.86	0.0931	0.0940	-0.940
50	0.1225	0.1209	1.31	0.3725	0.3759	-0.913
100	0.4900	0.4250	13.3	1.490	1.503	-0.872
200	1.960	1.307	33.3	5.960	5.990	-0.503
400	7.840	3.970	49.4	23.84	23.79	0.210
800	31.36	13.07	58.3	95.36	92.22	3.29
1000	49.00	19.16	60.9	149.00	140.9	5.41

† Primary results without applying the correction coefficient

†† Based on the Extrapolation results

The results shown in Table 5-13 agree with the preliminary expectation. These results show that the maximum difference between the prediction and extrapolation results (without applying CC) at 1.3 T is 60.9 % while at 1.8 T is 5.41 %.

5.5. Conclusion

In this chapter the eddy current power loss model of chapter 5 was implemented to predict eddy current power loss of magnetic laminations in a wide range of magnetising frequency and peak flux density. In order to support the analytical results, extrapolation method was developed to separate eddy current power loss from the measured total loss. Two different materials, conventional grain oriented (CGO) and non-oriented (NO), were used in the analytical modelling and experimental works.

Under low magnetising frequencies, a close agreement was found between the analytical and experimental results. However, significant discrepancies were found between the analytical and the experimental results at high frequency magnetisation. The difference is related to the skin effect of eddy current at high frequencies because in the modelling this effect and its impacts were considered while in the extrapolation method skin effect is neglected and uniform flux density distribution is assumed at all frequencies. Therefore in order to develop the extrapolation method to high frequencies, a dimensionless correction coefficient was defined based on the flux density distribution along the thickness of the lamination in the loss separation. A close agreement with the maximum difference of less than 4 % was found between the prediction results from the analytical modelling and the experimental results from the developed method.

Based on the analytical modelling it was found that determination of eddy current power loss and separation of loss components in a wide range of magnetising frequency and peak flux density depend on the hysteresis relation between ***B*** and ***H***, non-uniform flux density distribution and complex relative permeability; in which the last two factors are related to skin effect. The results highlighted that magnetising frequency and peak flux density are two determinant factors with significant effect on the magnetic properties of electrical steels and should be taken into account in the relevant studies of the magnetic properties of magnetic core.

References:

[5.1] Y Chen and P Pillay, "*An Improved Formula for Lamination Core Loss Calculations in Machines Operating With High Frequency and High Flux Density Excitation*," IEEE 37th IAS Annual Meeting, Vol. 2, pp. 759–766, 13-18 Oct 2002

[5.2] A Bermúdez, D Gómez and P Salgado, "*Eddy-Current Losses in Laminated Cores and the Computation of an Equivalent Conductivity*", IEEE Trans Magn Vol. 44, NO. 12, DECEMBER 2008, pp 4730-4738

[5.3] S Somkun, "*Magnetostriction and Magnetic Anisotropy in Non-oriented Electrical Steels and Stator Core Laminations*", PhD Thesis, Cardiff University, United Kingdom, 2005

[5.4] BS EN 10280:2001 + A1:2007, *Magnetic Materials - Methods of Measurement of the Magnetic Properties of Electrical Sheet and Strip by Means of a Single Sheet Tester*, British Standard, 2007

[5.5] UKAS M3003, "*The Expression of Uncertainty and Confidence in Measurement*", 1997

[5.6] T L Mthombeni and P Pillay, "*Physical Basis for the Variation of Lamination Core Loss Coefficients as a Function of Frequency and Flux Density*" in Proc. IECON, Paris, Nov. 6–10, 2006, pp. 1381-1387

[5.7] M Ibrahim and P Pillay, "*Advanced Testing and Modelling of Magnetic Materials Including a New Method of Core Loss Separation for Electrical Machines* "IEEE Transactions On Industry Applications, VOL. 48, NO. 5, Sep/Oct 2012 , pp. 1507 - 1515

[5.8] G Bertotti, "*General Properties of Power Losses in Soft Ferromagnetic Materials*," IEEE Trans Magn Vol. 24, January1988 pp. 621-630

[5.9] D M Ionel, M Popescu, S J Dellinger, T J E Miller, R J Heideman and M I McGilp, "*On The Variation With Flux And Frequency Of Core Loss Coefficients In Electrical Machine*", IEEE Trans. Magn Vol. 42, No. 3, pp. 658-666, May/June 2006

CHAPTER 6

Modelling and Analysis of Eddy Current Power Loss of Magnetic Cores Affected By Inter-Laminar Faults and Experimental Results

6.1. Introduction

The design and operation of electrical machines, i.e. generators, motors and transformers, requires accurate quantification of core losses over a wide range of frequency and magnetic flux density by taking into account critical circumstances. One of the major critical circumstances in electrical machines is inter-laminar fault between the laminations of the magnetic cores and its effects on the power loss and other magnetic properties.

In this chapter based on the resistive equivalent circuit of single strip lamination, developed in chapter 5, an equivalent configuration of magnetic laminations affected by inter-laminar faults is discussed. The effect of inter-laminar faults on the eddy current distribution and eddy current power loss of the magnetic cores over a wide range of magnetising frequency are also investigated by focusing on the skin effect and its consequences. 2-D FEM simulations were performed using COMSOL Multiphysics to visualise the eddy current distribution in the shorted laminations to help the modelling of the eddy current power loss in the magnetic cores with inter-laminar faults. In the experimental part of this investigation, packs of two, three and four Epstein sized laminations of conventional grain oriented (CGO) were shorted together artificially by melting lead-free solder to measure the extra eddy current power loss caused by the inter-laminar fault and support the analytical modelling. The extrapolation method from chapter 6, was used to separate eddy current power loss of each pack from the experimental measurements over a wide frequency range and compare to the analytical results.

6.2. Causes of inter-laminar core faults

As stated earlier, magnetic cores of electrical machines are constructed from laminations of electrical steel material alloyed with silicon to minimise the hysteresis and eddy current losses and achieve high efficiency operation [6.1]. Magnetic laminations are isolated from each other using insulating materials to prevent electrical conduction between them and restrict the circulation of eddy currents [6.2]. However since the materials used for the inter-laminar insulation are susceptible to decline and damage, short circuits between the laminations due to electrical failure could happen due to a number of reasons (It should be noted that, because of different structure of magnetic circuit of stator cores of rotary machines and transformer cores, causes of inter-laminar faults might be different for stator and transformer cores) as follow [6.3]–[6.5]:

- Manufacturing defects in laminations, known as edge burrs.
- Surface coating defects (poor inter-laminar insulation coating).
- Mechanical damage on the sides of the stacks during assembly, winding and inspections.
- Foreign particles introduced during assembly, inspection, and repair.

- Heat and chemical factors or mechanical forces applied when stripping windings during rewind.
- Stator-rotor rubs during assembly and operation (in rotary machines).
- Vibration of loose windings and laminations.
- Arcing from winding failure.

Inter-laminar faults created by one of the reasons above, lead to circulating eddy currents between the defected laminations, which are larger than in normal operation [6.5]-[6.7]. This current is the *inter-laminar fault current* and the created current loop is the *fault current loop* [6.8]. Typically fault current loops are formed between the shorted laminations and fault points which are perpendicular to the direction of the flux density in the core. Inter-laminar faults, which lead to the inter-laminar fault currents, are one of the main concerns at the design and manufacturing of the electrical machines and other magnetic devices [6.8]-[6.14].

6.2.1. Concept of edge burr as a source of inter-laminar faults

Since the magnetic laminations are coated with insulation material on either side to prevent electrical conduction between them; the probability of inter-laminar fault between the laminations in the heart of the cores is very low; so usually that possibility is not considered in the studies of inter-laminar faults [6.15]. However during manufacturing of the magnetic cores, punching and cutting of the electrical steels to the required dimensions might cause microscopic burrs which are one of the most serious concerns of the manufacturers and customers of electrical steels [6.11]-[6.14]. Burrs are most commonly created after machining operations, such as grinding, drilling, milling, engraving or turning [6.16]. However in manufacturing of the magnetic cores, punching and cutting are two major machining operations which cause burr at the cut edges or around the punched holes and could lead to inter-laminar short circuits between the laminations [6.11]-[6.14].

“Cutting processes are those in which a piece of sheet metal is separated by applying a great enough force to cause the material to fail” [6.17]. Usually cutting processes are performed by applying a shearing force to the sheet metal, and therefore they are sometimes known as shearing processes. By applying a large enough shearing force to the sheet metal, the applied force will exceed the maximum sustainable shear strength of the metal and will separate it at the cut location. Shearing forces are usually applied by two tools, to the top and the bottom of the steel sheet. These tools could be the punch and die of a punching machine or the upper and lower blades of a guillotine. The top tool applies a quick downward force to the sheet metal which settles over the bottom tool. A small gap between the top and bottom tools is necessary to facilitate the fracture of the material [6.17].

When the shear tools are not sharp enough, mechanical deformation appears at the edges which is capable to make high burrs at the edges. Burrs are formed in various machining process as a result of plastic deformation during mechanical manufacturing process and have been defined as “undesirable projections of material beyond the edge of a workpiece” [6.19]. Figs 6-1-a to 6-1-c show the different stages of cutting a lamination and Fig 1-d shows the edge burr caused by the cutting process [6.18].

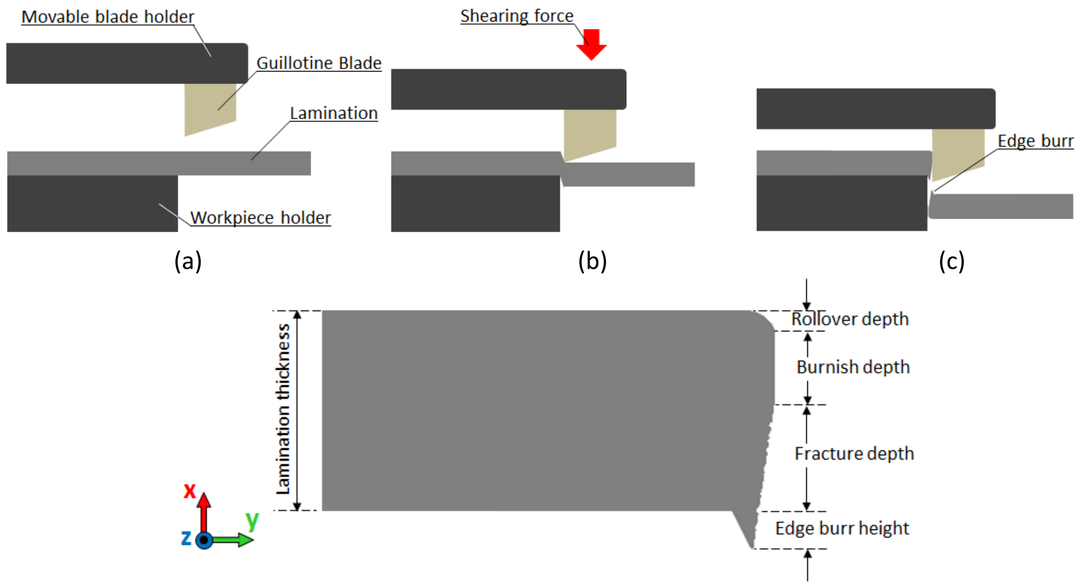

(a) (b) (c)

(d)

Fig 6.1 (a) Cutting process of a lamination and created edge burr
(b) concept of edge burr on a lamination, reproduced based on [6.18]

Burr height depends on many factors, e.g. sharpness of the tools, gap between the tools, thickness of the material, shearing process and properties of the material. However burr height is typically 2-10 % of the sheet thickness. In accurate manufacturing processes, burrs should be removed after the sheet is machined by a proper deburring process. However, deburring processes are usually not very accurate and may decrease the accuracy of the machined parts, damage the edge or surface of the sheet, and apply extra stresses on the work-piece. Furthermore, adding a deburring process requires an extra machining station and extra manufacturing time and therefore leads to extra cost [6.19].

Since burr generation in machining processes cannot be avoided completely and they might appear on the side of the magnetic cores during inspections and maintenances, it is very important to study their consequences on the magnetic and electrical properties of the electrical machines. Fig 6.2 shows how edge burrs make inter-laminar short circuits between the laminations in a magnetic core.

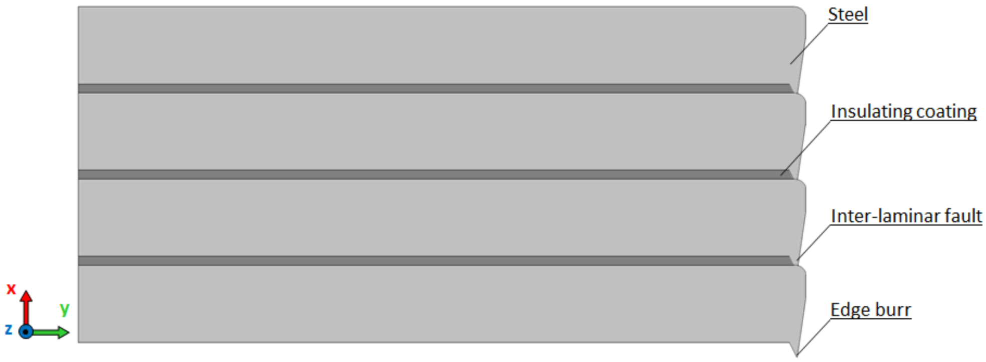

Fig 6-2 Inter-laminar short-circuit on stack of laminations caused by edge burrs

In order to demonstrate edge burrs physically, laminations of 0.3 mm thick of CGO Fe 3 % Si were cut by one sharp and two blunt guillotine blades. Cross sections of the samples are shown in Figs 6-3-a to 6-3-c, respectively. Figs 6-3-b and 6-3-c show that shape and height of the edge burr depends on the bluntness of the cutting tools. A stack of four laminations were then made with properly cut samples and the laminations with edge burr. Cross sections of one end of the stacks are shown in Figs 6-4-a and 6-4-b, respectively.

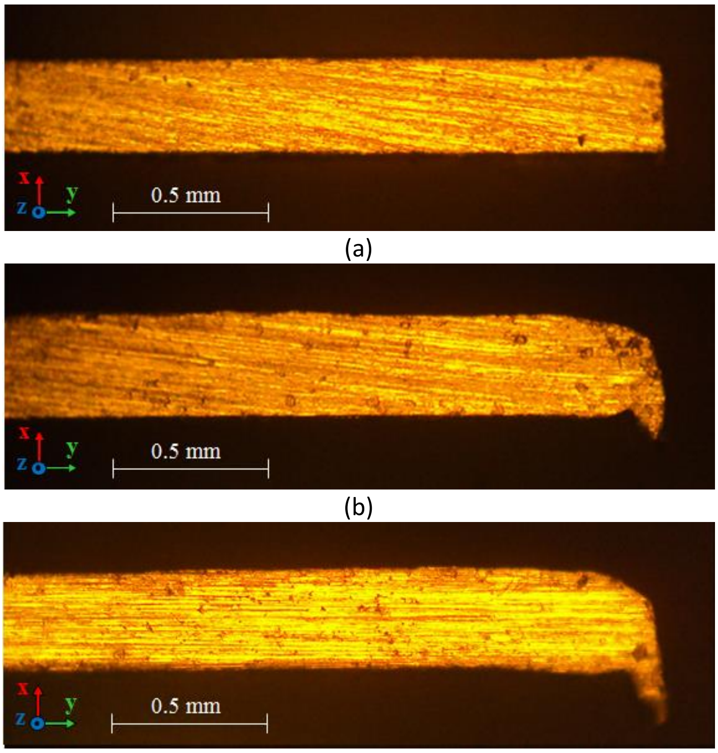

(a)

(b)

(c)

Fig 6-3 Cross section of a single strip lamination cut by a (a) sharp (b) and (c) blunt guillotine

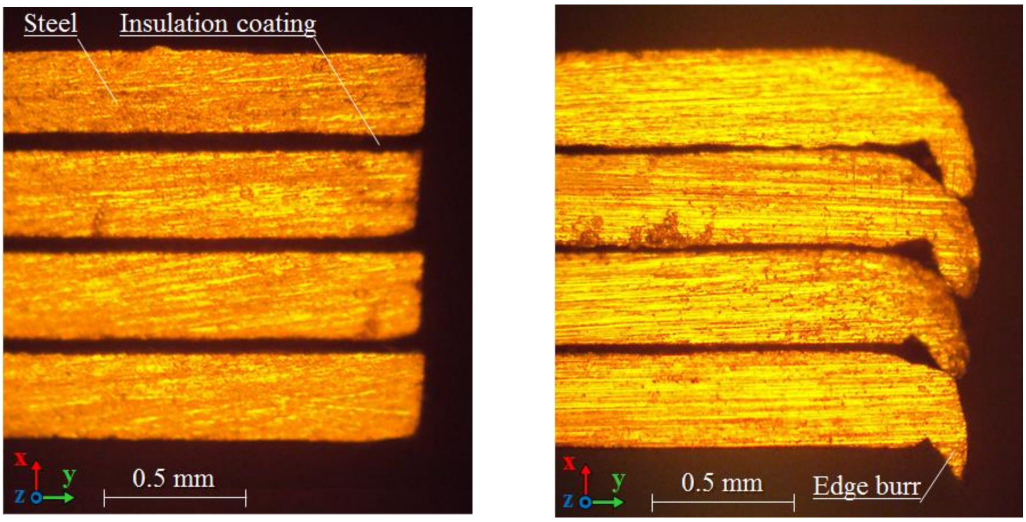

(a) (b)

Fig 6-4 Cross section of a stack of laminations with (a) properly cut samples
(b) samples with edge burr

Fig 6-4-a shows an ideal configuration of a magnetic core in which the laminations are properly insulated from each other. However Fig 6-4-b shows the inter-laminar shorts between the laminations caused by the edge burr.

6.2.2. Distinguishing destructive faults

Inter-laminar fault currents require a closed path perpendicular to the flux density in the core. Therefore in transformer cores if edge burrs appear between two sheets of the magnetic core on one side only, it does not create a closed current path and no change in the total loss of the core occurs. However, if the same two sheets are short-circuited on the other side as well, a closed conductive path will be available which will lead to a larger section for the flow of inter-laminar eddy currents resulting in elevated eddy current power loss [6.20]. This phenomenon in the stator cores of the rotating machines could be more distractive, because laminations of the stator cores are welded together or held together through either key bars or the case at the base of stator yoke [6.8] – [6.10]. The key-bars can be, but not always, insulated from the laminations or the frame of the stator to prevent the flow of current between cores and frame; but if not, it makes a permanent short circuit at the outer side of the core. Therefore if the stator laminations are shorted together, even on one side only, a circulating eddy current can be induced in the fault loop that consists of the fault, the shorted laminations and the key bar.

Perspective views of a transformer limb with three inter-laminar faults and a stator-rotor core with four inter-laminar faults are shown in Figs 6-5-a and 6-5-b, respectively. In order to visualise the distribution of the magnetic flux in both magnetic cores and distinguish the faults current loops, 2-D FE modelling was carried out using COMCOL Multiphysics; the results are shown in Figs 6-6-a and 6-6-b, respectively. According to the direction of the flux density in the cores, the short circuits shown in Fig 6-5 can be investigated individually as follows:

In Fig 6-5-a, Short circuit I is formed between the bolt hole and one side of the core step and short circuit II is formed between two sides of the core step. Both of these defects are perpendicular to the direction of the magnetic flux in the core and therefore make a fault current loop in the core. Short circuit III, on the other hand, does not meet the definition of fault current loop, because it does not make a closed loop perpendicular to direction of the magnetic flux in the core.

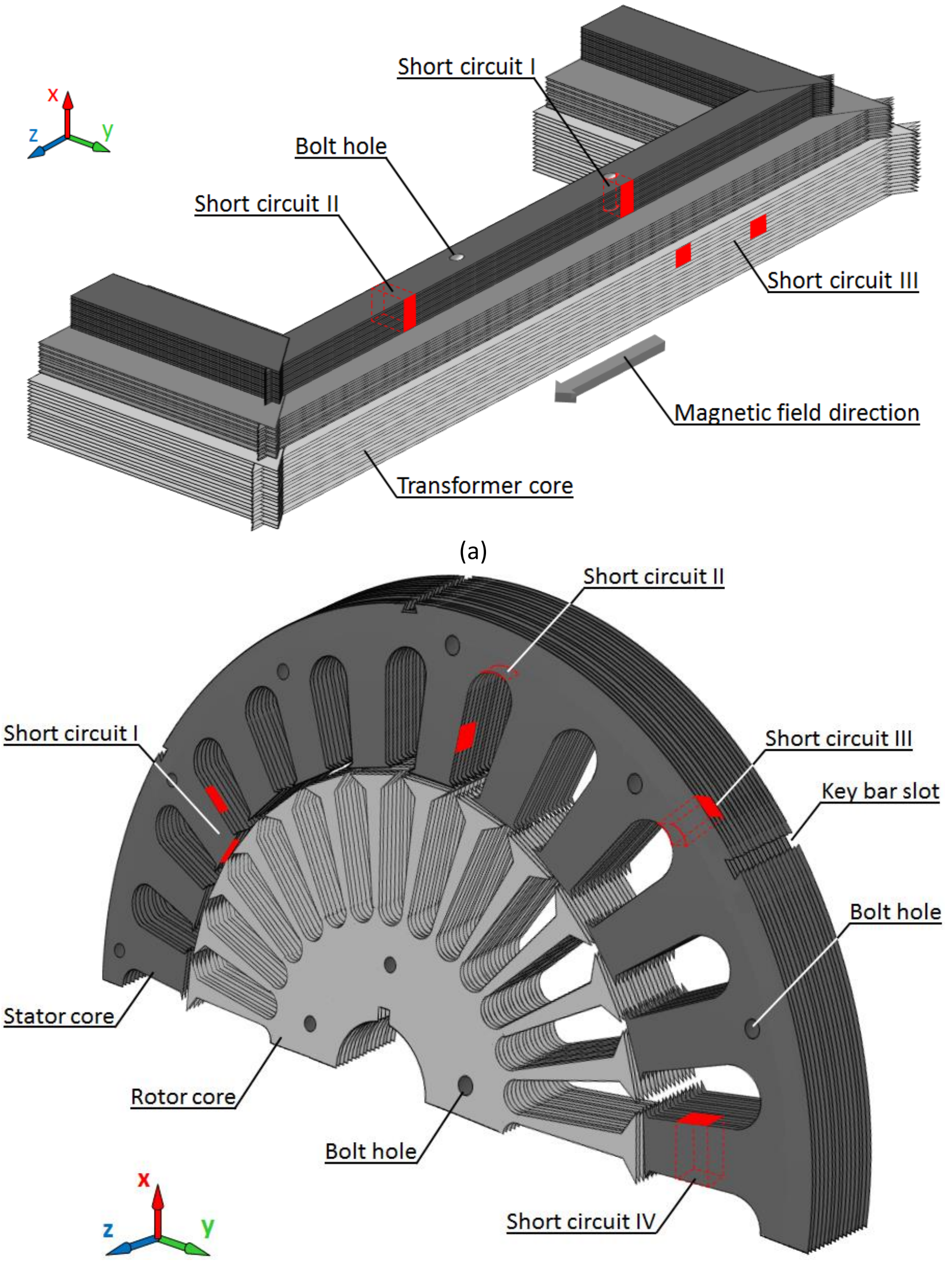

Fig 6-5 (a) Perspective view of a (a) transformer limb with inter-laminar short at three possible positions and (b) a stator-rotor core with inter-laminar short at four possible positions

A similar investigation could be carried out to find out the fault current loops of the stator core of Fig 6-5-b. FEM results of Fig 6-6-b show that the magnetic field lines pass in a continuous loop or magnetic circuit from the stator through the rotor and back to the stator again. It should be noted that the magnetic flux lines in the stator teeth are parallel to the teeth and perpendicular to the surface of the rotor.

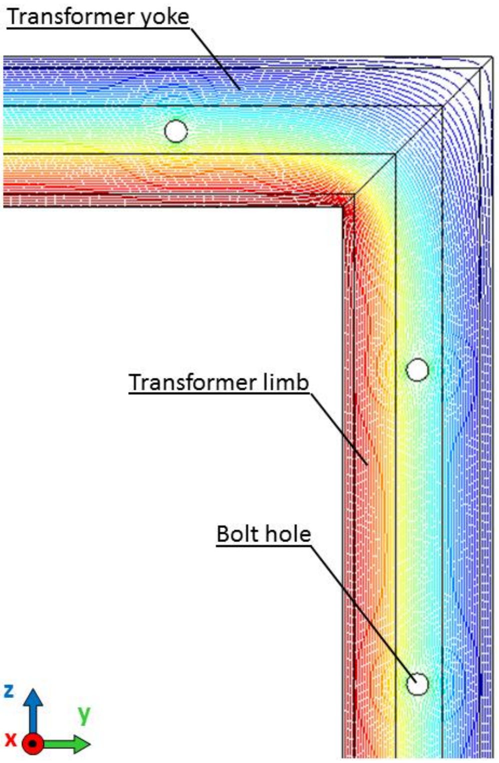

(a)

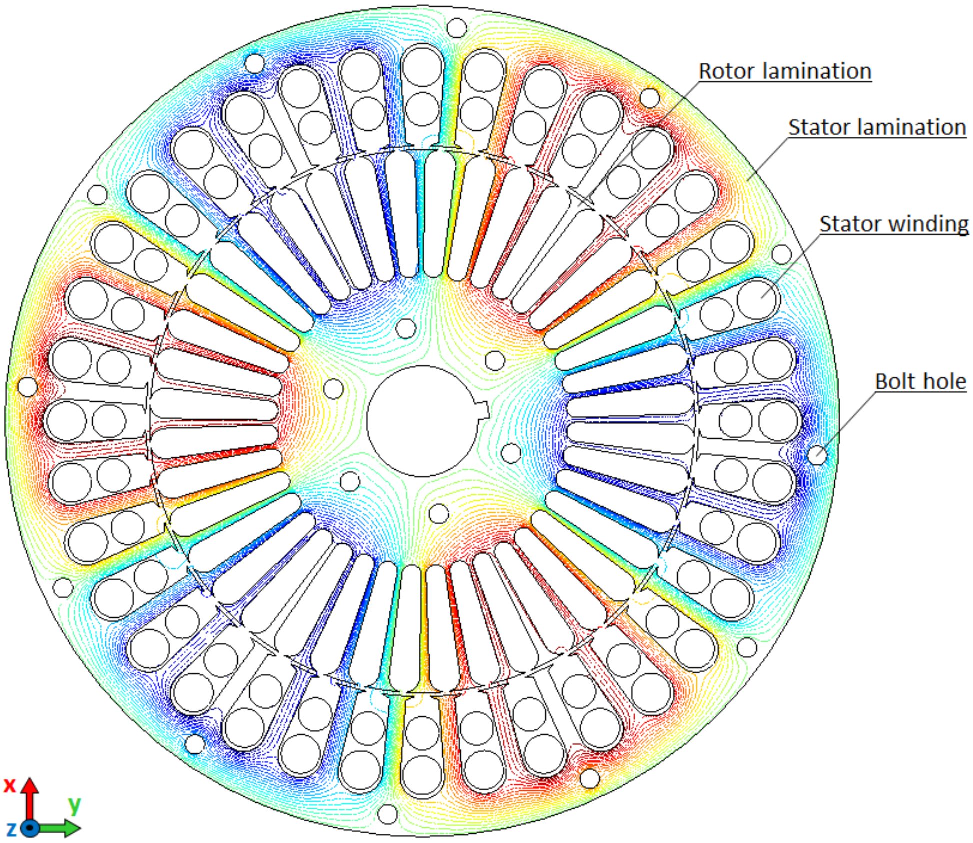

(b)

Fig 6-6 Magnetic flux path in (a) transformer core (b) three phase 6 poles stator-rotor core; contours represent the equipotential lines of magnetic flux in the cores

Furthermore the magnetic flux lines in the stator yoke or back iron is parallel to the outer diameter of the stator core. Therefore neither of short circuits I nor II of Fig 6-5-b cut the magnetic flux lines and hence don't meet the definition of fault current loops. On the other hand, short circuits III and IV make closed current loops perpendicular to the direction of the magnetic flux in the yoke and tooth respectively and therefore create fault current loops in the stator core.

As mentioned at the beginning of this part, fault current loops create inter-laminar fault current between the defected laminations which is larger than that in normal operation of the core. As an example, cross sectional views of stacks of three laminations without inter-laminar faults and two different types of inter-laminar faults are shown in Figs 6-7-a, 6-7-b and 6-7-c, respectively.

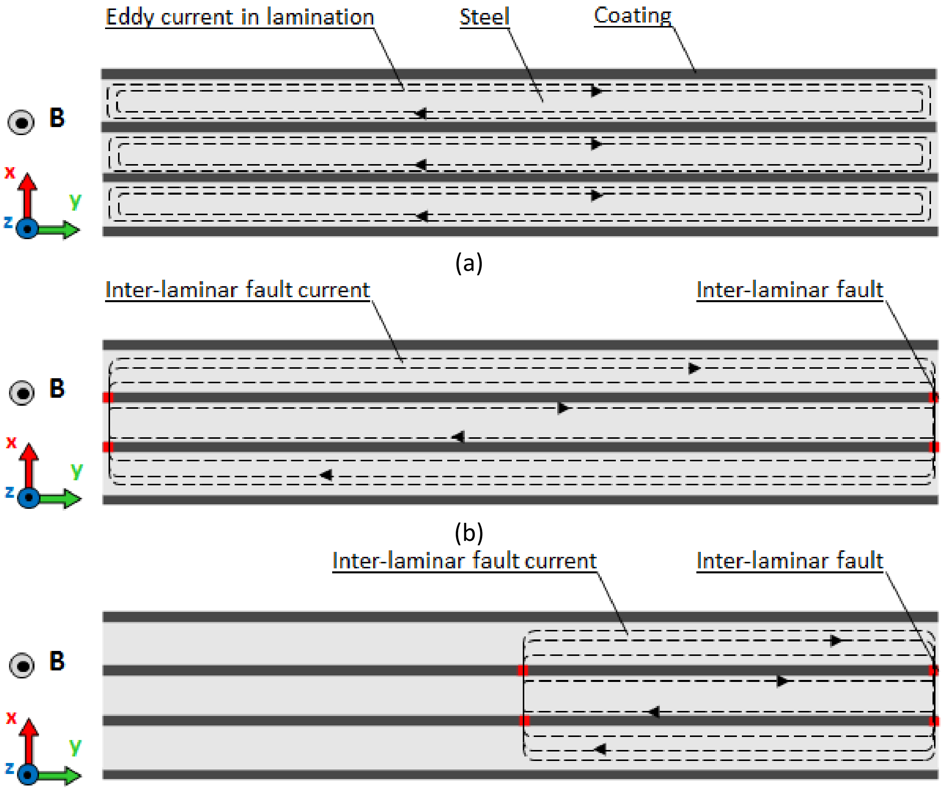

(c)

Fig 6-7 Cross section view of a stack of three laminations and (a) eddy current path in the laminations without inter-laminar fault (b) Inter-laminar eddy current path caused by inter-laminar fault on either side of the stack and (c) Inter-laminar eddy current path caused by inter-laminar fault between bolt hole and one side of the stack

In Fig 6-7-b the fault current loop is formed by the fault points on either side of the stack and shorted laminations; while in Fig 6-7-c fault current loop is formed by the fault points at the bolt hole, one side of the stack and shorted laminations. The eddy current distribution in the defected laminations and hence eddy current power loss caused by the inter-laminar fault current depends on the position of the fault points, the fault current loop and the number of shorted laminations.

A few fault current loops may not create a high inter-laminar eddy current; but with several faults in the core the induced inter-laminar fault currents could be large and cause excessive local heating in the damaged area [6.21]. If the generated heat cannot be dissipated properly, it causes more inter-laminar faults which is sometimes sufficient to cause burning or melting of the magnetic core and thus it raises the potential of a complete machine failure [6.22]-[6.24]. Localised heating due to the inter-laminar fault currents could also damage the excitation winding insulation and lead to ground faults [6.8]. Two examples of core melting caused by inter-laminar fault (in rotating machines) are shown in Figs 6-8 [6.8] and [6.24].

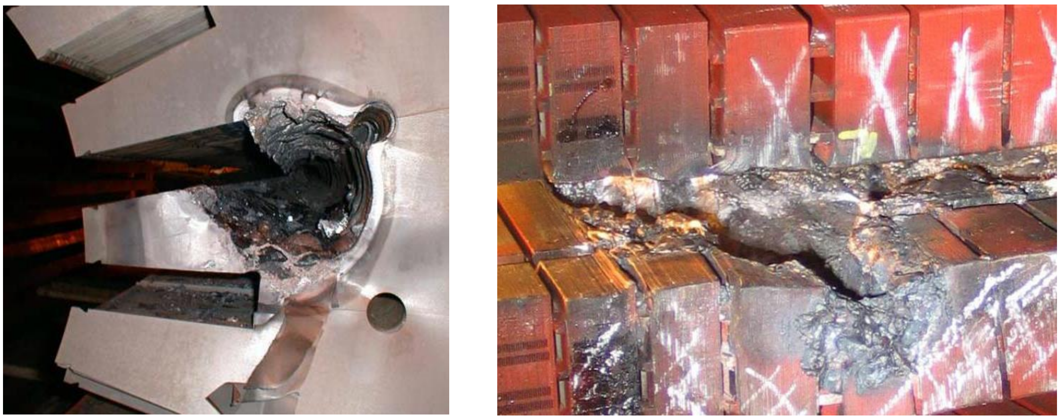

(a) (b)

Fig 6-8 Stator core melting caused by inter-laminar insulation failure
(a) core fault in tooth wall [6.8] (b) core fault in tooth bottom [6.24]

Therefore investigation of inter-laminar faults on the performance of electrical machines is required at the design and manufacturing stages. Reliable and accurate methods are also required to investigate and analyse the impact of inter-laminar faults on the magnetic cores.

6.3. Effect of inter-laminar faults on the equivalent configuration of a magnetic core

As discussed in section 6-2, inter-laminar faults could change the configuration of the laminated magnetic cores and hence the eddy current distribution in the magnetic laminations. The primary hypothesis about the effect of an inter-laminar fault on the magnetic core laminations is to change the configuration of the damaged laminations as a solid core with equivalent thickness of *2na*, where *n* is number of the damaged laminations and *a* is half of the thickness of one single strip lamination. Packs of two, three and four laminations with inter-laminar faults on both sides and the equivalent configurations are shown in Fig 6-9. An example of a stack of fourteen laminations in which five laminations are shorted on either side together with the equivalent configuration is shown in Fig 6-10.

According to this hypothesis, in a magnetic core with inter-laminar faults the damaged laminations can be replaced by a single lamination of thickness *2na*. However since the equivalent configuration of the shorted laminations is thicker, depend on the magnetising frequency, magnetic and electrical properties of the material, the skin effect can become significant and should be taken into account in the related studies. In chapters 5 and 6 it was shown that in the study of magnetic properties of the magnetic laminations, skin effect is a determinant factor at high frequencies and high permeabilities which has been considered in the literatures and papers [6.24]-[6-37]. However in thin laminations under low frequency magnetisation, e.g. power frequencies of 50 Hz or 60 Hz, this effect might be negligible due to the skin depth being significantly greater than the lamination thickness. But, in the presence of fault current loops in the magnetic cores, the effective thickness of the damaged laminations will increase. Therefore even at low frequencies, the effective thickness might become greater than the skin depth and hence skin effect might become significant; which is not addressed in the previous works.

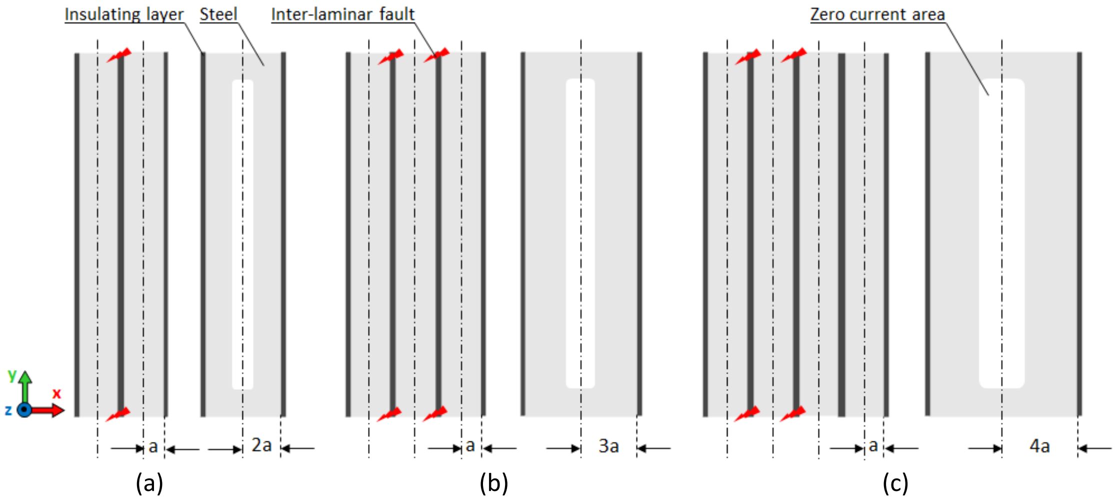

Fig 6-9 Cross section area of (a) two (b) three and (c) four magnetic laminations of thickness *2a* with short circuit on either sides and equivalent configurations

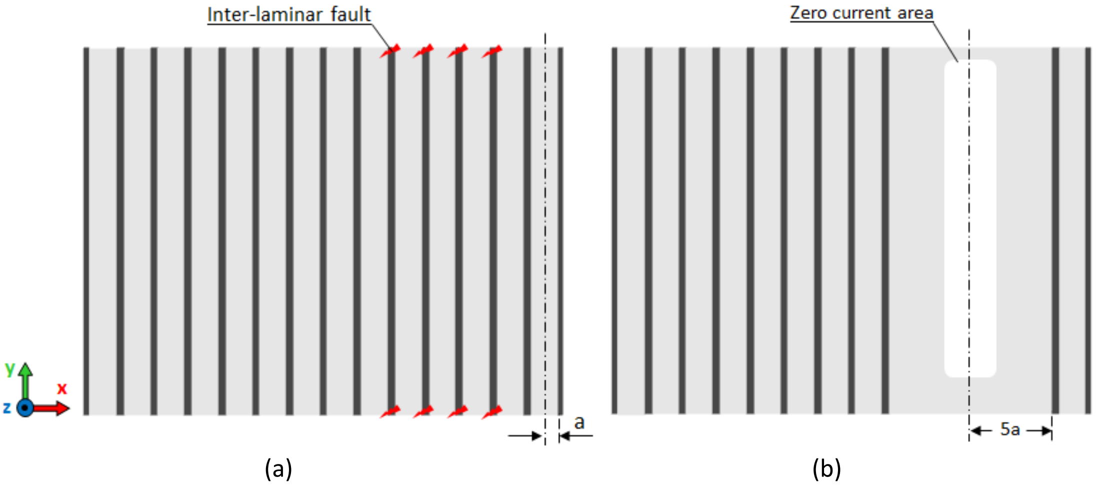

Fig 6-10 Cross section area of (a) a stack of laminations with five shorted laminations (b) equivalent configuration

6.3.1. FEM verification

In order to verify this hypothesis and visualise the eddy current distribution in the damaged sheets, 2-D FEM simulations for stacks of two, three, four and five laminates were performed using COMSOL Multiphysics. Fig 6-11 shows the FEM mesh model above the line of symmetry for a stack of five laminations with an inter-laminar short. Each lamination has a thickness of 0.3 mm and they are separated by an air gap of 20 µm. The laminations were exposed to a time-varying magnetic field (Out of the page). As the first part of this investigation, the laminations were magnetised without an inter-laminar fault and with an inter-laminar fault on one side only. The results of this investigation at a magnetising frequency of 50 Hz are shown in Figs 6-12-a and 6-12-b, respectively. Due to the known symmetry in *y*-direction, only one end of the laminations is shown.

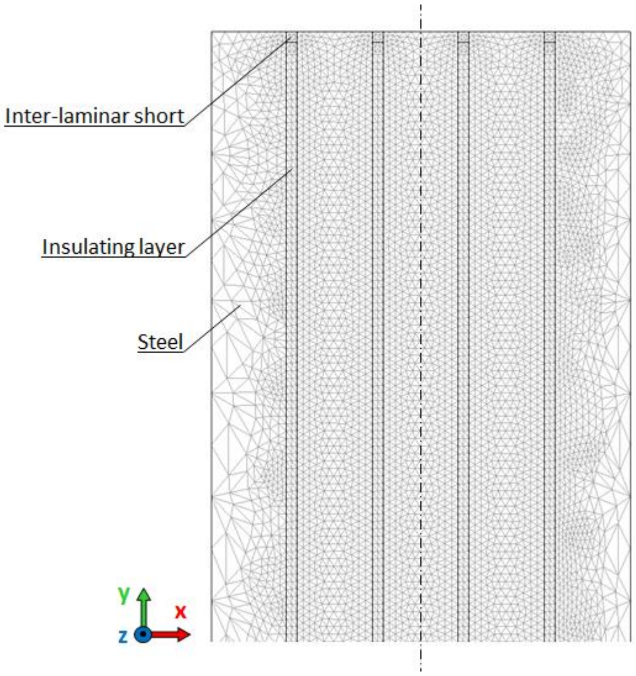

Fig 6-11 FEM mesh model of five laminations with partial inter-laminar short circuit of 20 µm thick

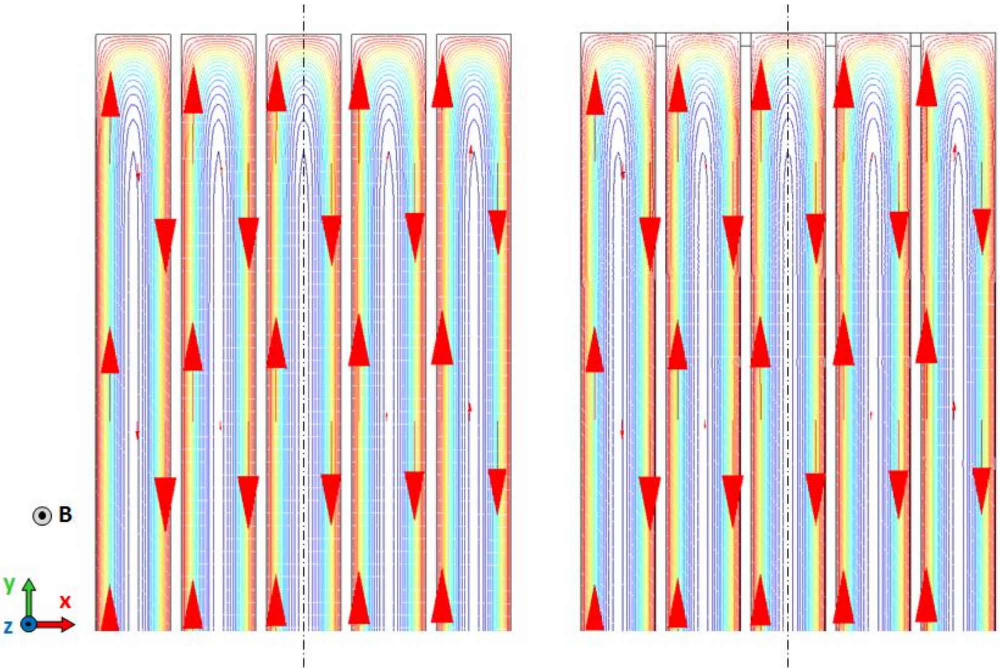

(a) (b)

Fig 6-12 Eddy current density distribution in a stack of five laminations (a) without inter-laminar fault (b) with inter-laminar fault on one side only; at 50 Hz

Fig 6-12-a shows the ideal performance of the magnetic cores, i.e. without an inter-laminar fault between the laminations, in which eddy currents are restricted to the individual laminations. On the other hand, as expected initially, eddy currents at the shorted end of Fig 6-12-b are still restricted to the individual laminations. This defect is similar to the short circuit III in Fig 6-5-a which do not create a closed current loop perpendicular to the flux density in the core. Therefore, as shown in Fig 6-12-b, if an inter-laminar fault appears between the laminations of the magnetic core on one side only, it does not create a fault current loop and no change in the eddy current distribution and hence eddy current power loss occurs.

The simulated laminations were then shorted together on either side. The eddy current distribution in the cores with two, three and five laminations with inter-laminar faults on both sides at magnetising frequencies of 50 Hz and 1000 Hz are shown in Figs 6-13 and 6-14, respectively. In commercial material, the height of inter-laminar faults, e.g. edge burr, is usually less than 20 µm in 0.28 mm thick sheet [6.13]. Therefore in order to simulate the eddy current distribution in the practical laminations (similar to Fig 6-2), the same material as the laminations with a thickness of 20 µm was used to simulate the inter-laminar faults.

The simulation results of the FEM analysis of Figs 6-13 and 6-14 show that there is only one eddy current loop in each pack of the shorted laminations. The inter-laminar shorts together with the shorted laminations make only one loop for the eddy current. Therefore, eddy current paths for individual laminations are closed through the shorted ends and hence a high eddy current density is created at these ends; consequently, extra local heat and local power loss occur at the shorted ends. This confirms the preliminary hypothesis about the equivalent configuration and hence the pattern of the eddy current distribution in the shorted laminations.

From equation (5-1) of chapter 5, for each conducting material with given permeability and conductivity, the penetration of the eddy current (which is quantified by skin depth, *δ)* is a constant at a given frequency and flux density. Therefore by increasing the thickness of the conductor and maintaining the frequency and flux density at a constant value, the skin depth will become significant. This issue is evident in the FEM simulation results of Figs 6-13 and 6-14. In these figures, configuration of the shorted laminations has been changed to be similar to a solid core by the inter-laminar faults and therefore skin effect becomes significant, even at 50 Hz. The sizes of the arrows indicated in these figures, and also the density of the contours, are proportional with the amplitude of the local eddy current, which in turn shows the impact of skin effect.

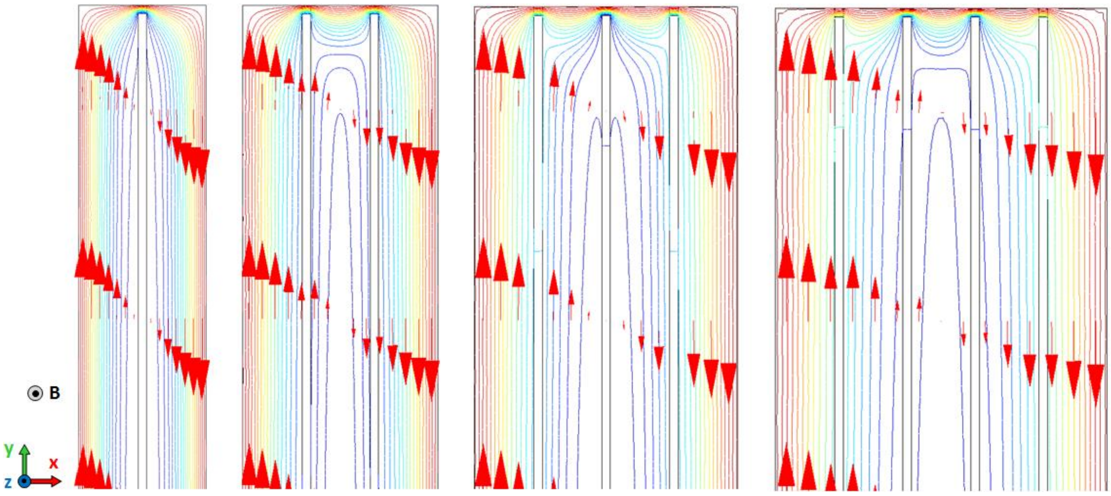

(a) (b) (c) (d)

Fig 6-13 Eddy current density distribution in magnetic laminations with partial edge burr of 20 µm thick at magnetising frequency of 50 Hz (a) two laminations (b) three laminations (c) four laminations and (d) five laminations

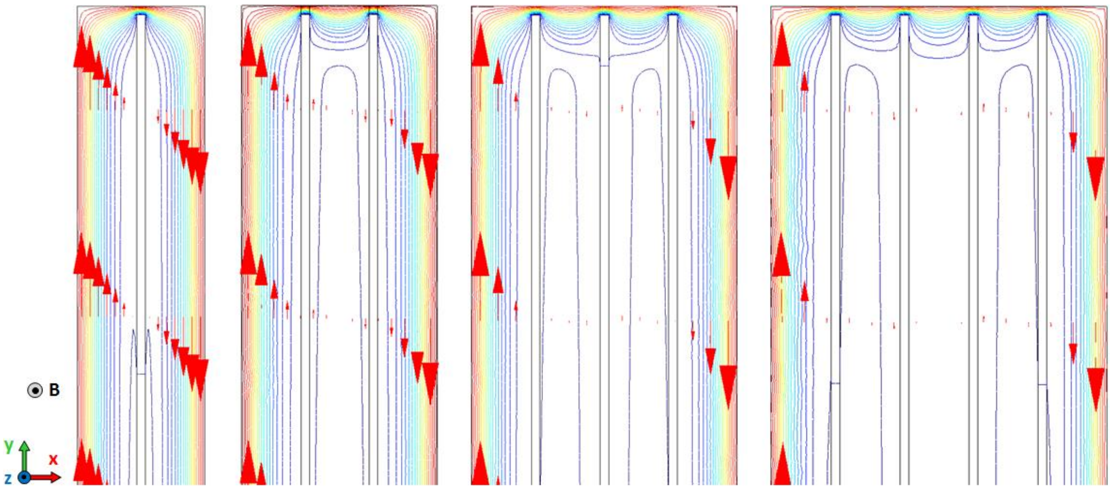

(a) (b) (c) (d)

Fig 6-14 Eddy current density distribution in magnetic laminations with partial edge burr of 20 µm thick at magnetising frequency of 1000 Hz (a) two laminations (b) three laminations (c) four laminations and (d) five laminations

Therefore, five important notes could be concluded from the FEM modelling of Figs 6-13 and 6-14:

1. There is only one eddy current loop in each pack of the shorted laminations; which can prove the primary hypothesis.
2. Inter-laminar faults change the configuration of the cores similar to a solid core which leads to inter-laminar fault current and larger eddy current loops.
3. As a result of increased effective thickness of the shorted laminations, eddy current density at the shorted ends is much higher than in the laminations which leads to an extra local heat and local power loss at the shorted ends.
4. Changing the configuration of the shorted laminations causes skin effect to become significant, even at low frequencies.
5. The equivalent configuration which is affected by the skin effect leads to a zero current area at the centre line of the equivalent configuration, as predicted in Figs 6-9 and 6-10 and proved by the FEM modelling. The position and width of the zero current area in the equivalent configurations depends on number of the shorted laminations, magnetising frequency and peak flux density.

Therefore to investigate the effect of inter-laminar faults on the magnetic properties of the magnetic cores, shorted laminations can be modelled by a solid core with equivalent thickness of *2na*. It can be also concluded that the importance of skin effect on the eddy current distribution and eddy current power loss is not only at high frequencies, but also at low frequencies when the core is affected by the inter-laminar faults, as shown in Fig 6-13 at 50 Hz. In order to visualise eddy current distribution along the shorted laminations, normalised eddy current density for the packs of two, three, four and five shorted laminations at magnetising frequencies of 50 Hz and 1000 Hz were obtained from the FEM modelling. The results are shown in Figs 6-15-a and 6-15-b, respectively.

Fig 6-15 shows that regardless the gaps between the shorted laminations, the induced eddy currents in the laminations at 50 Hz are a linear function of distance from the centre line, but not at 1000 Hz. This could be proved based on the induced *emf* in the laminations. In section 4-7-3 of chapter 4 by equation (4-43) it was shown that at low frequencies since flux density along the lamination thickness is almost constant, the induced *emf* in the lamination is a linear function of *x*. However at high frequencies the induced *emf* is not a linear function of *x*, equation (4-51), because in this case flux density distribution is non-uniform.

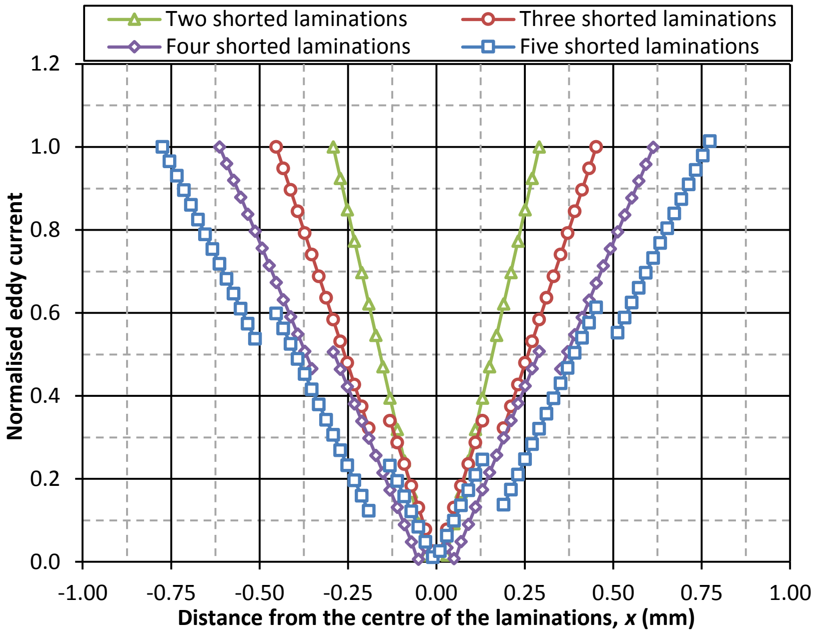

(a)

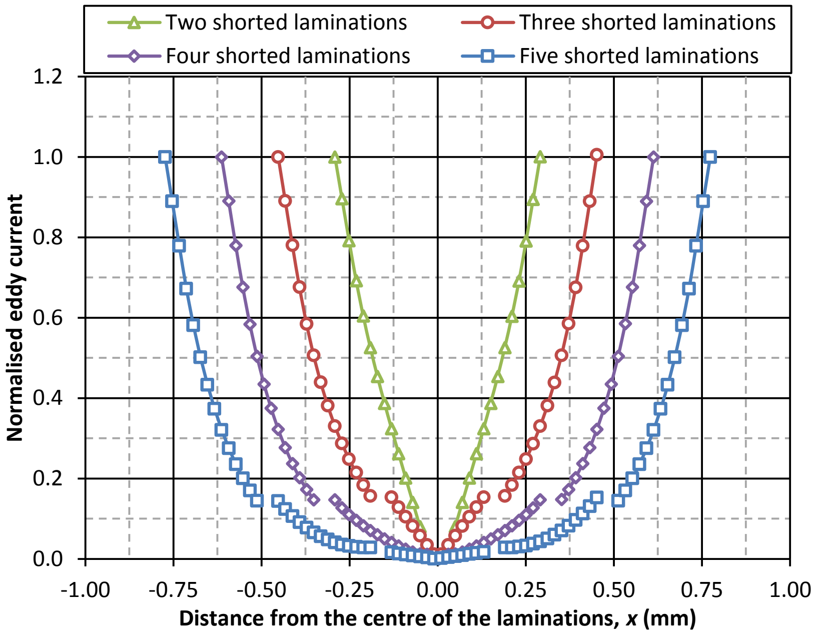

(b)

Fig 6-15 FEM result of normalized induced eddy current density in packs of two, three, four and five laminations at magnetising frequencies (a) 50 Hz (b) 1000 Hz

As outlined in part 6.2 the probability of electrical contact between the laminations in the heart of the core is very low [6.15]. However punching of the electrical steels, as a manufacturing process to apply clamping pressure on the core, might cause edge burrs and lead to inter-laminar short between the laminations around the bolt holes. In order to investigate effect of this type of fault on eddy current distribution, a stack of four laminations with bolt hole was modelled and 2-D FEM simulations were performed using COMSOL Multiphysics. A perspective view and cross section of the stack are shown in Figs 6-16-a and 6-16-b, respectively.

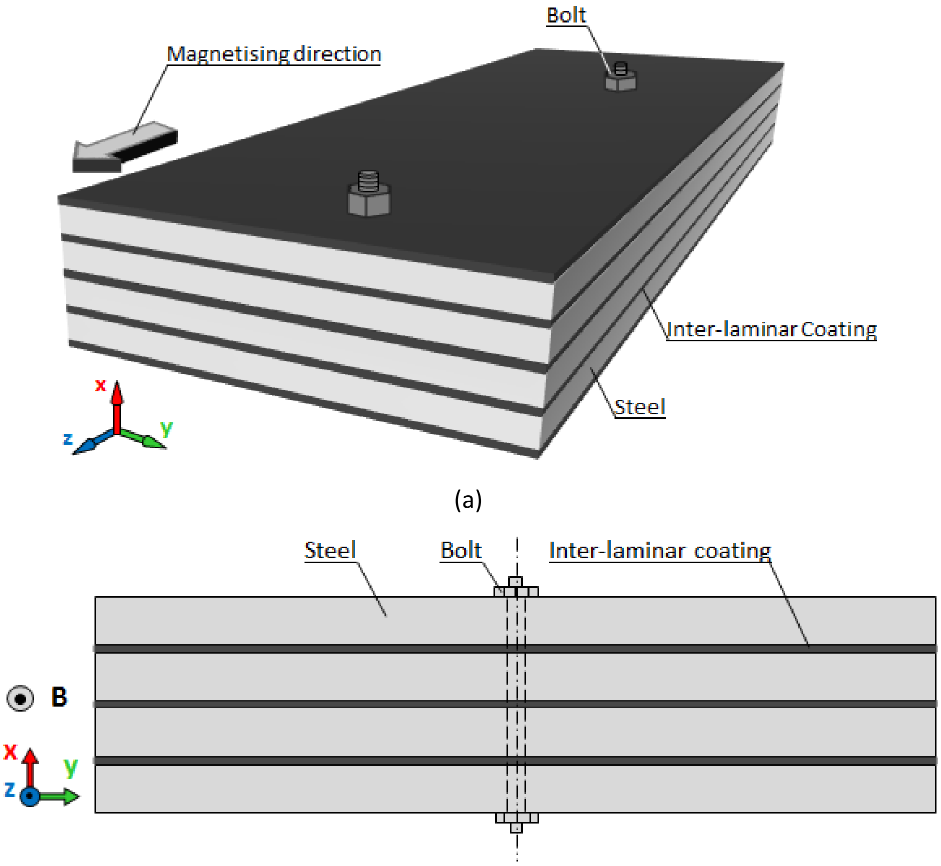

(a)

(b)

Fig 6-16 (a) Perspective view and (b) cross section of a stack of four laminations under time-varying magnetic field of 50 Hz

In the first part of this investigation, eddy current distributions in the stack without inter-laminar faults and then applying inter-laminar faults on either side of the stack were simulated. The results are shown in Figs 6-17-a and 6-17-b, respectively. Inter-laminar faults were then applied between the bolt hole and one side of the stack; the result is shown in Fig 6-17-c. In the last part of this study, in order to show an asymmetric fault current loop, a combination of the faults shown in Figs 6-17-b and 6-17-c were applied; the result is shown in Fig 6-17-d.

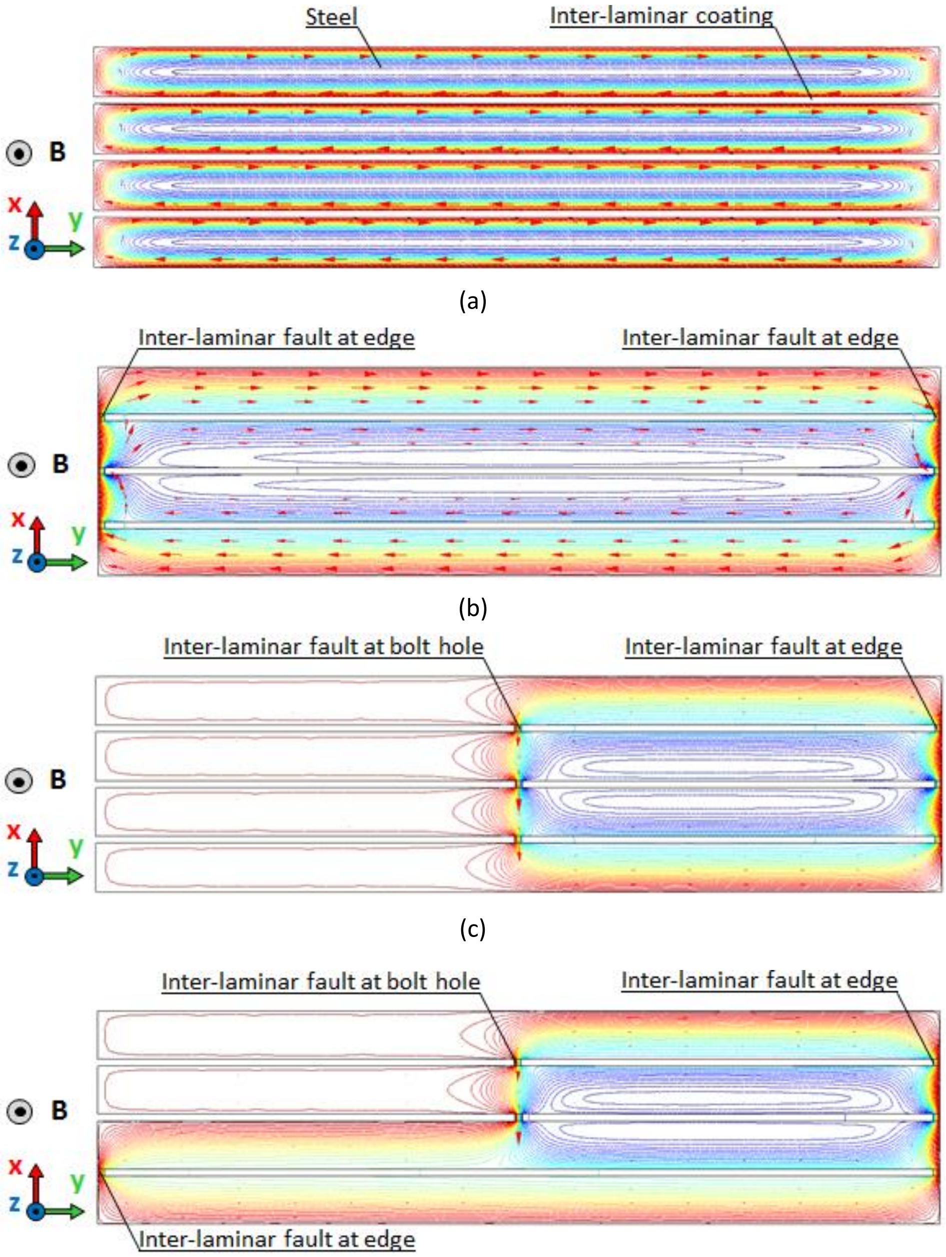

(d)

Fig 6-17 Eddy current density distribution in a stack of four laminations (a) without inter-laminar fault (b) with inter-laminar faults on either sides (c) with inter-laminar faults on bolt hole and one edge (d) combination of faults “*b*” and “*c*”

The FEM simulation presented in Fig 6-17 shows that inter-laminar faults between the bolt holes and one side of the stack create a smaller fault current loop, as shown in Fig 6-17-c. In this case, fault currents flow between the fault points and those parts of the steels which are shorted by the fault points. Eddy currents in the other parts of the steels are almost zero; because inter-laminar faults around the bolt hole make a short path with lower resistance to flow eddy current.

6.4. Effect of inter-laminar fault on flux density distribution

In Chapter 5 magnetic flux density distributions (normalised by the value at the surface) along the thickness of single strip lamination at different magnetising frequency *f* and flux density *B* were evaluated. In section 6.3 it was proved that inter-laminar faults can change the configuration of the shorted laminations as a solid core. Therefore regardless the thin insulation coating between the laminations, flux density distribution along the shorted laminations can be analysed by the similar method as used for single lamination. Based on equation (5-1), if in a hypothetical process the lamination thickness of a material increases, while the magnetic and electric properties remain constant, the skin depth becomes significant and it will affect the distribution of the magnetic properties along the thickness of the lamination. Therefore in a stack of laminations with an inter-laminar fault, non-uniform flux density distribution is expected, even at low frequencies. Before plotting the flux density distribution along the lamination thickness of the shorted laminations, an important note related to equation (5-25) is addressed here.

6.4.1. Relationship between lamination thickness and skin effect

From equation (5-25), distribution of the flux density along the thickness of the lamination depends on the thickness of the lamination (*2a*), magnetic and electric properties of the material (μ and σ) and magnetising frequency (*f*). However, the lamination thickness, *a,* and skin depth, δ*,* are also two determinant factors in the qualification of the flux density distribution along the lamination thickness. In time harmonic investigations it is usual to compare the thickness or diameter of the cross section of the conducting materials with the equivalent skin depth at each particular operating point. Therefore based on equation (5-25) it is useful to compare the ratio of half of the lamination thickness to the skin depth (a/δ) for different thicknesses, flux densities and magnetising frequencies. Figs 6-18 and 6-19 show these characteristics versus flux density for different thicknesses at magnetising frequencies of 50 Hz and 1000 Hz, respectively. These computations were performed for 3 % silicon grain oriented electrical steel. The curves of a=0.15 mm indicate a/δ ratio versus flux density of single strip lamination and the curves of a=0.3 mm, a=0.45 mm, a=0.6 mm and a=0.75 mm are equal to those of the packs of two, three, four and five shorted laminations, respectively.

Fig 6-18 shows that for a single strip lamination with a=0.15 mm (thickness of 0.3 mm) at 50 Hz frequency, $a/\delta<1$ for all flux densities. Therefore in this case skin effect can be neglected and the flux density distributes almost uniformly along the lamination thickness, as shown in Figs 5-15 and 5-16 of chapter 5. However since skin depth δ is a constant value at a given frequency and flux density, by increasing the thickness of the lamination it will become significant; i.e. the a/δ ratio becomes greater than unity even at low frequency, as shown in Fig 6-18 at 50 Hz. Therefore considering the effect of the inter-laminar faults on the configuration of the laminations, significant skin effect and non-uniform flux density distribution along the equivalent thickness of the shorted laminations are expected, even at low frequencies. A similar variation of the a/δ ratio versus flux density was observed at a magnetising frequency of 1000 Hz, as shown in Fig 6-19. However in this case even for a lamination of 0.3 mm thickness the a/δ ratio is greater than unity for almost all flux densities. Therefore, from Figs 6-18 and 6-19 it could be concluded that the a/δ ratio is a determinant factor to evaluate the consequences of the skin effect on the magnetic properties of the magnetic cores.

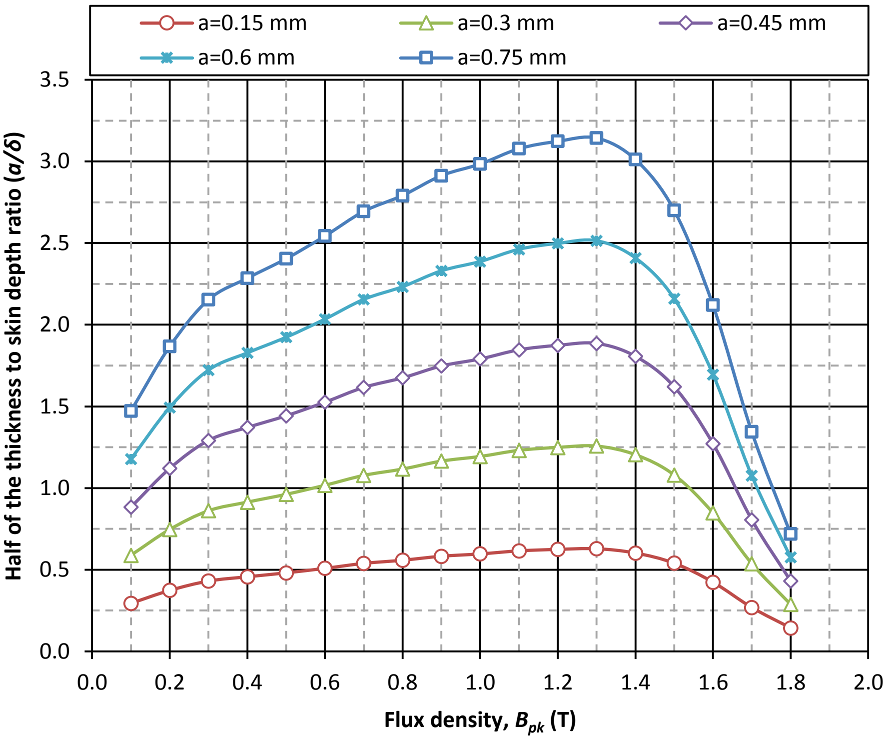

Fig 6-18 (a/δ) ratio versus flux density for different lamination thicknesses at magnetising frequency 50 Hz

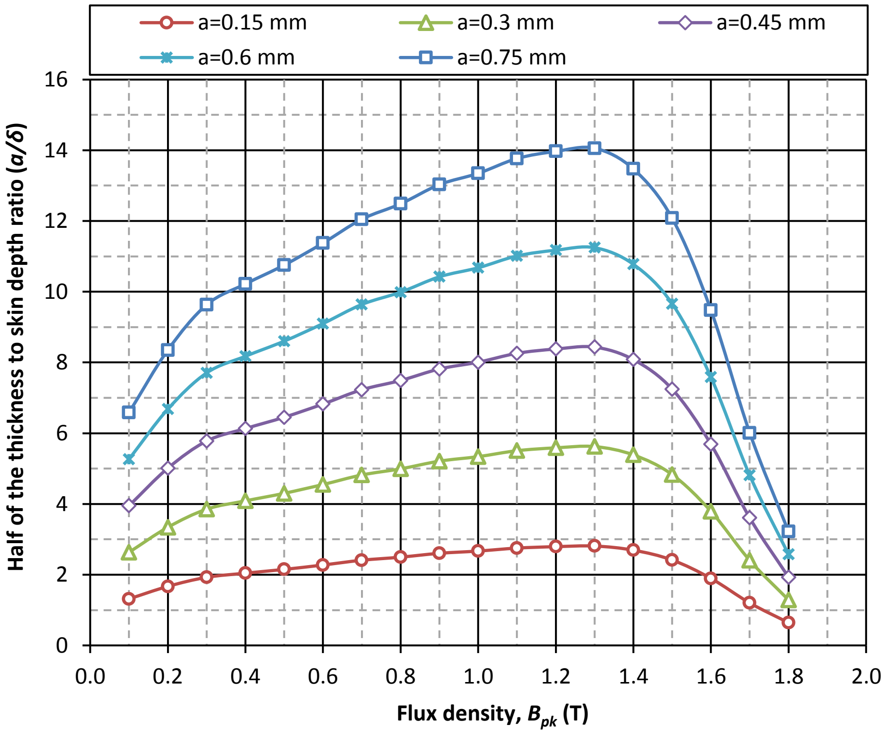

Fig 6-19 (a/δ) ratio versus flux density for different lamination thicknesses at magnetising frequency 1000 Hz

6.4.2. Effect of inter-laminar fault on complex relative permeability

From equation (5-37), skin effect δ and half of the lamination thickness a are also two key factors in determination of the complex relative permeability. Therefore inter-laminar short circuits also affect the complex relative permeability of the material. Using the same procedure as for the single strip lamination, the amplitude and phase angle of the complex relative permeability of the material with the specifications given in section 6.4.1 typically at surface flux density of B_S=1.5 T for five different thicknesses, a=0.15 mm to a=0.75 mm, are shown in Fig 6-20.

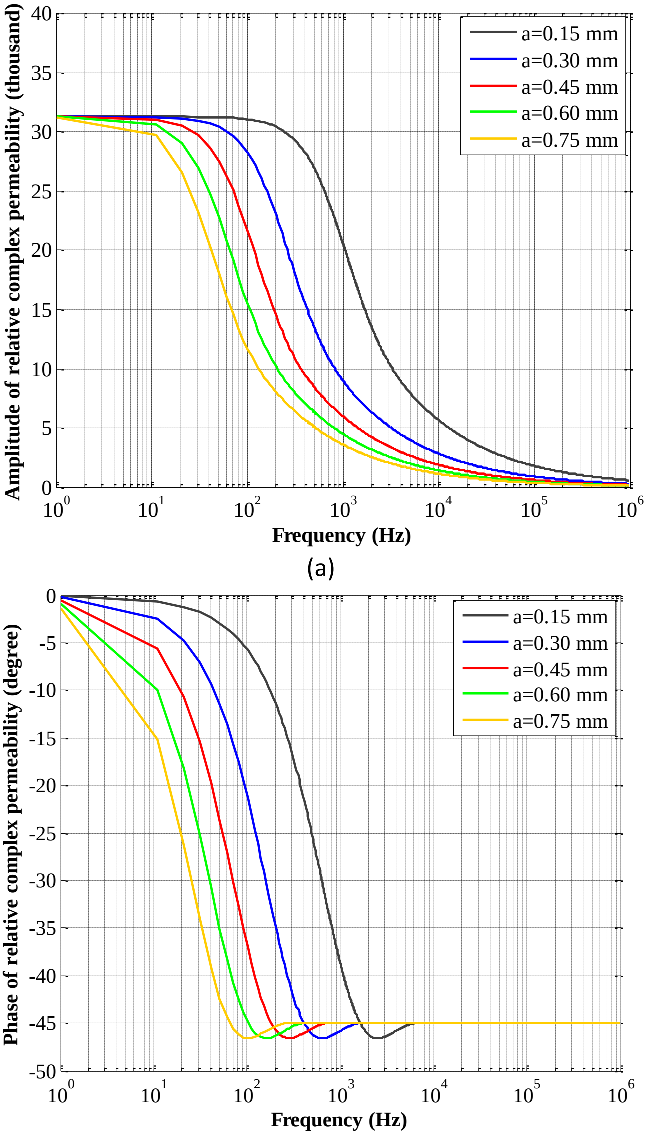

(a)

(b)

Fig 6-20 Frequency dependence of (a) amplitude and (b) phase angle of relative complex permeability of a magnetic lamination in rolling direction for different thicknesses at B_S=1.5 T

Fig 6-20 shows that the amplitude of the complex relative permeability decreases by increasing the magnetising frequency. However in the presence of inter-laminar faults, which lead to an increase of the effective thickness of the laminations, the amplitude of the complex relative permeability is reduced at lower frequencies, i.e. for laminations of 0.3 mm thickness complex relative permeability is constant up to about 100 Hz while for the lamination of 1.5 mm thickness it drops at a few Hertz. Therefore, in the presence of the inter-laminar fault the complex relative permeability becomes more significant and should be taken into account, even at low frequencies.

6.4.3. Flux density distribution in magnetic laminations with inter-laminar faults

Based on equation (5-25) and considering the effect of inter-laminar faults on the configuration of the magnetic laminations, the flux density distribution along the thickness was investigated for the same material as section 6.4.1 at different thicknesses. Similar to a single strip lamination, the flowchart of Fig 5-11 was implemented in the calculations. Figs 6-21 and 6-22 show the normalised flux density distribution along the lamination thickness at surface flux densities 1.1 T to 1.7 T and magnetising frequencies of 50 Hz and 1000 Hz for different thicknesses of the lamination from 0.3 mm to 1.5 mm.

The results presented in Fig 6-21 show that at magnetising frequency of 50 Hz the flux density is distributed almost uniformly along the lamination with a thickness of 0.3 mm; because in this case skin depth δ is greater than half of the lamination thickness ($\delta > a$). However by increasing the lamination thickness, at the same flux density and magnetising frequency, a will become greater than the skin depth δ and therefore the flux density drops from the edge of lamination to the centre line. This can be explained using the curves shown in Fig 6-18 for the lamination thicknesses greater than 0.3 mm, in which the a/δ ratio is greater than unity for almost all flux densities. A similar phenomenon was observed at higher frequency; however even for laminations with a thickness of 0.3 mm, as explained initially, the flux density distributes non-uniformly, as shown in Fig 6-22 for magnetising frequency of 1000 Hz.

As a final note, FEM analysis results, *a/δ* ratio curves and flux density distribution along the thickness of the lamination proved that skin effect is a key factor in the investigation of magnetic properties of magnetic cores. This effect is not only at high frequencies and high relative permeabilities but also at low frequencies when laminations are affected by inter-laminar fault, and should be taken into account in the accurate studies.

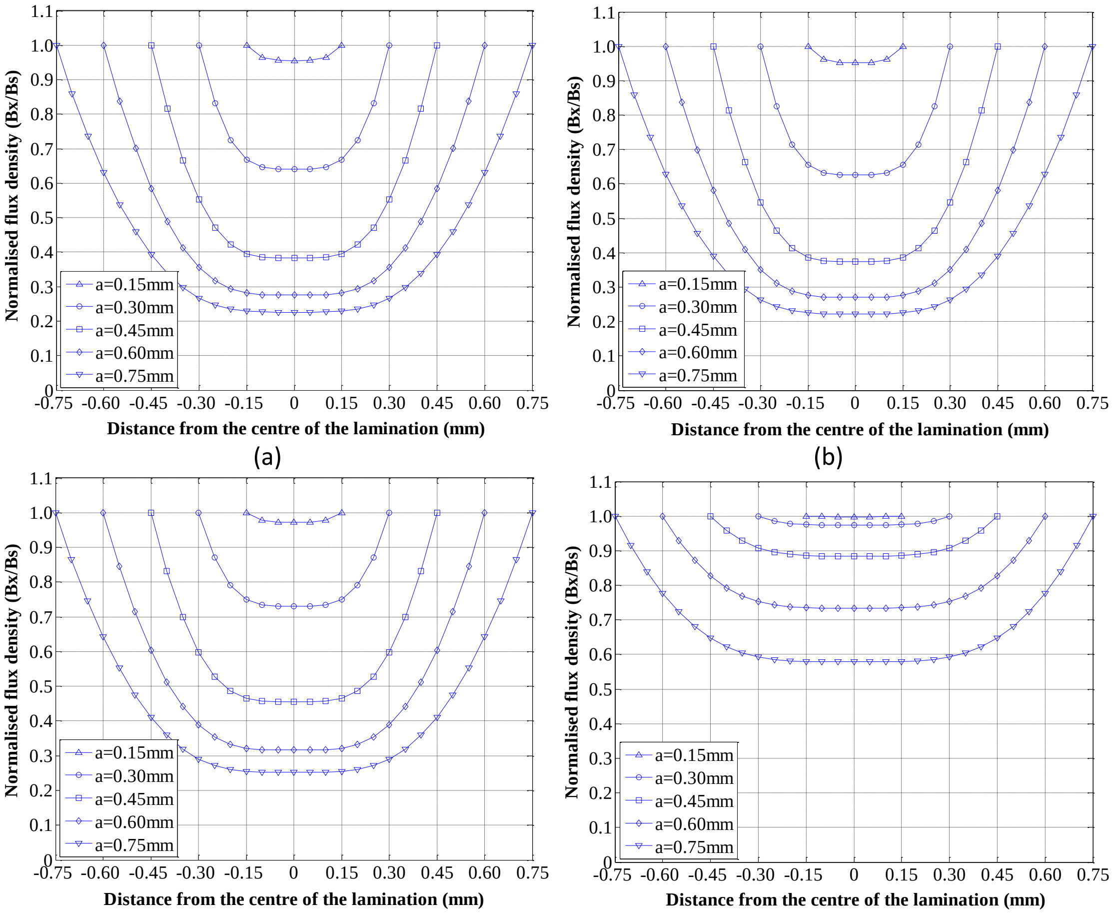

(a)

(b)

(c)

(d)

Fig 6-21 Flux density penetration into magnetic lamination of CGO at different thicknesses at 50 Hz
(a) B_s=1.1 T (b) B_s=1.3 T (c) B_s=1.5 T (d) B_s=1.7 T

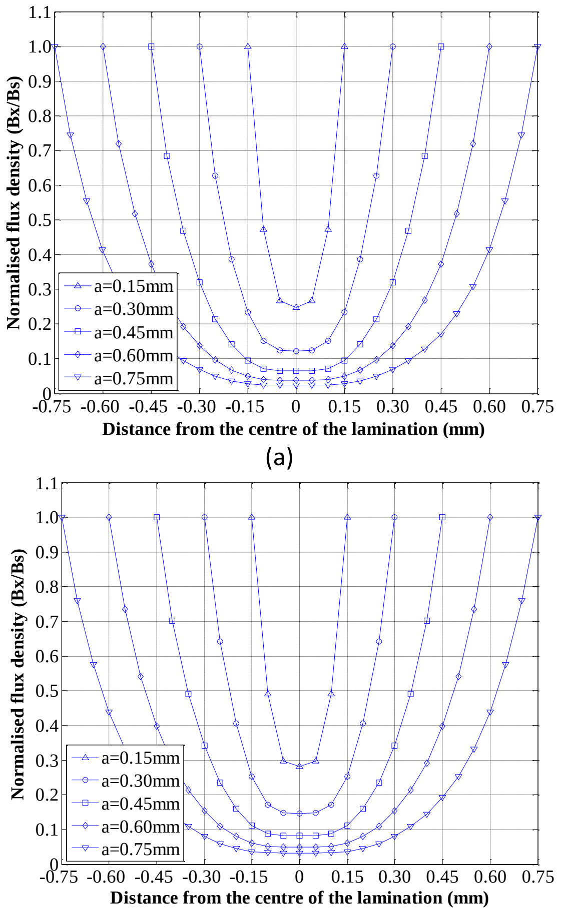

(a) (b) (c) (d)

Fig 6-22 Flux density penetration into magnetic lamination of CGO at different thicknesses at 1000 Hz (a) B_s=1.1 T (b) B_s=1.3 T (c) B_s=1.5 T (d) B_s=1.7 T

6.5. Eddy current power loss in a stack of magnetic laminations with inter-laminar faults

In section 4-7 eddy current power loss of single strip lamination was studied by modelling the eddy current path by an electric circuit. Components of the proposed model depend on the steel properties and physical dimensions of the eddy current path. This model can be extended to estimate eddy current loss in a stack of laminations. Based on the developed model, in a stack of magnetic laminations with equal flux density in all of the laminations, the total eddy current power loss can be obtained by summing the power dissipated in each loop of the core laminations. However since electrical steels are coated with insulating material on both sides, in order to develop a general equivalent circuit of magnetic cores it is necessary to take the effect of the inter-laminar insulating material into account. In this modelling the effect of the insulating material between the laminations should be modelled electrically to make an electrical link between the equivalent circuits of the individual laminations.

6.5.1. Equivalent electric network of magnetic cores

The surface coating of the electrical steels are made of high resistance materials to limit the inter-laminar eddy current in the cores and can be considered as a high resistor [6.38]. It is well known that a capacitance consists of two conducting sheets which are insulated by a di-electric plate. Therefore, in a stack of laminations adjacent laminations form a series of capacitors [6.39]. Therefore in order to develop an equivalent network for magnetic cores, the effect of the inter-laminar insulating material can be considered in two ways: considering the inter-laminar resistance between two adjacent laminations which lead to a pure resistive equivalent network or considering the inter-laminar capacitance between adjacent laminations which lead to an *RC* equivalent network. Fig 6-23-a shows a stack of magnetic laminations under time-varying flux density *B* in the rolling direction and Figs 6-23-b and 6-23-c show the pure resistive and *RC* equivalent networks of the core, respectively. R_2 and C_2 represent the inter-laminar resistance and capacitance between two adjacent laminations, respectively. Some techniques are available to measure these parameters [6.20], [6.39] and [6.40]-[6.44].

Figs 6-23-b and 6-23-c show two possible equivalent networks for the magnetic cores based on the equivalent circuit of single strip laminations and the impedance of the inter-laminar material between adjacent laminations. However, since the insulation coating used in electrical steels is quite thin, the resulting capacitance between adjacent laminations is high; e.g. for an Epstein size strip with approximately 3 µm insulation on both sides, the equivalent capacitance between two adjacent laminations is in the range of 5 nF [6-20]; and hence the equivalent capacitive reactance X_c, typically at power frequency of 50 Hz is about 0.637 MΩ. The magnetic field due to inter-laminar capacitive currents was solved in [6-45] and the result shows that the inter-laminar capacitive currents are negligible below 20 MHz for laminated cores in electrical machines. It should be noted that extra high frequency magnetisations make a strong capacitive coupling between the laminations which lead to inter-laminar eddy current flow between the laminations of the magnetic core [6-46].

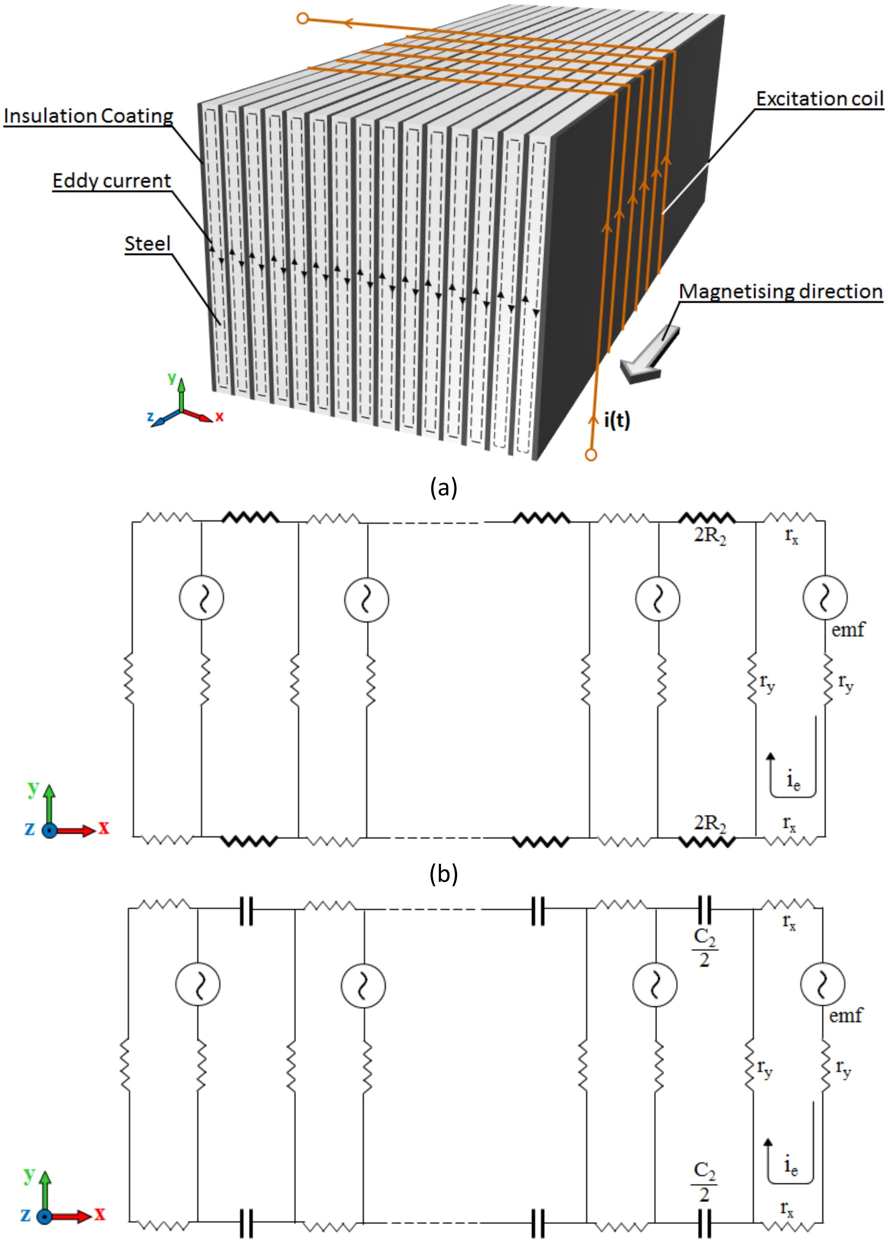

(a)

(b)

(c)

Fig 6-23 (a) Stack of magnetic lamination (b) pure resistive equivalent electric network (c) *RC* equivalent electric network

The coating material of the electrical steels has a large resistivity to limit the inter-laminar eddy current and hence the inter-laminar resistance of the electrical steels has a large value; e.g. for electrical steel coated with inorganic insulating coatings having surface insulation resistivities in excess of 30 KΩ-mm^2 [6.40]. Therefore compared to the resistance of the steel, which is in the range of μΩ, the impedance (resistive or capacitive) of the inter-laminar coating is extremely large and it does not affect the eddy currents in the lamination loops. Therefore in a stack of laminations without an inter-laminar fault, the total eddy current power loss at low frequencies could be calculated as $P_t=n\times P_1$; where n is number of the laminations and P_1 is the eddy current power loss of one single lamination. In the presence of inter-laminar faults on both sides of the magnetic cores the inter-laminar impedances are short-circuited by the defect and all of the damaged laminations form one loop in the equivalent circuit of the core. This issue was proved by the FEM modelling in section 6.3.1.

6.5.2. Modelling of inter-laminar short circuit faults

In previous works, in order to study the effect of inter-laminar faults different techniques have been implemented to make artificial short circuit between magnetic laminations [6.11]-[6.14] and [6.47]. Mazurek et al. [6.12] used 8 μm thick copper tape, pressed against the sides of the stack of laminations by wooden blocks and uniformly clamped by steel plates to make an artificial short circuit in a three phase power transformer. Moses and Aimoniotis [6.14] made an artificial short circuit by drilling 0.3 mm holes close to the edge of the laminations of a single phase transformer core and inserting a steel pin to short out the required number of laminations in the stack. Lamprecht and Gräf [6.48] coated the edges of a ring core by galvanic nickel with a thickness of roughly 0.1 mm.

In this project some possible materials were investigated to find a material to make artificial short circuit with close properties to the electrical steel. The resistivity and melting point of six materials at 20 °C to create inter-laminar short circuit between magnetic laminations are shown in Table 6-1.

Table 6-1 Resistivity and melting point of various materials at 20 °C

No.	Material	Resistivity ρ at 20 °C (Ω-m)	Melting point (°C)
1	GO electrical steel	4.60×10−7	1500
2	Copper	1.68×10−8	1085
3	Nickel	6.99×10−8	1455
4	Titanium	4.20×10−7	1668
5	Constantan	4.9×10−7	1221
6	Solder	13×10−8	221

Table 1 shows that, resistivity of copper and nickel is much lower than that of GO steel and they cannot be considered as a proper option in this work. The resistivity of titanium is very close to the resistivity of GO steel; but since its melting point is higher than that of GO steel it was impossible to use this material. Considering both resistivity and melting point of the materials, solder was found as the best option to make the artificial short circuit between the laminations. In this work, packs of two, three and four laminations of Epstein size 0.3 mm thick CGO 3 % *SiFe* laminations were shorted artificially by melting 3.3 % flux content lead-free solder in a soldering bath and putting the lamination sides into the bath. To prevent the solder penetrating between the laminations two iron strips of 5 mm thickness were used to clamp the laminations on either side. A schematic and photograph of the experimental setup are shown in Figs 6-24-a and 6-24-b, respectively.

Fig 6-25-a shows a top view of one pack of laminations with artificial inter-laminar short circuits on either side. In order to show the shorted edge of the laminations clearly, one side of the shorted laminations is magnified in Fig 6-25-b and a cross sectional view of the pack of four shorted laminations is shown in Fig 6-25-c.

6.5.3. Experimental results and comparison with analytical results

A single strip tester with reduced number of turns, N_1=108 and N_2=82, was made to magnetise the stacks of shorted laminations, as shown in Fig 6-26. The hardware and software of the measuring system are the same as measuring system described in section 5-2 of chapter 5.

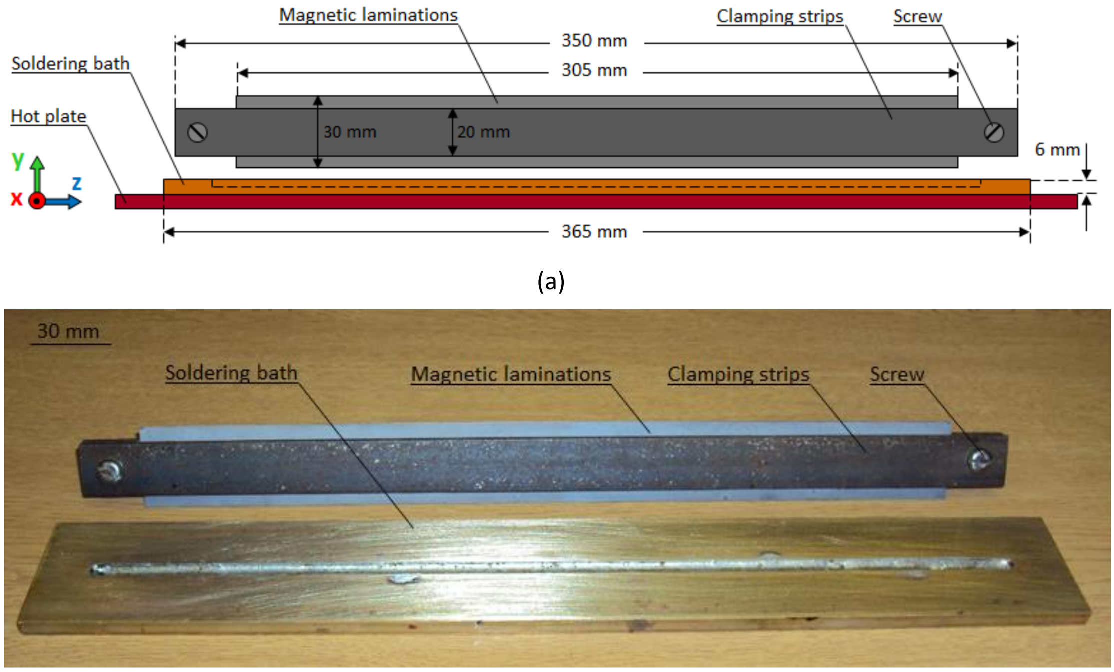

(a)

(b)

Fig 6-24 (a) Schematic of the experimental setup to make artificial short circuit between magnetic laminations (b) Top view of a pack of laminations with inter-laminar short circuit on either side

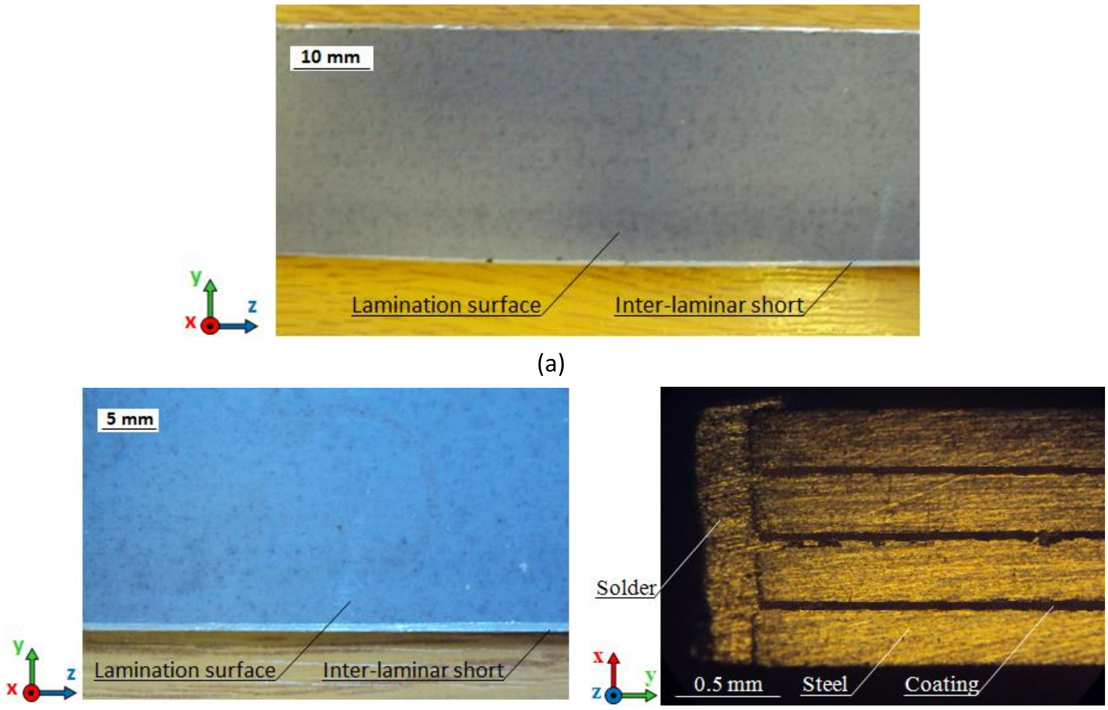

(a)

(b)

(c)

Fig 6-25 (a-b) Top view and (c) cross section of a pack of laminations with artificial inter-laminar short circuit

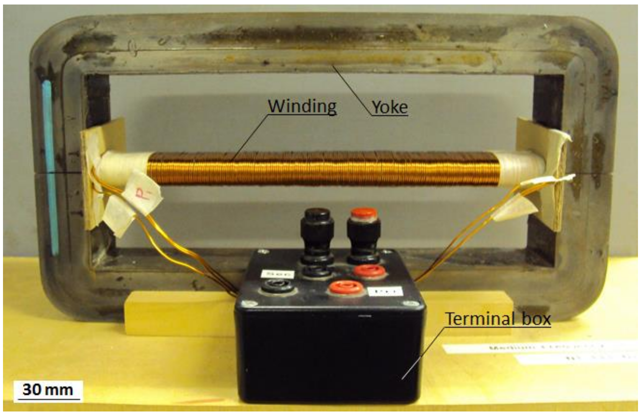

Fig 6-26 Single strip tester used in power loss measurement of the stack of magnetic laminations with artificial short circuit; N_1=108 and N_2=82

The specific core loss of the packs of two, three and four shorted laminations were measured at peak flux densities of 1.3 T, 1.5 T and 1.7 T and magnetising frequencies from 10 Hz up to 1 kHz. The results of the measurements that accompany the results of single strip laminations at flux densities 1.3 T, 1.5 T and 1.7 T and magnetising frequencies of 10 Hz, 50 Hz, 100 Hz, 200 Hz, 400 Hz and 1000 Hz are shown in Fig 6-27. In order to compare the measured losses of different packs of shorted laminations at different flux densities and frequencies, and especially to show the effect of the inter-laminar short circuits on core loss, specific power loss versus number of the shorted laminations at different frequencies and flux densities are shown in Fig 6-28.

A significant increase in the power losses of the shorted laminations can be observed from Figs 6-27 and 6-28; for example specific loss at 1.7 T and 1000 Hz for a single strip lamination and the pack of four shorted laminations increased from 178.9 W/Kg to approximately 2000 W/Kg. The extra loss is caused by the inter-laminar fault current and higher eddy current density at the shorted ends.

In this experiment all of the laminations in each stack were shorted together which could happen by edge burr caused by blunt guillotines. Therefore this experiment proves the importance of avoiding significant edge burr and also burr removal at cut edges. Furthermore this experiment shows the impact of inter-laminar faults on the magnetic losses and efficiency of the electrical machines.

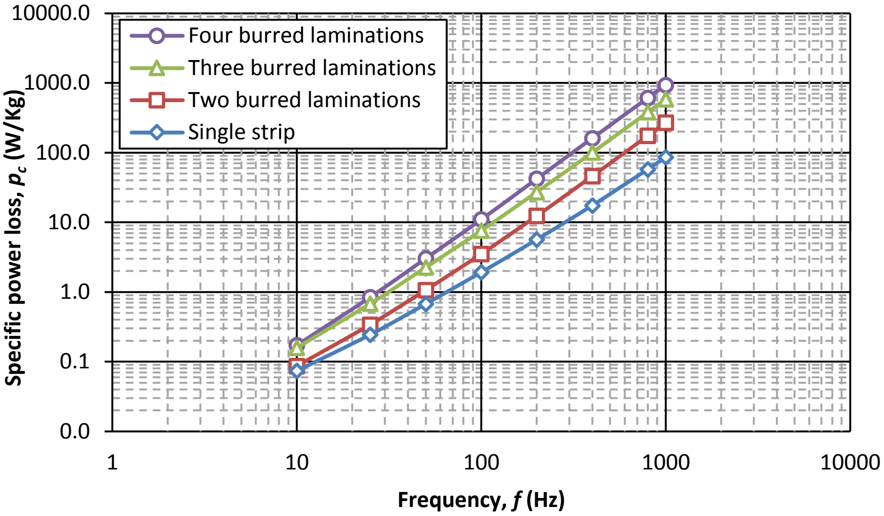

(a)

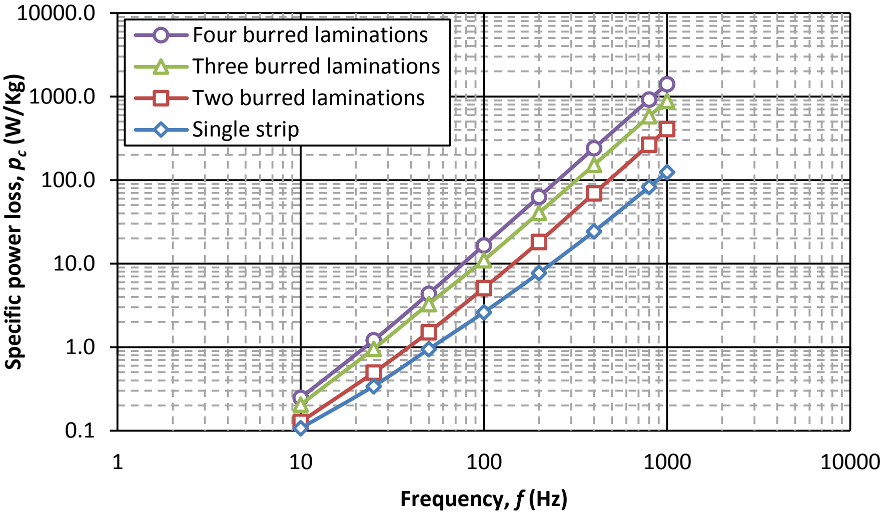

(b)

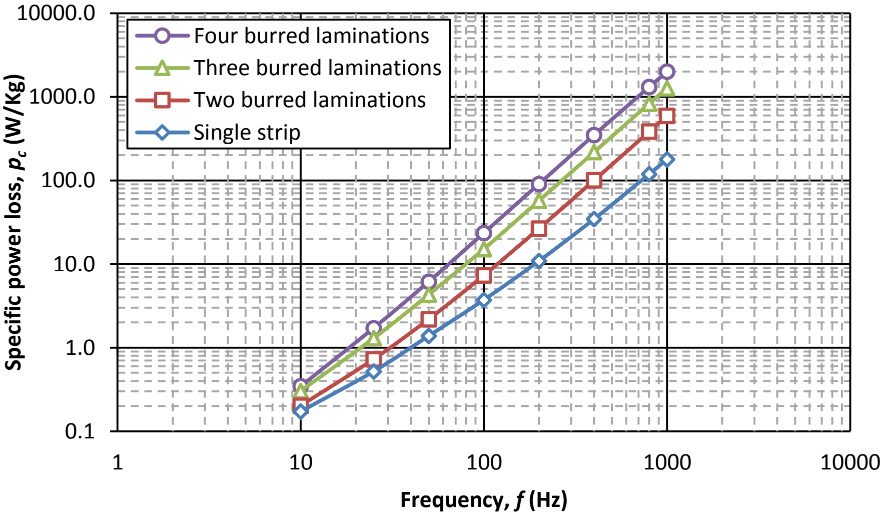

(c)

Fig 6-27 Specific core loss of single strip and packs of two, three and four burred laminations at peak flux densities (a) 1.3 T (b) 1.5 T and (c) 1.7 T

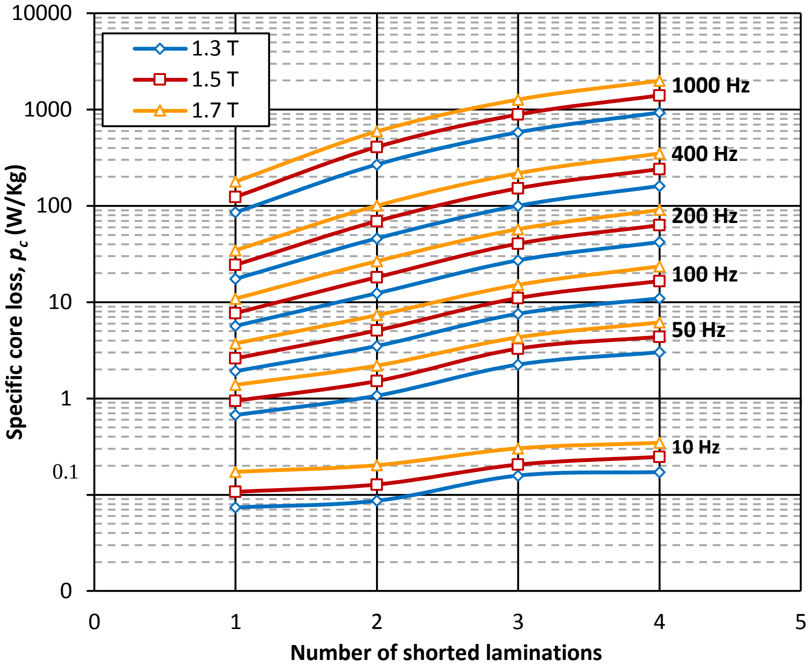

Fig 6-28 Specific core loss versus number of the shorted laminations at different peak flux densities and frequencies

Based on equation (6-13) correction coefficients of eddy current power losses were calculated for the packs of two, three and four shorted laminations; the results are shown in Fig 6-29. Loss components of the shorted laminations were separated at each flux density and frequency based on the developed extrapolation method described in section 5-4 of chapter 5. Eddy current power loss of each pack of shorted laminations was calculated based on equation (4-55) and the flowchart of Fig (4-20). The non-linear relationship of *B (H)* and complex relative permeability were considered to predict the losses. However because of the significant skin effect, these two factors were taken into account even at low frequencies.

Specific core losses per cycle versus square root of frequency, eddy current power losses and a comparison between the analytical and experimental results, separately at each flux density and each pack of shorted laminations, are shown in Figs 6-30 to 6-47 and Tables 6-2 to 6-10, respectively. Experimental results were obtained by applying the correction coefficients of Fig 6-29 to the eddy current loss obtained from the extrapolation method; and predicted values were obtained from equation (5-55) and the flowchart of Fig 5-20.

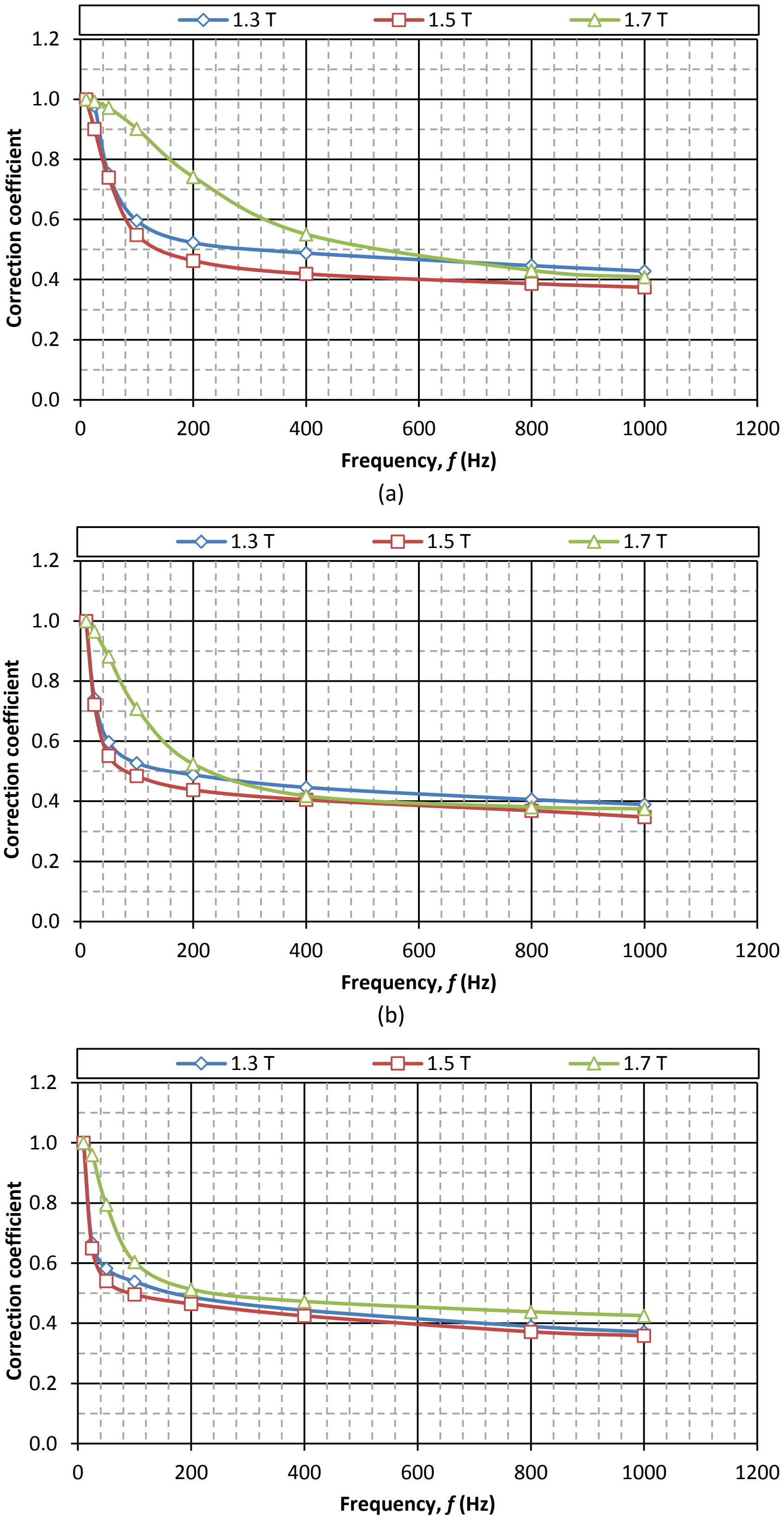

(a)

(b)

(c)

Fig 6-29 Correction coefficient of eddy current power loss of packs of (a) two (b) three and (c) four Epstein size laminations of CGO Fe 3 % Si of 0.3 mm thick

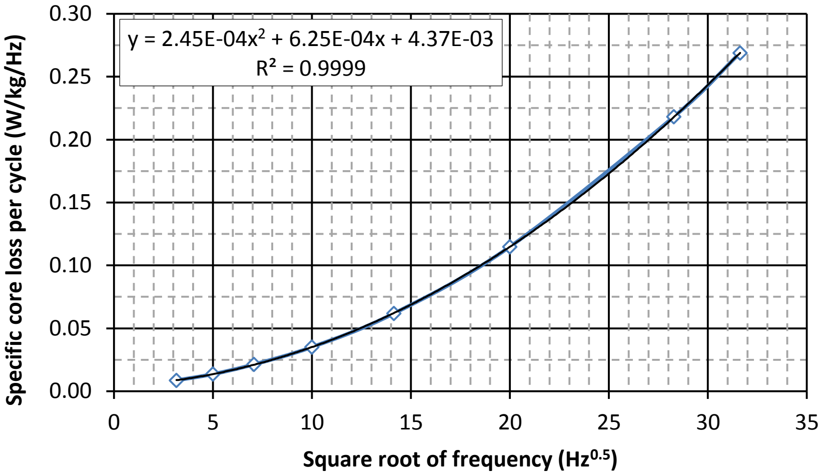

Fig 6-30 Specific core loss per cycle versus square root of frequency of pack of two shorted Epstein size laminations of CGO Fe 3 % Si of 0.3 mm thick at peak flux density 1.3 T

Table 6-2 Power loss components of a pack of two shorted Epstein size laminations of CGO Fe 3 % Si of 0.3 mm thick at peak flux density 1.3 T

Frequency (Hz)	***Total measured loss (W/kg)***	***P_{e1} (W/kg)***	***CC***	***$P_{e2}=P_{e1}\times CC$ (W/kg)***	***P_{e3} (W/kg)***	***Difference (%) $(P_{e3}-P_{e2})/P_{e3}$***
10	0.09	0.02	1.00	0.02	0.02	3.20
25	0.34	0.15	0.978	0.15	0.15	3.13
50	1.07	0.612	0.752	0.46	0.48	4.21
100	3.512	2.449	0.596	1.459	1.522	4.08
200	12.37	9.796	0.523	5.119	5.368	4.63
400	45.96	39.18	0.488	19.13	19.98	4.24
800	174.6	156.7	0.446	69.97	73.71	5.07
1000	268.9	244.9	0.428	104.9	111.5	5.89

P_{e1}: From extrapolation method, P_{e2}: From developed extrapolation method, P_{e3}: From modelling

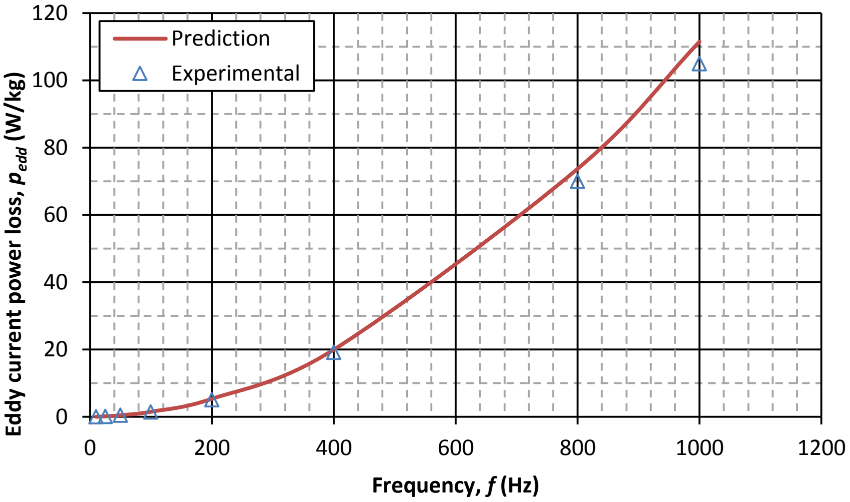

Fig 6-31 Comparison between prediction and experimental results eddy current power loss of two shorted Epstein size laminations of CGO Fe 3 % Si of 0.3 mm thick at peak flux density 1.3 T

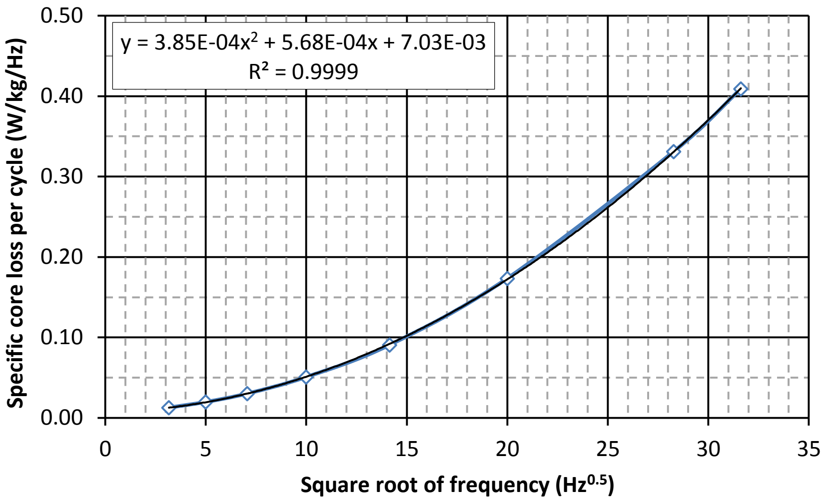

Fig 6-32 Specific core loss per cycle versus square root of frequency of pack of two shorted Epstein size laminations of CGO Fe 3 % Si of 0.3 mm thick at peak flux density 1.5 T

Table 6-3 Power loss components of a pack of two shorted Epstein size laminations of CGO Fe 3 % Si of 0.3 mm thick at peak flux density 1.5 T

Frequency (Hz)	***Total measured loss (W/kg)***	***P_{e1} (W/kg)***	***CC***	***$P_{e2}=P_{e1}\times CC$ (W/kg)***	***P_{e3} (W/kg)***	***Difference (%) $(P_{e3}-P_{e2})/P_{e3}$***
10	0.13	0.04	1.00	0.04	0.04	1.28
25	0.50	0.24	0.901	0.22	0.22	2.21
50	1.516	0.962	0.739	0.712	0.721	1.32
100	5.088	3.850	0.549	2.112	2.215	4.65
200	18.15	15.40	0.463	7.130	7.469	4.53
400	69.37	61.60	0.419	25.79	27.38	5.84
800	265.0	246.4	0.387	95.26	100.1	4.79
1000	409.2	385.0	0.374	144.1	155.0	7.06

P_{e1}: From extrapolation method, P_{e2}: From developed extrapolation method, P_{e3}: From modelling

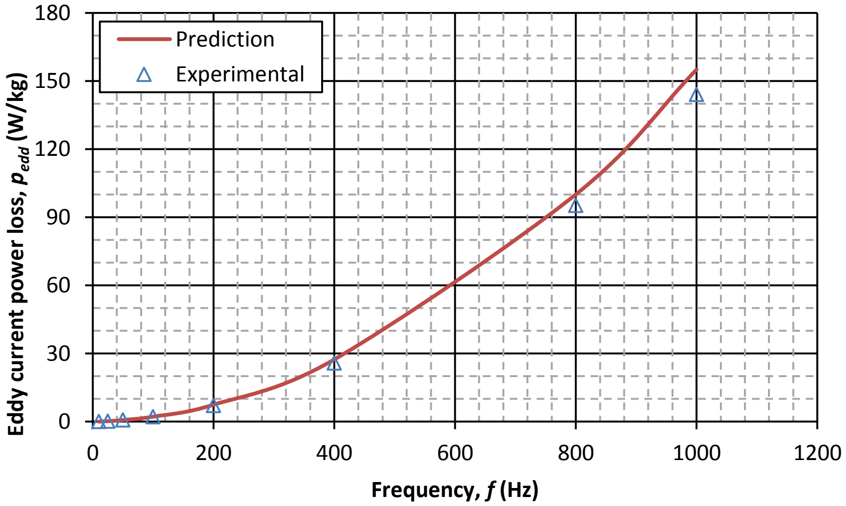

Fig 6-33 Comparison between prediction and experimental results eddy current power loss of two shorted Epstein size laminations of CGO Fe 3 % Si of 0.3 mm thick at peak flux density 1.5 T

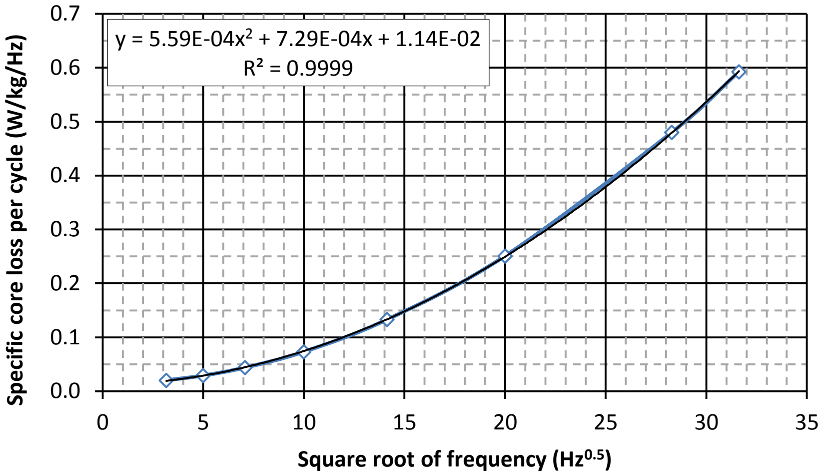

Fig 6-34 Specific core loss per cycle versus square root of frequency of pack of two shorted Epstein size laminations of CGO Fe 3 % Si of 0.3 mm thick at peak flux density 1.7 T

Table 6-4 Power loss components of a pack of two shorted Epstein size laminations of 3 % grain oriented silicon steel at peak flux density 1.7 T

Frequency (Hz)	***Total measured loss (W/kg)***	***P_{e1} (W/kg)***	***CC***	***$P_{e2}=P_{e1}\times CC$ (W/kg)***	***P_{e3} (W/kg)***	***Difference (%) $(P_{e3}-P_{e2})/P_{e3}$***
10	0.20	0.06	1.00	0.06	0.05	-3.33
25	0.73	0.35	0.993	0.35	0.34	-2.81
50	2.19	1.40	0.972	1.36	1.34	-1.43
100	7.325	5.590	0.902	5.043	4.561	-10.56
200	26.62	22.36	0.742	16.59	14.88	-11.57
400	100.4	89.44	0.551	49.26	45.67	-7.87
800	384.1	357.8	0.431	154.1	153.8	-0.22
1000	592.6	559.0	0.408	228.1	232.3	1.75

P_{e1}: From extrapolation method, P_{e2}: From developed extrapolation method, P_{e3}: From modelling

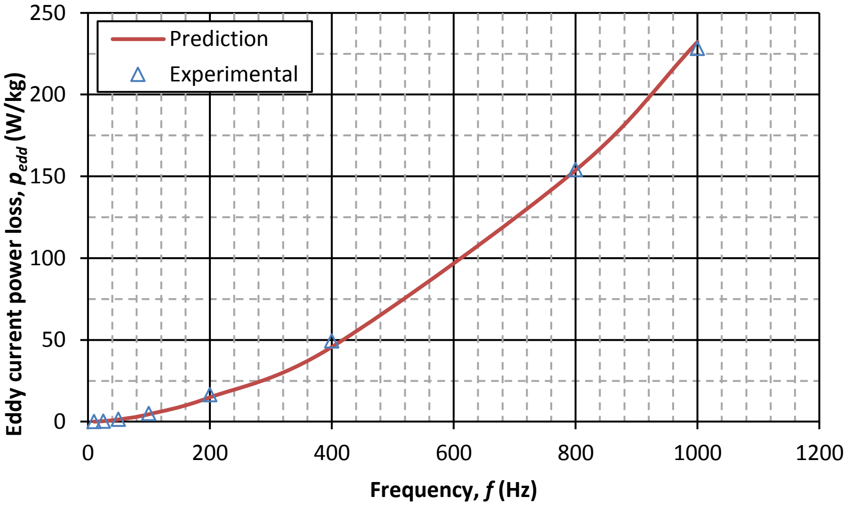

Fig 6-35 Comparison between prediction and experimental results eddy current power loss of two shorted Epstein size laminations of CGO Fe 3 % Si of 0.3 mm thick at peak flux density 1.7 T

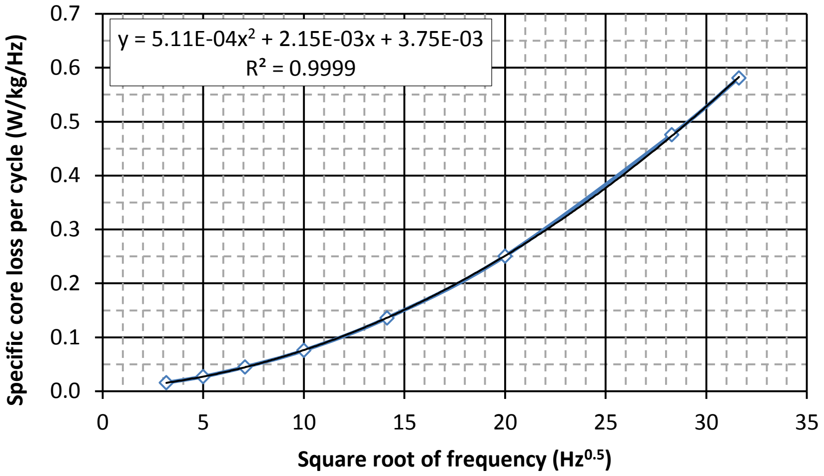

Fig 6-36 Specific core loss per cycle versus square root of frequency of pack of three shorted Epstein size laminations of CGO Fe 3 % Si of 0.3 mm thick at peak flux density 1.3 T

Table 6-5 Power loss components of a pack of three shorted Epstein size laminations of CGO Fe 3 % Si of 0.3 mm thick at peak flux density 1.3 T

Frequency (Hz)	*Total measured loss (W/kg)*	*P_{e1} (W/kg)*	*CC*	*$P_{e2}=P_{e1}\times CC$ (W/kg)*	*P_{e3} (W/kg)*	*Difference (%) $(P_{e3}-P_{e2})/P_{e3}$*
10	0.16	0.05	1.00	0.05	0.05	3.55
25	0.68	0.32	0.742	0.24	0.25	6.03
50	2.249	1.278	0.597	0.763	0.813	6.15
100	7.581	5.112	0.527	2.694	2.909	7.42
200	27.20	20.45	0.488	9.981	10.85	8.04
400	100.3	81.79	0.446	36.49	39.84	8.39
800	380.7	327.2	0.406	132.80	142.4	6.75
1000	581.2	511.2	0.389	199.1	213.9	6.94

P_{e1}: From extrapolation method, P_{e2}: From developed extrapolation method, P_{e3}: From modelling

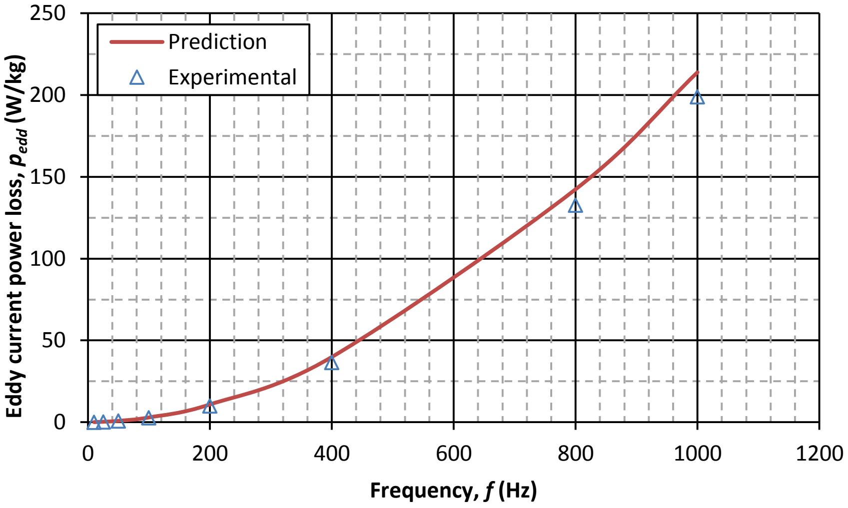

Fig 6-37 Comparison between prediction and experimental results eddy current power loss of three shorted Epstein size laminations of CGO Fe 3 % Si of 0.3 mm thick at peak flux density 1.3 T

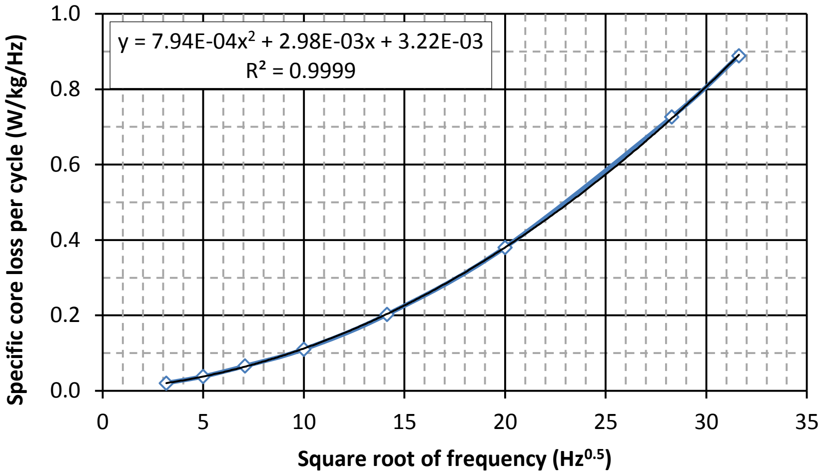

Fig 6-38 Specific core loss per cycle versus square root of frequency of pack of three shorted Epstein size laminations of CGO Fe 3 % Si of 0.3 mm thick at peak flux density 1.5 T

Table 6-6 Power loss components of a pack of three shorted Epstein size laminations of CGO Fe 3 % Si of 0.3 mm thick at peak flux density 1.5 T

Frequency (Hz)	***Total measured loss (W/kg)***	***P_{e1} (W/kg)***	***CC***	***$P_{e2}=P_{e1}\times CC$ (W/kg)***	***P_{e3} (W/kg)***	***Difference (%) $(P_{e3}-P_{e2})/P_{e3}$***
10	0.21	0.08	1.00	0.08	0.08	0.13
25	0.95	0.50	0.722	0.36	0.38	5.34
50	3.292	1.985	0.552	1.095	1.173	6.67
100	11.04	7.940	0.484	3.844	4.029	4.61
200	40.56	31.76	0.438	13.91	14.89	6.57
400	152.3	127.0	0.405	51.46	55.29	6.93
800	581.0	508.2	0.369	187.5	199.6	6.11
1000	888.7	794.0	0.348	276.1	300.3	8.11

P_{e1}: From extrapolation method, P_{e2}: From developed extrapolation method, P_{e3}: From modelling

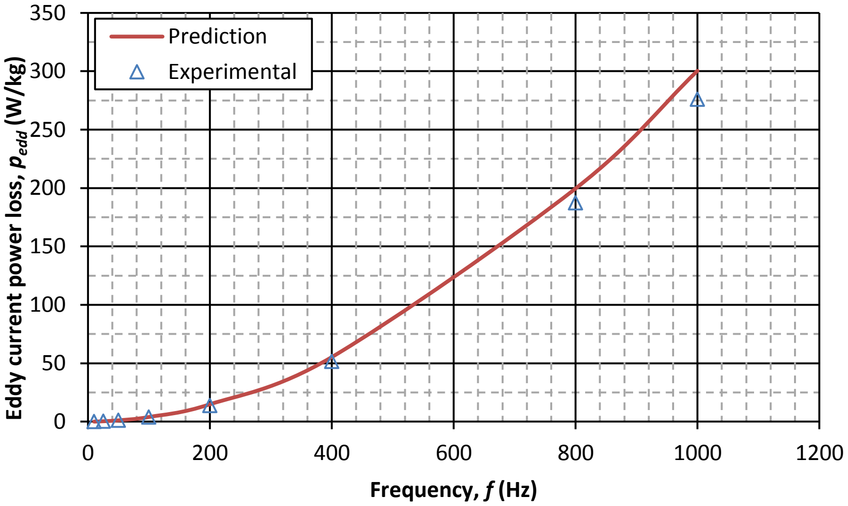

Fig 6-39 Comparison between prediction and experimental results eddy current power loss of three shorted Epstein size laminations of CGO Fe 3 % Si of 0.3 mm thick at peak flux density 1.5 T

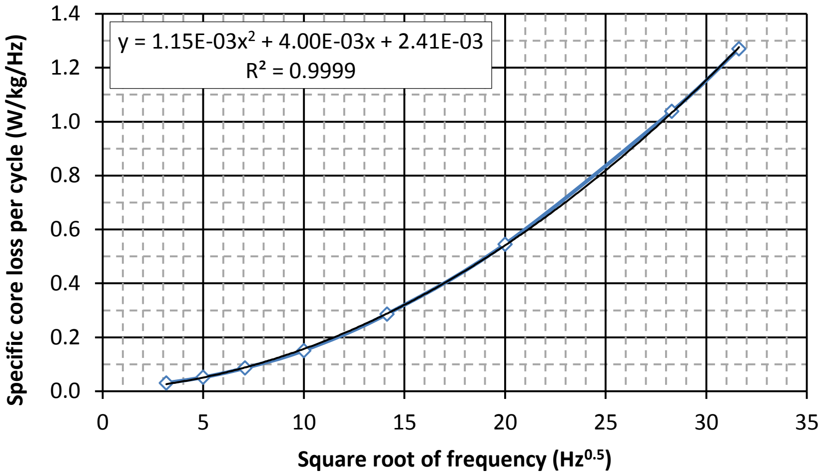

Fig 6-40 Specific core loss per cycle versus square root of frequency of pack of three shorted Epstein size laminations of CGO Fe 3 % Si of 0.3 mm thick at peak flux density 1.7 T

Table 6-7 Power loss components of a pack of three shorted Epstein size laminations of CGO Fe 3 % Si of 0.3 mm thick at peak flux density 1.7 T

***Frequency* (Hz)**	***Total measured loss* (W/kg)**	***P_{e1}* (W/kg)**	***CC***	***$P_{e2}=P_{e1}\times CC$* (W/kg)**	***P_{e3}* (W/kg)**	***Difference (%)* $(P_{e3}-P_{e2})/P_{e3}$**
10	0.30	0.12	1.00	0.12	0.11	-2.59
25	1.30	0.72	0.965	0.70	0.68	-2.38
50	4.312	2.868	0.882	2.528	2.446	-3.38
100	15.13	11.47	0.708	8.121	7.810	-3.98
200	57.32	45.88	0.524	24.05	24.18	0.51
400	218.2	183.5	0.418	76.72	82.94	7.50
800	830.8	734.1	0.381	279.7	306.3	8.68
1000	1271	1147	0.375	430.4	468.2	8.09

P_{e1}: From extrapolation method, P_{e2}: From developed extrapolation method, P_{e3}: From modelling

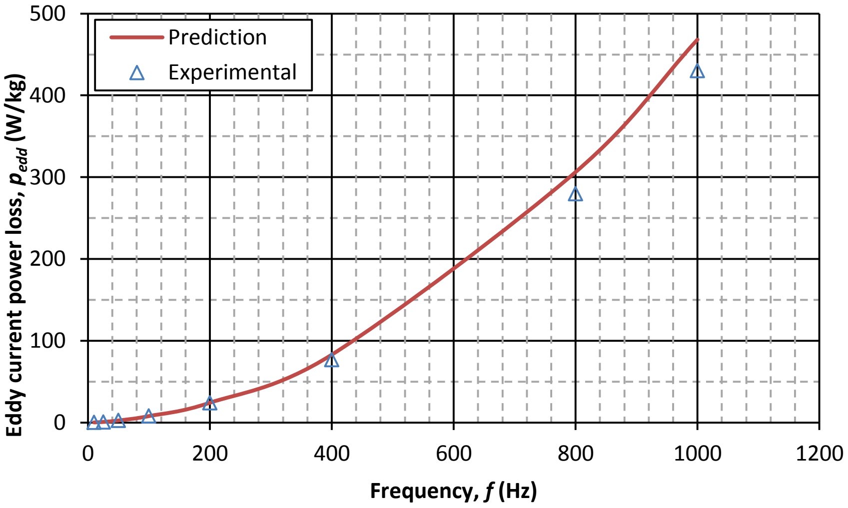

Fig 6-41 Comparison between prediction and experimental results eddy current power loss of three shorted Epstein size laminations of CGO Fe 3 % Si of 0.3 mm thick at peak flux density 1.7 T

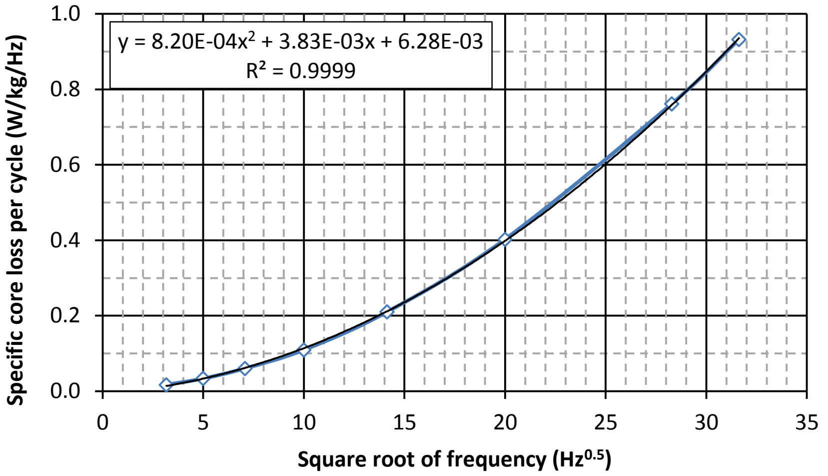

Fig 6-42 Specific core loss per cycle versus square root of frequency of pack of four shorted Epstein size laminations of CGO Fe 3 % Si of 0.3 mm thick at peak flux density 1.3 T

Table 6-8 Power loss components of a pack of four shorted Epstein size laminations of CGO Fe 3 % Si of 0.3 mm thick at peak flux density 1.3 T

Frequency (Hz)	*Total measured loss (W/kg)*	*P_{e1} (W/kg)*	*CC*	*$P_{e2}=P_{e1}\times CC$ (W/kg)*	*P_{e3} (W/kg)*	*Difference (%) $(P_{e3}-P_{e2})/P_{e3}$*
10	0.17	0.08	1.00	0.08	0.08	1.16
25	0.84	0.51	0.668	0.34	0.38	8.96
50	3.025	2.051	0.582	1.194	1.326	9.98
100	10.96	8.204	0.538	4.417	4.935	10.51
200	42.09	32.81	0.487	15.99	18.207	12.16
400	161.1	131.3	0.443	58.19	65.30	10.89
800	609.3	525.0	0.390	204.7	230.8	11.31
1000	931.9	820.4	0.371	304.7	345.6	11.83

P_{e1}: From extrapolation method, *P_{e2}*: From developed extrapolation method, *P_{e3}*: From modelling

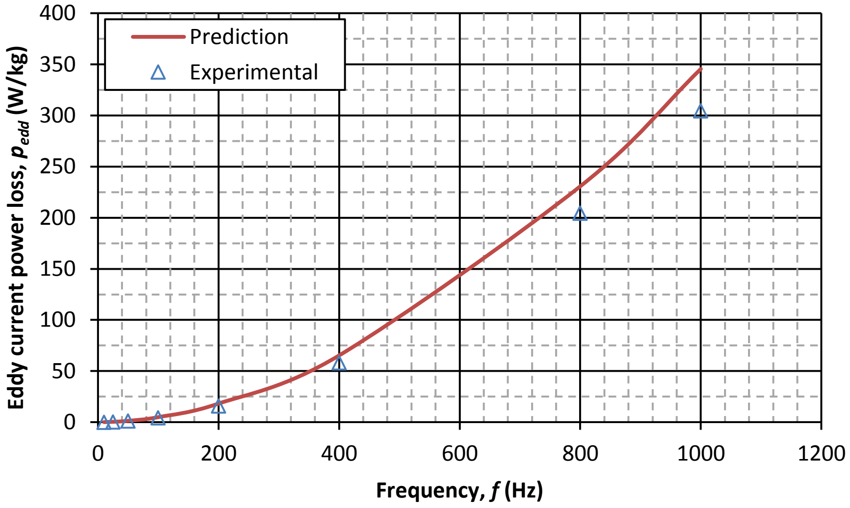

Fig 6-43 Comparison between prediction and experimental results eddy current power loss of four shorted Epstein size laminations of CGO Fe 3 % Si of 0.3 mm thick at peak flux density 1.3 T

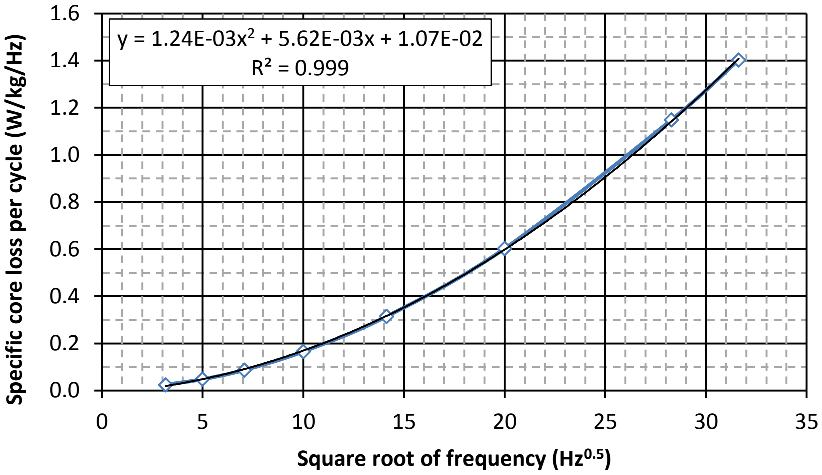

Fig 6-44 Specific core loss per cycle versus square root of frequency of pack of four shorted Epstein size laminations of CGO Fe 3 % Si of 0.3 mm thick at peak flux density 1.5 T

Table 6-9 Power loss components of a pack of four shorted Epstein size laminations of CGO Fe 3 % Si of 0.3 mm thick at peak flux density 1.5 T

Frequency (Hz)	***Total measured loss (W/kg)***	***P_{e1} (W/kg)***	***CC***	***$P_{e2}=P_{e1}\times CC$ (W/kg)***	***P_{e3} (W/kg)***	***Difference (%) $(P_{e3}-P_{e2})/P_{e3}$***
10	0.25	0.12	1.00	0.12	0.12	-0.57
25	1.21	0.78	0.649	0.50	0.55	7.92
50	4.365	3.105	0.541	1.679	1.845	8.98
100	16.57	12.42	0.496	6.158	6.767	9.01
200	62.96	49.68	0.465	23.09	25.21	8.40
400	241.1	198.7	0.425	84.41	91.43	7.68
800	919.0	794.9	0.372	295.7	324.9	8.97
1000	1403	1242	0.359	445.7	487.3	8.52

P_{e1}: From extrapolation method, P_{e2}: From developed extrapolation method, P_{e3}: From modelling

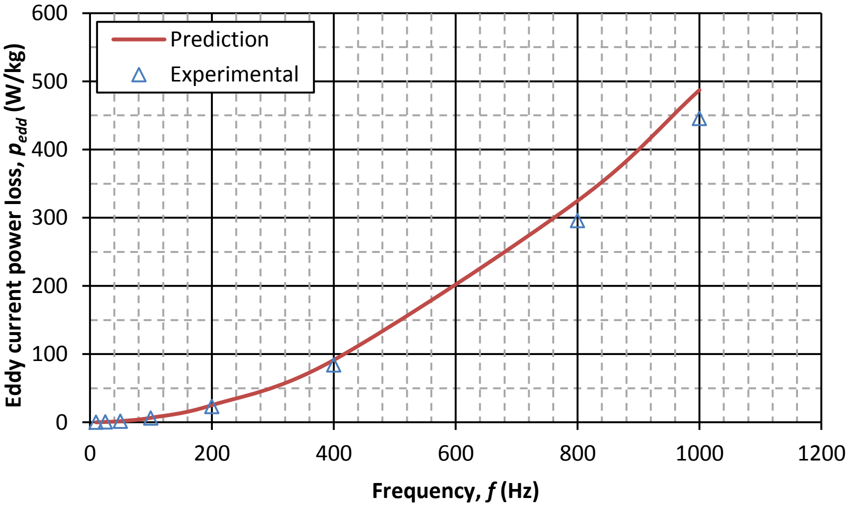

Fig 6-45 Comparison between prediction and experimental results eddy current power loss of four shorted Epstein size laminations of CGO Fe 3 % Si of 0.3 mm thick at peak flux density 1.5 T

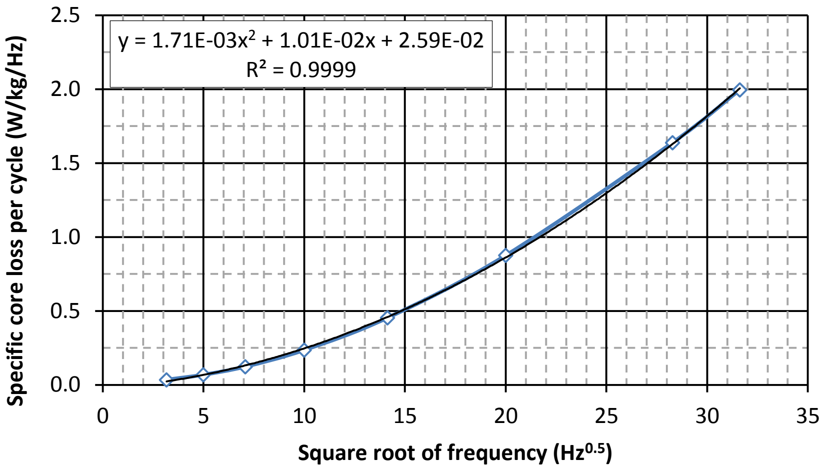

Fig 6-46 Specific core loss per cycle versus square root of frequency of pack of four shorted Epstein size laminations of CGO Fe 3 % Si of 0.3 mm thick at peak flux density 1.7 T

Table 6-10 Power loss components of a pack of four shorted Epstein size laminations of CGO Fe 3 % Si of 0.3 mm thick at peak flux density 1.7 T

Frequency (Hz)	***Total measured loss (W/kg)***	***P_{e1} (W/kg)***	***CC***	***$P_{e2}=P_{e1}\times CC$ (W/kg)***	***P_{e3} (W/kg)***	***Difference (%) $(P_{e3}-P_{e2})/P_{e3}$***
10	0.35	0.17	1.00	0.17	0.20	13.63
25	1.72	1.07	0.960	1.03	1.12	8.90
50	6.163	4.278	0.795	3.399	3.674	7.48
100	23.55	17.11	0.604	10.34	11.28	8.40
200	90.84	68.44	0.513	35.12	37.99	7.55
400	350.2	273.8	0.473	129.4	139.3	7.03
800	1311	1095	0.438	480.1	518.6	7.43
1000	1996	1711	0.425	727.7	787.9	7.65

P_{e1}: From extrapolation method, P_{e2}: From developed extrapolation method, P_{e3}: From modelling

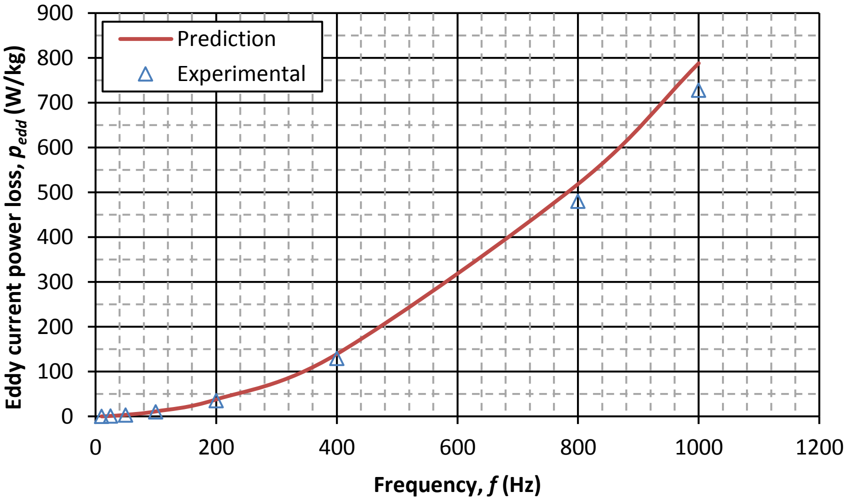

Fig 6-47 Comparison between prediction and experimental results eddy current power loss of four shorted Epstein size laminations of CGO Fe 3 % Si of 0.3 mm thick at peak flux density 1.7 T

In order to compare the results of the shorted laminations together and with the results of single strip laminations, experimental and prediction results of single strip lamination and packs of two, three and four shorted laminations versus magnetising frequency at different peak flux densities are shown in Fig 6-48.

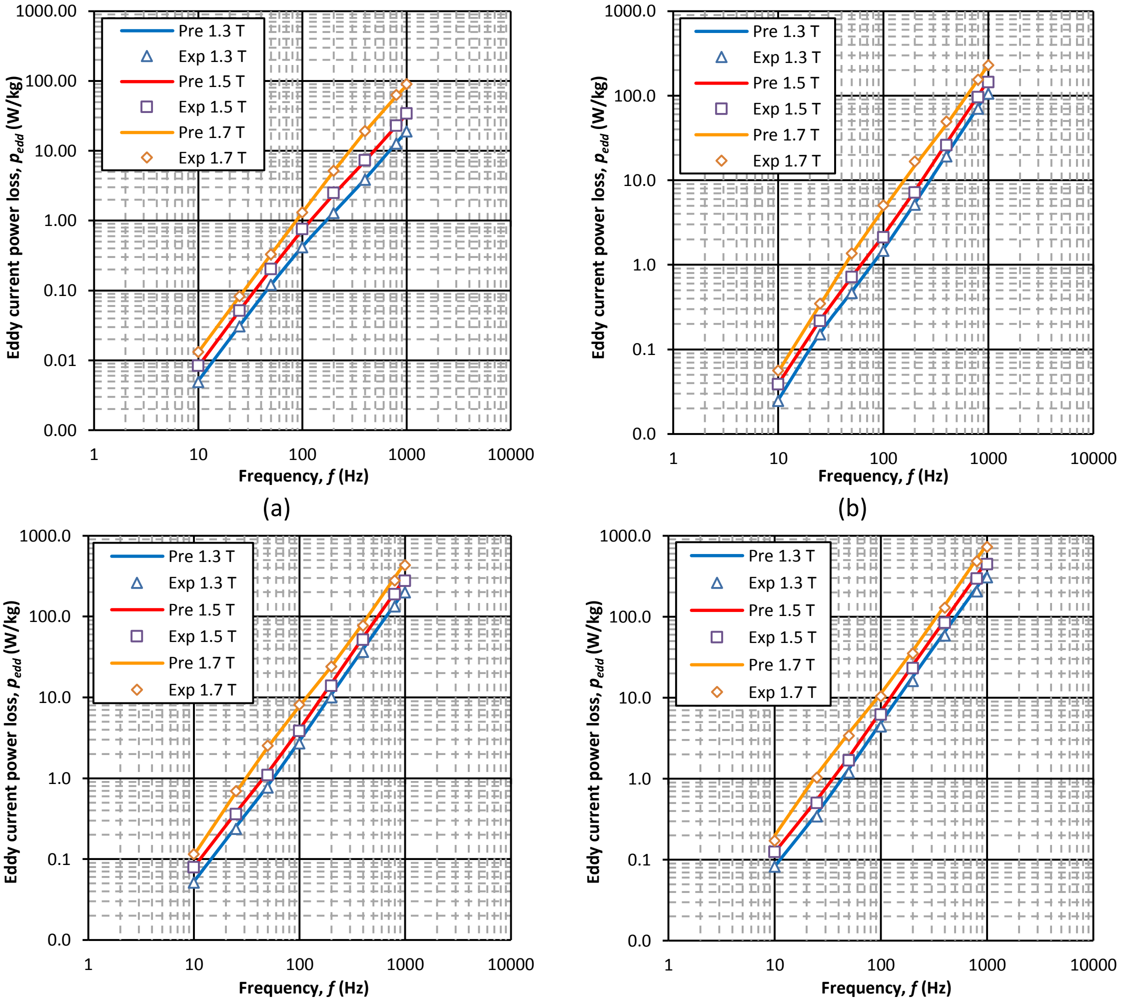

(a) (b)

(c) (d)

Fig 6-48 Comparison of prediction and experimental results of eddy current power loss of (a) single strip Epstein size lamination and packs of (b) two (c) three (d) four shorted laminations at peak flux densities 1.3 T, 1.5 T and 1.7 T

In the case of a single strip lamination, Fig 6-48-a, a close agreement with a maximum difference of less than 4 % was found between the prediction results from the analytical modelling and the experimental results from the developed extrapolation method. On the other hand in the case of shorted laminations the maximum difference between the prediction and experimental results at magnetising frequencies up to 400 Hz was approximately 6 %; however at higher frequencies the difference was increased to approximately 10 %. The differences could be related to the following issues:

- In the analytical model a solid core with thickness of *2na* (*n* number of shorted laminations and *a* half of the thickness of one lamination) was assumed for the shorted laminations; while in the practical measurements the laminations are separated by thin inter-laminar coating.
- Based on the analytical modelling and the equivalent circuit of the lamination, a solid core with uniform electrical properties has been considered; however in the experimental work, the laminations were shorted together by lead free solder with conductivity of 7.69E6 S/m which is about 3.5 times greater than conductivity of CGO electrical steel.
- As proved by the FEM modelling, eddy current density at the shorted ends is much higher than the steel; however in the analytical modelling, since the burred laminations are equalised by a solid core of *2na* thick, eddy current density at the end edges of the equivalent corers was considered almost the same as the steels. Figs 6-49 and 6-50 show eddy current distribution at the end edge of three and five burred laminations and the equivalent solid cores at magnetising frequency of 50 Hz.

In spite of that, since the analytical model is based on the physical dimension of the lamination, it is capable to develop the model and take into account the effect of the shorted edges and the inter-laminar insulating coating.

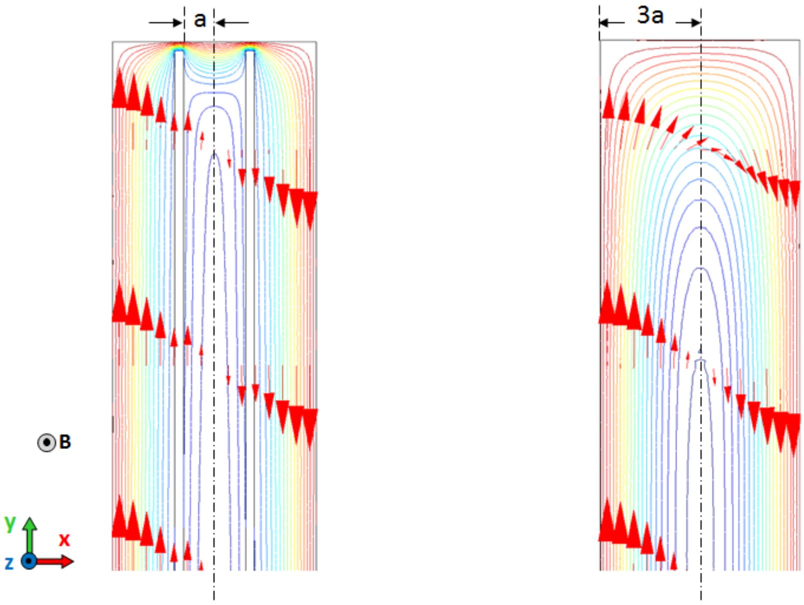

(a) (b)

Fig 6-49 Eddy current distribution at end edge of (a) three burred lamination of 0.3 mm thick (b) equivalent solid lamination of 0.9 mm thick; at 50 Hz

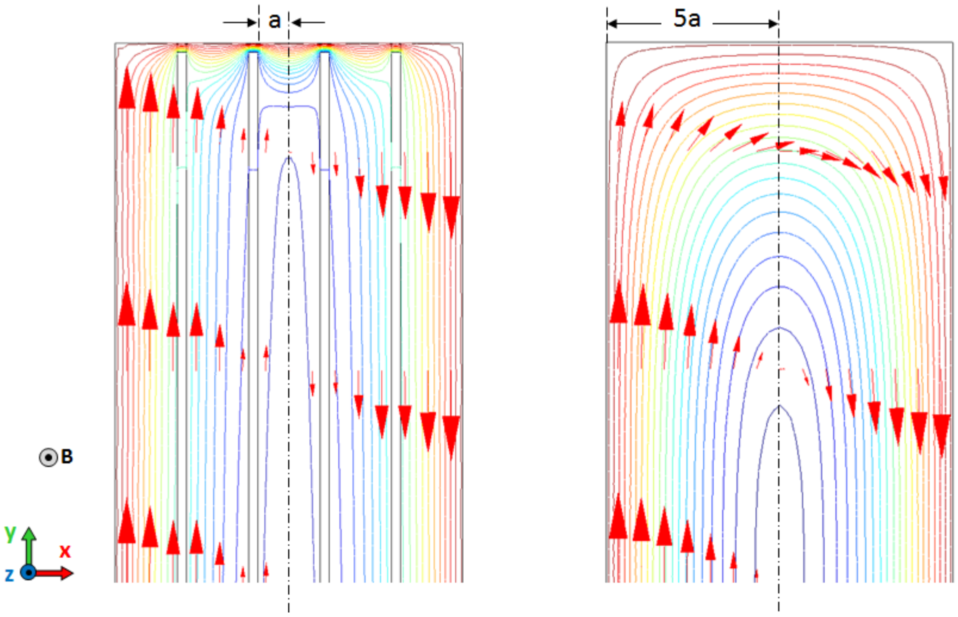

(a) (b)

Fig 6-50 Eddy current distribution at end edge of (a) five burred lamination of 0.3 mm thick (b) equivalent solid lamination of 1.5 mm thick; at 50 Hz

6.6. Conclusion

In this chapter fundamental concepts of inter-laminar faults and the consequences on magnetic cores were presented. Based on a preliminary hypothesis, an equivalent configuration was proposed for magnetic cores with inter-laminar faults. 2-D FEM modelling was performed to verify the equivalent configuration and visualise eddy current paths along the lamination thickness. Based on the FEM modelling and analytical results, it was found that skin effect is a key factor in the eddy current power loss investigation of magnetic cores not only at high frequencies, but also at low frequencies when the core is affected by the edge burrs.

Using the equivalent circuit of single strip lamination developed in chapter 5, an analytical model was proposed to calculate and predict the eddy current power loss of magnetic cores with inter-laminar fault. In the analytical modelling, skin effect and its consequences were considered. In addition, non-uniform flux density distribution, complex relative permeability and the non-linear *B (H)* characteristic have been considered in the eddy current modelling; therefore the proposed model provides accurate loss calculation for a wide range of flux density and magnetising frequency.

In order to support the analytical modelling, packs of two, three and four Epstein size CGO laminations were shorted together artificially and the total power loss was measured by using a single strip tester. Eddy current loss of each pack was then separated using the developed extrapolation method.

Experimental and analytical results of eddy current power loss measurement showed that inter-laminar faults have a significant effect on the magnetic properties of the magnetic cores. When inter-laminar faults create fault current loops, high inter-laminar fault currents are induced in the core. The values of these currents depend on the number of laminations being in electrical contact due to the faults, geometry and resistance of the fault current loop, clamping pressure at the defected area of the core and operating frequency and peak flux density.

As a general note the results presented in this chapter show the impact of inter-laminar faults on the performance of the magnetic cores and also the importance of edge burr removal, as a major source of inter-laminar fault.

References

[6.1] K Lee, J Hong, K Lee, S B Lee and E J Wiedenbrug, "*A Stator Core Quality Assessment Technique for Inverter-fed Induction Machines*", IEEE Industry Applications Society Annual Meeting, Oct 2008, pp 1-8

[6.2] J M Bourgeois and F Lalonde, "*Apparatus and Method for Evaluation a Condition of a Magnetic Circuit of an Electric Machine*," U.S. Patent 5 990 688, Nov. 23, 1999

[6.3] G B Kliman, S B Lee, M R Shah, R M Lusted, and N K Nair, "*A new method for synchronous generator core quality evaluation*," IEEE Trans. Energy Convers., Vol. 19, NO. 3, , Sep. 2004, pp. 576–582

[6.4] K Lee, J Hong, K Lee, S B Lee and E J Wiedenbrug, "*A Stator Core Quality Assessment Technique for Inverter-fed Induction Machines*", IEEE Industry Applications Society Annual Meeting, Oct 2008, pp 1-8

[6.5] S B Lee, G B Kliman, M R Shah, W T Mall, N K Nair and R M Lusted "*An Advanced Technique for Detecting Inter-Laminar Stator Core Faults in Large Electric Machines*" IEEE Trans On Ind. App, Vol. 41, NO. 5, Sep/Oct 2005, pp. 1185–1193

[6.6] S B Lee, G B Kliman, M R Shah, N K Nair and R M Lusted "*An Iron Core Probe Based Inter-Laminar Core Fault Detection Technique for Generator Stator Cores*" IEEE Trans. Energy Convers., Vol. 20, No. 2, Jun. 2005, pp. 344–351

[6.7] S B Lee, G Kliman, M Shah, D Kim, T Mall, K Nair and M Lusted, "*Experimental Study of Inter-laminar Core Fault Detection Techniques based on Low Flux Core Excitation*" IEEE Trans On Energy Convers, Vol. 21, No. 1, March 2006, pp 85-94

[6.8] H Hamzehbahmani, P Anderson, J Hall, and D Fox, "*Eddy Current Loss Estimation of Edge Burr-Affected Magnetic Laminations Based on Equivalent Electrical Network—Part I: Fundamental Concepts and FEM Modelling*", IEEE TRANSACTIONS ON POWER DELIVERY, VOL. 29, NO. 2, APRIL 2014, pp 642-650

[6.9] S B Lee, G B Kliman, M R Shah, W T Mall, N K Nair and R M Lusted "*An Advanced Technique for Detecting Inter-Laminar Stator Core Faults in Large Electric Machines*" IEEE Trans On Industry Applications, VOL. 41, NO. 5, Sep/Oct 2005, pp. 1185–1193

[6.10] S B Lee, G Kliman, M Shah, D Kim, T Mall, K Nair and M Lusted, "*Experimental Study of Inter-laminar Core Fault Detection Techniques based on Low Flux Core Excitation*" IEEE Trans On Energy Convers, Vol. 21, No. 1, March 2006, pp 85-94

[6.11] M B Aimoniotis and A J Moses, "*Evaluation of Induced Eddy Currents in Transformer Sheets Due to Edge-Burrs, Employing Computer Aided Design Programs*," in Athens Power Tech '93 Proc., 1993, vol. 2, pp. 847–849

[6.12] R Mazurek, H Hamzehbahmani, A J Moses, P I Anderson, F J Anayi and T Belgrand, "*Effect of Artificial Burrs on Local Power Loss in a Three-Phase Transformer Core*" IEEE Trans. Mag. VOL. 48, NO. 4, April 2012, pp 1653-1656

[6.13] A J Moses and M Aimoniotis, "*Effects Of Artificial Edge Burrs on the Properties of a Model Transformer Core*," Physica Scripta, Vol. 39, 1989, pp. 391–393

[6.14] R Mazurek, P Marketos, A J Moses and J N Vincent "*Effect of Artificial Burrs on the Total Power Loss of a Three-Phase Transformer Core*", IEEE Trans. Magn., VOL. 46, NO. 2, 2010, pp.638 -641

[6.15] J P Bielawski, S Duchesne, D Roger, C Demian and T Belgrand, "*Contribution to the Study of Losses Generated by Inter-Laminar Short-Circuits*", IEEE Trans. Magn., Vol. 48, NO. 4, April 2012, pp. 1397-1400

[6.16] Edge burr, Wikipedia, The Free Encyclopedia, Retrieved December 12, 2012, from http://en.wikipedia.org/wiki/Edge_burr

[6.17] IC LEARNING SERIES, "*Sheet Metal Fabrication*" Industrial Centre, The Hong Kong Polytechnic University, May 2012

[6.18] http://www.custompartnet.com/wu/sheet-metal-shearing

[6.19] W J Deng, Z C Xie, P L and T K Xu, "*Study on Burr Formation at the Top Edge in Rectangular Groove Cutting*", Journal of Advances in Materials Science and Engineering, Article ID 956208, Vol. 2012

[6.20] C A Schulz, S P Duchesne, D Roger and J N Vincent, "*Capacitive Short Circuit Detection In Transformer Core Laminations*", Journal of Magnetism and Magnetic Materials 320 (2008) e911–e914

[6.21] D B Paley "*Current Low Power Core Testing Using EL CID*" IEEE Colloquium "Understanding your condition monitoring (Ref. No. 1999/117)" April 1999, pp 7/1-7/4

[6.22] C A Schulz, S Duchesne, D Roger and J N Vincent "*Short Circuit Current Measurements between Transformer Sheets*", IEEE Trans Magn, Vol. 46, No. 2, Feb 2010, pp 536-539

[6.23] C A Schulz, D Roger, S P Duchesne and J N Vincent, "*Experimental Characterization of Interlamination Shorts in Transformer Cores*", IEEE Trans Magn, Vol. 46, No. 2, Feb 2010, 614-617

[6.24] D R Bertenshaw, J F Lau and D J Conley, "*Evaluation of EL CID Indications not Associated with Stator Core Inter-laminar Insulation Faults*" IEEE Electrical Insulation Conference, June 2011, pp 254- 260

[6.25] N Derebasi, I Kucuk, A J Moses, "*Mathematical Model for Estimation of Dynamic Losses of Grain Oriented 3% Sife Toroidal Wound Cores up To 1 KHZ*", Sensors and Actuators A: Physical vol. 106 issue 1-3 September 15, 2003. pp. 101-103

[6.26] Y Zhang, M C Cheng, P Pillay, "*Magnetic Characteristics and Excess Eddy Current Losses*", IEEE Industry Applications Society Annual Meeting, 2009, pp. 1-5

[6.27] A Bermúdez, D Gómez and P Salgado, "Eddy-Current Losses in Laminated Cores and the Computation of an Equivalent Conductivity", IEEE Trans Mahn , VOL. 44, NO. 12, DECEMBER 2008, pp. 4730-4738

[6.28] T L Mthombeni and P Pillay, "*Physical Basis for the Variation of Lamination Core Loss Coefficients as a Function of Frequency and Flux Density*," in Proc. IECON, Paris, France, Nov. 6–10, 2006, pp. 1381–1387

[6.29] Moreau, L Popiel and J L Pages, "*Proximity Losses Computation with a 2D Complex Permeability Modelling*", IEEE Trans Magn, VOL 34, NO 5, Sept 1998, pp. 3616-3619

[6.30] R Lebourgeoisa, S Berenguerb, C Ramiarinjaonab and T Waeckerle "*Analysis of the Initial Complex Permeability Versus Frequency of Soft Nanocrystalline Ribbons and Derived Composites*", Journal of Magnetism and Magnetic Materials 254–255, 2003, pp. 191–194

[6.31] D P Arnold, I Z and M G Allen "*Analysis and Optimization of Vertically Oriented, Through-Wafer, Laminated Magnetic Cores in Silicon*" Journal of Micromech. Microeng. No 15, 2005, pp 971–977

[6.32] D Roger, E Napieralska-Juszczak, A Henneton "*High Frequency Extension of Non-Linear Models of Laminated Cores*", COMPEL: The International Journal for Computation and Mathematics in Electrical and Electronic Engineering, Vol. 25 Iss: 1, 2006, pp. 140-156

[6.33] Ruifeng Huang and Daming Zhang, "*Experimentally Verified Mn–Zn Ferrites' Intrinsic Complex Permittivity and Permeability Tracing Technique Using Two Ferrite Capacitors*", IEEE Trans Magn, VOL. 43, NO. 3, MARCH 2007, pp 974-981

[6.34] K G N B Abeywickrama, A D Podoltsev, Y V Serdyuk, and S M Gubanski, "*Computation of Parameters of Power Transformer Windings for Use in Frequency Response Analysis*", IEEE Trans Magn, VOL. 43, NO. 5, MAY 2007, pp. 1983-1990

[6.35] K G Nilanga, B Abeywickrama, T Daszczynski, Y V Serdyuk and S M Gubanski," *Determination of Complex Permeability of Silicon Steel for Use in High-Frequency Modeling of Power Transformers*", IEEE Trans Magn, VOL. 44, NO. 4, April 2008, pp. 438-444

[6.36] C A Schulz, D Roger, S Duchesne, J N Vincent, "*E.M.F. Between Magnetic Transformer Sheets: Theoretic Aspects*", XIV International Symposium on Electromagnetic Fields in Mechatronics, Electrical and Electronic Engineering, France, Sept. 2009

[6.37] S D Mitchell and J S Welsh, "*The Influence of Complex Permeability on the Broadband Frequency Response of a Power Transformer* ", IEEE Trans. ON Power Delivery, VOL. 25, NO. 2, April 2010, pp. 803-813

[6.38] J Wang, H Lin, Y Huang and L Huang, “*Numerical Analysis of 3D Eddy Current Fields in Laminated Media Under Various Frequencies*” IEEE Trans. Mag. VOL. 48, NO. 2, February 2012, pp 267-270

[6.39] A Geri, A Salvini and G M Veca “*Displacement Eddy Current Computation in Magnetic Laminates*” IEEE Trans. Mag. VOL. 30, NO. 2, March 1994, pp. 1075-1077

[6.40] A 937/A937 M-01, “*Standard Method for Determining Inter-Laminar Resistance of Insulating Coatings Between Two Adjacent Test Surfaces*”

[6.41] Z Godec “*Comparison Of Tests For Insulating Coatings On Steel Sheet*” IEEE Transaction on Electrical Insulation, Vol. EI-15 No.2, April 1980, pp. 95-103

[6.42] BS EN 10282:2001 “*Method Of Test for the Determination of Surface Insulation Resistance of Electrical Sheet and Strip*”

[6.43] M C Marion-Pera, A Kedous-Lebouc, T Waeckerle, and B Comut, “*Characterization of SiFe Sheet Insulation*”, IEEE Trans Magn, VOL 31 . NO 4. July 1995, pp 2408-2415

[6.44] M C Marion-Péra, A Kedous-Lebouc, B Cornut, P Brissonneau, “*Analysis and Comparison of Magnetic Sheet Insulation Tests*” Journal of Magnetism and Magnetic Materials 133 (1994) pp. 396-398

[6.45] P J Tavner, R J Jackson “*Coupling of Discharge Currents Between Conductors of Electrical Machines Owing to Laminated Steel Core*”, IEE Proceedings-B Electric Power Applications 135(6) Nov 1988, pp. 295-307

[6.46] D Yao and C Sullivan, “*Effect of Capacitance on Eddy-Current Loss in Multi-Layer Magnetic Films for MHZ Magnetic Components*,” in IEEE Energy Conversion Congress and Exposition, Sep. 2009, pp. 1025 – 1031.

[6.47] E Lamprecht, R Gräf, “*Fundamental Investigations of Eddy Current Losses in Laminated Stator Cores Created Through the Impact of Manufacturing Processes*” 1st International conference on Electric Drives Production (EDPC), Sept. 2011, pp. 29-35

CHAPTER 7

Experimental Study on Inter-Laminar Short Circuit Faults at Random Positions in Laminated Magnetic Cores

7.1. Introduction

Analytical and experimental studies have been performed to detect inter-laminar faults and investigate their effect on the magnetic properties of the laminated cores [7.1]–[7.9]. However in most of these methods it was assumed that the inter-laminar faults occur between the adjacent laminations of the core at set points which result in a short circuit volume with a well-known location and physical dimensions; while in practice they appear at random positions which create different patterns of inter-laminar short circuits.

Apart from the magnetisation condition, e.g. operating flux density and magnetising frequency, magnetic permeability and other magnetic and electric properties of the magnetic cores, the impact of number of the shorted laminations, location of the fault, distance and angle between the fault points of each particular fault current loop on the extra power loss are difficult to define precisely. Investigating the effect of these parameters requires a detailed 3-D FEM or analytical model of the core in which the properties of the material in three directions, and other related parameters and criteria, are considered. However accurate experimental works will aid the categorisation of inter-laminar faults and distinguish the most important and critical faults.

The main aim of this chapter is to model inter-laminar insulation faults with different configurations and investigate their influence on the magnetic properties of laminated magnetic cores.

7.2. Experimental set-up

In this chapter the effect of inter-laminar short circuit faults with different configurations on the total power loss of the magnetic cores was investigated on stacks of four Epstein size laminations of CGO Fe 3 % Si of 0.3 mm thick (M105-30P). Different configurations of inter-laminar short circuit faults, which might occur in real scale magnetic cores, were applied artificially on each stack as follows:

- Modelling of inter-laminar fault caused by key-bar of the stator cores
- Modelling of inter-laminar fault at set positions
- Modelling of inter-laminar fault with step-like positions
- Modelling of inter-laminar fault at off-set positions
- Modelling of inter-laminar fault at multiple off-set positions

Similar to the experiments reported in chapter 6 lead-free solder was used to apply artificial short circuits on the stacks. Each pack of laminations was magnetised separately using the measuring system described in chapter 6 and the single strip tester developed in chapter 7 at peak flux densities of 1.1 T, 1.3 T, 1.5 T and 1.7 T and magnetising frequencies from 50 Hz up to 1000 Hz. Total power loss of each stack was measured and recorded in separate databases. Power loss measurements were repeated three times at each flux density and frequency in all experiments with repeatability [7.10] of better than 0.4 %. Experimental results presented in this chapter are the average of three measurements. To ensure that each stack has no inherent inter-laminar fault, and also in order to qualify the results of the loss measurement after applying the artificial faults, total loss was initially measured in the case of no applied fault; the results are shown in Table 7-1 and Fig 7-1.

Table 7-1 Specific core loss of a stack of four Epstein size laminations at different flux densities and magnetising frequencies

B_{pk} (T)	Total measured power loss (W/Kg)				
	50 Hz	100 Hz	200 Hz	500 Hz	1000 Hz
1.1	0.504	1.47	4.41	19.6	61.9
1.3	0.685	2.01	6.05	27.2	88.5
1.5	0.899	2.65	7.99	36.9	125
1.7	1.19	3.44	10.4	50.3	177

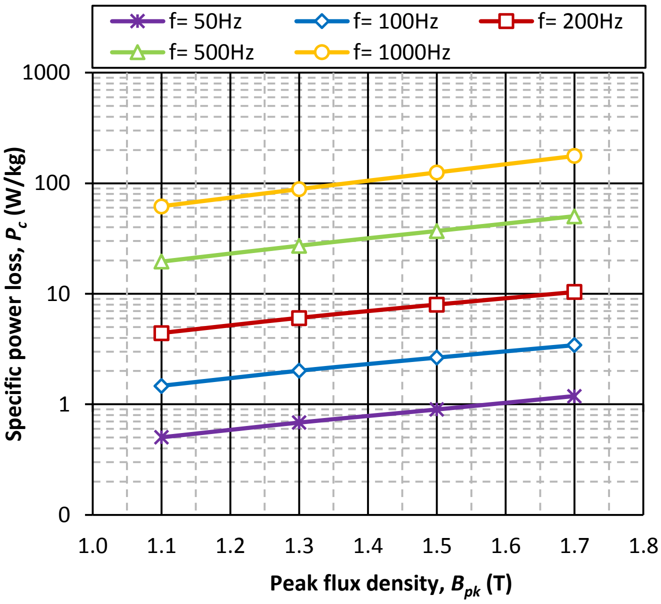

Fig 7-1 Specific power loss of a pack of four Epstein size lamination of CGO vs. peak flux density at different frequencies

Nominal power loss of the material shown in Table 7-1 and Fig 7-1 and power loss of a stack with inter-laminar fault of 10 mm wide applied at set-points were considered as two reference values to compare the results of each measurement.

7.3. Modelling of inter-laminar faults caused by the key-bar of stator cores

As outlined in section 6.2.2 of chapter 6, there might be a permanent short circuit between the stator laminations at the outer diameter, which is caused by the key-bar, welds or housing. Therefore possible inter-laminar faults at any points between the laminations could result in fault current loop. Considering this fact, two kinds of faults on a section of stator core are shown schematically in Figs 7-2-a and 7-2-b. In Fig 7-2-a the outer diameter of the core is totally shorted and a partial fault is applied in one of the stator slots; while in Fig 7-2-b two partial faults are applied on opposite sides of the core slot at set points. As the first part of the study, these faults were modelled separately on stacks of four laminations. A schematic and photograph of top view of the stacks showing location of the applied short circuits are shown in Figs 7-3 and 7-4, respectively.

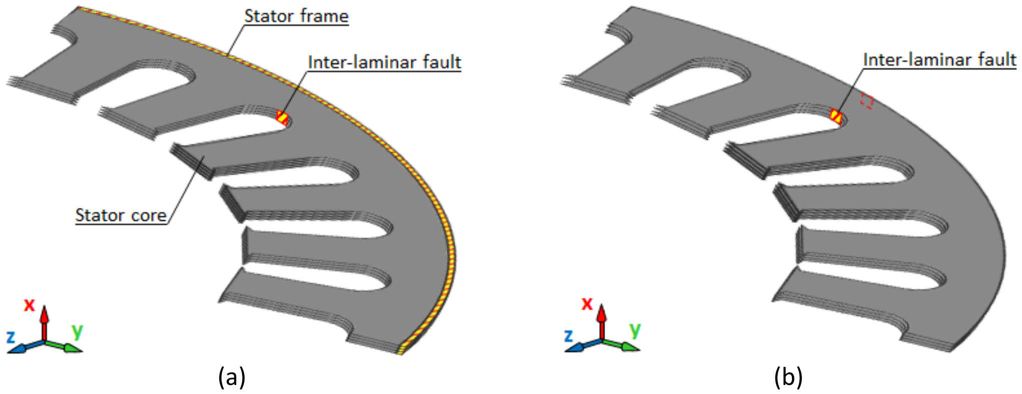

(a) (b)

Fig 7-2 Perspective view of a stator lamination with (a) permanent short in the outer frame and inter-laminar fault in core slot (b) inter-laminar fault between the outer frame and core slot

Total power loss of each stack was measured separately; the results together with the nominal loss of the material versus peak flux density at different frequencies are shown in Fig 7-5. Experimental results showed extra power loss in the shorted stacks compare to the normal power losses which is caused by the created fault current loops in the stacks. However power loss of the pack 1, with a short on one side, was higher than that of the pack 2 at all flux densities and frequencies with the maximum difference of about 18 %.

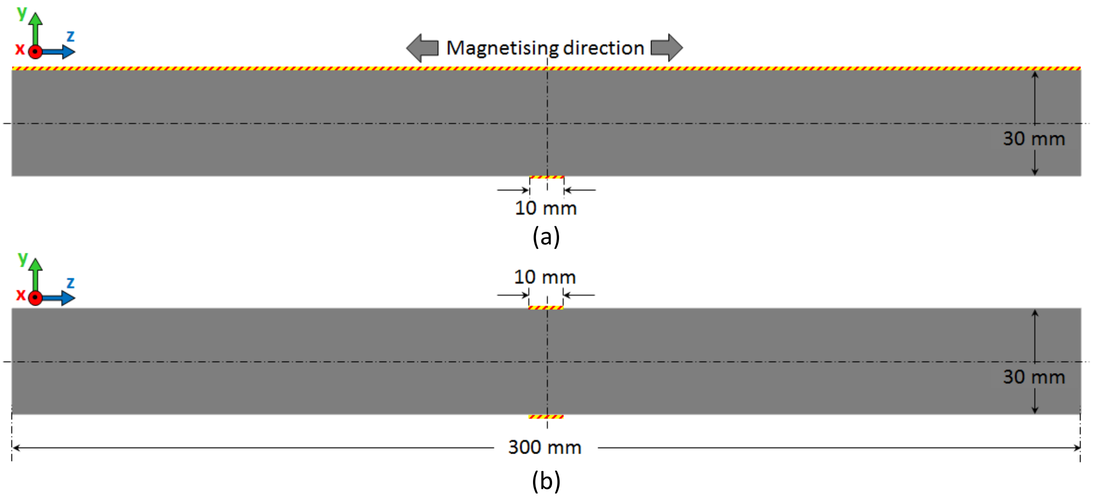

Fig 7-3 Top view of a stack of laminations with inter-laminar short circuit to model the inter-laminar faults of Fig 7-2 (a) pack # 1 (b) pack # 2

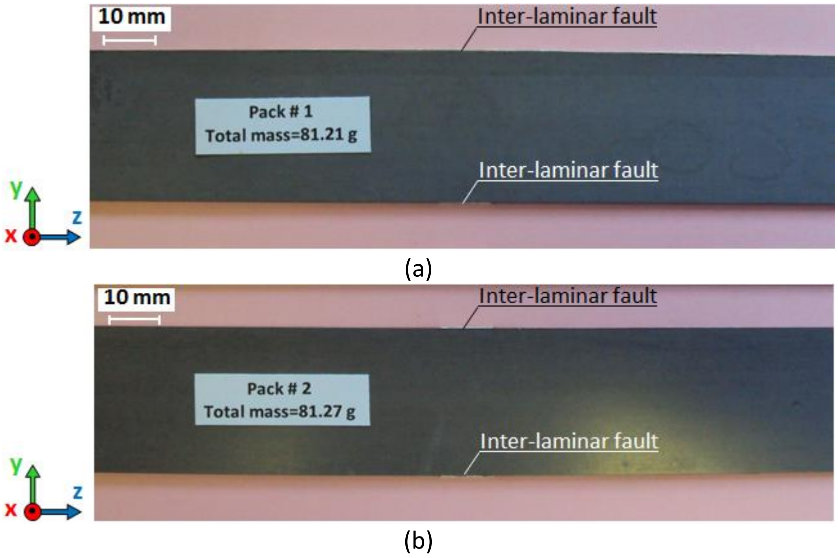

Fig 7-4 Photograph of top view of a stack of laminations with an inter-laminar short circuit to model the inter-laminar faults of Fig 7-2 (a) pack # 1 (b) pack # 2

Although the bottom sides of both packs are shorted with artificial shorts of the same width the higher power loss of pack 1 indicates a larger fault current loop than pack 2. As a result, a permanent short circuit caused by the key-bar or welded frame should be considered in the study of inter-laminar faults on the stator cores. Furthermore in order to reduce the risk of creation of fault current loops, the laminations preferably should be isolated from the key-bar of the stator frame.

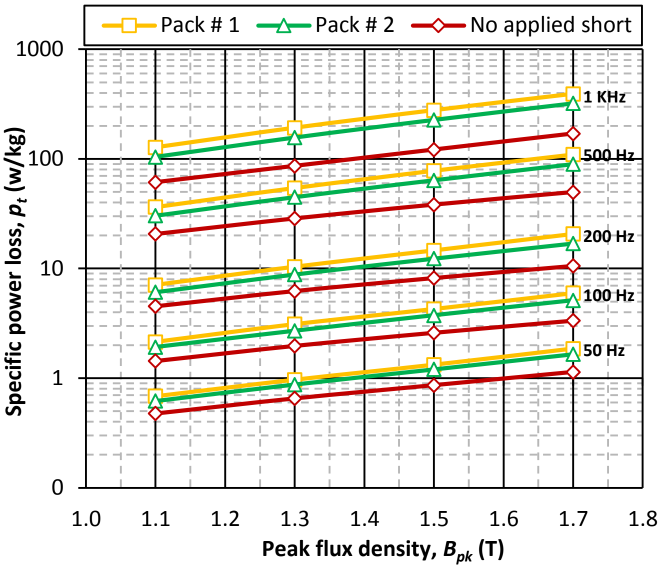

Fig 7-5 Comparison of total power loss of the packs # 1 and # 2 of Fig 7-3 with the normal loss of the material versus peak flux density at different frequencies

7.4. Modelling of inter-laminar faults in a stack of laminations at set positions

In the next part of the experiments, the effect of inter-laminar short circuits at set positions on total power loss was studied. The specific power loss of the stack without inter-laminar fault was measured and then artificial shorts, 10 mm wide, were applied at three positions and the total power loss of the stack was measured at each stage. Schematics of the side view of the stacks with one, two and three shorts are shown in Figs 7-6-a to 7-6-c, respectively. A schematic and photograph of the top view of the stack with three shorts are also shown in Fig 7-7 and Fig 7-8, respectively. In order to obtain the extra power loss caused by the applied short circuits, the specific power loss in normal operation was subtracted from the total power loss of each stage. The extra power losses versus the number of the applied short circuits at different frequencies are shown in Fig 7-9.

Experimental results of Fig 7-9 show a linear relation between the extra power loss caused by the applied short circuits and the number of applied shorts at all flux densities and magnetising frequencies. The reason is related to the tendency of the electric currents to flow through the path of least resistance, i.e. in the configuration of Fig 7-7 electrical resistance between points *a-a´* is less than that of points *a-b´* or *a-c´*, which result in independent fault current loops in the stack. Therefore it can be concluded that the artificial shorts applied to the stack create three independent fault current loops in the stack and hence there is no current flow between the shorted volumes.

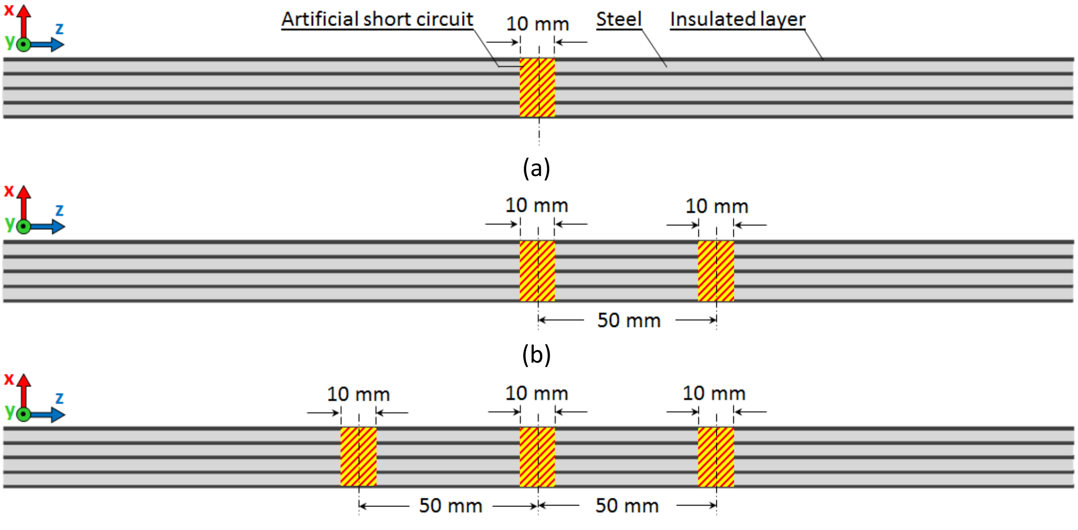

Fig 7-6 Side view of a stack of four laminations with inter-laminar short circuits applied at (a) one set point (b) two set points and (c) three set points

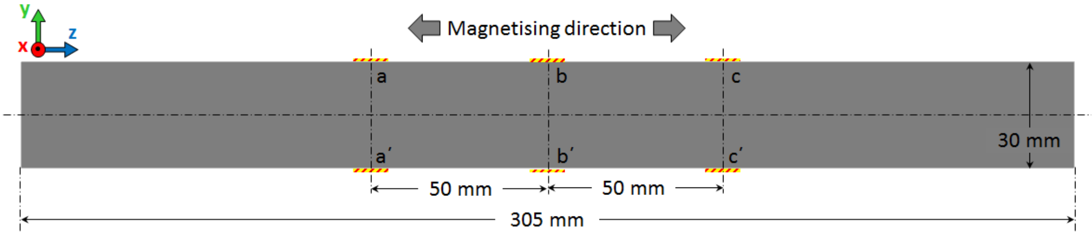

Fig 7-7 Top view of a stack of laminations with inter-laminar short circuits applied at three set points

Fig 7-8 Photograph of top view of a stack of laminations with inter-laminar short circuits applied at three set points

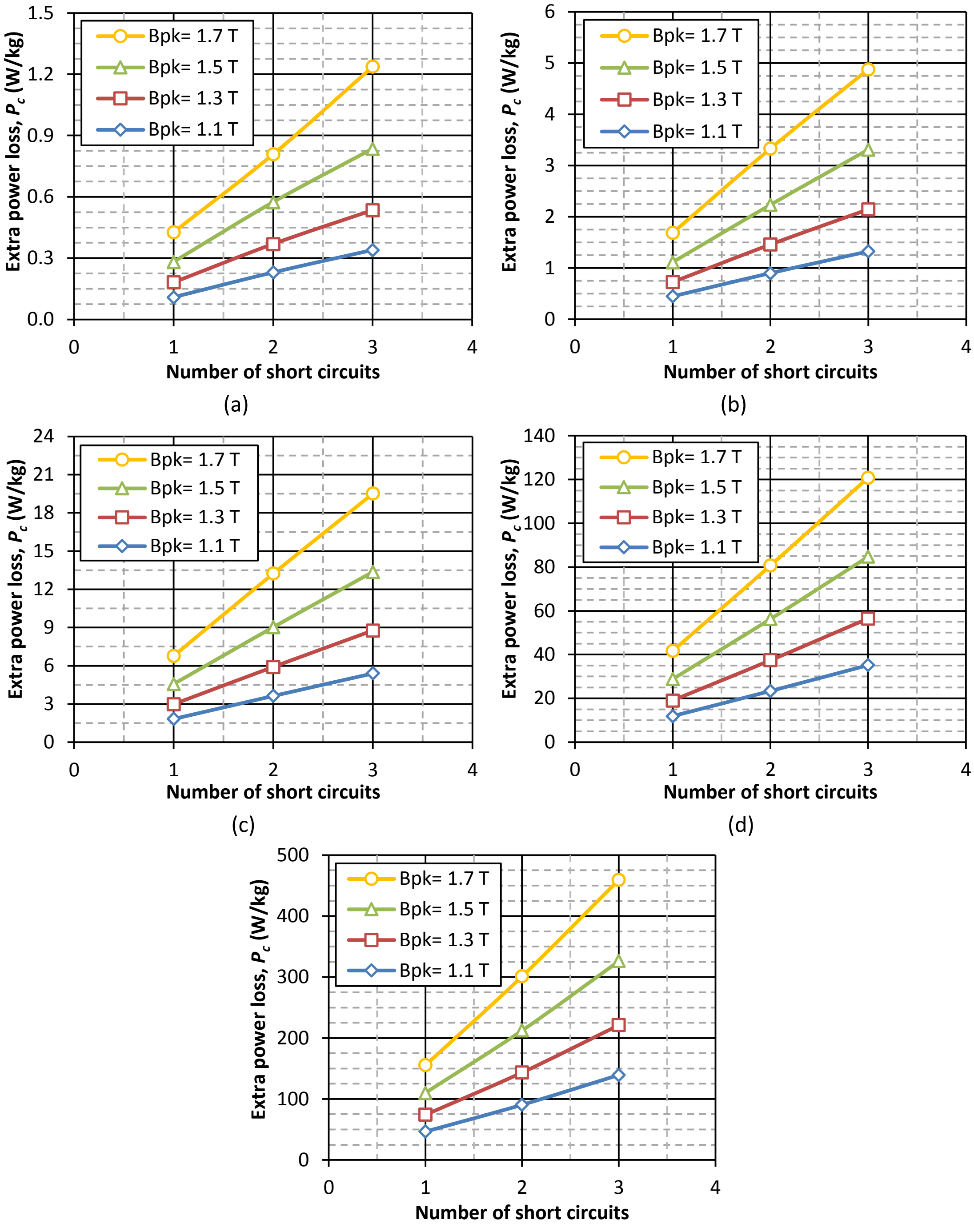

(a) (b) (c) (d) (e)

Fig 7-9 Extra power loss caused by the artificial faults of Fig 7-8 at frequency of (a) 50 Hz (b) 100 Hz (c) 200 Hz (d) 500 Hz and (e) 1000 Hz

Although this issue might be more complicated in real scale magnetic cores, especially in stator cores of rotary machines, the electrical resistance between the shorted points on opposite sides of the magnetic cores was found to be a key factor in determination of the fault current loops.

In chapter 5 an analytical model was developed to predict eddy current loss of single strip laminations over a wide range of flux density and frequency. The developed model was then used in chapter 7 to calculate the extra power loss caused by an inter-laminar fault along the whole length of both sides of stacks of laminations. In a quantitative investigation, extra power loss caused by a single short circuit of the configuration of Fig 7-8 was calculated based on the same procedure as chapter 7. A comparison of the analytical results and the experimental results versus flux density at different frequencies is shown in Figs 7-10 and 7-11.

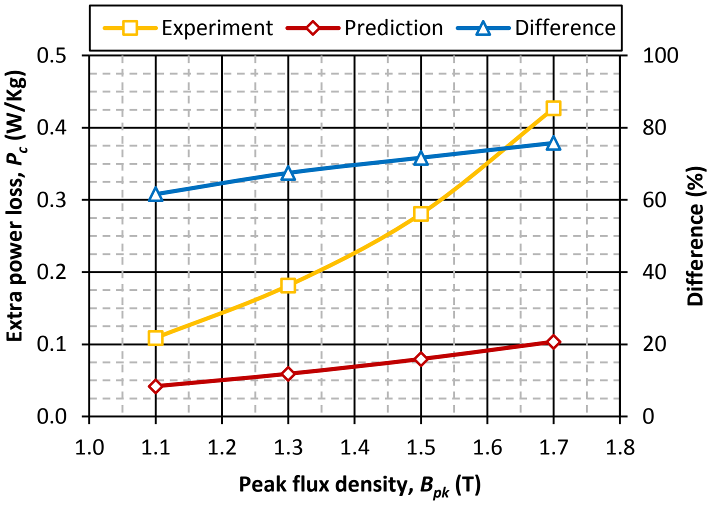

(a)

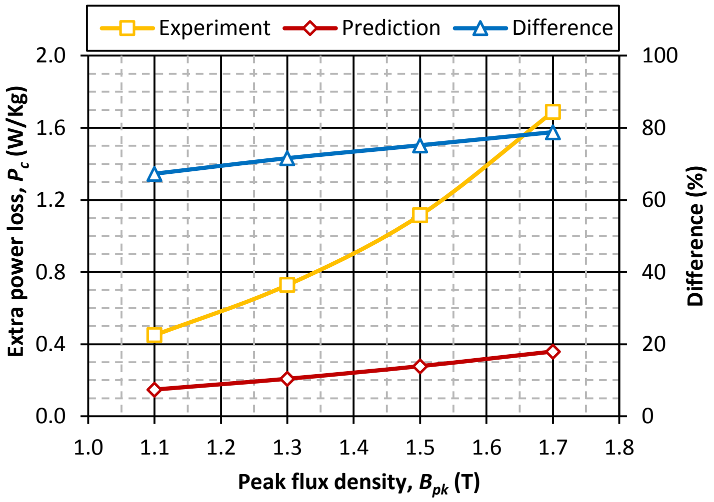

(b)

Fig 7-10 Comparison of prediction and experimental results of extra power loss caused by a single short circuit at set position at frequency of (a) 50 Hz (b) 100 Hz

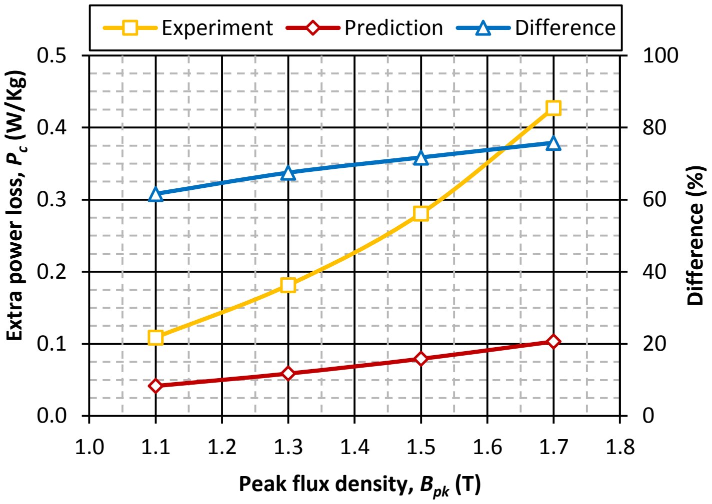

(a)

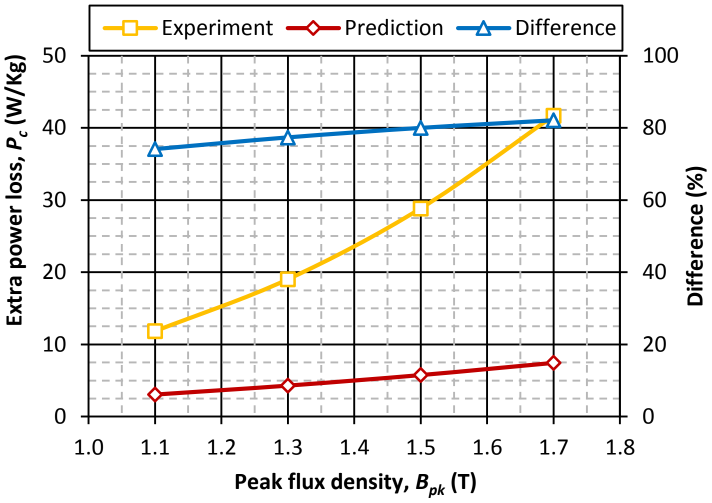

(b)

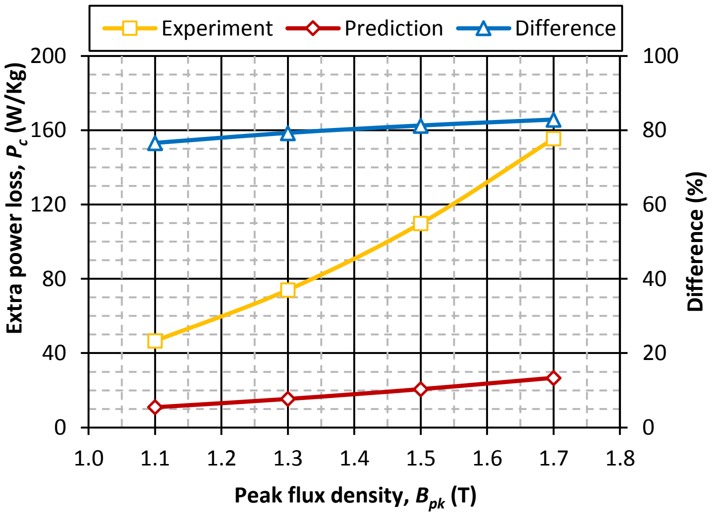

(c)

Fig 7-11 Comparison of prediction and experimental results of extra power loss caused by a single short circuit at set position at frequency of (a) 200 Hz (b) 500 Hz (c) 1000 Hz

Unlike chapter 6, Figs 7-10 and 7-11 show a big difference between the prediction and experimental results. In chapter 7 artificial shorts were applied along the whole length of both sides of the stacks, and hence distribution of the power loss along the stack was uniform. The extra loss caused by the applied faults was modelled, based on the hypothesis of section 7.3 of chapter 7, as a solid core with equivalent thickness of *2na*.

But in the analytical results of Figs 7-10 and 7-11 a short circuit volume of 30 mm wide, 1.2 mm high and 10 mm long was considered; while the experimental results show that a wider part of the stack is involved in the determination of the extra power loss caused by the applied short circuit. Experimental studies were performed to investigate the effect of artificial short circuits at set positions on local power loss of a 350 kVA, three-phase transformer core by means of the *initial rate of rise of temperature method* [7-11]. The results showed that profile of the local temperature and hence local power loss along the artificial shorts decreases gradually by increasing the axial distance from the applied short. The results confirmed that the extra loss caused by the applied short circuit is not only related to the main shorted volume in the core but also related to the outside of the shorted zone; which is the main reason of the difference shown in Figs 7-10 and 7-11. Therefore the analytical model of chapter 6, by itself, is not able to predict the extra loss caused by the artificial faults shown in Fig 7-8.

7.5. Modelling of inter-laminar faults in a stack of laminations with step-like positions

As outlined in the introduction, in practice inter-laminar faults occur at random positions. In order to model this kind of defect, packs of four laminations were shorted in a step-like configuration with inter-laminar faults between two laminations in each step, as shown in Fig 7-12-a. In order to compare the results with those of inter-laminar shorts at set positions another pack of laminations, with the same material, was shorted at set points, as shown in Fig 7-12-b.

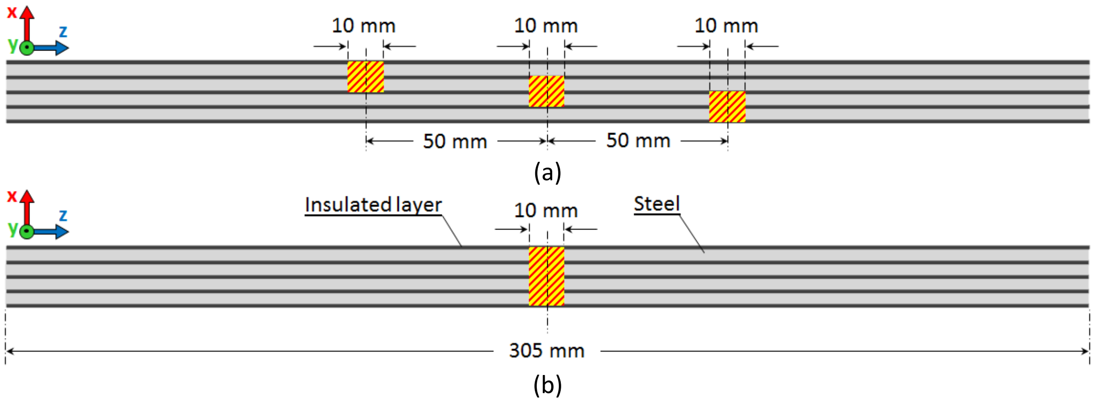

Fig 7-12 Side view of a stack of four laminations with inter-laminar short circuits at (a) three step-like points (b) one set point

The stacks were then magnetised at the same flux densities and frequencies as in section 7-4 and the total magnetic loss of each stack was measured at each flux density and frequency. The results together with the nominal power loss of the material versus peak flux density at different frequencies are shown in Fig 7-13.

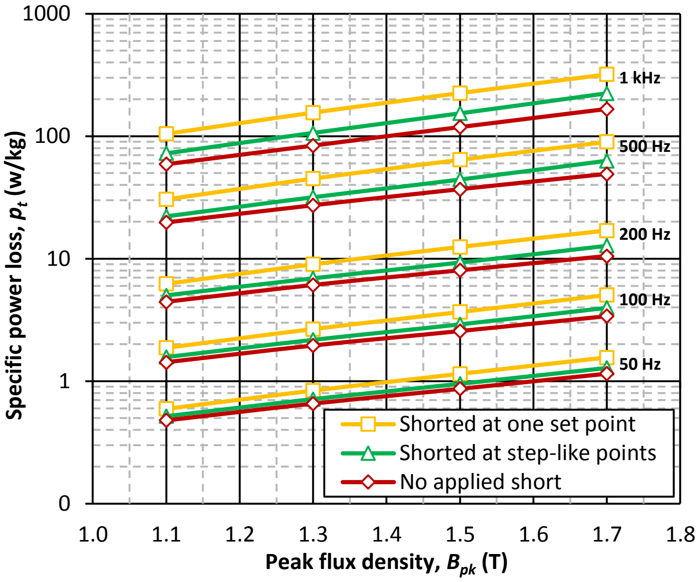

Fig 7-13 Total power loss caused by the artificial faults of Fig 7-12 versus peak flux density at magnetizing frequencies of 50 Hz to 1000 Hz

Although in both configurations of Fig 7-12 all of the laminations are shorted together, experimental results show that total power loss of the stack of Fig 7-12-a, is less than that of Fig 7-12-b. The reason is related to the nature of the fault current loops caused by the artificial shorts. In order to make it clear and to visualise the fault current loops caused by each defect and to show the distribution of the inter-laminar fault current in each pack of the shorted laminations, 2-D FEM modelling was performed using COMSOL Multiphysics at magnetising frequencies of 50 Hz and 1000 Hz. The results are shown in Figs 7-14-a and 7-14-b, respectively. Furthermore, based on the flowchart of Fig 4-11 of chapter 4, the distribution of normalised flux density along the thickness of the shorted packs of Figs 7-12-a and 7-12-b at magnetising frequencies of 50 Hz and 1000 Hz and typical surface flux density of 1.3 T were calculated; the results are shown in Figs 15-a and 15-b.

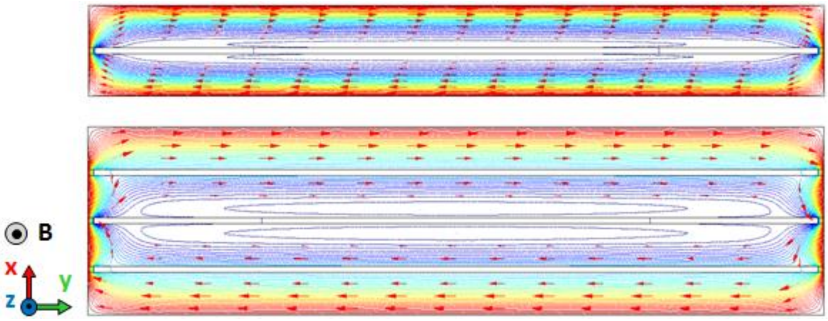

(a)

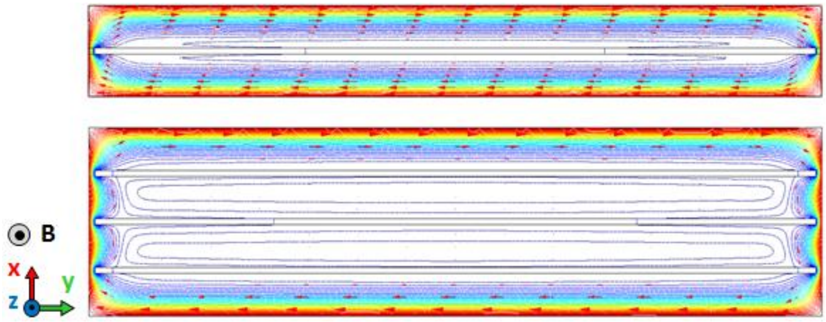

(b)

Fig 7-14 2-D FEM modelling of fault current loop and inter-laminar fault current between two and four laminations at magnetizing frequency of (a) 50 Hz and (b) 1000 Hz

From the FEM results of Fig 7-14 and flux density distributions of Fig 7-15 it can be seen that distribution of the inter-laminar fault current and flux density in the faulted laminations strongly depend on the length of the fault current loop; which in turn depends on the number of the shorted laminations. In the configuration of Fig 7-12-a although there are three fault current loops the total power loss is less than that of the configuration of Fig 7-12-b with only one fault current loop due to the larger length of the fault current loop in the configuration of Fig 7-12-b.

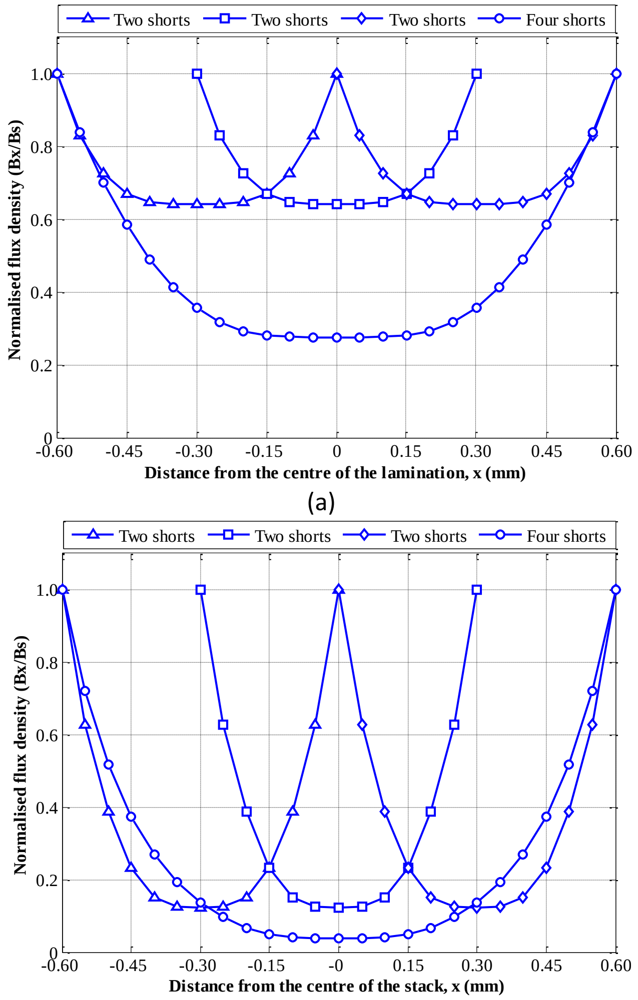

(a)

(b)

Fig 7-15 Normalized magnetic flux density penetration into the stack of Fig 7-12 at peak flux density of B_{pk}=1.3 T and magnetizing frequencies (a) 50 Hz and (b) 1000 Hz

As a conclusion on this investigation, the position and number of the inter-laminar faults in each fault current loop are also two key factors in the determination of the fault current loops and resulting inter-laminar fault current in the core. Large numbers of shorted laminations leads to larger fault current loop which in turn results in higher power loss in the faulted area of the core.

7.6. Modelling of inter-laminar faults at off-set positions

Inter-laminar faults can be displaced or off-set between the axes of the shorted points of the existing fault current loops in the core. This may occur when the laminations are shorted together at random points by edge burr. The concept of the axial off-set between the shorted points on side view and top view of a stack of four laminations is shown schematically in Figs 7-16-a and 7-16-b, respectively. In order to model these kinds of defect, inter-laminar faults with axial off-sets from 10 mm up to 200 mm were applied separately on opposite sides of packs of four laminations, according to the schematic of Fig 7-16. As an example, a photograph of top view of the stack with axial off-set of 60 mm is shown in Fig 7-17.

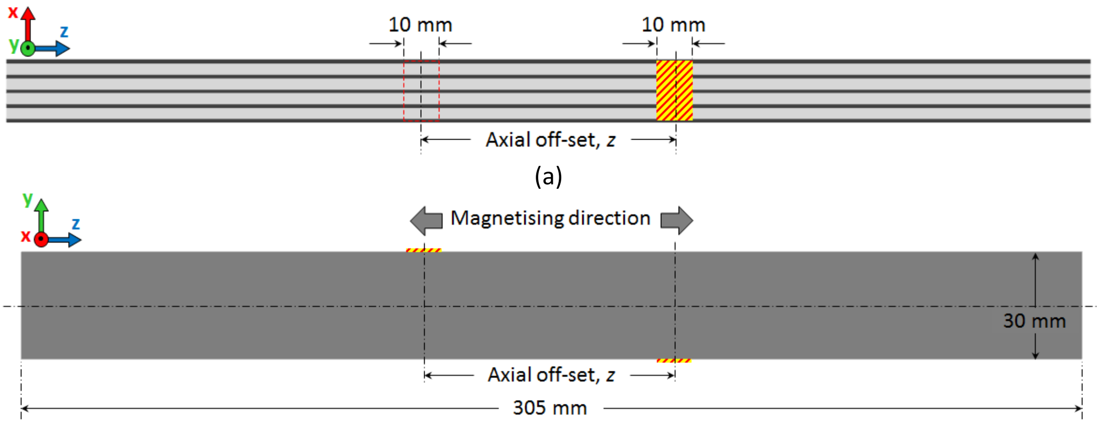

(b)

Fig 7-16 (a) Side view and (b) top view of a stack of four laminations with an inter-laminar short circuit with axial off-set position

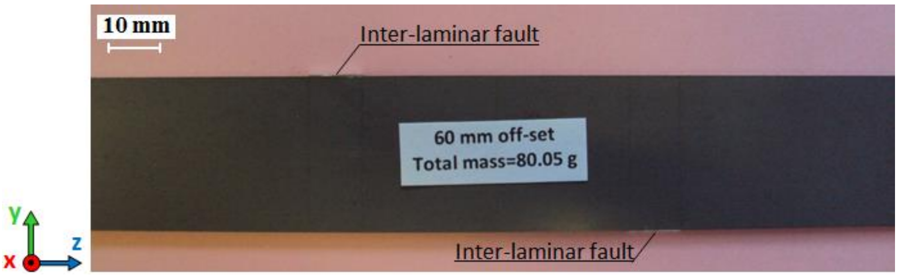

Fig 7-17 (a) Side view and (b) top view of a stack of four laminations with an inter-laminar short circuit with axial off-set position

Each pack of laminations was then magnetised and the total magnetic power loss of each stack was measured and recorded separately at each flux density and magnetising frequency. The measured power loss versus axial off-set at different flux densities and frequencies are shown in Figs 7-18 and 7-19. Similar to other parts of the work and in order to make a reference to compare the results, nominal power losses of the stacks, in the case of no inter-laminar fault, were measured at each flux density and frequency; the results are shown in Figs 7-18 and 7-19.

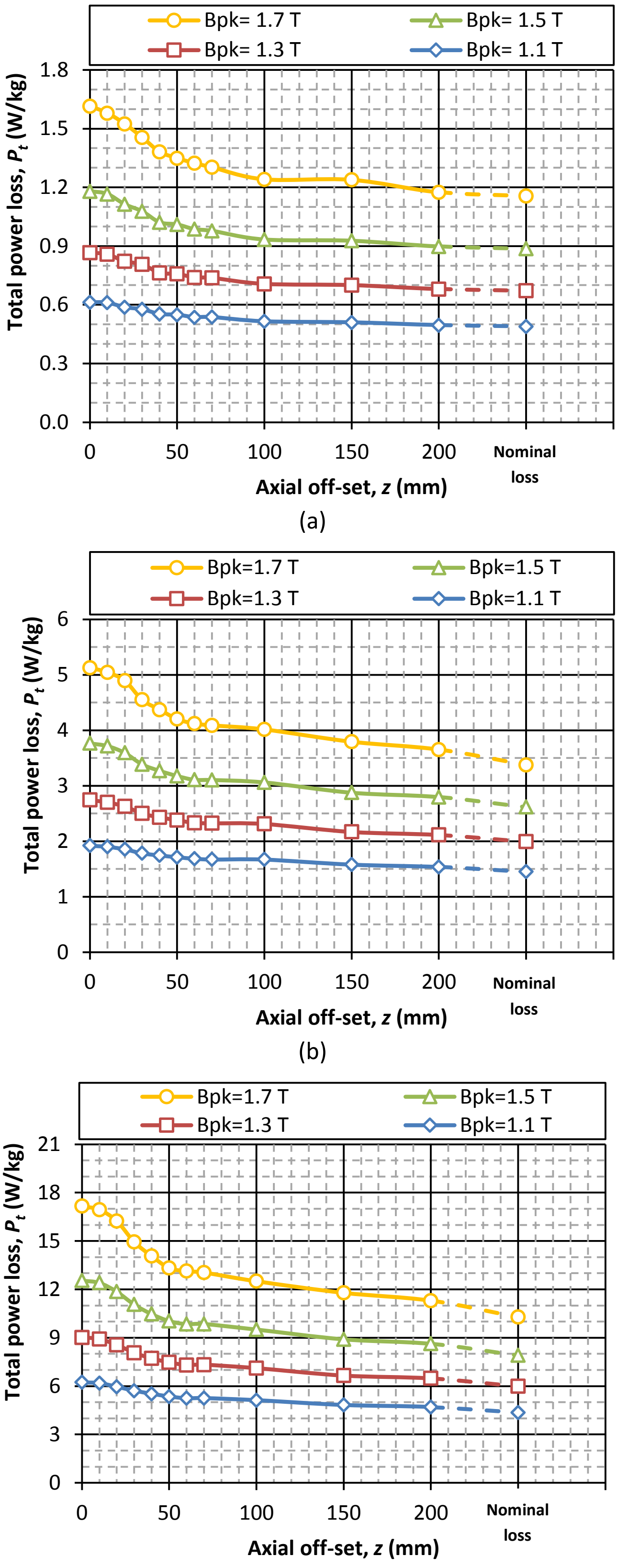

(a)

(b)

(c)

Fig 7-18 Specific power loss of stack of four with inter-laminar short circuit fault applied with axial off-set at magnetizing frequency of (a) 50 Hz (b) 100 Hz (c) 200 Hz

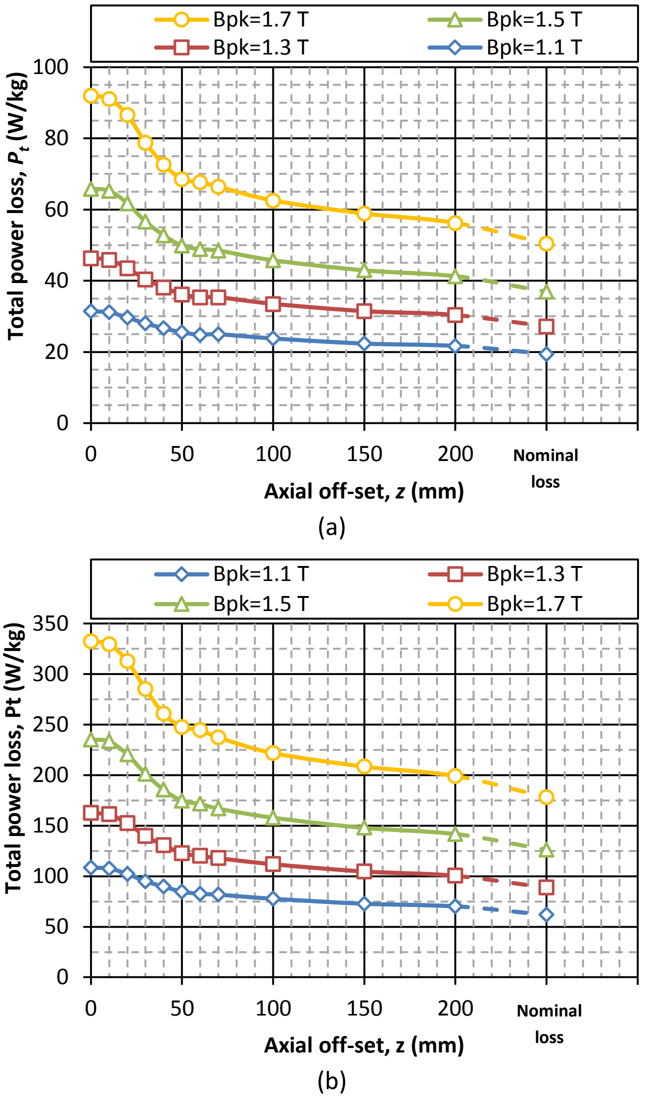

Fig 7-19 Specific power loss of stack of four with inter-laminar short circuit fault applied with axial off-set at magnetizing frequency of (a) 500 Hz (b) 1000 Hz

Four important notes could be concluded from the experimental results of Figs 7-18 and 7-19 at all flux densities and frequencies as follow:

1. When the fault points are applied at set points on the same axes, the resistance of the fault current loop is at a minimum which leads to the maximum inter-laminar fault current and hence the maximum power loss in the stack.

2. By increasing the axial off-set between the fault points, resistance of the fault current loop is increased, which results in a reduction of the inter-laminar fault current and total power loss of the stack.

3. Significant reduction in power loss was observed up to approximately 70 mm off-set between the axes of the fault points.

4. Power loss is approaching to the nominal loss of the material when the off-set is above 100 mm.

By increasing the axial displacement between the fault points, the angle between the magnetising direction and the axis of the applied faults decreases. This issue is shown schematically in Fig 7-20-a. This angle in the case of inter-laminar shorts at set points is 90°. The relationship between this angle and the axial off-set between the shorted points is shown in Fig 7-20-b.

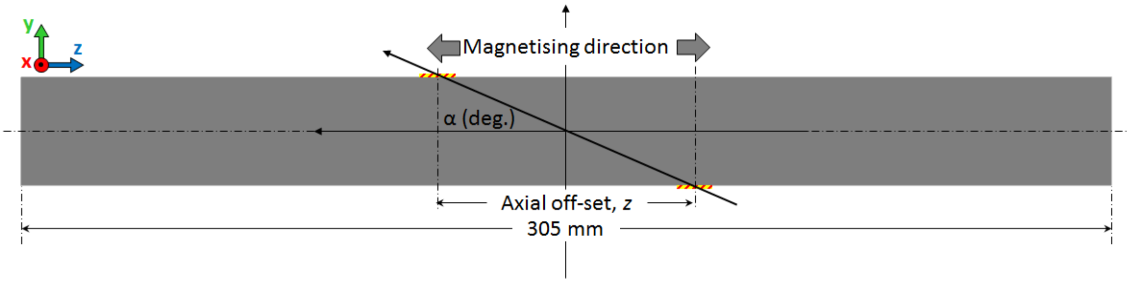

(a)

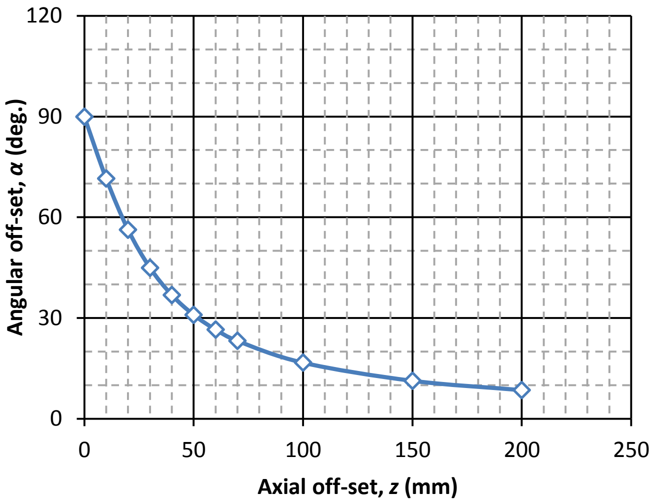

(b)

Fig 7-20 (a) Top view of a pack of shorted laminations with angular off-set between the axes of the shorted points (b) angular off-set versus axial off-set

The curve of Fig 7-20-b shows a similar rate of reduction in the angular and axial off-set between the fault points and the measured power losses of Figs 7-18 and 7-

19. As a result of this part of the investigation, axial displacement between the fault points of the fault current loop is another key factor in the determination of inter-laminar fault currents and the resulting extra power loss. Depending on the application and importance of the quality of the magnetic core, inter-laminar shorts with high off-set between the shorted points could be ignored.

7.7. Modelling of inter-laminar faults in a stack of laminations at multiple off-set positions

In the last part of this study the effect of inter-laminar faults at multiple off-set points was investigated. In this work two stacks of four laminations were assembled and each pack was shorted at four points with different displacements between the shorted points to make multi off-set faults. Schematics and photographs of top views of both packs are shown in Fig 7-21 and 7-22, respectively.

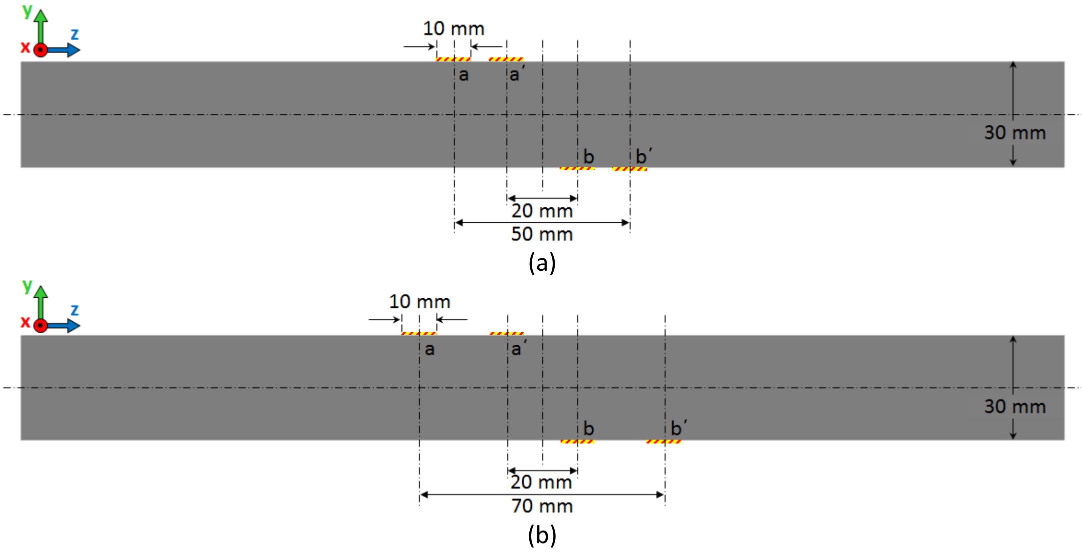

Fig 7-21 Top view of a stack of four laminations with inter-laminar short circuits at multi off-set positions (a) pack #1 (b) pack #2

According to the experimental results of section 7-4 configurations of the shorted points of Fig 7-22 could be considered as two independent fault current loops, e.g. points *a-b* and points *a′-b′* create two fault current loop in each stack, independently. On the other hand based on the experimental results of section 7-6 fault current loops of Fig 7-22 could be considered between points *a′-b* and *a-b′*.

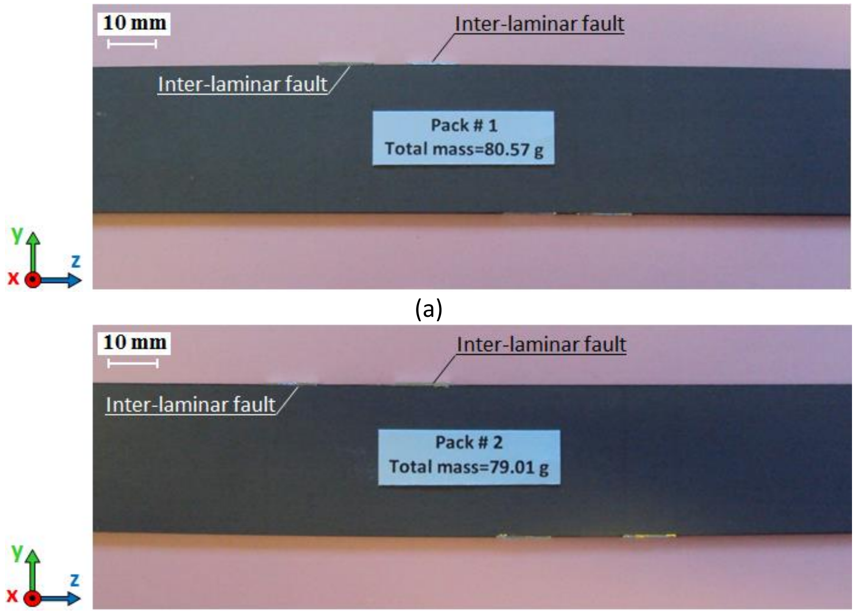

(a)

(b)

Fig 7-22 Photograph of top view of a stack of four laminations with inter-laminar short circuits at multi off-set positions (a) pack #1 (b) pack #2

Similar to the other parts of the work, total power loss of each pack was measured separately. The results of both packs were very close to that of the pack with one short with 20 mm off-set between the shorted points. Comparison between the total power loss of each stack and power loss of the stack with 20 mm off-set and nominal loss of the material are shown in Figs 7-23-a and 7-23-b, respectively.

Therefore, unlike the preliminary hypothesis, the fault current loop in each pack is closed through short circuit points *a´* and *b*, and short circuit points *a* and *b´* don't make a significant impact on the formation of the fault current loop, inter-laminar fault current and hence extra power loss. The reason is related to the tendency of electric current to pass through low resistance path which in the configurations of Fig 7-22 is created between the shorted points *a´* and *b*.

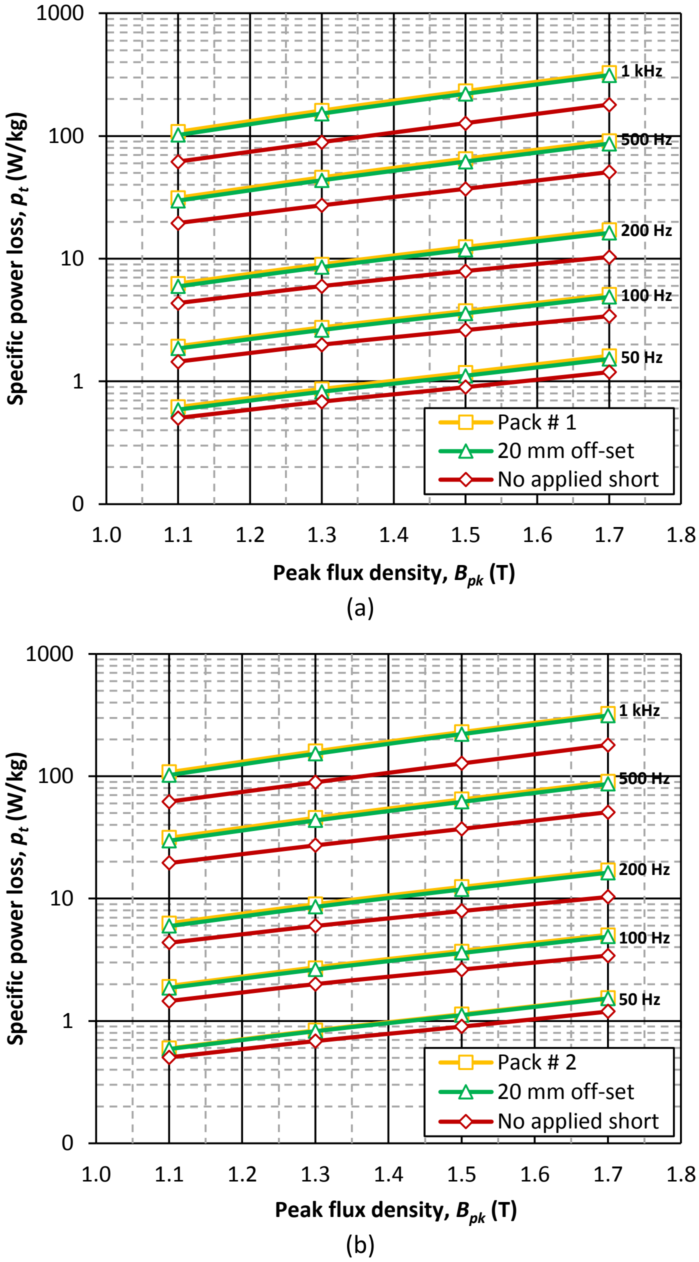

Fig 7-23 Comparison of total power loss of the packs #1 and #2 of Fig 16 with the normal loss of the material vs. peak flux density at different frequencies

As a result of this part of the study, in the presence of multi shorted points on opposite sides of a stack of laminations the fault current loop closes between the shorted points with the shortest distance between their axes.

7.8. Conclusion

In this chapter experimental studies have been performed to investigate the effect of inter-laminar short circuit faults with different configurations on total power loss of stacks of laminations. The studies were performed on stacks of four Epstein size CGO laminations over a wide range of flux density and magnetising frequency. Based on the experimental results, it was found that numbers of the inter-laminar shorts, position of the fault points, angular off-set between the fault current loop and magnetising direction, electrical resistance between the fault points are key-factors in the determination of the fault current loops and the extra loss caused by the inter-laminar fault.

Although the situation of inter-laminar short circuit fault in real scale electrical machine, especially in the stator cores, is more complicated, the results presented in this chapter could be extended to the practical magnetic cores of the electrical machines.

References

[7.1] S B Lee, G B Kliman, M R Shah, N K Nair and R M Lusted "*An Iron Core Probe Based Inter-Laminar Core Fault Detection Technique for Generator Stator Cores*" IEEE Trans. Energy Convers., Vol. 20, No. 2, Jun. 2005, pp. 344–351

[7.2] S B Lee, G B Kliman, M R Shah, W T Mall, N K Nair and R M Lusted "*An Advanced Technique for Detecting Inter-Laminar Stator Core Faults in Large Electric Machines*" IEEE Trans On Ind. App, Vol. 41, NO. 5, Sep/Oct 2005, pp. 1185–1193

[7.3] Z Posedel, "*Inspection of Stator Cores in Large Machines with a Low Yoke Induction Method—Measurement and Analysis of Interlamination Short-Circuits*", IEEE Trans on Energy Conversion, Vol. 16, NO. 1, March 2001, pp. 81-86

[7.4] G B Kliman, S B Lee, M R Shah, R M Lusted, and N K Nair, "*A New Method for Synchronous Generator Core Quality Evaluation*," IEEE Trans. Energy Convers., Vol. 19, NO. 3, , Sep. 2004, pp. 576–582

[7.5] J M Bourgeois and F Lalonde, "*Apparatus and Method for Evaluation a Condition of a Magnetic Circuit of an Electric Machine*," U.S. Patent 5 990 688, Nov. 23, 1999

[7.6] K Lee, J Hong, K Lee, S B Lee and E J Wiedenbrug, "*A Stator Core Quality Assessment Technique for Inverter-fed Induction Machines*", IEEE Industry Applications Society Annual Meeting, Oct 2008, pp 1-8

[7.7] J P Bielawski, S Duchesne, D Roger, C Demian and Th Belgrand, "*Contribution to the Study Of Losses Generated by Inter-Laminar Short-Circuits*", IEEE Trans On Magn, Vol. 48, No. 4, April 2012, pp 1397-1400

[7.8] E Lamprecht and R Graf, "*Fundamental Investigations of Eddy Current Losses in Laminated Stator Cores Created Through the Impact of Manufacturing Processes*" Proceeding of 1st International Electric Drives Production Conference (EDPC), 2011, pp. 29-35

[7.9] P Handgruber, A Stermecki, O Biro and G Ofner, "*Evaluation of Inter-Laminar Eddy Currents in Induction Machines*", Industrial Electronics Society, IECON 2013 - 39th Annual Conference of the IEEE, pp. 2792-2797

[7.10] UKAS M3003, "*The Expression of Uncertainty and Confidence in Measurement*", 1997

[7.11] H Hamzehbahmani, A J Moses and F J Anayi "*Opportunities and Precautions in Measurement of Power Loss in Electrical Steel Laminations Using the Initial Rate of Rise of Temperature Method*" IEEE Trans. Mag. VOL. 49, NO. 3, March 2013, pp 1264- 1273

CHAPTER 8

Inter-laminar Insulation Fault Detection in Magnetic Cores Using a Flux Injection Probe

8.1. Introduction

In chapter 6 the effect of inter-laminar faults on the equivalent configuration of magnetic cores, eddy current loss and other magnetic properties of the magnetic materials were discussed. Based on the FEM simulations, analytical modelling and experimental work it was proved that inter-laminar faults between laminations of the magnetic cores increase core losses and could cause major damage to the electrical machines. Therefore assessment of the quality of the magnetic cores is always a major concern not only for the manufacturer of magnetic laminations and electrical machines but also for their customers [8.1]-[8.10].

The aim of the work presented in this chapter is to develop an experimental technique to detect inter-laminar faults and study of the quality of the magnetic cores. A prototype of a **F**lux **I**njection **P**robe (FIP) was developed to magnetise magnetic core locally and measure the local power loss at the magnetised zone. Power loss measurement resulted from the injected flux into the magnetic core can be used as an indicator to qualify the magnetised zone of the core. Experimental works were first performed to calibrate the measuring system and quantify its accuracy over a wide measurement range. Application of a prototype FIP to quality assessment of transformer core laminations was investigated in two different stages: inspection of stack of laminations with known inter-laminar faults applied by artificial shorts and inspection of stack of laminations with un-known quality. The experimental results show that the developed system is able to detect inter-laminar fault between as few as 2 laminations.

8.2. Principle of Flux Injection Probe (FIP)

In chapter 3 some of the existing methods to detect inter-laminar faults between the laminations of the magnetic cores were reviewed. In most of these methods, the magnetic cores under test are magnetised either totally [8.5]-[8.8] or locally [8.9]-[8.10]. A common method to magnetise the magnetic cores locally is to inject magnetic flux into the core by using a C-shape (or U-shape) core including an excitation winding. This magnetic core is known as **F**lux **I**njection **P**robe (FIP) [8.9]-[8.10]. A perspective view of an FIP is shown in Fig 8.1. Applications of an FIP to magnetise a stator core and a 5 stack transformer core locally are shown in Figs 8-2-a and 8-2-b, respectively.

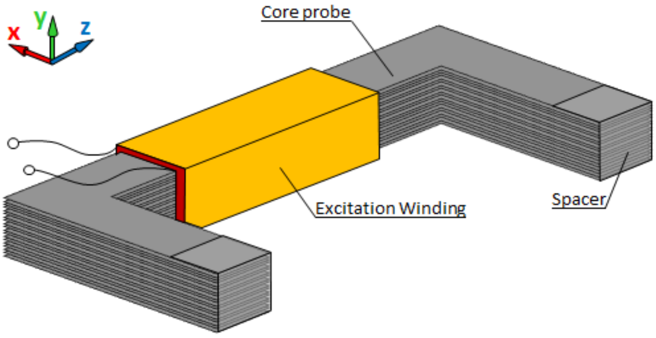

Fig 8-1 Perspective view of a flux injection probe to inject magnetic flux into the magnetic cores

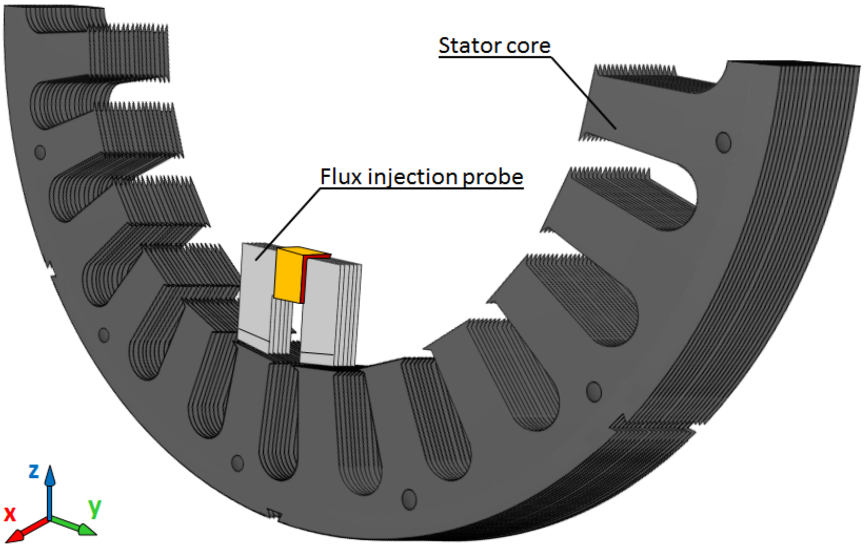

(a)

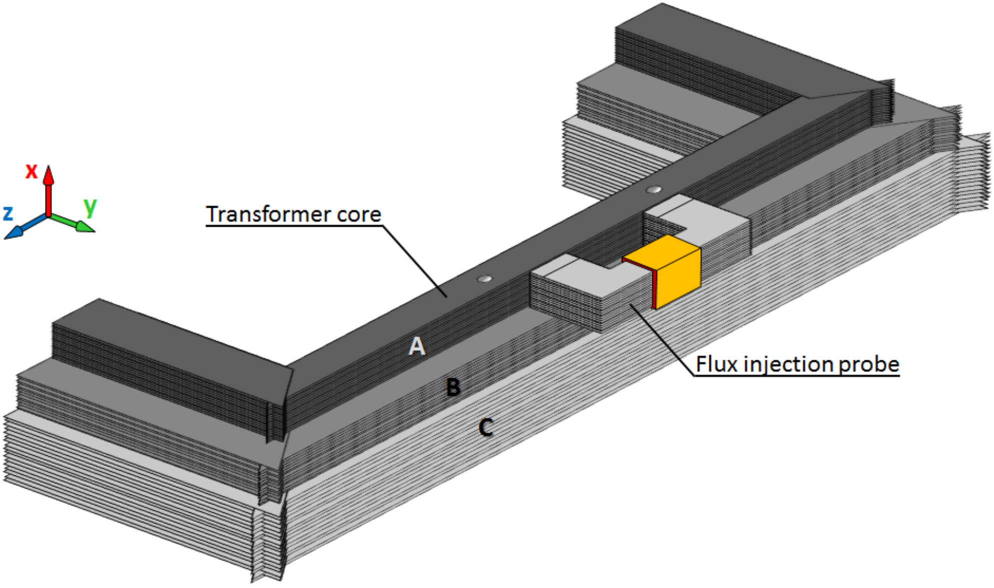

(b)

Fig 8-2 Schematic of (a) stator core (b) 5 stacks transformer limb under test by a flux injection probe

Fig 8.2 shows that magnetic circuit of the FIP closes through that part of the magnetic core under test placed between the two prongs of the probe. This part of the magnetic core is known as the *test zone*, *magnetised zone* or *excited zone* [8.9]-[8.10]. In order to specify the magnetic circuit of the FIP and visualise the distribution of the injected magnetic field in the core, 2-D FEM simulations were performed using COMSOL Multiphysics. The results for the stator core and stacks *A*, *B* and *C* of the transformer core are shown in Figs 8.3 and 8.4, respectively.

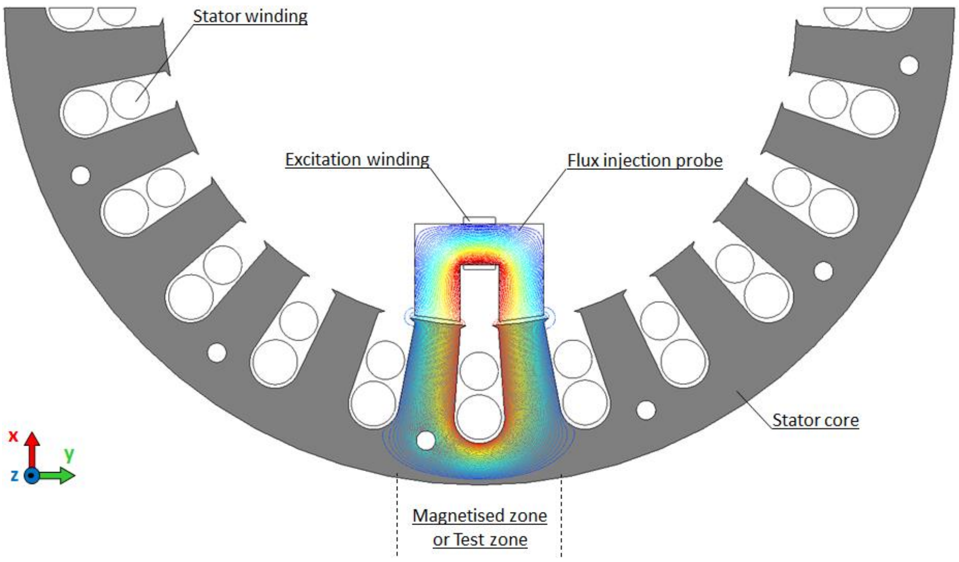

Fig 8-3 2-D FEM modelling of distribution of injected magnetic flux in stator core by an FIP

In the relevant test methods, all regions of the magnetic core should be magnetised by sliding the FIP on all sides of the magnetic core. An electric or magnetic signal is then measured resulting from the injected magnetic flux using a suitable sensor. Possible inter-laminar faults between the laminations of the magnetic core could be then detected by analysing and processing the measured signal. The measured signal could be magnetic flux [8.5], flux leakage [8.8] or induced voltage [8.9].

8.2.1. Inter-laminar fault detection using FIP

One of the major drawbacks of the fully magnetised inter-laminar fault detection methods is the requirement of a high level power supply to provide rated flux density in the magnetic core under test. Kliman et al. [8.10] proposed a low power non-destructive magnetic method to detect inter-laminar faults, particularly between laminations of synchronous generator cores, by means of a Flux Injection Probe. The basic idea of this method is to scan side of the core under test by the FIP and measuring iron power loss of the magnetised zone. Therefore an extra winding, known as *measurement winding* or *sense winding*, is required to measure an induced voltage resulting from the injected flux into the test zone. A schematic of an FIP with measurement winding to measure magnetic loss is shown in Fig 8-5.

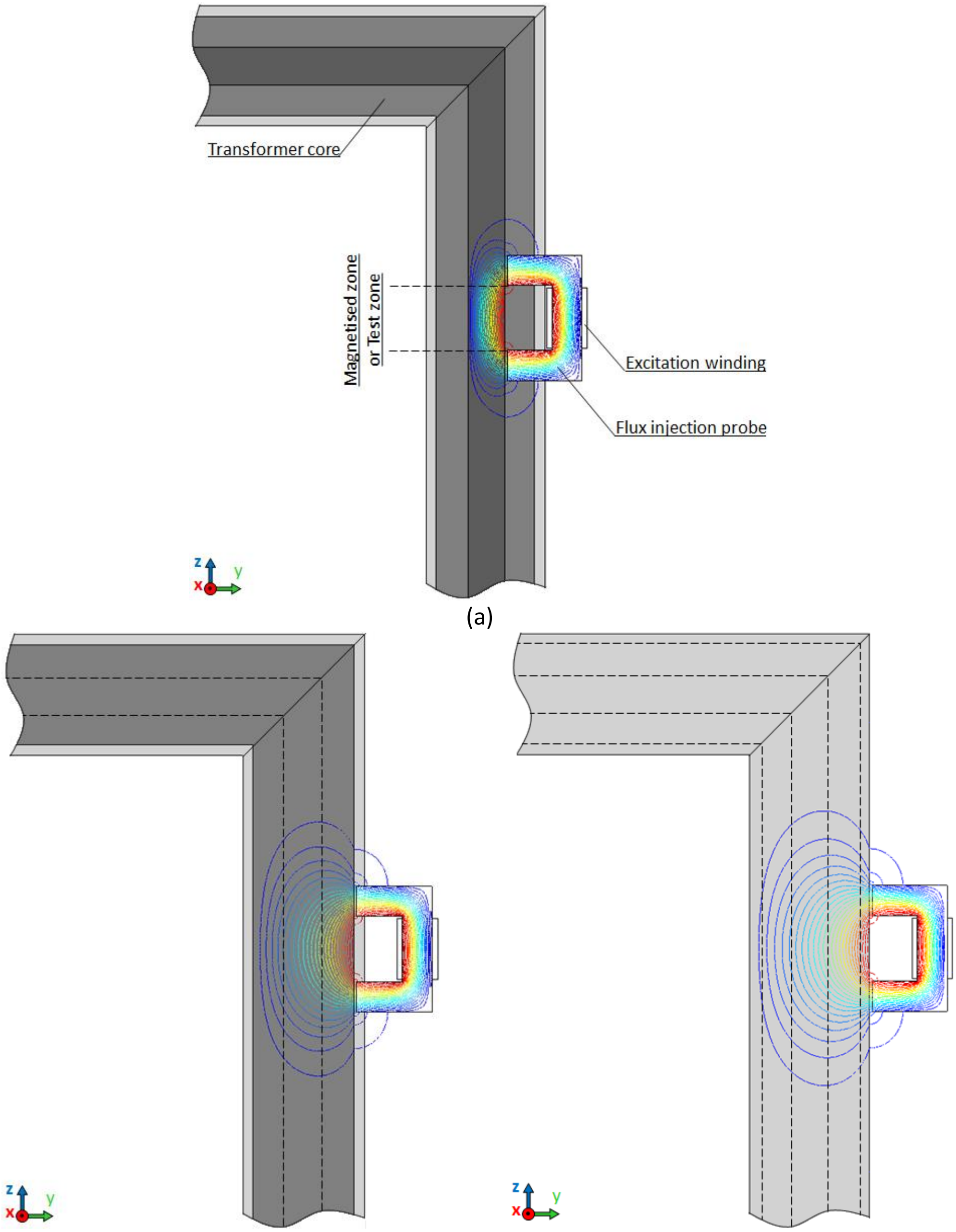

(a)

(b)

(c)

Fig 8-4 2-D FEM modelling of injected magnetic flux distribution in (a) stack **A** (b) stack **B** and (c) stack **C** of a 5 stacks transformer core using flux injection probe

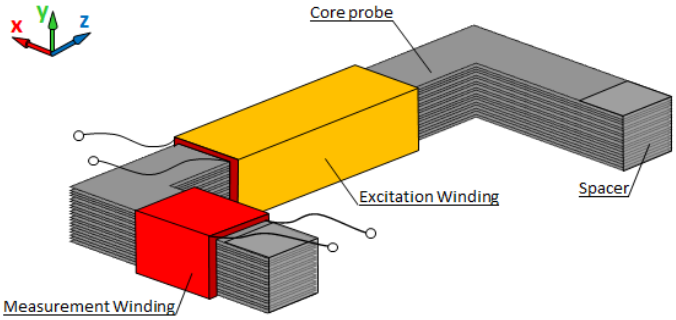

Fig 8-5 Schematic of an FIP with measurement winding to measure magnetic power loss

The resulting power loss from the injected current into the excitation winding and induced voltage into the measurement winding can be obtained by [8.10]:

$$p = \frac{1}{T}\int_{t}^{t+T} \frac{N_e}{N_m} v_m(t) i_e(t) dt \tag{8-1}$$

where N_e and N_m are the number of turns of excitation and measurement windings and $i_e(t)$ and $v_m(t)$ are the current flowing in the excitation winding and induced voltage in the measurement winding, respectively. Based on the equivalent circuit of a single phase transformer, using the induced voltage across the measurement winding $v_m(t)$ instead of the voltage across the excitation winding leads to the copper losses of the excitation winding to be eliminated in the loss calculation.

The resulting power loss of (8-1) being indicative of the condition and quality of the test zone formed of the FIP core and test zone in front of the probe. When the laminations of the magnetic core are well insulated from each other, i.e. there is no inter-laminar fault between the laminations; the measured loss resulting from the injected flux is in the range of nominal loss of the core at the flux density and magnetising frequency applied by the excitation winding. However if inter-laminar faults exist between the laminations of the test zone, extra power loss caused by inter-laminar fault current can be sensed and measured by the flux injection probe. Therefore the quality of the magnetic core could be evaluated by scanning all regions of the core and measuring instantaneous values of the injected current into the excitation winding and the induced voltage into the measurement winding. Using equation (8-1) a pattern of power loss versus position of the probe can be then recorded. Irregularities in the pattern of the core loss represent inter-laminar fault at that particular point [8.9]-[8.10].

8.3. Prototype model of FIP and experimental set-up

In this project a prototype model of FIP was developed to magnetise magnetic cores locally and detecting inter-laminar faults in the core. The magnetic core of the probe was made of 34 layers of magnetic laminations of *HiB Fe* 3 % *Si* of 0.3 mm thick with a standard grade of M105-30P. Laminations of the core were clamped together using a non-magnetic frame and nylon nuts and bolts. A 328 turn winding of enamelled copper wire, 1.00 mm thick, was wound around the yoke as an excitation winding and a 32 turn winding of enamelled copper wire of 0.525 mm was wound around one of the prongs as the measurement winding. As stated initially, in this method the sides of the core are scanned by the FIP, therefore the presence of an air gap between the end faces of the probe prongs and side of the core under test is unavoidable. In order to minimise the variation of the gaps and also prevent electrical connection between the probe and the core under test, the end faces of the prongs were covered by a plastic layer of 0.135 mm thick. The layout of the laminations, clamping frame, photograph of the assembled core, perspective view with physical dimensions and a photograph of the prototype model of FIP are shown in Fig 8-6.

8.3.1. Block diagram and flowchart of the FIP system

Since the principle of the loss measurement using FIP is similar to the single strip tester, the computer-controlled system of Fig 6-1 and the flowchart of Fig 6-3 described in chapter 6 were used here. However because of the difference in the geometry of the magnetic circuits and procedure of the measurements, minor changes in the setting of the software and hence flowchart were required. Fig 8-6 shows schematic diagram of the measuring system, specifically for this type of measurement. Similar to the measuring system of SST, this measuring system comprises a personal computer (PC) in which LabVIEW version 8.5 from National Instruments was already installed, a NI PCI DAQ-6120 data acquisition card, a power amplifier, a 1 Ω shunt resistor (R_{sh}) and an FIP. The magnetising voltage of the excitation winding was generated by the LabVIEW program via a voltage output of the DAQ card and power amplifier. The voltage drop across the shunt resistor (R_{shunt}) and the induced voltage in the measurement winding (e_m) were read for the calculation of flux density and magnetic field strength, respectively.

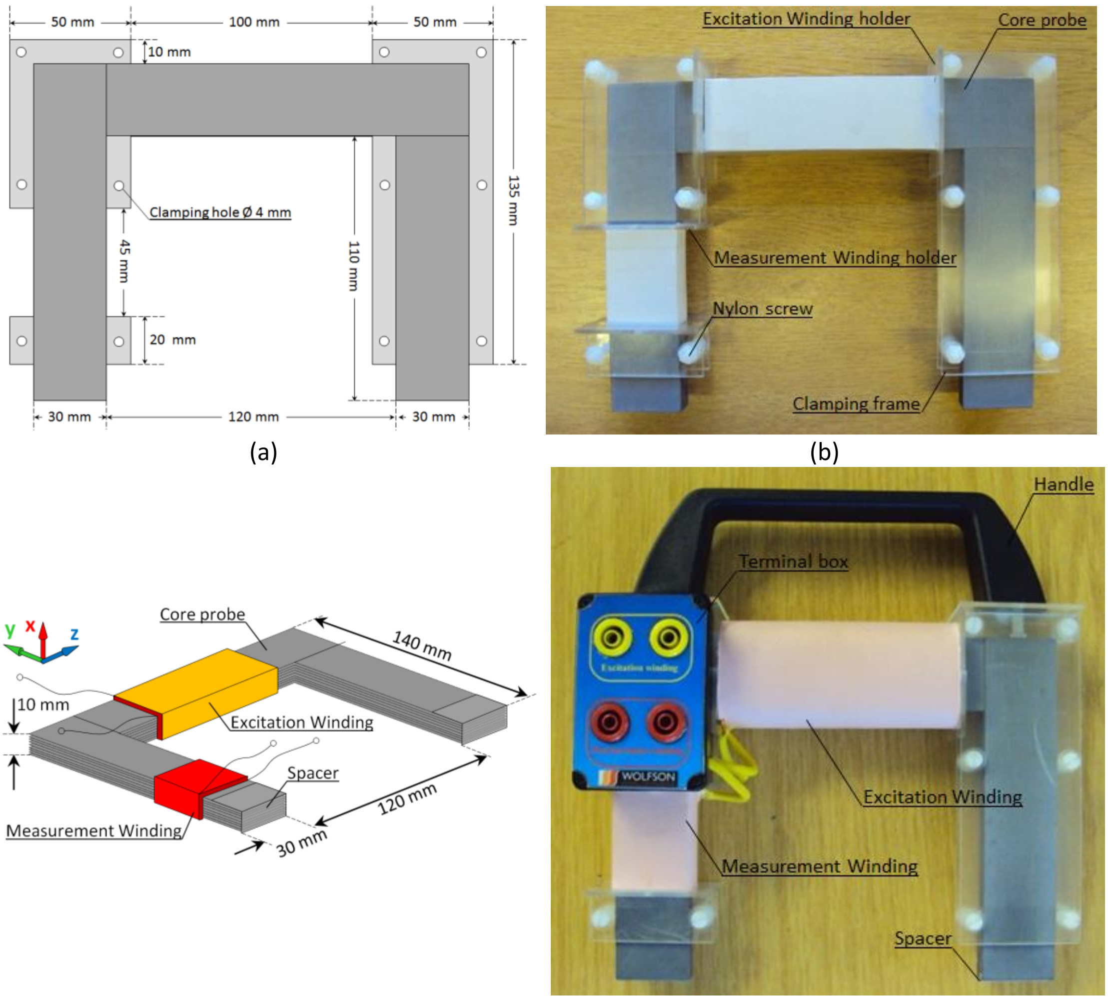

(a) (b)

(c) (d)

Fig 8-6 (a) Layout of the laminations and clamping frame (b) assembled core (c) schematic view and (d) photograph of a prototype flux injection probe

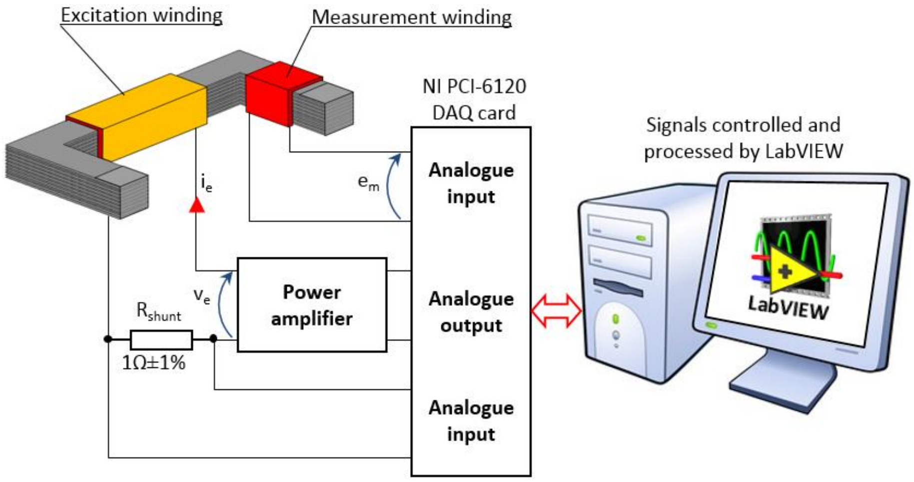

Fig 8-7 Schematic diagram of computer-controlled measurement system of inter-laminar fault detection using FIP

The flowchart of the inter-laminar fault detection procedure using the FIP is shown in Fig 8-8. According to the designed flowchart, first a table of *B* values and the measurement criteria which are the maximum 0.02 % error of *B* and the ideal *FF* of the induced voltage in the measurement winding are read. Then, the first magnetising waveform is applied to the excitation winding of the FIP. If the criteria are met, the *b* and *h* waveforms will be averaged to minimise random errors, otherwise the magnetising waveform is adjusted by the feedback algorithm. After averaging, the criteria are re-checked then power loss of the magnetised zone (test zone) is calculated and the measurement data for this zone is saved. This procedure is repeated by positioning the FIP near the surface of the magnetic core until all regions of the core have been tested. Finally a pattern of measured power loss versus position of the probe will plot.

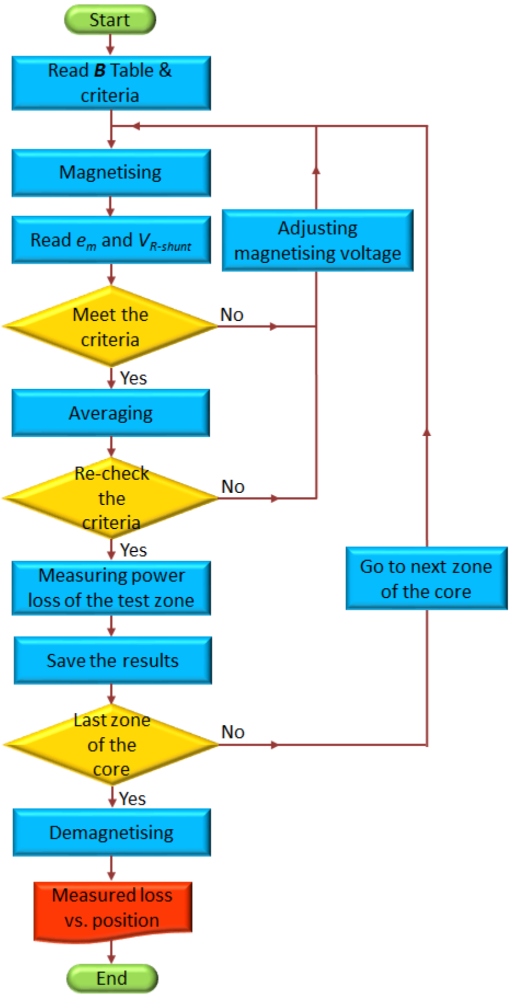

Fig 8-8 Flowchart of the inter-laminar fault detection by flux injection probe

8.4. Experimental Set-up

Although the principle of inter-laminar fault detection using the FIP is similar to loss measurement of the electrical steels using an SST, there are two major issues which make them different: unavoidable air gaps in the magnetic circuit and direction of the injecting flux into the samples of the test zone.

The air gaps between the ends faces of the probe prongs and side of the core under test increase the magnetic reluctance $\mathcal{R}_m$ of the magnetic circuit which result in higher demand of magnetic strength $\boldsymbol{H}$ to achieve a specific amount of magnetic flux $\boldsymbol{\varphi}$ in the sample. As a consequence, higher current is required to inject a specific amount of flux density into the core under test.

The direction of magnetisation of the test zone is another issue which should be considered in these types of inspections. Comparing the direction of the magnetic flux lines in the stator and transformer cores under normal operation, Figs 7-6-a and 7-6-b, to those injected by the FIP, Figs 8-3 and 8-4 illustrate this issue. The magnetising direction of the injected flux by the FIP in the teeth and yoke of the stator core is the same as normal operation of the machine. But in transformer cores, magnetic flux is initially injected into the samples of the test zone in transverse direction. Therefore this issue does not affect the inspection of the stator cores because of the isotropic property of NO steels. In transformer cores on the other hand, since the core material is GO steel which has anisotropic properties, this issue affects the circumstance of the inspection and should be considered in the design and control stages.

Considering the above issues, the prototype model of FIP for the quality assessment of the magnetic cores was investigated in three different stages: calibrating the measuring system, inspection of stack of laminations with known inter-laminar faults applied by artificial short circuits and inspection of stack of laminations with unknown inter-laminar faults. The results are presented and discussed in three sections separately.

8.4.1. Calibrating the system using a stack of Epstein sizes laminations

As stated in section 8-2, the magnetic core of the FIP is a part of the whole magnetic circuit and hence the measured power loss defined by the equation (8-1) takes into account the power loss of both test zone and the FIP itself. Therefore in order to calibrate the FIP and verify the accuracy of the measuring system and inter-laminar fault detection, the FIP should be initially evaluated properly.

In order to calibrate the FIP and its quality assessment, a pack of 34 standard Epstein strips with the same material as the FIP core was stacked. The prototype model of FIP was then placed on the side of the stack. The position of the FIP and the stack under test were kept fixed using clamping devices during the experiments to avoid any vibrations and change in the magnetic circuit. The specific core loss of the stack was measured at peak flux densities of 0.5 T up to 1.5 T and magnetising frequency of 50 Hz. As discussed in the introduction of section 8-4, setting of the software in the LabVIEW program was modified to calibrate the system and achieve nominal loss at each particular flux density and frequency. Laminations were then shorted together artificially on either side, using copper tape of 8 µm thick and 30 mm width and 6 different sizes of high to short out 5 laminations up to 30 laminations. The copper tapes were stuck to wooden blocks and pressed against the sides of the stack of laminations and uniformly clamped by a clamping device, as found to be an effective way of reproducing the effect of burrs [8.11]-[8.13]. A schematic and a photograph of the experimental set-up are shown in Fig 8-9.

Specific power loss versus the number of shorted laminations at different flux densities and a magnetising frequency of 50 Hz are shown in Table 8-1 and Fig 8-10-a. Specific power loss versus number of shorted laminations at different flux densities are also plotted in Fig 8-10-b. Power loss measurements were repeated three times at each flux density with repeatability [8.14] of better than 0.0135 %. The values presented in Table 8-1 and Figs 8-10-a and 8-10-b are the average of three measurements. In the horizontal axis of Fig 8-10-b, 0 represents the normal condition of the core, i.e. without applying artificial burr.

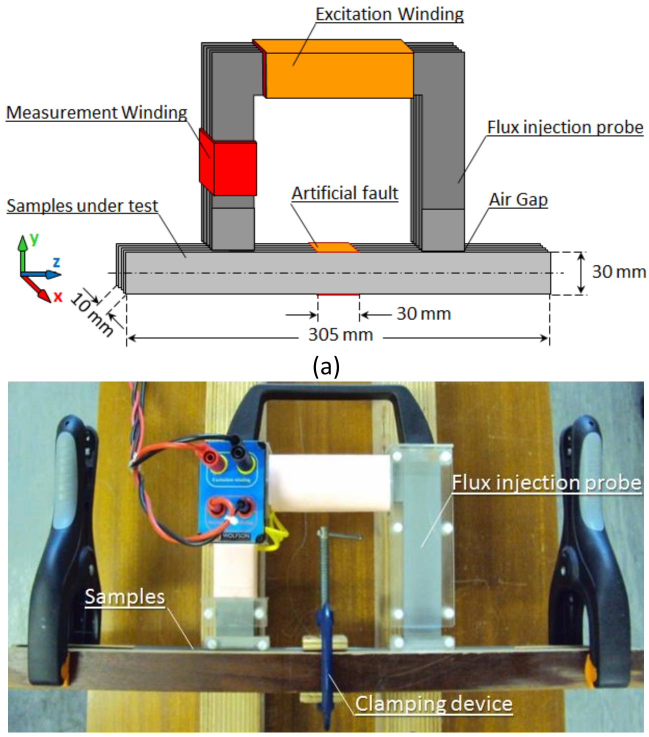

(a)

(b)

Fig 8-9 (a) Schematic and (b) photograph of the experimental set-up of calibrating of the prototype model of FIP

The results shown in Fig 8-10 show that power loss increases significantly by increasing number of the inter-laminar shorts; for example specific measured loss at 1.5 T for normal condition of the core and applying artificial burr on 30 laminations increased from 0.893 W/Kg to approximately 2.82 W/Kg. However the increased power loss from the normal condition to that of inter-laminar fault between 5 laminations is not large enough to be measured and detected by the FIP.

As proved in chapter 6, the main effect of inter-laminar faults in the magnetic cores is inter-laminar fault current and hence extra eddy current loss in the damaged area. On the other hand eddy current power loss itself is proportional to f^2 [8.15]; therefore increasing the magnetising frequency leads to increased eddy current power loss and hence total power loss. Based on the fact mentioned above, the inter-laminar fault between a small number of laminations could be detected by magnetising the core at higher frequencies. Power loss measurement of the stack of Fig 8-9, under the same circumstances, was repeated at a magnetising frequency of 100 Hz. The results are shown in Table 8-2 and Figs 8-11-a and 8-11-b.

Table 8-1 Specific core loss of a stack of Epstein size laminations under artificial inter-laminar faults at different flux densities and a magnetising frequency of 50 Hz

B_{pk} (T)	Total measured power loss (W/Kg)						
	No Burr	5 Burred	10 Burred	15 Burred	20 Burred	25 Burred	30 Burred
0.5	0.0798	0.0812	0.0828	0.0878	0.0937	0.1073	0.1604
0.6	0.1084	0.1107	0.1129	0.1201	0.1291	0.1500	0.2322
0.7	0.1414	0.1443	0.1473	0.1579	0.1702	0.2023	0.3196
0.8	0.1800	0.1838	0.1883	0.2017	0.2189	0.2667	0.4260
0.9	0.2254	0.2303	0.2353	0.2539	0.2790	0.3473	0.5537
1.0	0.2772	0.2827	0.2898	0.3146	0.3539	0.4460	0.7033
1.1	0.3372	0.3429	0.3523	0.3841	0.4465	0.5640	0.8796
1.2	0.4063	0.4125	0.4242	0.4672	0.5628	0.7073	1.084
1.3	0.4893	0.4966	0.5117	0.5714	0.7121	0.8843	1.326
1.4	0.6032	0.6126	0.6316	0.7194	0.9170	1.120	1.644
1.5	0.8927	0.9079	0.9493	1.163	1.525	1.983	2.819

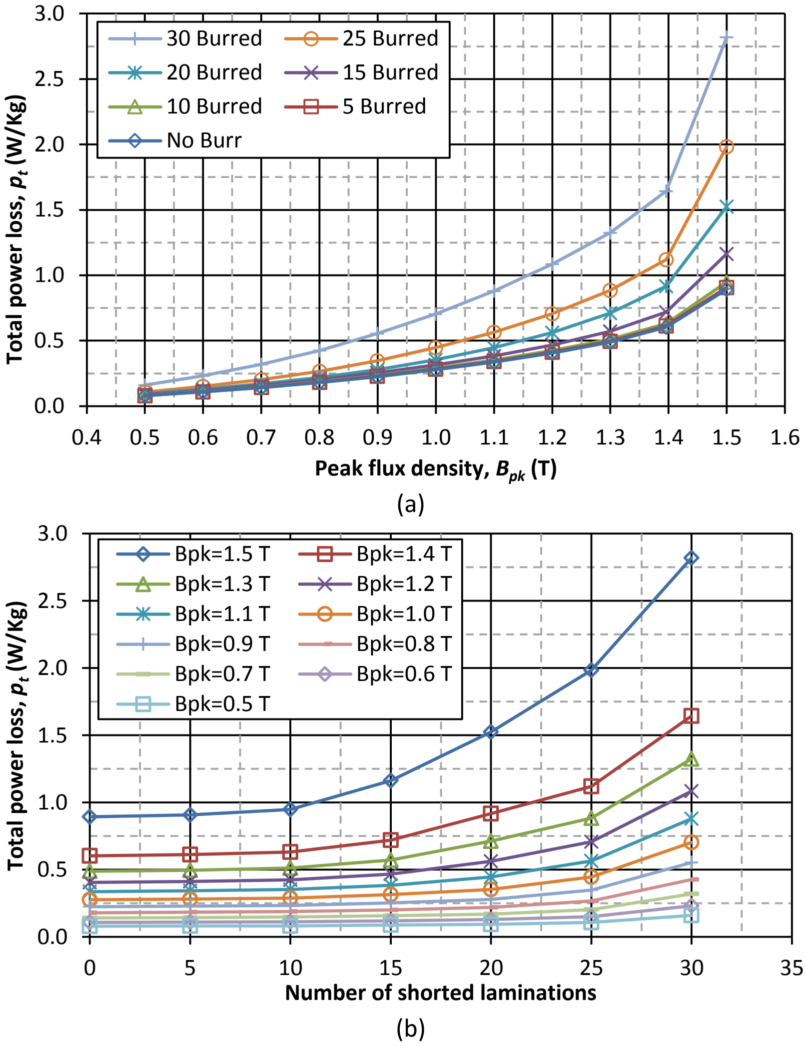

(a)

(b)

Fig 8-10 Specific core loss of a stack of Epstein size laminations under artificial inter-laminar fault (a) versus peak flux density at different number of shorts (b) versus number of shorted laminations at different flux densities; and a magnetising frequency of 50 Hz

Table 8-2 Specific core loss of a stack of Epstein size laminations under artificial inter-laminar faults at different flux densities and a magnetising frequency of 100 Hz

B_{pk} (T)	Total measured power loss (W/Kg)						
	No Burr	5 Burred	10 Burred	15 Burred	20 Burred	25 Burred	30 Burred
0.5	0.2180	0.2228	0.2260	0.2415	0.2588	0.3131	0.4759
0.6	0.2987	0.3060	0.3117	0.3336	0.3590	0.4488	0.7022
0.7	0.3915	0.4021	0.4095	0.4399	0.4736	0.6168	0.9840
0.8	0.5000	0.5155	0.5252	0.5672	0.6124	0.8338	1.328
0.9	0.6293	0.6492	0.6626	0.7178	0.7847	1.109	1.761
1.0	0.7752	0.8025	0.8175	0.8916	1.002	1.456	2.278
1.1	0.9408	0.9766	0.9940	1.091	1.293	1.874	2.894
1.2	1.134	1.180	1.194	1.326	1.677	2.384	3.621
1.3	1.368	1.428	1.442	1.619	2.168	3.003	4.475
1.4	1.681	1.762	1.783	2.031	2.854	3.835	5.562
1.5	2.422	2.646	2.756	3.405	4.940	6.830	9.316

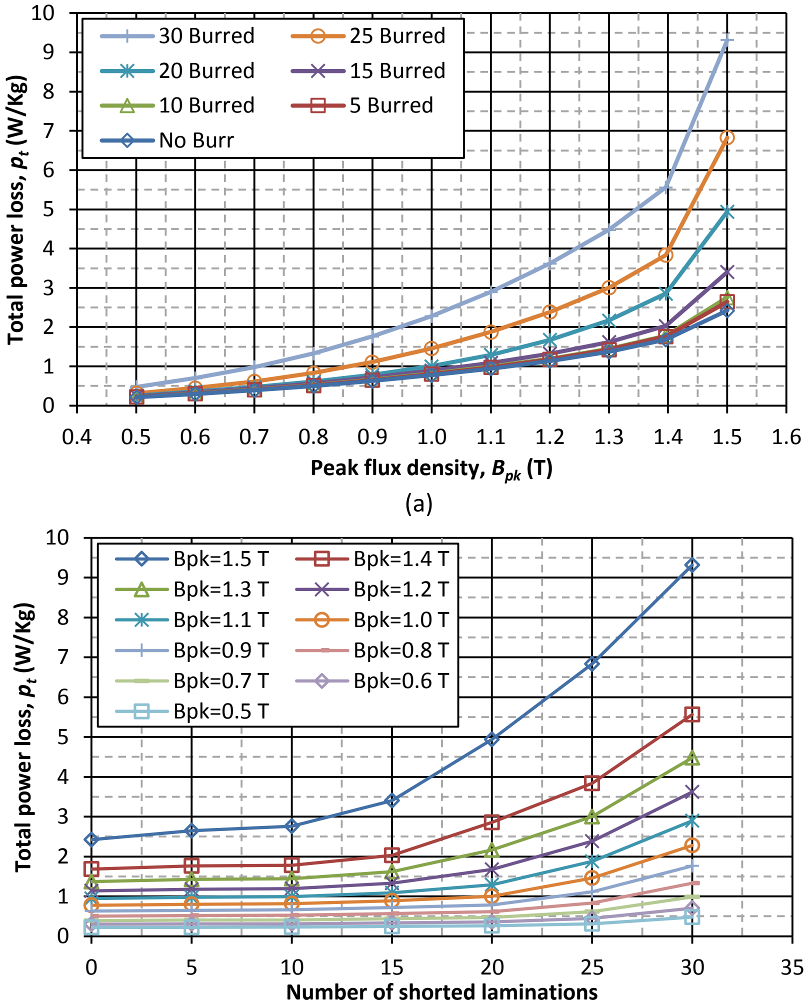

(a)

(b)

Fig 8-11 Specific core loss of a stack of Epstein size laminations under artificial inter-laminar fault (a) versus peak flux density at different number of shorts (b) versus number of shorted laminations at different flux densities; and a magnetising frequency of 100 Hz

Experimental results of Fig 8-11 show that total power loss of the stack was increased from 2.422 W/Kg in normal condition to 2.646 W/Kg in the case of inter-laminar fault between 5 laminations, which the difference between them is high enough to be detected by the FIP.

From the results represented in Figs 8-10 and 8-11 it can be concluded that inter-laminar faults with large number of shorts could be easily detected even at low flux densities and frequencies; e.g. specific power loss of the stack was increased from 0.0798 W/Kg in normal condition to about 0.1604 W/Kg when 30 laminations were shorted together at flux density of 0.5 T and frequency of 50 Hz which could be detected by this method. However in order to detect inter-laminar faults between a few numbers of laminations the core should be magnetised at high flux density and high magnetising frequency. For example inter-laminar fault between 5 laminations does not have significant impact on the power loss at 50 Hz frequency, even at flux density of 1.5 T; while the increased power loss at magnetising frequency of 100 Hz is large enough to be detected by the FIP.

8.5. Case study I: quality assessment of a stack of transformer laminations with artificial short

The prototype model of FIP was used in a quality assessment of a real scale lamination stack. The stack, 700 mm long and 150 mm wide, 0.3 mm thick, of Conventional Grain Oriented (CGO) Fe 3 % Si was assembled to make it 10 mm high. An artificial short circuit was introduced in the stack in two different stages:

1. Inter-laminar short on either sides of the stack
2. Inter-laminar short between one side of the stack and bolt hole

8.5.1. Artificial faults on sides of the stack

In the first part of this investigation, similar to section 8.4.1, artificial faults made from copper tape of 8 µm thick and 30 mm width were applied on either side of the stack at the centre position at 3 different stages to form a short circuit between 10, 20 and 30 laminations. A schematic and photograph of the experimental setup is shown in Figs 8-12-a and 8-12-b, respectively.

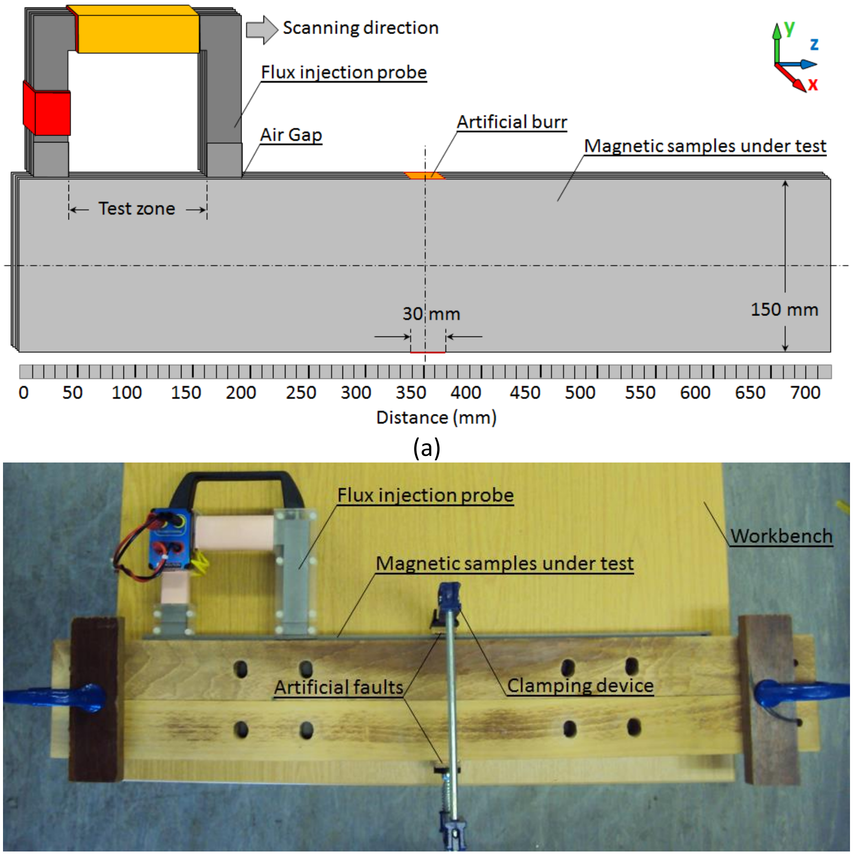

(b)

Fig 8-12 (a) Schematic and (b) photograph of the experimental setup of detection of inter-laminar fault applied on opposite sides of a stack of transformer core laminations by FIP

The stack was then magnetised locally by injecting magnetic flux using the FIP based on the flowchart of Fig 8-8. The side of the stack was scanned by sliding the FIP and the power loss of the test zone was measured at increments of 10 mm and the results were recorded in a database. A pattern of the measured power loss versus axial position along the core side was plotted for each experiment. The results of the measurement in the case of no-fault and applying artificial short circuits between 10, 20 and 30 laminations at peak flux densities of 1.0 T up to 1.4 T and frequency of 50 Hz are shown in Figs 8-13-a to 8-13-d, respectively. The frequency of the injected flux was then increased to 100 Hz when inter-laminar fault was applied to shorting up 5 laminations. The result is shown in Fig 8-14.

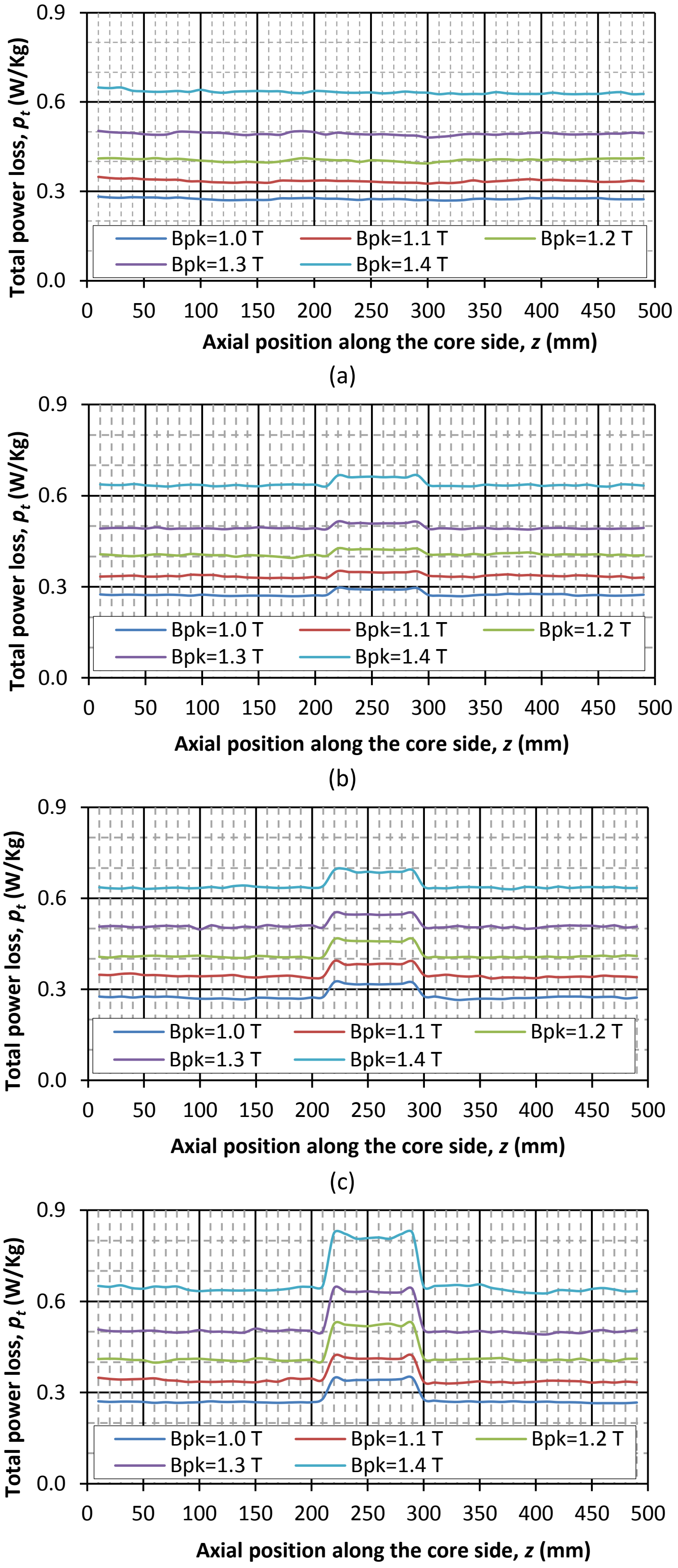

(a)

(b)

(c)

(d)

Fig 8-13 Specific core loss versus axial position along the core side (a) No fault (b) 10 inter-laminar shorts (c) 20 inter-laminar shorts (d) 30 inter-laminar shorts on either side of stack of transformer laminations at 50 Hz

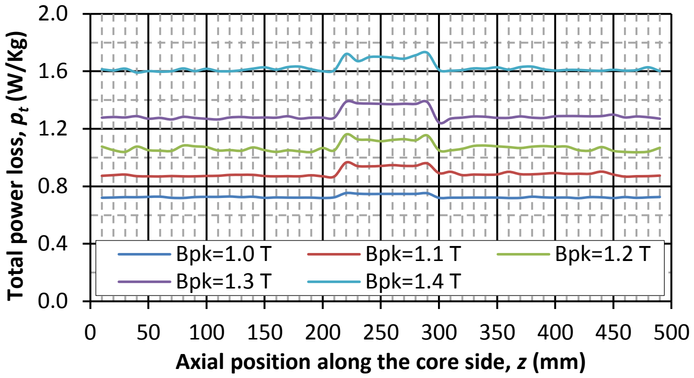

Fig 8-14 Specific core loss versus axial position along the core side with 5 inter-laminar shorts on either side of the stack at 100 Hz

Five important points could be concluded from the experimental results of Figs 8-13 and 8-14 as follow:

1. Power losses of the stack without applying inter-laminar short circuit correspond with the nominal loss of the steel.
2. In the presence of inter-laminar fault in the test zone, an increase of the value of the power loss can be observed.
3. Power loss of the faulted zone increases by increasing number of the shorts which is one of the major factors in determination of power loss of the defected zone.
4. Inter-laminar faults between a large number of laminations could be detected easily even at low flux density and low frequency.
5. To increase the resolution of inter-laminar fault detection, e.g. to detect inter-laminar fault between a few number of laminations, the FIP should be excited at high flux densities and frequencies.

8.5.2. Artificial fault between one side and bolt hole

In the next part of this work an inter-laminar fault was applied artificially between one side of the core and a bolt hole. 10 mm diameter holes were created at the centre of each lamination by electric discharge machining (EDM). A schematic of the experimental setup, position of the bolt hole and a photograph of the FIP near the bolt hole are shown in Figs 8-15-a to 8-15-c, respectively. Measurements were repeated at the same flux densities and magnetising frequencies and under the same procedure as in section 8.4.2.1. The results are shown in Fig 8-16.

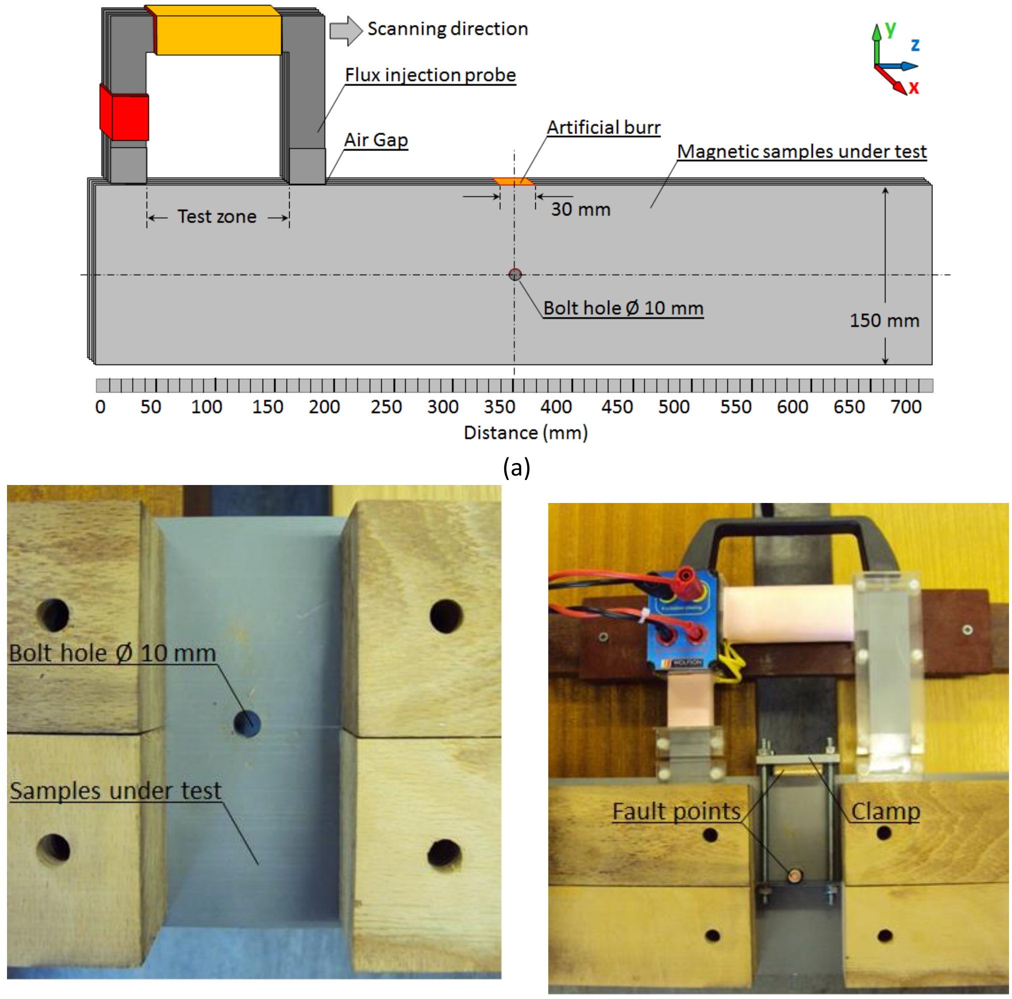

(a)

(b)

(c)

Fig 8-15 (a) Schematic diagram (b) stack of laminations with a 10 mm diameter hole at the centre (c) experimental set-up of inter-laminar fault detection between one side and bolt hole of a stack of transformer core laminations by FIP

The same notes as session 8.4.2.1 could be concluded from Fig 8-16; however specific power loss of the faulted zone of Fig 8-15 is less than the result of Fig 8-12 for the same number of shorted laminations, injected peak flux density and magnetising frequency. The reason for this is related to the electrical resistance of the fault current loop.

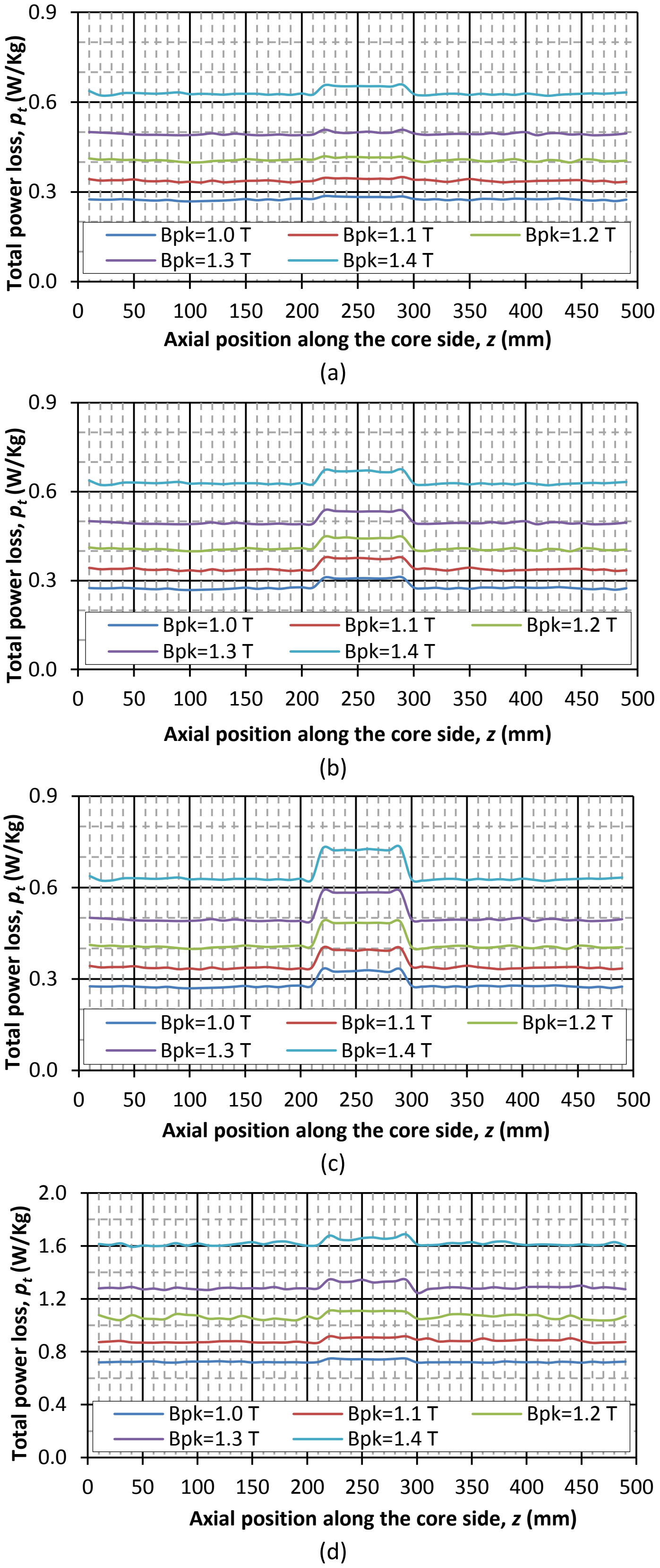

Fig 8-16 Specific core loss versus axial position along the core side (a) 10 inter-laminar shorts (b) 20 inter-laminar shorts (c) 30 inter-laminar shorts between one side and bolt hole of stack of laminations at 50 Hz (d) with 5 inter-laminar shorts at 100 Hz

According to the definition of fault current loop, there are two different fault current loops for the setups of Figs 8-12 and 8-15. In the setup of Fig 8-12 fault points of the fault current loops are formed by the copper tapes of 30 mm width, while in the setup of Fig 8-15 one side of the fault loop is actually formed by a narrow strip of copper with an approximate width of 15.7 mm (half of the bolt hole circumstance). This creates higher resistance in the fault current loop and leads to lower eddy current and hence eddy current loss in the damaged zone.

Furthermore, the setup of Fig 8-12 creates a larger fault current loop which results in higher induced fault current. Typical fault current loops created by the inter-laminar faults of Figs 8-12 and 8-15 for stacks of four laminations are shown in Figs 8-17-a and 8-17-b, respectively. According to the eddy current loss modelling of equation (4-54) developed in chapter 4, a wider fault current loop (*w*) lead to higher power loss in the core.

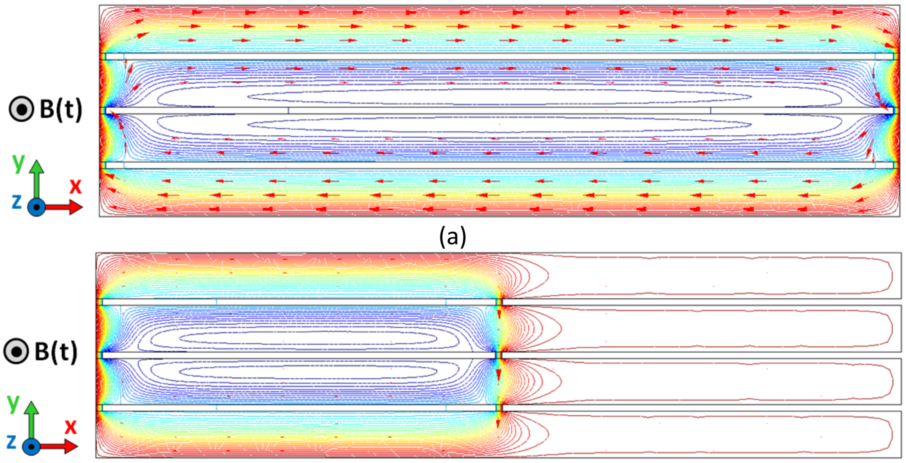

(a)

(b)

Fig 8-17 Fault current loop created by (a) inter-laminar fault on either side of the stack (b) inter-laminar fault on one side and bolt hole

8.6. Case study II: quality assessment of a stack of transformer laminations of un-known quality

In the last part of this investigation, the quality of two different types of magnetic materials was assessed using the prototype model of FIP. Two coils of GO steel were provided by Cogent Power Ltd. with the following specifications:

Coil A: 848129, SJ1110, 0.27×150 mm, M095-27P

Coil B: 846151, SI6217, 0.30×150 mm, M105-30P

Each coil was cut with dimensions of 700 mm long and 150 mm wide. Stacks of 10 mm high were then assembled using each sample. The stacks were then assessed for inter-laminar faults. The experiments were carried out in two stages:

1. Scanning each side of the stacks in normal condition.
2. Scanning one side of each stack while the other side is shorted artificially.

Possible inter-laminar fault current loops in the stacks could be detected in the first stage of the experiment and single shorts between the laminations could be detected in the second stage.

Experimental results of the stage one showed that power losses of both stacks were almost constant along the axial position of the stack and correspond with the nominal loss of the material. Therefore potentially no fault current loop was found in the stacks. In order to detect any possible inter-laminar fault on each single side of the stacks, one side of each stack was shorted artificially using copper tape and insulation block and the other side was scanned by the FIP with the same procedure as section 8.5. Therefore when the laminations are shorted on one side, possible shorts on the other side will make a fault current loop and could be detected by this technique. Two photographs of the experimental set-up are shown in Fig 8-18.

(a) (b)

Fig 8-18 Experimental set-up after applying artificial short on one side of the stack

No change in the power loss was recorded regarding the coil B (846151); but elevated power loss on side 1 of the stack A (848129) at position of 390 mm to 490 mm was found when the other side was shorted artificially. The profile of the power loss versus axial position of this case at flux densities of 1.1 T up to 1.4 T and a magnetising frequency of 50 Hz is shown in Fig 8-19.

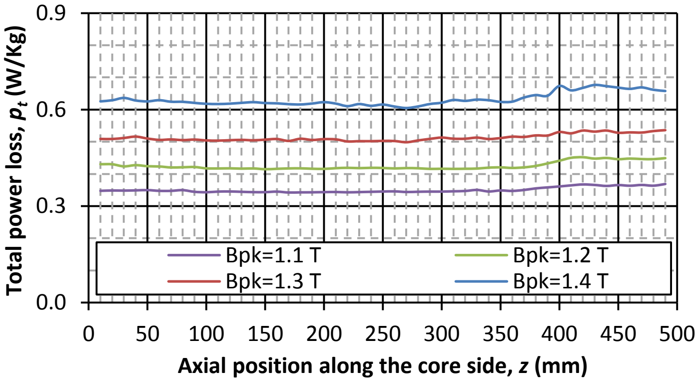

Fig 8-19 Specific core loss versus axial position along the core side of coil A on side 1; while other side is shorted artificially

Therefore it could be concluded that inter-laminar faults between the laminations of coil A on side 1 is possible. To investigate this issue, side 1 of the stack A was imaged using a microscopic digital camera with resolution of 32 megapixels. The results at positions of 250 mm, 300 mm and 350 mm as three points with normal power loss and positions of 400 mm, 425 mm and 450 mm as three points with elevated power loss are shown in Figs 8-20 and 8-21, respectively.

Fig 8-20 shows that the laminations are isolated properly at the positions of 250 mm, 300 mm and 350 mm which correspond to normal power loss points; while Fig 8-21 shows inter-laminar shorts between laminations number 5 and 6 at positions of 400 mm, 425 mm and 450 mm which correspond to the elevated power loss points. In order to show the inter-laminar fault between the suspected laminations of 5 and 6, side view of the stack at positions of 400 mm and 450 mm are magnified in Figs 8-22-a and 8-22-b, respectively.

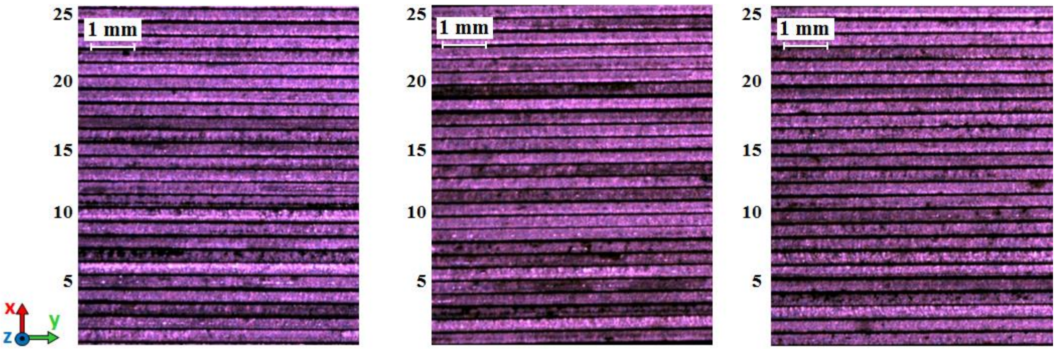

(a) (b) (c)

Fig 8-20 Side view of stack A at distances (a) 250 mm (b) 300 mm and (c) 350 mm

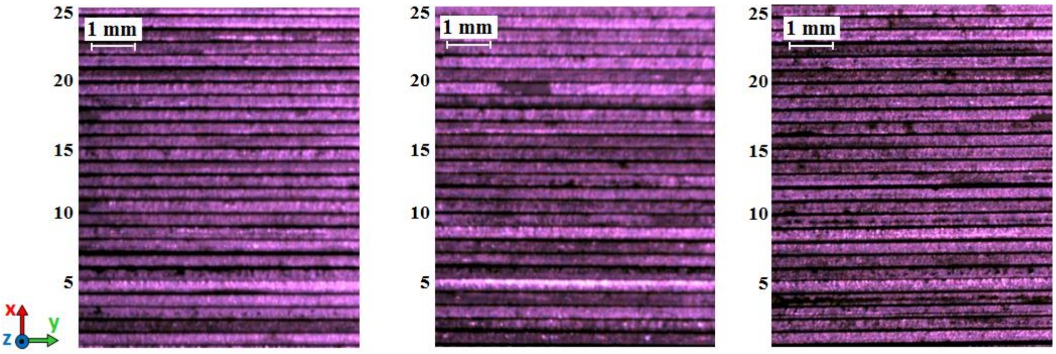

(a) (b) (c)

Fig 8-21 Side view of stack A at distances (a) 400 mm (b) 425 mm and (c) 450 mm

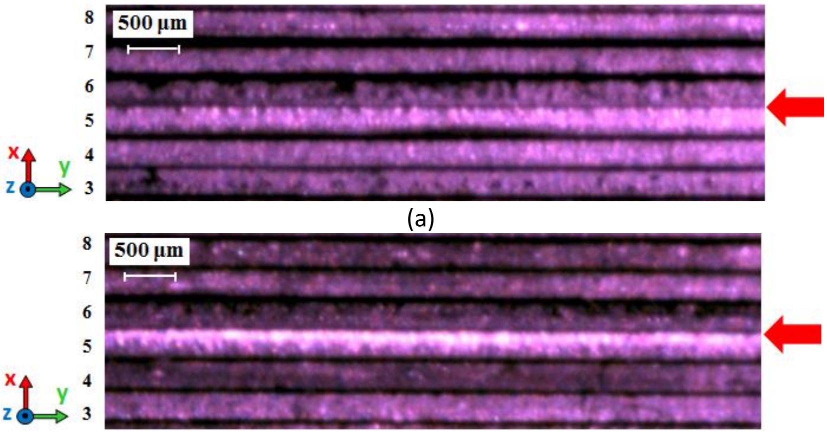

(a)

(b)

Fig 8-22 Side view of stack A at distances (a) 400 mm and (b) 450 mm

In the next step of this work, stack A was laminated and laminations number 5 and 6 were replaced. The side of the stack was then scanned under the same conditions as the previous experiment and total power loss of the stack was recorded; the result is shown in Fig 8-23.

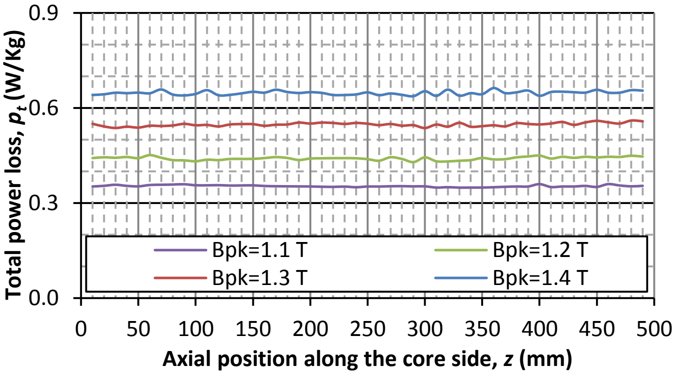

Fig 8-23 Specific core loss of side 1 of coil A versus axial position while side 2 is shorted artificially; after replacing laminations number 5 and 6

It can be seen from the results of Fig 8-23 that power loss of the stack after replacing the defected laminations corresponds to the nominal power loss of the core and is almost constant along the axial position of the stack. Laminations number 5 and 6 were investigated to find the reason of the inter-laminar fault. Burr size of the laminations was initially measured at 10 random points at positions of 400 mm to 500 mm using a digital micrometre. The results are shown in Table 8-3.

Table 8-3 Burr height of the suspected laminations of coil A (848129)

Thickness at surface (mm)	Thickness at edge (mm)	Burr height (µm)
0.263	0.273	10
0.261	0.273	12
0.261	0.273	12
0.262	0.273	11
0.261	0.273	12
0.263	0.273	10
0.261	0.273	12
0.264	0.273	9
0.262	0.273	11
0.263	0.273	10

As shown in Table 8-3 no high edge burr was found at the edge of the suspected laminations. Therefore the inter-laminar fault of Fig 8-20 could not be as a result of height edge burr.

Surface resistance close to the edge between the suspected laminations at positions of 100 mm to 130 mm as the perfect zone of the stack and positions of 410 mm to 440 mm as the defected zone was then measured using Franklin tester [8-16] provided by Cogent Power Ltd. According to mode A of IEC 404-11, coefficients of surface insulation resistance C were calculated [8-17]. The results are shown in Table 8-4.

Table 8-4 Result of Franklin tester on the suspected laminations

Position (mm)	Measured current (mA)		C (Ω Cm^2)	
	Sample # 5	Sample # 6	Sample # 5	Sample # 6
100	10	0	319.3	inf
110	12	0	265.6	inf
120	64	45	47.17	68.44
130	0	0	inf	inf
410	174	435	15.31	4.191
420	216	73	11.71	40.95
430	432	348	4.241	6.041
440	93	112	31.45	25.57

The results show high surface resistance at positions of 100 mm to 130 mm with normal loss; while low surface resistance was detected at positions 410 mm to 440 mm which correspond to the high power loss zone of the stack.

Considering the microscopic pictures of Figs 8-21, and 8-22 burr size measurement and the results of the Franklin tester, it is not surely clear whether the increase in power loss was as a result of local contact at the edge of these strips or directly to do with the lower levels of the surface insulation on the suspected laminations. Also it should be remembered that in the experimental set-up of this test, one side of the stack was totally shorted which is unlikely ever to be the situation in the transformer cores.

8.7. Effect of clamping stress on local power losses

In order to maintain mechanical stability, transformer core laminations are clamped together using a clamping structure [8.18]. A conventional clamping structure comprises upper and lower pieces which hold and press the laminations through bolt holes applied on the core. However the punched hole changes the normal distribution of flux density and local power loss in the core and might introduce edge burr around the hole and lead to inter-laminar fault at heart of the core. In order to avoid punching hole on the laminations, in the recent design of the transformers clamping stress is applied using bands around the limb and yoke of the core. Conventional and new clamping structures of transformer core are shown in Figs 8-24-a and 8-24-b, respectively.

Clamping stress has a significant effect on flux density distribution, vibration, acoustic noise and power loss of the transformer cores [8.18] and [8.21] – [8.23]. Measuring local power loss of the transformer cores, and other magnetic devices, by the flux injection probe method can be used to investigate quality of the clamping structure and applied stress on the core [8-10].

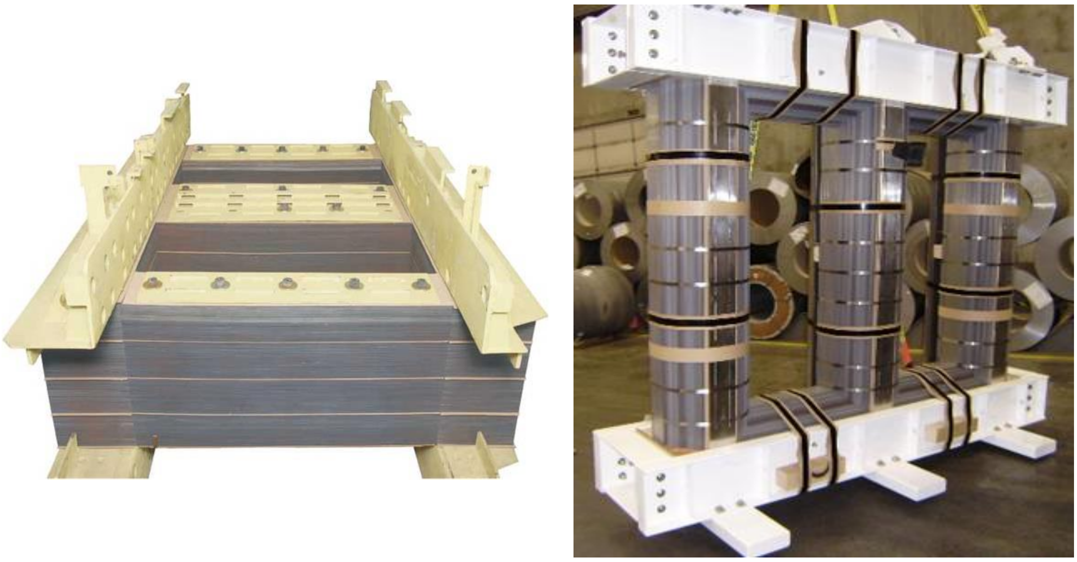

(a) (b)

Fig 8-24 Three phase transformer core clamped with (a) bolt and nuts [8.19]
(b) band around the limbs and yokes [8.20]

Similar to section 8.4.1 a stack of Epstein size lamination of *HiB Fe* 3 % *Si* of 0.3 mm thick were assembled and the prototype model of FIP was placed on side of the stack. The laminations were clamped by 30 mm × 100 mm Teflon clamps and tightened with fibre reinforced plastic bolts. Clamping torque *T* of the bolts was increased from 1 Nm up to 6 Nm in 1 Nm intervals. A schematic of the measuring set-up is shown in Fig 8-25 and two photographs of the measuring set-up with and without clamping devices are shown in Figs 8-26-a and 8-26-b, respectively. Total power loss of the stack was initially measured in case of no applied stress from the set-up of Fig 8-26-a. Clamping torque was then applied from 1 Nm up to 6 Nm in 1 Nm interval and the total power loss was recorded at each stage. The results versus clamping torque at different flux density are shown in Fig 8-27.

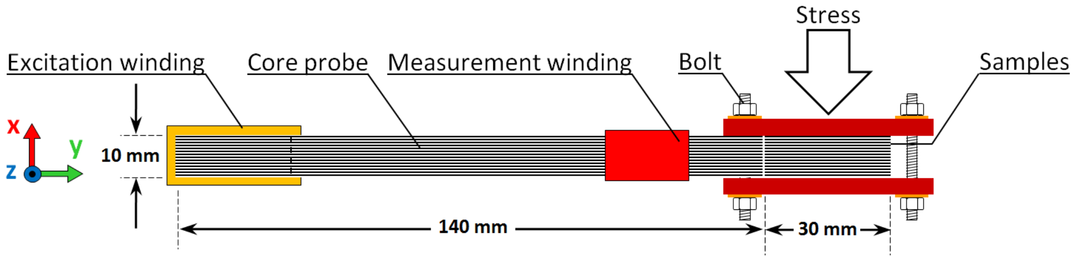

Fig 8-25 Schematic of the experimental set-up

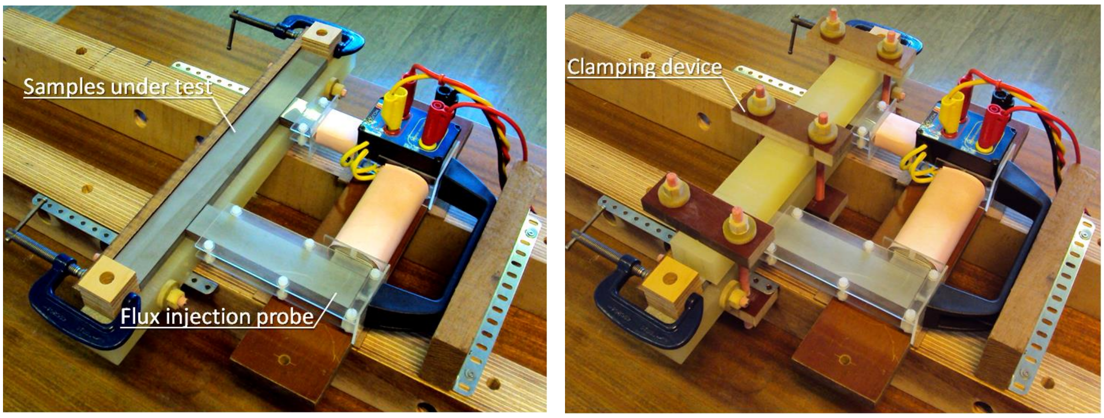

(a) (b)

Fig 8-26 Photograph of the experimental set-up (a) no applied stress
(b) with clamping stress on the samples

It can be seen from Fig 8-27 that power loss of the stack is maximum in the stress-free case and decreases by increasing the stress at all flux densities, which indicates the importance of clamping stress on power loss of the magnetic cores. According to the results of Fig 8-27, the maximum difference between the stress-free and applied stress by clamping torque of 6 Nm is 28.15 % at peak flux density of 1.4 T.

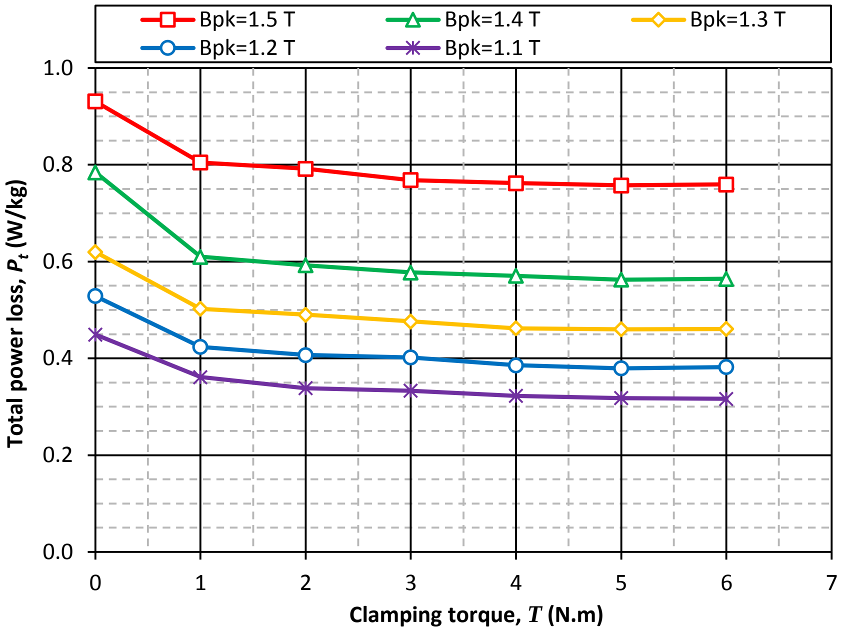

Fig 8-27 Effect of clamping torque on total power loss of a stack of Epstein size laminations of HiB *Fe* 3 % *Si* of 0.3 mm thick

In the magnetic cores, clamping pressure plays an important role on inter-laminar resistance [8.24]–[8.25] and hence inter-laminar short circuit fault. The micro-structure of the lamination surface is rough and includes some peaks which are distributed randomly over the lamination surface. Although the laminations are coated by insulation material on either side, in case of extremely high local pressure the coating material might be damaged or displaced and therefore the peaks between two adjacent laminations create electrical contact between the laminations. A typical example of the microstructure surface of a 0.5 mm thick lamination and electric contact between two adjacent laminations caused at high pressure are shown in Figs 8-28-a and 8-28-b, respectively [8.25].

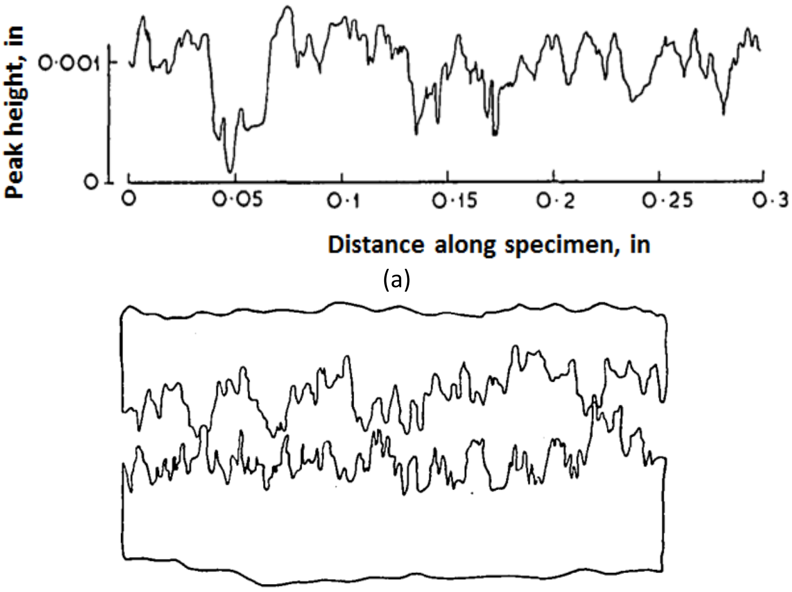

(a)

(b)

Fig 8-28 Surface micro-topology (a) microstructure of a 0.5 mm thick lamination (b) magnified illustration of two surfaces in contact [8.25]

The relationship between the inter-laminar resistance and applied pressure is basically related to the number of the surface peaks coming into electric contact by increasing the applied pressure on the core [8.25]. Therefore quality of the clamping devices and amount of the clamping pressure should be investigated not only in the manufacturing process, but also in the frequent tests and inspections.

8.8. Conclusion

In this chapter a non-destructive method was implemented to detect inter-laminar faults on magnetic cores using a flux injection probe. In this method since the magnetic core is magnetised locally a low power source is required to excite the magnetic core under test; which could be considered as the main advantage of this method. Compared to the other methods, e.g. EL CID, interpretation of the output results is much easier and the fault detecting procedure by this method is very quick. However in order to detect an inter-laminar fault between a few laminations, the test zone of the core should be magnetised at high frequency and flux density. Two case studies were carried out to evaluate the application of the developed system to detect inter-laminar faults on stack of transformer laminations. The results proved that inter-laminar faults between as few as 2 laminations can be detected by this system.

This method might also be used to verify the quality of the magnetic cores of the electrical machines during core assembling. Power loss of the core at each step of the core assembling can be measured by the FIP. If an inter-laminar fault is located, corrective action can be taken to find and replace the defected lamination. This method could be also implemented to evaluate the influence of clamping pressure on the magnetic cores after assembly and during inspection.

References

[8.1] S B Lee, G B Kliman, M R Shah, W T Mall, N K Nair and R M Lusted "*An Advanced Technique for Detecting Inter-Laminar Stator Core Faults in Large Electric Machine*s" IEEE Trans On Ind. App, Vol. 41, NO. 5, Sep/Oct 2005, pp. 1185–1193

[8.2] S B Lee, G B Kliman, M R Shah, N K Nair and R M Lusted "*An Iron Core Probe Based Inter-Laminar Core Fault Detection Technique for Generator Stator Cores*" IEEE Trans. Energy Conv., Vol. 20, No. 2, Jun. 2005, pp. 344–351

[8.3] S B Lee, G Kliman, M Shah, D Kim, T Mall, K Nair and M Lusted, "*Experimental Study of Inter-laminar Core Fault Detection Techniques based on Low Flux Core Excitation*" IEEE Trans On Energy Convers, Vol. 21, No. 1, March 2006, pp 85-94

[8.4] H Hamzehbahmani, P Anderson, J Hall and D Fox, "*Eddy Current Loss Estimation of Edge Burr affected Magnetic Laminations Based on Equivalent Electrical Network-Part I Fundamental Concepts*", IEEE Trans. on Power Delivery, VOL. 29, NO. 2, April 2014, pp. 642-650

[8.5] D R Bertenshaw, J F Lau and D J Conley, "*Evaluation Of EL CID Indications Not Associated With Stator Core Inter-Laminar Insulation Faults*" IEEE Electrical Insulation Conference, June 2011, pp 254- 260

[8.6] J. Sutton, "*El-CID—An Easier Way to Test Stator Cores*," Elect. Rev., Jul. 1980

[8.7] D B Paley "*Current Low Power Core Testing Using EL CID*" IEEE Colloquium "Understanding your condition monitoring (Ref. No. 1999/117)" April 1999, pp 7/1-7/4

[8.8] Z Posedel, "*Inspection of Stator Cores in Large Machines with a Low Yoke Induction Method-Measurement and Analysis of Interlamination Short-Circuits*", IEEE Trans on energy conv., Vol. 16, NO. 1, March 2001, pp. 81-86

[8.9] J M Bourgeois and F Lalonde, "*Apparatus and Method for Evaluation a Condition of a Magnetic Circuit of an Electric Machine*," U.S. Patent 5 990 688, Nov. 23, 1999

[8.10] G B Kliman, S B Lee, M R Shah, R M Lusted, and N K Nair, "*A New Method for Synchronous Generator Core Quality Evaluation,*" IEEE Trans. Energy Convers., Vol. 19, NO. 3, , Sep. 2004, pp. 576–582

[8.11] R Mazurek, P Marketos, A J Moses and J N Vincent "*Effect of Artificial Burrs on the Total Power Loss of a Three-Phase Transformer Core*", IEEE Trans. Magn., Vol. 46, No. 2, 2010, pp.638 - 641

[8.12] R Mazurek, H Hamzehbahmani, A J Moses, P I Anderson, F J Anayi and T Belgrand, "*Effect of Artificial Burrs on Local Power Loss in a Three-Phase Transformer Core*" IEEE Trans. Mag. VOL. 48, NO. 4, APRIL 2012, pp 1653-1656

[8.13] H Hamzehbahmani, A J Moses and F J Anayi “*Opportunities and Precautions in Measurement of Power Loss in Electrical Steel Laminations Using the Initial Rate of Rise of Temperature Method*” IEEE Trans. Mag. VOL. 49, NO. 3, March 2013, pp 1264- 1273

[8.14] UKAS M3003, “*The Expression of Uncertainty and Confidence in Measurement*”, 1997

[8.15] H Hamzehbahmani, P Anderson, J Hall and D Fox, “*Eddy Current Loss Estimation of Edge Burr affected Magnetic Laminations Based on Equivalent Electrical Network-Part II Analytical modelling and Experimental Results*”, IEEE Trans. on Power Delivery, Vol. 29, No. 2, April 2014, pp. 651-659

[8.16] M C Marion-Pera, “*Characterization of SiFe Sheet Insulation*”, IEEE Trans On Magn, Vol 31 . No 4. JULY 1995

[8.17] BS EN 10282: 2001 “*Method of Test for the Determination of Surface Insulation Resistance of Electrical Sheet and Strip*”

[8.18] R S Girgis , E G Nijenhuis , K Gramm and J E Wrethag "*Experimental Investigations on Effect of Core Production Attributes on Transformer Core Loss Performance*", IEEE Trans. Power. Del., vol. 13, no. 2, pp.526 -531 1998

[8.19] Bil Energy Systems Limited, Available at www.bilenergy.com/, July 2014

[8.20] Intermountain Electronics, Inc., Available at www.intermountainelectronics.com/, July 2014

[8.21] I Daut and A J Moses, "*Some Effects of Clamping Pressure on Localized Losses and Flux Distribution in a Transformer Core Assembled From Power core Strip*", IEEE Trans. Magn., Vol. 27, pp.5262 -5264, 1991

[8.22] B Weiser, A Hasenzagl, T Booth, and H Pfützner, "*Mechanisms of Noise Generation of Model Transformer Cores*," Journal of Magnetism and Magnetic Materials, vol. 160, pp. 207-209, 1996

[8.23] B Weiser and H Pfützner, "*Relevance of Magnetostatic Forces for Transformer Core Vibrations*," J. Phys. IV France, vol. 08, pp. Pr2-591-Pr2-594, 1998

[8.24] Z Godec, “*Comparison of Tests for Insulating Coatings on Steel Sheet*” IEEE Trans on Electrical Insulation Vol. EI-15 No.2, April 1980, pp. 95-103

[8.25] J H Walker, G J Rogers and R L Jackson, "*Pressing and Clamping Laminated Cores*", Proc. IEE (London), Vol. III, No. 3, 1964

CHAPTER 9

General Conclusion and Suggestions

9.1. Conclusion

Magnetic properties of the electrical steel laminations, *i.e.* flux density distribution, eddy current, eddy current power loss and complex relative permeability, were studied over a wide range of magnetisation. The investigations have shown that these properties strongly depend on skin effect, especially at high frequencies and high permeabilities. At low frequencies where skin effect is negligible, flux density along the thickness of the lamination is distributed almost uniformly. Increasing the magnetising frequency leads to the distribution of the flux density to be non-uniform and decreases from the surface to the centre of the lamination. The distribution pattern of flux density has a strong dependence on the magnetising frequency and relative permeability of the material.

An equivalent circuit model was proposed for the magnetised laminations to calculate and predict the eddy current loss over a wide range of magnetisation. An experimental-analytical model was also developed to separate core loss components using the total core loss measurements. It was found that the determination of eddy current loss and separation of loss components depend on the relationship between ***B*** and ***H***, non-uniform flux density distribution and complex permeability; in which the last two factors are related to skin effect.

The enhanced eddy current model will also be useful for higher frequency operation of laminated stacks particularly in areas such as traction and other electric transportation.

The developed model of eddy current loss was then implemented to study the influence of a wide range of magnetising frequencies and relative permeabilities on the magnetic properties of the GO electrical steels. The results highlighted that magnetising frequency and peak flux density are two determinant factors with a significant effect on the magnetic properties of electrical steels and should be taken into account in the relevant studies of the magnetic properties of steel cores.

Inter-laminar short circuit faults, as an un-desirable phenomenon in magnetic cores, were modelled and simulated to show their influence on the performance of magnetic cores. The developed analytical model of eddy current loss of a single strip lamination was modified to predict the extra eddy current loss caused by inter-laminar short circuit faults. 2-D FE modelling was performed to study the effect of inter-laminar faults on the configuration of magnetic cores and visualise eddy current paths along the lamination thickness. Based on the FE modelling and analytical results, skin effect was found as a determinant factor on the magnetic properties of magnetic cores not only at high frequencies, but also at low frequencies when the core is affected by the inter-laminar faults.

High values of inter-laminar fault currents, the extra losses and heating were interpreted as a result of increasing the effective thickness of the shorted laminations. As a consequence, distribution of flux density, complex relative permeability, eddy current and hence eddy current loss are significantly affected by the inter-laminar faults, even at low frequency magnetisation. This effect becomes more significant by increasing number of the shorted laminations in the core.

Inter-laminar short circuit faults were modelled experimentally on stacks of Epstein sized laminations of GO steel in two different stages: inter-laminar faults at set positions along side of packs of laminations, inter-laminar faults of different configurations and distributed at random positions. Based on the experimental results, it was found that numbers of the shorted laminations, position of the fault points, angular off-set between the fault current loop and magnetising direction, electrical resistance between the fault points are key-factors in the formation of the fault current loops and determination of the extra power loss and hence extra local heat caused by the inter-laminar faults.

The models developed will enable the significance of faults discovered to be assessed. It is likely that most large stacks will exhibit some inter-laminar faults but, as shown in this work, depending on the size, number and arrangement, they may be insignificant.

It was also indicated that the extra losses caused by the applied short circuit occur in a larger region than that of the shorted zone. This suggests that inter-laminar fault currents do not flow in a straight line just between the shorted points of the fault current loops.

In the last part of this project a non-destructive electro-magnetic method was developed to detect inter-laminar short circuit faults on magnetic cores based on a Flux Injection Probe (FIP). Low-power requirement, easy to implement and easy to interpret the results are the main advantages of this technique. Experimental results showed that this technique is able to detect inter-laminar faults between as few as 2 laminations. Apart from the inter-laminar fault detection, quality of the clamping pressure on magnetic cores can be evaluated by this method. This can be implemented during core assembling, before putting the winding on the core and during the periodic inspections of electrical machines.

The FIP assessment technique has already attracted interest from a large international transformer manufacturer as a method of non-destructively evaluating the core stacks prior to transformer assembly. By enabling this evaluation, the method will avoid the detection of faults after final assembly (including assembly of windings, tanking, oil filling, adding bushings etc) or, in the worst case, in service. The additional cost, time and inconvenience of stripping down a transformer, or even taking it out of service, could be avoided through the use of this step.

9.2. Suggestions

Although the hypothesis, methodologies, results and achievements of this thesis can be extended to real scale magnetic cores, the situation of the inter-laminar short circuit faults in real scale electrical machine, especially in stator cores, is more complicated. The importance of these kinds of faults is well-known to the manufacturers and customers of the electrical machines, therefore the following notes can be suggested as future work in this area.

Develop a detailed 3-D FE or analytical model of the laminated cores including electric and magnetic properties of the material in 3 directions, and other related parameters and criteria, in high accuracy modelling of the inter-laminar fault.

Accurate inspection of the defected laminations detected by the FIP, or other inter-laminar fault detection methods, and investigation of the effect of clamping pressure, especially non-uniform distributed pressure, on the inter-laminar fault detection.

This information and the relevant results can be very important for manufacturers of electrical steel laminations and electrical machines to qualify the magnetic cores and further characterise and predict the effect of inter-laminar faults at the design and operating stages.

APPENDIX I – LIST OF PUBLICATIONS

Journal papers:

1. **H Hamzehbahmani**, P I Anderson, J Hall and D Fox, "*Eddy Current Loss Estimation of Edge Burr affected Magnetic Laminations Based on Equivalent Electrical Network-Part I Analytical modelling and Experimental Results*", IEEE Transactions on Power Delivery, Vol. 29, NO. 2, April 2014, pp 642-650
2. **H Hamzehbahmani**, P I Anderson, J Hall and D Fox, "*Eddy Current Loss Estimation of Edge Burr affected Magnetic Laminations Based on Equivalent Electrical Network-Part II Analytical modelling and Experimental Results*", IEEE Transactions on Power Delivery, Vol. 29, NO. 2, April 2014, pp 651-659
3. **H Hamzehbahmani**, A J Moses and F J Anayi "*Opportunities and Precautions in Measurement of Power Loss in Electrical Steel Laminations Using the Initial Rate of Rise of Temperature Method*" IEEE Trans. Mag. VOL. 49, NO. 3, March 2013, pp 1264- 1273
4. **H Hamzehbahmani,** P I Anderson, J Hall and K Jenkins, "Inter-laminar Insulation Faults Detection and Quality Assessment of Magnetic Cores Using Flux Injection Probe", IEEE Transaction on Power Delivery, (Accepted to be published, 2015)
5. **H Hamzehbahmani,** P I Anderson and S Preece, "An application of an Advanced Eddy Current Power Loss Modelling to Electrical Steel in a Wide Range of Magnetizing Frequency" IET Science, Measurement & Technology (Accepted to be published, 2015)
6. **H Hamzehbahmani,** P I Anderson and K Jenkins, M Lindenmo, "Experimental Study on Inter-Laminar Short Circuit Faults at Random Positions in Laminated Magnetic Cores", IEEE Transactions on Magnetic, August 2014 (Under review)

Conference papers:

1. **H Hamzehbahmani**, P Anderson, J Hall, K Jenkins, "Inter-laminar insulation faults detection and quality assessment of magnetic cores using flux injection probe", 6th International Conference on Magnetism and Metallurgy, Cardiff-UK, June 2013, pp.428-433
2. **H Hamzehbahmani**, P Anderson, J Hall, D Fox, "Inter-laminar insulation faults detection in magnetic cores using flux injection probe", Soft Magnetic Materials Conference (SMM21), Budapest-Hungary, (2013)
3. **H Hamzehbahmani**, P Anderson, J Hall, D Fox, "Modeling inter-laminar insulation faults at random positions in laminated magnetic cores", Soft Magnetic Materials Conference (SMM21), Budapest-Hungary, (2013)

APPENDIX II – REMEMBRANCE

In memory of the physicists and scientists (Sorted by date):


Khawaja Nasir Tūsī
1201-1274


William Gilbert
1544-1603


Blaise Pascal
1623-1662


Isaac Newton
1643-1727

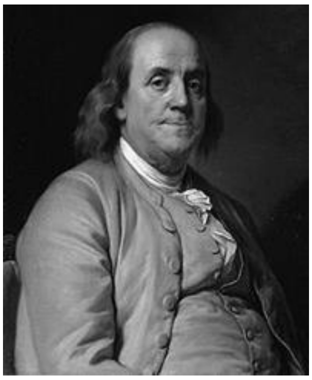
Benjamin Franklin
1706-1790

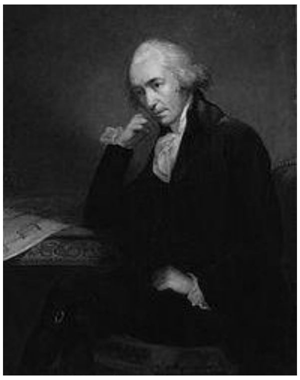
James Watt
1736-1819


Alessandro Volta
1745-1827


Jean Baptiste Joseph Fourier
1768–1830

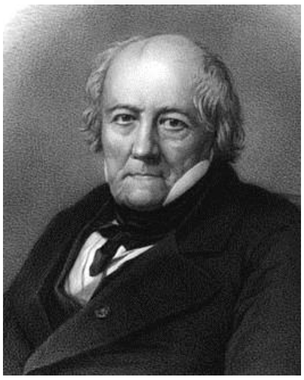
Jean Baptiste Biot
1774 - 1862

André-Marie Ampère
1775-1836

Carl Friedrich Gauss
1777-1855

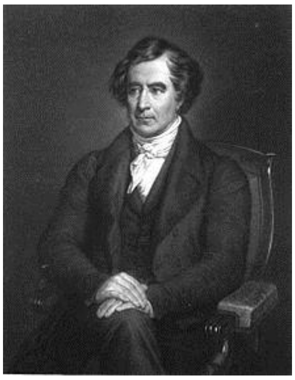

François Arago
1786–1853

Georg Ohm
1789-1854

Michael Faraday
1791-1867

Joseph Henry
1797-1878

Heinrich Lenz
1804-1865

Wilhelm Weber
1804-1891

Léon Foucault
1819-1868

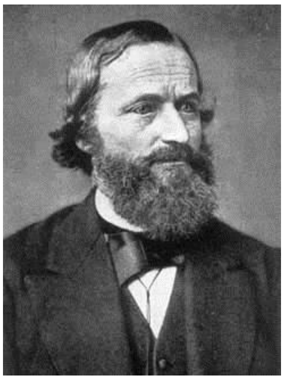

Gustav Robert Kirchhoff
1824 - 1887

James Clerk Maxwell
1831-1879

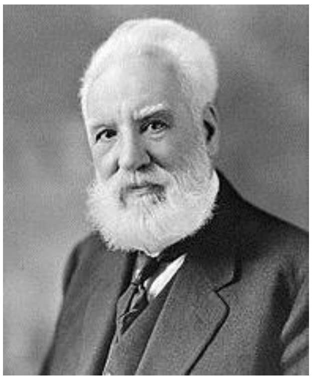

Alexander Graham Bell
1847-1922

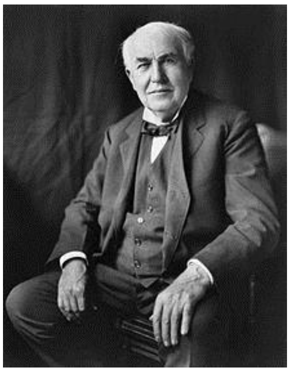

Thomas Alva Edison
1847-1931

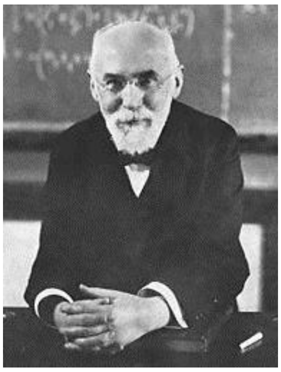

Hendrik Antoon Lorentz
1853-1928

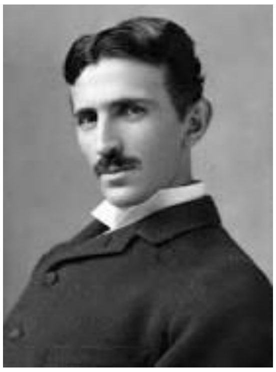

Nikola Tesla
1856-1943

Heinrich Rudolf Hertz
1857–1894

Léon Charles Thévenin
1857-1926

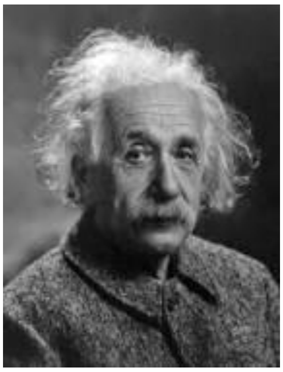

Albert Einstein
1875-1955

Edward Lawry Norton
1898-1983

Norman P. Goss
1902–1977

Lotfali Askar Zadeh
1921-

Rudolf (Rudy) Emil Kálmán
1930-

Anthony John Moses
1942-

Stephen Hawking
1942-